

Trinity College Dublin
Coláiste na Tríonóide, Baile Átha Cliath
The University of Dublin

On the hydrogen embrittlement of an additively manufactured CoCrFeMnNi high entropy alloy

Jan Mellrick Dugenio

A thesis submitted in fulfillment of the requirements for the degree
Doctor of Philosophy
at Trinity College Dublin, *the University of Dublin*, Ireland.

Supervisor: Dr. Rocco Lupoi

Co-supervisor: Dr. Minh-Son Pham

July 2025



Trinity College Dublin
Coláiste na Tríonóide, Baile Átha Cliath
The University of Dublin

On the hydrogen embrittlement of an additively manufactured CoCrFeMnNi high entropy alloy

Jan Mellrick Dugenio







Declaration

I have read and understood the plagiarism provisions in the General Regulations of the University Calendar for the current year, found at http://www.tcd.ie/calendar.

I have also completed the Online Tutorial on avoiding plagiarism 'Ready Steady Write', located at http://tcd-ie.libguides.com/plagiarism/ready-steady-write.



JanMell Dugenio, July 2025

Acknowledgments

A massive thank you to all the people who have contributed to the completion of this thesis. I am indebted to a large number of them some of which I may have missed but know that I am truly grateful.

First, I would like to express my gratitude to my supervisor, Prof. Rocco Lupoi and my co-supervisor Prof. Minh-Son Pham for the insights that helped me in every stage of the PhD. Moreover, thank you for being gracious and forgiving and always advocating for me. My sincerest thanks to the members of my examination panel for their suggestions and corrections that improved this work: to Prof. Domenico Maisano of Politecnico di Torino, my external examiner; Prof. Daniel Trimble, my internal examiner and to Prof. Michael Gibbons, the panel chair.

The most important portion of this research was done in collaboration with Dr. Alfredo Zafra and Dr. Emilio Martinez-Paneda. Truly, this thesis would not have been possible without the guidance, time and effort of Dr. Zafra and the opportunity provided by Prof. Martinez-Paneda by agreeing to collaborate. Their research group, Mechanics of Materials, which was formerly based in Imperial College London and now in the University of Oxford welcomed me warmly. From Dr Livia Cupertino Malheiros who helped me with my samples to Maciej, Theo, Lorenzo and Evzen who have become good friends of mine, thank you so much.

The bulk of the characterisation techniques employed in this thesis was done with the help of the wonderful staff and students in the Advanced Microscopy Laboratory (AML) and Additive Research Laboratory (ARL) in Trinity College Dublin. Thank you very much to Meghan, Clive, Raman, Mina, and Cathal, and to former staff Dermot and Hugh for never hesitating to lend a hand and train not just me but a lot of students on advanced characterisation techniques.

During my PhD journey I have spent some time in Imperial College London conducting experiments. Thank you to my fellow PhD students especially to Claudia, who is the brightest ray of sunshine ever, for going out of her way to help me with my experiments. Thank you to Alex and Jessica, Cynthia and Parul, and to Son's research group members for making my Imperial visits memorable.

Possibly one of the coolest experience I have had while doing my PhD was when I spent five months in Max Planck Institute for Sustainable Materials in Düsseldorf, Germany. Thank you very much to the Atom Probe Tomography Group led by Dr. Baptiste Gault for hosting my placement. A million thanks to Dr Aparna Saksena for the time and effort in assisting and conducting APT experiments and data analysis for me. To Mr. Andreas Sturm and Mr.

Christian Bross for the training sessions, thank you very much. To everyone in the institute who have been very helpful, to Ezgi, Yonqiang, Gabby, Mr. Ray, Xizhen, Eric, the rest of the APT group and to my best bud Selase, thank you.

I would like to thank Professor Lewys Jones for the invaluable support and advice not just academically but also in life. Thank you for always showing me your willingness to listen and help in bad times and sharing a laugh or two in good times. Thank you to Professor Valeria Nicolosi for the encouragement and the inspiration to be a strong, empowered woman. I will always keep your wise words in mind. Thank you to the CDT-ACM and AMBER staff and personnel as well as to the former Centre Manager, Sandra.

I express my appreciation to my fellow PhD students in the CDT, AML and in Rocco's group and to the ever helpful personnel in Parson's Building. Thank you most especially to Connie, Arnie, Kavin, Megha, Theo, Rob and Patrick for being supportive and uplifting and creating a wonderful environment around me.

Finally, I would like to thank my family and friends, especially my mom Imelda and my late father Eric. I am also deeply thankful to my best friend Malu and to my Notley family. To my friends Crismehel, Leo and Camille and the Pinoy PhDs bunch Michael, Crisron, Arnie, Tracy, Roland, Gian and most especially, Charmaine. Thank you all for keeping me sane, always having my back and encouraging me to move forward.

JanMell

iii

To my late father, Eric, who, if he were still alive, would never really read this thesis but would surely drink to it.

"The speed with which all of them vanish- the objects in the world, and the memory of them in time. And the real nature of the things our senses experience, especially those that entice us with pleasure or frighten us with pain or are loudly trumpeted by pride. To understand those things- how stupid, contemptible, grimy, decaying, and dead they are- that's what our intellectual powers are for."

-Marcus Aurelius, Meditations 2.12

Abstract

The field of study on the hydrogen embrittlement of CoCrFeMnNi high entropy alloy manufactured by laser powder bed fusion are wrought with issues related to short electrochemical charging durations leading to low hydrogen ingress into the sample. This cascades to the subsequent analysis of the hydrogen trapping and diffusion parameters which are essential in characterising hydrogen behaviour in successfully designing hydrogen resistant alloys. That is, trapping and diffusion analysis are mostly done with simplifying assumptions that are not validated such as whether the diffusion is lattice-dominated or dissociation -controlled. Moreover, there is a lack of understanding on the role of additive manufacturing microstructure in hydrogen trapping and embrittlement and lack of reports that identify the challenges in mapping hydrogen-alloy interactions using atom probe tomography. To address these issues, prolonged electrochemical hydrogen charging to ensure hydrogen saturation of specimens were conducted. Moreover, thermal desorption analysis was utilised as a microstructure sensitive technique to relate microstructural conditions to hydrogen trapping as well as to calculate hydrogen diffusivity for the alloy in the as-printed, annealed and wrought conditions for comparison. Atom probe tomography was employed for direct detection and mapping of hydrogen on microstructural defects and challenges in the successful utilisation of the technique were identified.

The prolonged hydrogen charging at elevated temperature resulted to 0.5 mm-thick specimens to be saturated with hydrogen with approximately 100% brittle fracture zone in the gauge fracture surface, and increased hydrogen penetration depth in 1 mm thick samples. The hy-

drogen saturation entails maximum trap occupancy allowing for the validity of the assumption of local equilibrium necessary for the correct application of the McNabb and Foster and Oriani models of hydrogen trapping. With these conditions satisfied, it was shown that the alloy in both as-printed and annealed conditions contains mostly weak, reversible traps of similar binding energies (∼20 kJ/mol). However, the annealed samples have a trap density an order of magnitude less than the as-printed specimen. These weak traps were associated with dislocations and grain boundaries and possibly coherent secondary particles such as nano-oxides or nano-precipitates. This correlates to the presence of numerous dislocations arranged in a network of interconnected cells in the as-printed sample which were reduced and disintegrated after annealing. The annealed samples were shown to have significantly less hydrogen content than the as-printed sample with calculated diffusivities of 2.52 x 10^{-14} m^2/s for the as-printed sample and 1.24 x 10^{-15} m^2/s for the annealed sample. For reference, the diffusivity for the wrought sample was calculated to be 8.05 x 10^{-16} m^2/s which is the lowest among the three specimens. The presence of a relatively higher reversible trap density and hydrogen diffusivity manifested in severe hydrogen embrittlement of as-printed samples during slow strain rate testing. Annealed samples showed a significant recovery of ductility, measured in terms of reduction in area, of up to 30%. The decrease in the hydrogen embrittlement susceptibility of annealed samples point to the role of dislocations and dislocation network in hydrogen-assisted cracking. For as-printed samples, the intact interconnected dislocation network with dense dislocations on cell walls resulted to high local hydrogen concentration, facilitating hydrogen mobility and thus, hydrogen-assisted cracking along the cell boundaries and interdendritic regions in addition to grain boundary decohesion due to the high hydrogen concentration. On the other hand, reduction of dislocation density and disintegration of the dislocation network resulted to relatively lower localised hydrogen concentration with hydrogen facilitating the mobility of dislocations instead. This resulted to increased plasticity which can explain the recovery of ductility in the tensile tests. Moreover, the hydrogen concentration may have been reduced to within a range

that is enough to lower the stacking fault energy of the atoms and trigger nanotwinning in the annealed samples. Fractography revealed a typical transgranular ductile fracture due to microvoid coalescence in both as-printed and annealed samples without hydrogen. In contrast, hydrogen pre-charged samples exhibited a brittle fracture zone that is mainly intergranular and interdendritic with regions of quasi-cleavage for as-printed samples and a similar fracture surface for annealed samples albeit with the increased presence of ductile features such as microvoids in certain regions and slip traces. As expected, the brittle fracture zone was greater in the as-printed samples. These observations, in conjunction with the analyses of fractographs point to hydrogen enhanced decohesion (HEDE) mechanism as the dominant hydrogen embrittlement mechanism in the as-printed sample whereas for the annealed sample, a synergy of hydrogen enhanced localised plasticity with hydrogen enhanced decohesion, or plasticity-mediated HEDE. Direct detection of hydrogen in microstructural traps by atom probe tomography were met with challenges in sample preparation and deuterium gas charging, with deuterium unable to penetrate into additively manufactured samples and focused ion beam and energetic electrons from Transmission Kikuchi Diffraction inducing damage to the specimen making it difficult to identify inherent traps in the microstructure.

Contents

1 Introduction **1**

1.1 Additive Manufacturing as Fabrication Route 3

1.2 Hydrogen properties of the Cantor alloy 5

1.3 Aim and scope of present investigation 8

1.4 Overview of the study 9

2 Literature Review **10**

2.1 What is additive manufacturing? 10

2.2 On the CoCrFeMnNi HEA manufactured by laser powder bed fusion 16

2.3 Hydrogen and the Cantor alloy 20

2.3.1 Introduction to hydrogen embrittlement 20

2.3.2 Hydrogen trapping and kinetics 23

2.3.3 Mechanisms of hydrogen embrittlement 28

2.3.4 Quantifying and mapping hydrogen-metal interactions 31

2.3.5 Hydrogen embrittlement in CoCrFeMnNi HEA 35

2.4 Summary 41

3 Experimental Methods and Characterisation Techniques **42**

3.1 Powder Analysis 43

3.2 Additive Manufacturing 44

3.3 Phase Determination and Elemental Analysis 44

3.4 Metallurgical Sample Preparation 45

3.5 Mechanical Testing 45

3.6 Microstructure Characterisation and Fractography . . . 46
3.7 Hydrogen charging . . . 46
3.8 Thermal Desorption Spectroscopy . . . 47
3.9 Atom Probe Tomography . . . 50
3.10 Summary . . . 51

4 Microstructure and properties of an equiatomic CoCrFeMnNi high entropy alloy manufactured by laser powder bed fusion 53

4.1 Introduction . . . 54
4.2 Experimental Methods . . . 56
4.2.1 Microstructural Characterisation . . . 56
4.2.2 Mechanical Testing . . . 58
4.3 Results . . . 58
4.3.1 Physical Characteristics of the build . . . 58
4.3.2 Microstructure of AM CoCrFeMnNi HEA . . . 59
4.3.3 Discussion . . . 77
4.4 Summary . . . 83

5 Evaluation of hydrogen diffusion, trapping and embrittlement in an additively manufactured CoCrFeMnNi high entropy alloy 85

5.1 Introduction . . . 86
5.2 Methods . . . 87
5.2.1 Hydrogen charging . . . 88
5.2.2 TDS measurements . . . 90
5.2.3 Tensile tests . . . 93
5.2.4 Atom Probe Tomography . . . 93
5.3 Results . . . 95
5.3.1 Hydrogen diffusivity . . . 103
5.3.2 Effect of hydrogen charging on tensile properties . . . 104
5.3.3 Fractography . . . 106
5.3.4 Challenges in the direct detection and mapping of hydrogen using atom probe tomography . . . 108

5.4 Discussion 123
5.4.1 Effect of specimen thickness on hydrogen diffusion and trapping 123
5.4.2 Isothermal TDS measurements and H-diffusivity 124
5.4.3 Quantifying and mapping hydrogen 125
5.4.4 Influence of dislocation cells in hydrogen embrittlement mechanism 127
5.5 Summary 129

6 Conclusions and outlook **132**

Bibliography **160**

Appendices **161**

A Design of Experiment **162**

B Indexing of XRD Data and Multiple Whole Profile Method **165**

C Initial TDS experimental run **166**

D ITDS Fitting **170**

E TDS Simulator **175**

F Sample preparation for atom probe tomography **179**

List of Figures

2.1 The laser powder bed fusion process. 12

2.2 Parameters involved in the LPBF process. 13

2.3 Basic scanning strategies in the ProX 200 DMP. They differ from machine to machine. 14

2.4 Characteristic pores in LPBF parts: A) gas pores, b) incomplete melting pores, c) lack of fusion pores d) cracks. Reproduced from Sola, *et.al.* 2019[39]. 15

2.5 SEM micrographs and TEM images showing the "fish scale" microstructure, dislocation cells and oxide-rich nanoprecipitates and fine epitaxially growing columnar cells undergoing side-branching in response to changes in thermal gradient direction. Reproduced from Pham *et.al.* 2020[16]. 18

2.6 STEM-EDX analysis showing elemental segregation in LPBF CoCrFeMnNi HEA. Reproduced from Jin, et.al. 2020[47] 19

2.7 Schematic diagram of the effects of annealing on the microstructure of as-printed HEA (adapted from Torralba, et.al., 2020[53]) 20

2.8 Schematic diagram of hydrogen adsorption on metal surface and hydrogen absorption inside the metal. Energies of hydrogen in H-metal equilibria: E_s, energy of solid solution; E_m, migration energy; E_b, trap binding energy. Adapted from [26], [60]. 23

2.9 Octahedral and tetrahedral interstitial sites in fcc and bcc lattices (shaded circles) and illustration of the lattice distortion in FCC high entropy alloy. Reproduced from [56], [64] 25

2.10 Various types of lattice defects in metals(adapted from [65], [66]) 26

2.11 Schematic illustration of energy states of hydrogen in lattice and trap sites in metals. 27

2.12 Examples of fracture surfaces for different fracture modes. Dimples characteristic of microvoid coalescence (a1,b1) suggest ductile fracture in the absence of hydrogen. Brittle fracture due to hydrogen includes cleavage (a2), intergranular cracking (a3,b3) and quasi-cleavage(b2)(adapted from Wang,et.al., Martin, et.al., and Wada, et.al.[71]–[73]) 29

2.13 Schematic diagram showing interaction of lattice defects such as vacancies and certain solutes, dislocations, grain boundaries, phase interfaces, triple points, precipitates, micro- and nano-cracks, surface steps, voids, and surface oxide layers. Adapted from Koyama, *et.al.* 2017. 30

2.14 Plastic slip bands at hydrogen-assisted integranular fracture facet in Ni alloy (a); tear ridges on grain boundary facets of Cd-plated steel (b). Reproduced from Martin, *et.al.*, (2012) and Lynch, (2019) [72], [78]. 32

2.15 Schematic illustrations of the three dominant mechanisms of hydrogen embrittlement, HEDE (top), HELP (middle) and HELP+HEDE (bottom) [79], [80]. . . . 33

2.16 Schematic of a hydrogen desorption profile together with indication of the corresponding trap sites. Reproduced from Abe,at.al.(2011)[95] 34

2.17 (a) APT revealing the deuterium distribution at a vanadium carbide precipitate. (b) Comparison of deuterium and hydrogen distributions in Ag, revealing that deuterium is more indicative when aiming to reveal microstructure-related effects. Reproduced from Koyama,et.al.2017[74]. 36

2.18 Schematic of the lattice distortion in example HEA and 3D isosurface of electronic density. Reproduced from Ren, *et.al.* (2019)[101]. 37

3.1 Coordinate system and schematic of sample cut direction. 45

3.2 Tensile specimens. Thicknesses of 0.5 mm, 1 mm and 2 mm were used in the study. 46

3.3 (a)The electrochemical hydrogen charging set-up. Reproduced from Zafra, *et.al.* (2022)[116] (b) Dimensions of the specimens used for TDS. 47

3.4 Schematic setup of the TDS measurement. A shielded and differentially pumped quadropole mass spectrometer preferentially detects desorbing gas from the front side of the heated sample. Reproduced from Ogura, et.al.(2018)[117]. 48

3.5 Schematic representation of the thermal desorption spectrometer used in this work. Reproduced from Zafra, et.al. (2022) [116]. 49

3.6 Schematic diagram of the mechanism underlying APT measurements. Reproduced from Chen, et.al. (2023)[111] 51

4.1 Powder feedstock used for printing SLM CoCrFeMnNi (a), with the average particle size of 17.5 μm (b), the scanning strategy employed when printing is normal, back and forth with interlayer rotation of 67° (c), Tensile specimens were extracted parallel to the build as indicated, dog-bone tensile specimens have dimensions specified in (d). 57

4.2 Dimensions of the tensile specimens that were used for the mechanical testing for this chapter. 58

4.3 Defects and lack of fusion in the preliminary build 59

4.4 Optical microscope images of the polished surfaces for (a) as-printed samples and (b) annealed specimen 60

4.5 XRD spectra of the powder and printed builds. 61

4.6 SEM image with the elemental distribution map, elemental composition and EBSD phase map. 62

4.7 Grain size comparison for two specimens at different microstructural conditions. The median is used as a measure of central tendency to reduce the influence of extreme values. 63

4.8 EBSD IPF-Z maps showing grain structure of (a,c) LPBF-AP and (b) LPBF-Ann samples 64

4.9 Pole figures associated with the (a) LPBF-AP and (b) LPBF-Ann specimens. . . 65

4.10 Etched microstructure of the as-printed specimen 66

4.11 (a,b) Surface of as-polished LPBF-Ann specimen as seen under the SEM. (c,d) Etched microstructure of the LPBF-Ann specimen showing numerous etch pits. Fusion boundaries are less pronounced. 67

4.12 Comparison of SEM images of pores in (a) LPBF-AP and (b) LPBF-Ann specimens. 67

4.13 Electron channeling contrast (ECC) images showing the dislocation network in (a) LPBF-AP and (b) LPBF-Ann specimens. The yellow arrows indicate nano-oxides. 68

4.14 Kernel Average Misorientation (KAM) maps of (a) LPBF-AP and (b) LPBF-Ann specimens Step size: 50 nm. 68

4.15 Geometrically necessary dislocation (GND) maps of (a) LPBF-AP sample with the GND density distribution (b) and (c) LPBF-Ann sample with its associated GND density distribution (d) 69

4.16 Summary of the grain boundary character of the LPBF-AP and LPBF-Ann specimens. 70

4.17 Atom probe tomography reconstructed maps of the (a) bulk as-printed sample at 30 at.% Mn isoconenctration surface showing fine particles with region of interest indicated by cylinder (b) 1-D concentration profile of selected nanoparticle along the longitudinal axis of the cylinder (c) LPBF-Ann reconstructed map of the bulk sample showing region with nanoparticle and (d) 1-D concentration profile of selected particle along the long axis of the cylinder as region of interest. 71

4.18 Atom probe tomography reconstructed maps of the LPBF-AP specimen showing (a) all major distribution of ions overlaid on a manganese isosurface showing region of elemental segregation (b) top view of the specimen tip (c) proxigram of a cylinder constructed across the region of elemental segregation showing enrichment of Mn and Ni. 74

4.19 True stress-strain curves of 2 mm-thick as-printed samples. 2-mm thick samples were used in conformance to a modified ASTM-E8 standard for better comparison with other studies in Table 4.2 75

4.20 Representative stress-strain curves for the as-printed and annealed specimen (1 mm thickness) 76

4.21 Fractured surfaces of the as-printed specimen (a,b). Comparison of dimples for as-printed (c) and annealed (d) fractured surfaces at 5000x magnification. 76

4.22 Illustration of the oxidation mechanism of equiatomic CoCrFeMnNi. Reproduced from Agustianingrum, *et.al.* (2020)[140]. 78

4.23 Interaction of dislocations with a nano-oxide. 79

4.24 Deformed sample showing the intact dislocation network in the vicinity of a crack. 82

5.1 Dimensions of the (a)Tensile specimens (b) TDS specimens used for this chapter. 88

5.2 The electrochemical hydrogen charging set-up 89

5.3 The atom probe tomography set-up within the Laplace Project at the Max Planck Institut für Nachhaltige Materialien (Max Planck Institute for Sustainable Materials) in Düsseldorf, Germany comprising of the (a) CAMECA LEAP R5108 XR, (b) the React Hub Module showing the specimen puck (c) inside the chamber for deuterium charging and (d) the pre-cooled UHV suitcase that allows for the transfer of the specimen to the atom probe. 94

5.4 Fitted TDS spectra of (a) as-printed LPBF and (b) wrought CoCrFeMnNi HEA. The TDS samples have thicknesses of less than 0.5 mm. Note that these samples are assumed to be saturated with hydrogen after 7 days of charging. 96

5.5 Comparison of the TDS spectra of 1-mm thick as-printed vs annealed LPBF samples. 98

5.6 Linear fit of Kissinger's formula for the LPBF-AP and LPBF-Ann specimens. . . 101

5.7 Using the inference fitting capabilities of *TDS Simulator* to gain insight into the trapping characteristics of an AM Cantor alloy: experimental and simulated desorption curves, with the latter being obtained using TDS Simulator's optimization algorithm, and contribution of each relevant type, as determined by *TDS Simulator* for (a,b) LPBF-AP and (c,d) LPBF-Ann. In (b and d), traps are ordered from smaller to larger absolute binding energy, $\Delta H = E_b$. Goodness of fit measured by coefficient of determination (adjusted R^2): (a) 0.9981 (c)0.9984 110

5.8 Isothermal TDS and numerical fitting for diffusivity calculations. Isothermal TDS (ITDS) experiments performed at (a) 22°C and (b) 200°C and the best fit to 1-D hydrogen transport FE simulations. 111

5.9 Hydrogen diffusivity at different temperatures fitted to the Arrhenius relationship D = D_0exp(-E_a/RT) where D_0 is the pre-exponential factor and E_a is the activation energy for diffusion. 113

5.10 Engineering stress-strain curves of hydrogen pre- charged and uncharged tensile samples: as-printed and annealed. The dashed lines represent replicates. 114

5.11 Necking observed in fractured tensile specimens: (a) LPBF-AP (b) LPBF-Ann . 115

5.12 SEM micrographs of the neck region in the fractured tensile specimens for (a) as printed and (b) annealed. 116

5.13 Caption 117

5.14 SEM micrographs of fracture surfaces of LPBF-AP specimen showing (a) step-wise cracking (b) hydrogen-affected zones (c) magnified image of ductile region in the middle of the fracture surface (d) magnified brittle region showing intergranular fracture with quasi-cleavage like features. 118

5.15 SEM micrographs of fracture surfaces of LPBF-Ann specimen showing (a) step-wise cracking (b) hydrogen-affected zones (c) magnified image of ductile region in the middle of the fracture surface (d) magnified brittle region showing intergranular fracture with quasi-cleavage like features. 119

5.16 LPBF-AP vs LPBF-Ann fracture surfaces. LPBF-AP(top) shows uniform, flat surface ridges, while LPBF-Ann(bottom) shows the presence of microvoids on the edges of surfaces (tear ridges). Also at higher magnification, slip bands on the cleavage facets are visible. All these point to 'plasticity-mediated' HEDE mechanism. 120

5.17 Electron back-scattered diffraction image of a step-wise crack on the surface of a charged fracture specimen showing intergranular decohesion both at grains with large and small misorientation. 121

5.18 Atom probe tomography reconstruction of the LPBF-AP specimen showing (a) all major distribution of ions, (b) Nickel distribution and cylinder for 1-D concentration profile (c) mass spectra (d) proxigram of all major elements between bulk sample and region of interest. 121

5.19 Atom probe tomography reconstruction of the LPBF-Ann specimen showing (a) all major distribution of ions,(b) 1-D concentration profile along the z-axis showing significant Mn depletion supporting the previous report of Mn evaporation (c) mass spectra showing no peak corresponding to Deuterium and (c) distribution of oxygen in the specimen. 122

5.20 Atom probe tomography reconstruction of the HEA-W specimen showing (a) all major ion distributions, (b) the mass spectra with peaks corresponding to deuterium, (c) the total distribution of H/D in the sample and (d) top view isosurface showing H/D clusters 122

5.21 EBSD scan of a long crack propagating along the gauge area of the tensile specimen (a) LPBF-AP (b) LPBF-Ann 126

5.22 ECC image and corresponding Kernel Average Misorientation map of a crack in the LPBF-AP sample showing a possible path for crack propagation following dislocation cells network. 127

5.23 Schematic illustration of the hydrogen embrittlement mechanism of (a) LPBF-AP specimen showing dense dislocation network and possible path of hydrogen-assisted cracking along the cellular interdenditic regions and grain boundary decohesion (HEDE) and (b) LPBF-Ann where dislocation density is reduced and dislocation network has disintegrated owing to reduced hydrogen decoration in the cell walls giving rise to possible microvoid coalescence and other plastic features signifying plasticity (HELP) mediated HEDE. 128

5.24 Deformation nanotwins in proximity to a crack in LPBF-Ann samples. 129

A.1 A schematic representation of central composite design for a system with 3 parameters consisting of a centre point (pentagon), star(axial) points (squares), and fractional points(circles). 162

A.2 Arrangement of specimens on the build plate 164

C.1 (a) Predicted concentration profile for $D_H = 9.6 \times 10^{-15}\ m^2/s$ for 7 days vs (b) predicted concentration profiles for $D_H = 6.54 \times 10^{-13} m^2/s$ for different charging times. 167

C.2 (a) Engineering stress-strain curves for uncharged and pre-charged 0.5 mm thick samples (b) tensile curves for uncharged LPBF-AP and LPBF-Ann with thickness of 1 mm. 168

C.3 Fracture surface of (a) uncharged, (b) hydrogen pre-charged tensile samples. . . . 168

C.4 The entire length and width of the gauge area showing brittle fracture. 168

C.5 TDS desorption spectra of the three 0.5 mm thick LPBF-AP HEA samples. . . . 169

D.1 Filtered Data in Matlab® 171

D.2 Matlab® interface showing the (a) main code and (b) output of the COMSOL® fitting. 172

D.3 Output graph of the fitting for LPBF-AP at 22°C 173

D.4 Isothermal TDS and numerical fitting for diffusivity calculations. Isothermal TDS (ITDS) experiments performed at (a) 100°C and (b) 300°C and the best fit to 1-D hydrogen transport FE simulations. 174

E.1 Main graphical user interface (GUI) of the *TDS Simulator* in Matlab® and the four main tabs: a), model parameters tab (b), hydrogen traps tab (c), fit experimental data tab (d). 176

E.2 *TDS Simulator* raw output for LPBF-AP sample showing fit to the experimental data and the iterative process (bottom figure). 177

E.3 *TDS Simulator* raw output for LPBF-AP showing the trap densities and binding energies related to the fitting of experimental data. 178

F.1 (a) Lamella lift-out showing grain boundary, (b) sharpened tip of annealed specimen 179

List of Tables

2.1 Summary of types of hydrogen embrittlement[19]. 21

3.1 Elemental composition of the HEA powder 43

4.1 Parameters used for printing in the ProX® 200 DMP obtained from parametric study detailed in Appendix A 56

4.2 Tensile properties of the CoCrFeMnNi high-entropy alloy used in this study vs those reported in previous studies. Values for this study are averaged over duplicate samples. 72

4.3 Summary of the mechanical properties of the 1mm-thick as-printed and annealed tensile specimens 72

5.1 Diffusivity parameters used for predicted concentration profile. 95

5.2 Peak temperature and total hydrogen concentration for the wrought, as-printed and annealed LPBF samples. 97

5.3 Total hydrogen desorbed for the as-printed and annealed 1-mm LPBF samples. . 98

5.4 Calculated parameters for Kissinger's formula of the as-printed sample using 0.5 mm thick, hydrogen saturated TDS samples. 100

5.5 Activation energies of the peaks identified as trap sites in the TDS spectra of the specimens. 100

5.6 Average binding energies, E_b, and densities, N_t, of the two main trapping sites of LPBF-AP and LPBF-Ann specimens obtained from the *TDS Simulator* App. . . 103

5.7 Hydrogen diffusivity, D, obtained from isothermal TDS at different temperatures for as-printed, annealed and wrought specimens. 103

5.8 Comparison of hydrogen diffusivity values in literature for the CoCrFeMnNi HEA. Note the agreement of the calculated D_0 values in this work to previous work which validates ITDS as a viable method for calculating the diffusivity. 112

5.9 Mechanical properties of hydrogen pre-charged and uncharged 1-mm thick tensile samples of additively manufactured specimens 113

5.10 Brittle zone depth and brittle zone area fraction (BZAF) of hydrogen charged AM CoCrFeMnNi 113

A.1 Parameters of the CCD design of experiment 162

A.2 Experimental design parameters and densities of the builds. 163

C.1 Desorbed hydrogen concentration from TDS experiments. 169

D.1 The R^2 values for all the diffusivity fittings. 171

Nomenclature

LPBF	Laser Powder Bed Fusion
AM	Additive Manufacturing
HE	Hydrogen Embrittlement
H	Hydrogen
SLM	Selective Laser Melting
SS	Stainless Steel
HEA	High Entropy Alloy
CCA	Compositionally Complex Alloys
FCC	Face- Centered Cubic
SEM	Scanning Electron Microscopy
TEM	Transmission Electron Microscopy
EDM	Electric Discharge Machining
EBSD	Electron Backscatter Diffraction
APT	Atom Probe Tomography
TDA	Thermal Desorption Analysis
VED	Volumetric Energy Density
SSRT	Slow Strain Rate Test
HELP	Hydrogen Enhanced Local Plasticity
HEDE	Hydrogen Enhanced Decohesion
FIB	Focused Ion Beam
GB	Grain Boundary
OI	Octahedral Interstitial
TI	Tetrahedral Insterstitial
TG	Transgranular
IG	Intergranular
TD1	Transverse Direction 1
TD2	Transverse Direction 2
BD	Build Direction
ECCI	Electron Channeling Contrast Imaging
TDA	Thermal Desorption Spectroscopy
PIC	Peripheral Interface Controller
RC	Resistor Capacitor Circuit
OM	Optical Microscope
LPBF-AP	LPBF-As-Printed
LPBF-Ann	LPBF-Annealed
HEA-W	Wrought

Chapter 1

Introduction

In metallurgy it has long been thought that combining many metals in equal proportions results in the formation of numerous intermetallic and metastable compounds that compromise the mechanical properties and subsequently, the performance of the resulting alloys. Hence, conventional alloying techniques, which have persisted for millenia, are often done with one metallic element present in a relatively higher concentration based upon a primary property requirement followed by the addition of alloying elements to impart secondary properties. For instance, stainless steel 316L has iron as its major component to which chromium is added to confer corrosion resistance and nickel to counter brittleness. However, in 1981, an undergraduate student by the name of Alain Vincent working under Prof. Brian Cantor at the University of Sussex made a rather unusual but important discovery. They found that by simple melting and casting, an alloy of the metals cobalt (Co), chromium (Cr), iron (Fe), manganese (Mn) and nickel (Ni) written as CoCrFeMnNi in equimolar proportions ($Co_{20}Cr_{20}Fe_{20}Mn_{20}Ni_{20}$) has a stable, single-phase face-centered cubic A1 structure and almost entirely free of brittle intermetallics. This became known as the Cantor alloy [1]. Research into this novel class of alloys, however, did not kick off substantially until the early 2000s when Prof. Jin Wei Yeh and his team at National Tsing Hua University in Taiwan independently developed the same idea of an unconventional alloying strategy. It started with three MSc theses in 1996, the first one entitled *"A study on the multicomponent alloy systems containing equal mole elements"* with the alloy MoTiVFeNiZr[2]. In the following years, they were able to show that equiatomic alloys of CrFeCoNiCu with varying aluminium content have simple single-phase structures such as FCC for low Al concentrations and BCC for high Al concentrations. Yeh, et.al. were able to test their hypothesis that the reason for the unexpected formation of a stable, single-phase composition is

because the high configurational entropy of mixing- which refers to the entropy associated with the conformational fluctuations of a molecule in a solution- exceeds the enthalpy of compound formation thereby deterring the formation of intermetallic compounds. Because of this high configurational entropy brought by the presence of many components in equal amounts (five or more), they named this class of materials **high-entropy alloys** (HEA) which includes the original Cantor alloy, CoCrFeMnNi. Alternative names in literature include compositionally complex alloys (CCAs), multi-principal element alloys (MPEAs) and multi-component alloys. Although in later years, as the research on this new class of materials progressed, it was discovered that configurational entropy is not the sole useful predictor of which alloys are simple solid solutions and that most multi-component alloys form several intermetallic phases, the term high-entropy alloy is still frequently used.

The discovery by Cantor's group and Jin-Wei Yeh's team opened the door for research into a myriad of materials that include medium-entropy alloys, multi-phase alloys, and metallic glasses to name some. George, et.al. wrote:

"HEAs provide a unique advantage in that they offer a vast compositional space in which the different mechanisms may be tuned and optimised more effectively to develop new alloys with superior properties[3]"

Since then, numerous studies have focused on the discovery of other high-entropy alloys from 3d transition metals Al, Co, Cr, Cu, Fe, Mn, Ni, Ti and V and the refractory metals Hf, Mo, Nb, Ta, Ti, V, W and Zr, with freedom to choose components by equiatomic substitution or subtly altering their compositions. This gives rise to millions of different alloy combinations with differing compositions for this class of materials. Conservative estimates go up to 10^{100} or 1 googol, greater than the number of atoms in the universe[4]. Even so, the quinary CoCrFeMnNi has remained, to this date, the most extensively studied of the single-phase HEAs with its promise of real world applications. For one, it is reported to exhibit exceptional mechanical properties especially at cryogenic temperatures, reaching an ultimate tensile strength of 1 GPa, ductility of up to 100 % and a fracture toughness exceeding 200 MPa $m^{-\frac{1}{2}}$ at 77 K. In general, the mechanical properties of the single-phase Cantor alloy are comparable and at times superior to other materials such as high-strength alloy steels, nickel superalloys and complex ceramics[5]. The outstanding combination of strength, ductility and toughness, according to Gludovatz,

et.al., "exceeds that of virtually all pure metals and metallic alloys." Moreover, this alloy also shows promise in their functional properties such as radiation and corrosion resistance, wear resistance and hydrogen storage[4].

1.1 Additive Manufacturing as Fabrication Route

In most of these studies, the dominant fabrication methods for the CoCrFeMnNi high entropy alloy are conventional vacuum arc or induction melting followed by casting and mechanical alloying and spark plasma sintering. As these alloys are relatively complex systems, it is logical to assume that their implementation will be limited to highly demanding applications, where the potential benefit of HEAs will overcome the inherent complexity and high levels of control required to produce them[6]. For example, melting is time-consuming as the cast alloys need to be remelted several times to eliminate non-homogeneity of the alloys. Furthermore, higher cooling rates are beneficial to HEAs since it suppresses the formation of intermetallics[7]. Although thermal and mechanical post-processing techniques such as annealing and hot-isostatic pressing can mostly help eliminate structural defects such as cracks, voids and porosities, when it comes to fabricating parts with complex geometry, the application of HEAs by conventional processes are constrained[8].

A way to sidestep these difficulties is by additive manufacturing (AM). It has provided new opportunities for fabricating geometrically complex HEAs with the possibility of in-situ tailoring of their microstructure. Simply put, metal additive manufacturing is a progressive layer-by-layer fabrication process in which a metallic feedstock, which are often pre-alloyed powders, is fully melted by the high-energy input of a laser, electron beam or plasma, and bonded together layer by layer to form a part of any geometry. Although there are several types of AM techniques, which differ by the nature of energy source and interlayer binding mechanism, they all share the common characteristic of layer-by-layer manufacturing process. This layer-by-layer nature of AM processes implies some intrinsic advantages such as complex geometry fabrication, design freedom and higher heating and cooling rates[7]. This high cooling rate can significantly hinder atomic diffusion and hence suppress phase transition and intermetallic formation during the fabrication process. Moreover, it was mentioned that the vast compositional space that HEAs possess means there is an uncharted universe of high-entropy materials to explore. The ability

of AM to rapidly create a system or part representation before final release or commercialisation (also called *rapid prototyping*) needing only some basic dimensional details and understanding of how the AM equipment is operated and the materials used enables high-throughput alloy production and property-oriented screening of potential alloy combinations and compositions[9][10][11]. It seems therefore that AM has a high potential as a fabrication route for HEAs with intricate shapes and chemically graded compositions tailored for specific functions[11].

The additive manufacturing of the CoCrFeMnNi HEA has been well-studied and demonstrated. CoCrFeMnNi parts and coatings have been printed using AM technqiues such as direct energy deposition, binder-jetting and cold-spray techniques. In this study a well-known AM technique called laser powder bed fusion will be employed. Laser powder bed fusion (LPBF) is the general term for AM processes that use a powder bed, in which a blade or roller spread the powders on a building substrate. This includes selective laser sintering and selective laser melting or SLM. Selective laser melting is a powder bed-based process in which a 3D component is fabricated in a layer-by-layer mode thru the selective melting and consolidation of thin layers of metal powders using a high-energy laser beam. This technique has been widely used for manufacturing HEA parts, although only a few papers have been published before 2018. The first studies on the equiatomic CoCrFeMnNi by Li, et.al. and Zhu, et.al. in 2018 have come to the same findings that the mechanical properties of SLM CoCrFeMnNi were superior to those of its arc-melted counterparts due to the fine microstructure and the presence of strengthening phases[12][13]. Efforts to understand how this processing technique affects the structure, properties and performance of the alloy were carried out by Dovgyy, et.al., (2020) an d Piglione, et.al.(2018) and Pham, et.al.(2020), to name a notable few. They investigated the effects of several SLM printing parameters such as laser power, scan speed, hatch spacing and scan strategy to the solidification microstructure of the alloy. Optimal printing parameters resulting in good consolidation and outstanding mechanical properties have been reported[14]–[16]. Aside from these, additively manufactured CoCrFeMnNi is also found to possess interesting functional properties. Ren, et.al. (2019) reported superior corrosion resistance that is due to the uniform elemental distribution and minimal microporosty in the solidification microstructure[17]. A recent study by Xu, et.al in 2021 described the superior corrosion resistance of the alloy, which opens an opportunity to study 3D-printed parts[18]. In addition, magnetic properties

and hydrogen storage properties are just some of the promising properties that are currently of interest.

1.2 Hydrogen properties of the Cantor alloy

A property that is of prime interest to this work is the alloy's response to hydrogen exposure. Most metals, especially high-strength alloys, experience a degradation of its mechanical properties because of hydrogen exposure during processing or in performing intended functions such as hydrogen transport or storage. This phenomenon is known as hydrogen embrittlement (HE), a process resulting in a decrease in the fracture toughness and/or ductility of a metal due to the presence of atomic hydrogen[19]. Its consequences can be serious and dangerous as it can lead to the catastrophic failure of the material. The decrease in ductility and reduction of the fracture toughness is much more drastic for high-strength steels and alloys in general than for low to medium strength ones, which has significant consequences to the use of high-strength alloys in many industries and applications. Previously, concerns about hydrogen embrittlement and its deleterious consequences have been contained in extreme applications in aggressive environments such as those found in off-shore structures in the energy industry. However, with the wide application of high strength steels and alloys, the problem of hydrogen embrittlement to otherwise benign environments. First, high-strength alloys are used in buildings, bridges and cars and their structural integrity may be compromised by hydrogen embrittlement. Examples include the Cheesegrater Tower in London losing its third bolt in three months in 2015 and the failure of the San Francisco Oakland Bay Bridge in 2013[20], [21]. Moreover, solutions to the problem of hydrogen embrittlement becomes of prime importance as most of the major world economies are shifting into a more sustainable form of energy generation and consumption, e.g. green hydrogen, where the aim is to support an economy that will replace the current reliance on fossil fuels. In fact, a so-called dedicated European Hydrogen Backbone, a network of hydrogen pipelines and storage facilities with the goal of connection industrial clusters to an emerging hydrogen infrastructure by 2040 is being envisioned [22]. Hence, research into materials that would enable this hydrogen economy has piqued in recent decades. As CoCrFeMnNi HEA has a potential as next-generation structural materials and other applications, it will be likely exposed to hydrogen in its working environment. Examples of this are the hydrogen concentrated cooling water of nuclear power plants, hydrogen gas in aerospace structures, hydrogen generated

by electrochemical processes and liquefied or gaseous hydrogen storage in vehicles and vessels. Some, if not most of these parts may require a non-conventional manufacturing technique such as additive manufacturing via laser powder bed fusion (LPBF). Also, due to several factors that are inherent to it, additive maufacturing often introduces higher defect densities such as lack of fusion, gas entrapments, keyholing, high residual stresses, voids and porosities that are stochastic in nature which is going to affect its hydrogen response.Thus,it is important to understand the causes, effects and mechanism of hydrogen embrittlement in the additively manufactured alloy. Indeed, several studies have been done on this and they have shown that there is strong evidence to suggest that the alloy exhibits better resistance to hydrogen embrittlement at room and cryogenic temperatures compared to type 304 and 316L stainless steels[23][24]. Interestingly however, other studies show quite the contrary[25]. These contradictions only reinforce the fact that hydrogen embrittlement (HE) may have been studied for 150 years but it is still not well understood due to its interdisciplinary attribute and the experimental difficulty of directly detecting hydrogen behaviour[26]. This does not mean, however, that no progress has been made in the fundamentals of the phenomenon. For example, it is now well-established that when it comes to embrittlement, the interactions of hydrogen with various lattice defects are crucial. Hydrogen tends to locate at lattice interstitial sites and various trap sites such as precipitates, dislocations, grain boundaries- features of a material's crystal structure and microstructure. The hydrogen can either diffuse and move from one lattice site to another (diffusible hydrogen), or remain bound to these traps (trapped hydrogen). Between the two, the former has been observed to play a significant role in hydrogen induced cracking. It makes sense therefore that trap sites, where hydrogen may be unable to diffuse, are key to understanding hydrogen embrittlement susceptibility. This is given by so-called *trapping parameters*, such as the energy required to trap or 'bind' the hydrogen atom, also known as trap binding energy and the density of these trap sites. However, reports so far have been conflicting. On one hand, some studies show that microstructures which bestow high strength and hardness, having several distinct microstructural features such as precipitates and inclusions may interact with hydrogen and increase embrittlement susceptibility. On the other hand, there are reports that the presence of defects, i.e. lattice iregularities such as dislocation twins, etc. have been shown to contribute to HE resistance. What then is the real story?

Due to the rapid solidification and high cooling rate in LPBF, unique microstructural features are observed in alloys manufactured using this technique, which often depends on a multitude of factors from powder quality to post-processing. For instance, LPBF CoCrFeMnNi strengthened by in-situ oxides exhibited yield strengths of up to 729.6 MPa and has an excellent hydrogen embrittlement resistance due to high hydrogen solubility and easy deformation twin formation[27]. However, this study did not elucidate the relationship of the microstructure evolution to the observed results. In a more recent study, dislocation cells that are part of the hierarchical microstructure common to LPBF alloys were modified to improve HE. Building on this, several aspects of HE such as the mechanisms of hydrogen uptake, diffusion and trapping and its relationship to the microstructural features were discussed[28]–[31]. Furthermore, measurement of the hydrogen content has been shown to correlate with the operative failure mechanisms. It is well-established that differences in hydrogen-metal interactions alone can affect susceptibility to hydrogen induced degradation[32]. Hence, developing a clear understanding of fundamental hydrogen-material interactions is crucial in the study of material degradation due to hydrogen embrittlement, and although these aspects have been investigated considerably, there are still several issues that need to be addressed such as:

a. the method of hydrogen charging. The electrochemical hydrogen pre-charging involved is often limited to a short duration (mostly 48 h) which does not sufficiently characterise severe hydrogen exposure over long durations in actual conditions. Literature data show moderate penetration of hydrogen of only a few microns and some, due to the low hydrogen ingress have even reported hydrogen induced ductilisation for the LPBF alloy[28] which would be interesting to investigate at longer charging times.

b. reports on the hydrogen trapping parameters such as trap activation energy, trap density and pre-exponential factor are based on models with simplifying assumptions without validation. Important pre-requisites in the correct application of these models such as uniform hydrogen concentration, significant trap occupancy and local equilibrium between lattice and trap sites are often neglected. This also applies to the calculation of the apparent hydrogen diffusivity, D_{app}, an important parameter in characterising the hydrogen uptake.

c. Also, post-processing heat treatment techniques such as annealing may introduce microstructural changes such as dislocation cell annihilation, recrystallisation, grain growth, oxi-

dation, and precipitation. The effect of these changes to the hydrogen trapping and diffusion and embrittlement of the AM CoCrFeMnNi requires further understanding as well.

d. Direct detection of hydrogen in microstructural features like grain boundaries and dislocations has been investigated but there are very few that focus on the LPBF Cantor alloy with its complex microstructure and thus, challenges in achieving this goal have not been reported.

1.3 Aim and scope of present investigation

The objective of this study is *to provide a detailed description of the hydrogen effects on an additively manufactured CoCrFeMnNi high entropy alloy that addresses the issues enumerated in the preceding section.*

The scope and limitations of the research are laid out from the start. First, I make it clear that the current investigation serves as a study of the AM CoCrFeMnNi alloy in its own right, and although the findings may have implications to HEAs as a class of materials, this is not a case study for HEAs in general. Second, the mathematics of diffusion in the models used to describe hydrogen diffusion and trapping including the derivation and solutions of relevant differential equations are not discussed and the readers are referred to relevant literature. Third, although wrought and/or conventionally manufactured CoCrFeMnNi is frequently mentioned, I focus only on the additively manufactured alloy and use data of the wrought alloy only when comparison is relevant for the ensuing discussion. Also, I understand that hydrogen uptake and diffusion can be affected by variables such as surface conditions and surface chemistry. Hence, consistent surface polishing procedures were employed across all specimens and the effect of surface conditions are outside the scope of the study. Also, in this study there are a limited number of experimental replicates. Replication was constrained by the capacity and cost of producing samples by laser powder bed fusion and vacuum arc melting (for wrought samples) as well as machining constraints. It is also informed by accepted practices in hydrogen embrittlement studies such as in the case of isothermal TDS experiments for the determination of hydrogen diffusivities. Lastly, it is important to note that the investigation of the mechanisms of hydrogen embrittlement are based on post-mortem observation of fractured samples and hence this approach cannot provide direct evidence.

1.4 Overview of the study

This thesis consists of five additional chapters within two main parts. In Part 1 (Chapters 2 and 3), I situated the current study in related literature and establish the research methodology. In Chapter 2, I discussed additive manufacturing in more detail and the science of hydrogen diffusion, trapping and embrittlement. I also expanded on the arguments I presented in the first chapter that underscore the need for this investigation into the hydrogen embrittlement aspects of the AM CoCrFeMnNi high-entropy alloy. In Chapter 3, I enumerated the steps needed to achieve the singular aim of this study and provided a discussion of the methods employed within these steps. Part 2 (Chapters 4 and 5) addressed the aim of the study as two separate investigations. In Chapter 4, I laid out an investigation into the additively manufactured CoCrFeMnNi with an emphasis on the microstructure and microstructural change post heat treatment. After ensuring the satisfactory mechanical properties of the alloy in the as-printed and heat-treated conditions I investigated its hydrogen embrittlement in Chapter 5, which includes analysis of hydrogen diffusion and trapping as well as the mechanisms involved. Finally, Chapter 6 contains the conclusions and reflective evaluation of the study as well as prospects for future investigations.

Chapter 2

Literature Review

The hydrogen embrittlement of conventionally manufactured high entropy alloys such as the Cantor alloy has been well studied, and research has expanded to include additively manufactured ones. However, since improvements in additive manufacturing technology in techniques such as laser powder bed fusion are relatively more recent, there is still a need to investigate the effects of hydrogen exposure to these alloys. This includes hydrogen uptake and diffusion. This chapter presents a detailed description of the science behind hydrogen embrittlement and the technologies relevant to the current investigation. Embedded in this discussion is a critical review of the literature on the hydrogen embrittlement of AM high-entropy alloys eventually focusing on the CoCrFeMnNi and highlighting the issues of the state of the art due to the complex nature of hydrogen interactions.

2.1 What is additive manufacturing?

Additive manufacturing is the process of fabricating objects layer by layer from 3D numerical models as opposed to traditional subtractive manufacturing technologies[33]. First developed as a functional rapid prototyping system laid out by David E.H. Jones in 1974, it quickly became a concept from an article series in the New Scientist to a functional manufacturing process in 1981 with the additive manufacturing of materials by Hideo Koyama. At the outset, the technique was applied to photopolymers but since then, it has been used to fabricate several types of materials such as composites and metals. The growth and popularity of additive manufacturing

stems from its many enticing advantages and applications over conventional manufacturing most notably the fabrication of complex components with intricate shapes at reduced lead time and lower costs. In contrast, conventional manufacturing equipment has very few or even single functions which limit the products processed. Moreover, 3D-printing produces a near net-shape output which means little to no machining is required. This allows for customisation and personalisation. Products can be printed on demand or locally, which can save resources compared to mass production that may lead to unsold products. Thus, 3D-printing is often used for rapid prototyping of novel materials, geometrically complex materials and other high-value added parts in biomedical and aerospace applications, to name a few. In addition, AM is a key enabler for the development of advanced materials such as architected materials– multiphase and/or cellular materials in which the topological distribution of phases is carefully controlled and optimised for specific functions or properties[34].

However, additive manufacturing is not free of its own disadvantages. There are post-processing requirements, lack of repeatability and reproducibility, slow manufacturing speed and inefficiency for mass production and cost[35], [36]. Looking forward for example, producing high-entropy alloys (HEAs), using additive manufacturing (AM) involves notable cost implications due to several factors. First, HEAs often require high-purity, multi-element feedstocks, which are more expensive than conventional alloy powders. Second, processing parameters in AM must be carefully optimized to ensure uniform elemental distribution and prevent segregation, adding to development and production costs. Additionally, the low production volumes, limited recyclability of powders, and specialized equipment needed for consistent AM of HEAs further increase overall costs. This however has not prevented its growth and extension to the fabrication of metallic parts. In 1995, the Fraunhofer Institute in Aachen, Germany developed the first metal additive manufacturing technique called selective laser melting.

Selective laser melting is a powder bed fusion (PBF) technique in which metal powder from a feed piston is spread evenly by a roller on a flat build plate on top of a sintering piston which is then hit by a laser according to a predetermined design layer of a build. The laser power is strong enough so that the metal undergoes complete melting (in contrast to selective laser sintering). This is done layer-by-layer as the roller spreads powder with a certain programmed layer thickness until the part is complete, as illustrated by the schematic diagram below.

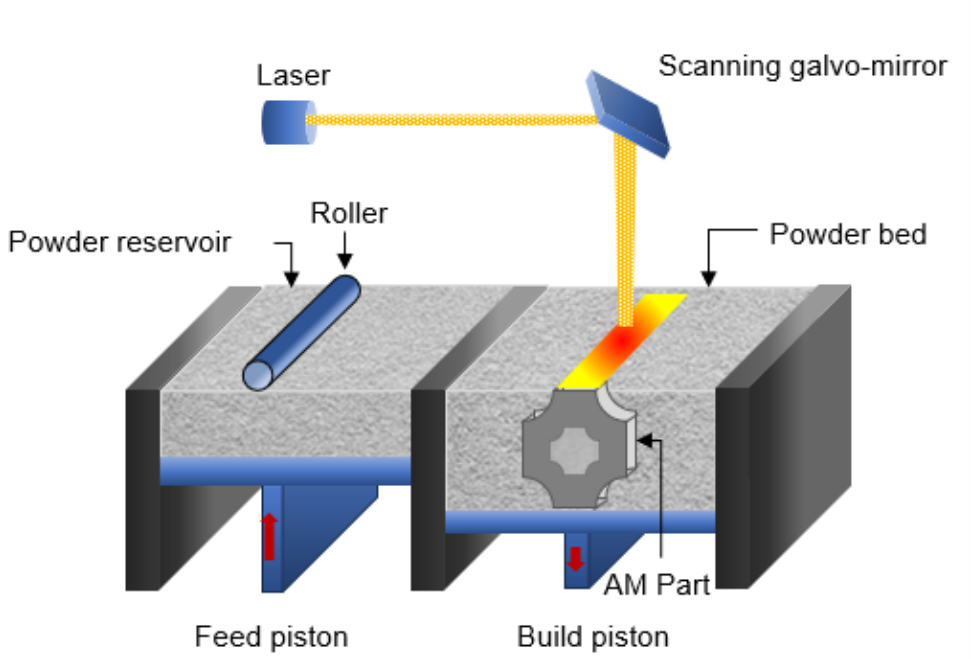


Figure 2.1: The laser powder bed fusion process.

In this study, selective laser melting is done on the ProX 200 Direct Metal Printer. As with many laser powder bed fusion (LPBF) systems, there are many parameters that govern the entire process from powder morphology to post-processing such as heat-treatment. The mechanism of how some or all these numerous parameters influence the build quality is not the main goal of this work. However, it worth mentioning that an interplay of these parameters influence the build quality of the AM part. Perhaps the most studied parameter is the volumetric energy density (VED) which is defined mathematically as:

$$E_v = \frac{P}{vhd}$$

where:

- P is the laser power (W),
- v is the scan speed (mm/s),
- h is the hatch spacing (mm),
- d is the layer thickness (mm).

The laser power is given as percentage of the total nominal laser power. In the case of ProX 200 DMP, the maximum laser power is 300 watts. When the laser beam hits the bed, it creates

a melt pool depth and width of which depends primarily but not only on the intensity of the laser and its effective spot size (or beam diameter). In the ProX, the spot size is 120 μm. The scan speed (which is known as mark speed in the ProX), is the speed in which the laser beam scans through the powder bed as it traces the build pattern layer. The hatch spacing is the distance between each successive scans of the laser beam across the powder bed measured from the centre of one meltpool to the centre of the next meltpool. The layer thickness is the depth of the powder that is spread by the roller for every successive layer of the process. The following schematic diagram illustrates the mentioned parameters in LPBF.

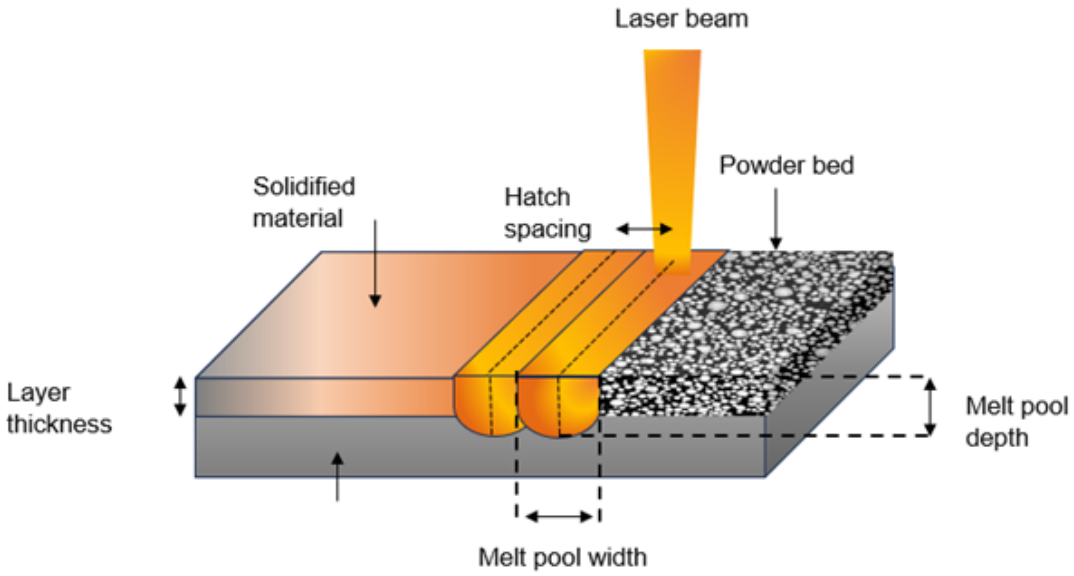


Figure 2.2: Parameters involved in the LPBF process.

Another important parameter is the scan strategy. This is defined as the pattern the laser beam follows in the scanning of the powder bed for each successive layer. The scan strategy options vary from printer to printer but normal scan strategies in which the laser beam scans a series of parallel lines (in the same or opposite directions) with or without rotation for the next layer are common.

The interplay of these parameters together with the nature of the process promotes rapid melting and solidification, in which the layers undergo a very quick succession of low and high thermal cycles reaching up to 10^6 K s^{-1}. This rapid melting and solidification characteristic of LPBF is the subject of continued interest because it creates refined grain sizes and prevents the formation of intermetallic compounds in high entropy alloys. Chemical segregation of alloying

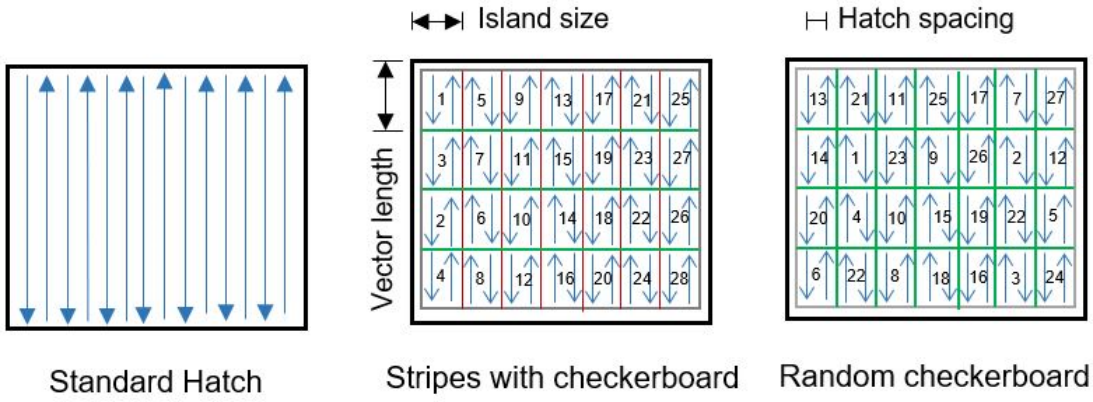


Figure 2.3: Basic scanning strategies in the ProX 200 DMP. They differ from machine to machine.

elements also take place at a smaller length scale. Hence, chemical composition is more uniform throughout the part resulting in higher strength than as-cast counterparts[37].

Most LPBF research revolves around three metals: iron, titanium, and nickel. As research continue to progress, many other metals such as aluminium, copper and tungsten have been demonstrated to be printable. Printability is defined as the ability of the material to be consolidated layer-upon-layer to form a designated part with desired microstructure and properties that ensure the performance of the printed material over its intended service life[38]. A key measure of printability is relative density, which measures the extent to which the part is free from defects and imperfections such as solidification and liquation cracks, pores, and voids. Other defects include inclusions, contaminations and metal oxides, unmelted or partially melted particles, anomalous grain growth and crystallographic textures[39]. A detailed discussion of these defects are out of the scope of this work and can be found elsewhere[40]–[42]. According to their mechanisms of formation, these defects illustrated in Figure 2.4 can be classified as equipment-related, powder-related and process-related. Also, defect formation involves a large number of processing parameters. For example, lack of fusion pores result primarily from low energy density as a consequence of low laser power, and keyhole formation is mainly influenced by excessive energy density, but a lot of factors are at play. This results to the complex and stochastic nature of the porosity and other defects that render the production of a 100% defect-free part close to impossible. However, a variety of post-processing techniques such as annealing, furnace sintering, and hot isostatic pressing can be employed to considerably reduce residual porosities and thus increase consolidation in the as-printed part[39].

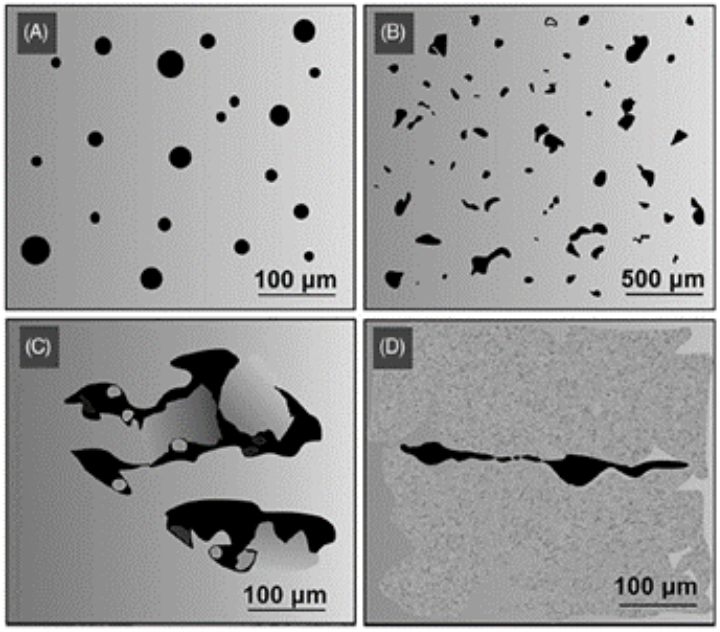


Figure 2.4: Characteristic pores in LPBF parts: A) gas pores, b) incomplete melting pores, c) lack of fusion pores d) cracks. Reproduced from Sola, *et.al.* 2019[39].

Consolidation is often measured by the relative density using the Archimedes principle. It is defined as the ratio of measured density of the part to the theoretical density of the fully dense material (obtained from the crystal structure and atomic weight). A 100% relative density means an essentially pore-free material, although unmelted particles in lack of fusion pores and sparse porosities that have negligible mass but can compromise mechanical properties might not be accounted for. Nevertheless, this method may be used to quantify the volume fraction of microstructural porosity and is often reported in literature. One of the pioneering studies on the consolidation of LPBF parts was done by Tolosa, et.al. where they achieved 99.9% relative density with stainless steel[43]. Since then, discovering other printable alloys have been the goal and in 2018, research on 3D-printed high entropy alloys have gained traction. This is supported by the fact that even though there are disadvantages most notably the costs, the superior performance of HEAs—such as exceptional strength-to-weight ratios, thermal stability, corrosion resistance, and wear properties—can justify these costs in niche, high-value applications including (a) aerospace components (e.g., turbine blades, fasteners, or heat shields), where weight savings and high-temperature performance are critical and can lead to substantial fuel efficiency and durability gains; (b) specialty valves and seals for nuclear or chemical processing, where corrosion and radiation resistance are essential; (c) medical implants (e.g., hip or spinal implants), where the combination of biocompatibility, strength, and wear resistance can extend

service life and reduce revision surgeries; and (d) defense applications, such as armor components or missile structures, where extreme mechanical performance justifies higher material and processing costs. In these scenarios, the long-term performance benefits, reduced maintenance, and life-cycle advantages offered by AM-fabricated HEAs can outweigh the upfront investment, making them an attractive solution for demanding environments.

2.2 On the CoCrFeMnNi HEA manufactured by laser powder bed fusion

The equimolar or near-equimolar CoCrFeMnNi can be described as a multi-principal element alloy (MPEA) due to the fact that no single element is present in a relatively higher concentration, and as a high-entropy alloy because of the high configurational entropy that hinders intermetallic phase formation and that influences the thermodynamics of the system to form a stable solid solution[44]. This high configurational entropy is but one of the four **core effects** that give this material its interesting properties. The other three are sluggish diffusion, lattice distortion and cocktail effect. Sluggish diffusion involves the kinetics of the system. The number of constituent elements promotes a low diffusion rate, which increases thermal stability, resulting in an increase of the recrystallisation temperature which in turn slows grain growth and phase separation. Moreover, the movement of large and small atoms causes lattice strain making the entire framework distorted. Lattice distortion prompts solid solution strengthening by restricting dislocations, the displacement occurring at each lattice spot relies on the atom dwelling on that spot. Lastly, the cocktail effect includes the compositional mixtures of elements where the consequence of the blend is both unpredictable and unexpected because of the distinctive properties the individual element provides. As described in the first chapter, these core effects play a major role in the characteristic properties of the CoCrFeMnNi HEA.

In theory, it is known that the CoCrFeMnNi HEA is highly printable because the material develops a stable FCC single-phase structure upon rapid cooling- eliminating the risk to form cracks associated with phase transformations during thermal cycles. High melting temperature oxides can prevent the flow of molten metal, resulting in an increased risk of forming lack of fusion porosity. Therefore, a high concentration of Cr in the alloy results in high oxidation resistance, minimizing the formation of porosity associated with oxidation during printing, and

thereby improving consolidation[11]. The low thermal expansion coefficient minimizes internal stresses while a relatively low freezing range helps in preventing solidification cracking[45].

In 2017 Eißman, et.al. reported the production of a single-phase Cantor alloy sample without any visible precipitations having a relative density of 97 % by selective electron beam melting (SEBM), a type of powder bed fusion process that uses an electron beam instead of a laser[46]. However, this study did not provide in-depth investigations of solidification microstructures. In the following year, Piglione, et.al. examined how microstructures form and evolve during rapid cooling following repeated deposition of the metal, this time, using LPBF. They showed that the rapid cooling of molten metal on existing grains leads to the epitaxial growth of fine cells in meltpools and the remelting induced by the repeated deposition of the metal leads to grain selection via competitive growth, and that the alloy has good printability with high consolidation and a uniformly high hardness without macrosegregation in the microstructure[15]. In other subsequent investigations, massive dislocation pile-ups, nanotwins, tetragonal σ phase, lattice distortion and Mn segregation at the boundaries of meltpools were revealed. Moreover, numerous microcracks and micropores were present in the as-printed LPBF specimen but hot isostatic pressing (HIP) was able to increase the relative density from 98.2 % to 99.1 %. The mechanical properties were reported to be superior to those of arc-melted specimens due to the fine microstructure and the presence of the tetragonal σ phase both contributing to strengthening[12], [13]. Dovggy et.al. reported that a good consolidation ($>$ 99 % relative density) can be achieved with an optimal processing window of an energy density in the range of 62.7 J/mm^3 to 109.8 J/mm^3, a meander scan strategy with 67° rotation between odd and even layers. The solidification microstructure is hierarchical. At lower magnifications it can be described as that of "fish scales" associated with the fusion lines formed due to variations in chemical composition and solidification microstructure along weld beads. A closer look reveals that each bead contains fine cellular substructures that range from 300 nm to 1000 nm in diameter, whose boundaries have a higher dislocation density compared to the cell interior. This is no surprise since LPBF is known to produce high-density dislocations which provide a path for atomic diffusion and facilitate their own mobility. Nano-sized oxides are detected as well (Figure 2.5). Scan strategy is the most influential in microstructure development since the scan strategy rotation angle controls the extent in which epitaxial growth can occur, and hence the crystallographic texture

and grain morphology. This understanding provides explanations to the observed mechanical properties such as flow stress and plastic anisotropy of the alloy[14].

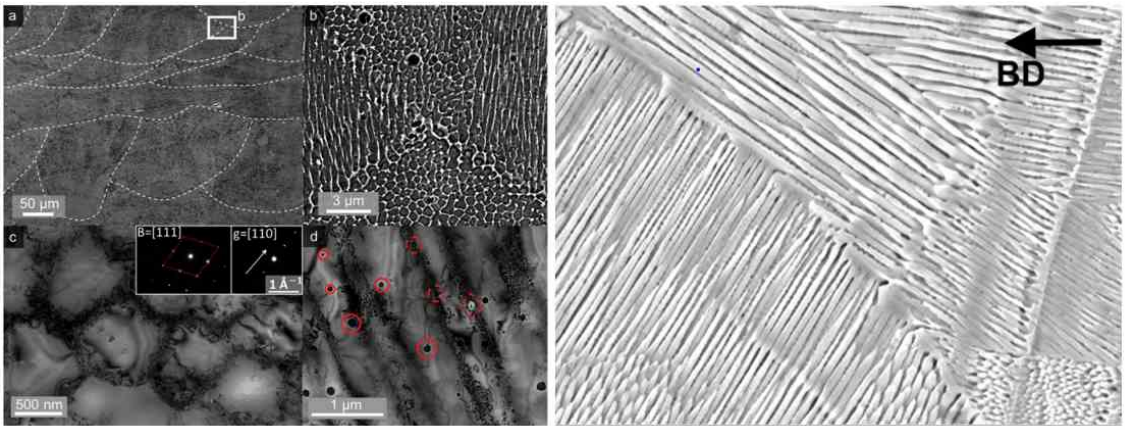


Figure 2.5: SEM micrographs and TEM images showing the "fish scale" microstructure, dislocation cells and oxide-rich nanoprecipitates and fine epitaxially growing columnar cells undergoing side-branching in response to changes in thermal gradient direction. Reproduced from Pham *et.al.* 2020[16].

Moreover, the microstructure development in LPBF is greatly influenced by the direction and magnitude of the thermal gradient and to some extent, the presence of pores. Cells growing epitaxially parallel to the direction of the thermal gradient is no longer preferable for the growing cells. This can happen even inside a single meltpool, leading to complex growth paths and complicated grain morphologies. Consequently, grains that appear equiaxed in 2D cross sections mapped via electron back-scattered diffraction (EBSD) are actually columnar cells that underwent side-branching. Porosity, in turn, can cause disruptions in crystal growth, causing fine cells to coarsen in the vicinity of larger voids such as lack-of-fusion pores[16]. Microstructural features have been shown to be directly responsible for the properties of the LPBF Cantor alloy. For instance, one study has shown that compared to the as-cast counterparts, the as-printed samples showed higher pitting resistance and greater polarisation resistance. This indications of superior corrosion resistance is attributed to the homogeneous elemental distribution and lower density of micropores[17]. Although the LPBF processed alloy does not exhibit macrosegregation, elemental segregation during solidification has been observed revealing than Mn and to some extent, Ni, segregated to the boundaries of the cellular substructures while Cr. Co and Fe segregated to the cell core. Moreover, Mn-based nano-oxides were also detected[47].

Furthermore, heat treatment of the as-printed part can significantly affect the macro and microstructure as well and can lead to improved mechanical and functional properties. Hot

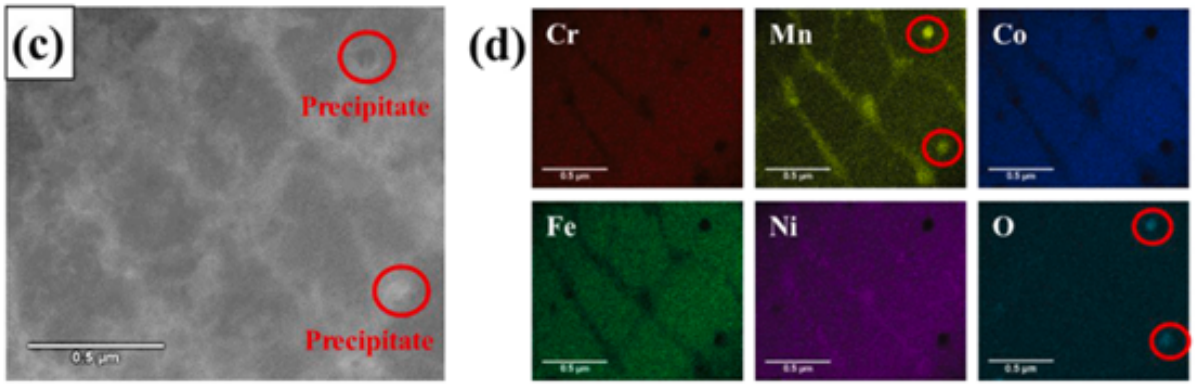


Figure 2.6: STEM-EDX analysis showing elemental segregation in LPBF CoCrFeMnNi HEA. Reproduced from Jin, et.al. 2020[47]

isostatic pressing (HIP) has been shown to increase the ultimate tensile strength of the LPBF Cantor alloy with an increase in elongation[48]. Moreover, HIP rendered a more homogeneous distribution of Mn and eliminated the said segregation[12]. In addition to this, thermal residual stresses occur because of complex temperature cycles in LPBF and this can induce cracks in the substructure. Annealing heat treatment has been shown to reduce residual stresses in several LPBF HEAs and it can also significantly alter the hierarchical microstructure[49]–[52]. For instance, annealing at 900°C for an hour in an argon atmosphere results to the disappearance of the cellular substructures by dislocation elimination. On a related note, a study of a Cantor alloy derivative, CoCrFeNi, also a single-phase FCC HEA revealed that annealing at 1173 K and below for 32 hours followed by furnace cooling decreases the density of the dislocation density of cells. Dislocations with high distortion energy transforms into regular low-energy lattice structures when subjected to high temperatures. Furthermore, annealing at 1272 K and above for 2 hours induces recrystallisation of predominantly equiaxed grains with many twins. The twins connect and block dislocation movement and form dislocation walls at grain boundaries, maintaining the alloy's high tensile strength after heat treatment[53].

From the state-of-the-art it is obvious that microstructure evolution unique to HEAs manufactured by LPBF and the subsequent annealing post-processing dictates the alloy's properties and performance. The excellent mechanical properties such as strength and ductility that is a result of tailoring these microstructures by additive manufacturing has made the CoCrFeMnNi HEA an alloy of interest in many potential applications, including ones that involve exposure to hydrogen. Hydrogen, the lightest and smallest element, is detrimental to high-strength metals and their alloys because it causes a phenomenon known as hydrogen embrittlement.

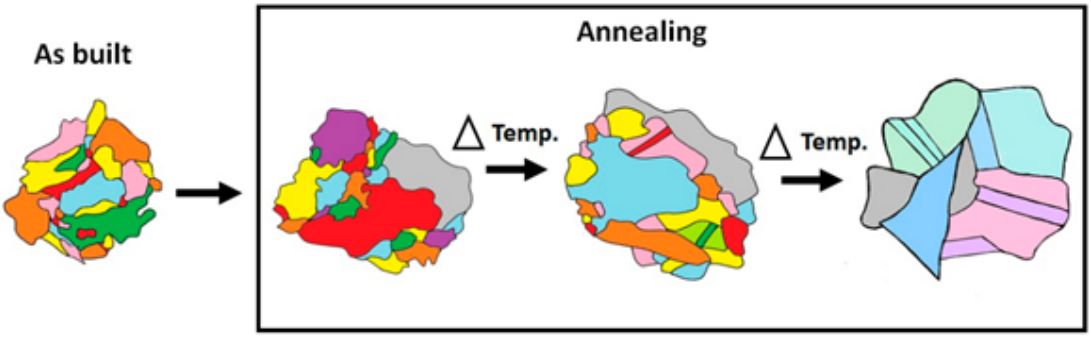


Figure 2.7: Schematic diagram of the effects of annealing on the microstructure of as-printed HEA (adapted from Torralba, et.al., 2020[53])

2.3 Hydrogen and the Cantor alloy

2.3.1 Introduction to hydrogen embrittlement

First discussed in detail by Johnson in a seminal paper entitled "On some remarkable changes produced in iron and steel by the action of hydrogen and acids," hydrogen embrittlement (HE) was initially described as the extraordinary decrease in toughness and breaking strain of iron caused by its immersion in hydrochloric and sulfuric acids. The acids acted as sources of "nascent" hydrogen, i.e., atomic hydrogen which diffuses into the metallic structure and renders it brittle. He wrote:

> *"After a few minutes of immersion in strong hydrochloric acid or dilute sulfuric acid– a piece breaking after being sent once on itself, while before immersion it would bear bending on itself and back again two or three times before breaking"[54]*

It was also shown to be temporary since the metal regains initial mechanical properties after some time. As more attention is given to this phenomenon, hydrogen embrittlement was defined as the process that results in a *decrease in the fracture toughness or ductility of a metal due to the presence of atomic hydrogen.* Materials embrittled by hydrogen can fail (or fracture) even when subjected to loads lower than the yield strength. However, the real menace of HE lies in the nature of the cracks associated with it. Hydrogen has a significant effect on the crack initiation and growth behaviour. Unlike stress corrosion cracking that produces numerous branched cracks, HE cracks are sharp and singular and they can grow rapidly with minimal macroscopic signs of deformation even for ductile materials[55].

Hydrogen embrittlement thru hydrogen-metal interactions can be classified into three: hydrogen environmental embrittlement (HEE), internal hydrogen embrittlement (IHE) and hydrogen reaction embrittlement (HRE). The following table summarizes their differences.

Table 2.1: Summary of types of hydrogen embrittlement[19].

Type	**Characteristics**	**Source of hydrogen**	**Applied stress necessary for failure**
HEE	Crack initiation occurs at the surface near a notch or surface defect	Intentional high-pressure hydrogen gas environment	Yes
IHE	Internal cracks occuring near root of an internal defect	Electrochemical processes such as electroplating, corrosion, cathodic charging, often unintentional during forming or finishing	Yes
HRE	Microstructural features such as inclusions, impurity and defects can lead to brittle rupture through the formation of voids, blisters and microcracks	Same as IHE and HEE with the hydrogen reacting internally with the alloy components to form compounds such as metal hydrides or methane	No

Due to its small radius of 106 pm, hydrogen enters metals in the form of atoms, the "nascent" hydrogen described by Johnson. They locate at various sites in metals with respective energies at sites schematically shown in Figure 2.8. High-pressure hydrogen gas, electrochemical hydrogen charging, and corrosion reactions are typical sources of hydrogen metals in service. For high-pressure hydrogen gas, the dissolution of hydrogen involves three steps: 1) physical adsorption on a solid surface due to the van der Waals interactions between hydrogen gas and the surface, 2) chemical absorption where the hydrogen molecule interacts with the metal and dissociates into atoms, and 3) hydrogen dissolution where hydrogen atoms diffuse toward the interior of the materials due to the concentration gradient. The default hydrogen concentration follows Sievert's law as [26]:

$$C_H = S\sqrt{P_{H_2}} \tag{2.1}$$

where:

- S is the solid solubility of hydrogen and,
- P is the hydrogen gas pressure

For electrochemical hydrogen charging or corrosion reactions, the **hydrogen evolution reactions (HER)** are given by:

Volmer reaction (acidic solution):

$$H_3O^+ + M \leftrightarrow MH_{ads} + H_2O \tag{2.2}$$

Volmer reaction (neutral or alkaline):

$$H_2O + M + e^- \leftrightarrow MH_{ads} + OH^- \tag{2.3}$$

Heyrovsky (acidic solution):

$$MH_{ads} + H_3O^+ + e^- \leftrightarrow M + H_2 + H_2O \tag{2.4}$$

Heyrovsky (neutral or alkaline):

$$MH_{ads} + H_2O + e^- \leftrightarrow M + H_2 + OH^- \tag{2.5}$$

Tafel reaction:

$$2MH_{ads} \leftrightarrow 2M + H_2 \tag{2.6}$$

where M represents the free metal surface of MH_{ads} that is occupied by adsorbed hydrogen. In this mechanism, hydrogen *adsorption* described by the Volmer reaction is followed by electrochemical (Heyrovsky, with solvated protons or water molecules) or chemical (Tafel) *desorption* reactions. In the presence of hydrogen *absorption*, the transfer of the surface-adsorbed hydrogen into the metal surface is represented by:

$$MH_{ads} \leftrightarrow MH_{abs} \tag{2.7}$$

Equation 2.7 is then followed by hydrogen diffusion into the bulk of the metal phase as illustrated in Figure 2.8. It is important to note that hydrogen absorption requires an additional energy and these reactions are reversible, that is, absorbed hydrogen atoms can escape and recombine into a hydrogen molecule in the surface of the metal and eventually back into the solution[56]. For electrochemical hydrogen charging, the hydrogen content is determined by current density, charging potential, charging time, type of electrolyte, poisoning agent, charging temperature, and charging method. The complete description of the charging set-up will be discussed in the succeeding chapter. Compared with gaseous hydrogen charging, the equivalent charging pressures caused by electrochemical charging are higher[57]. For a comprehensive discussion of the physics of the mechanisms of hydrogen evolution reactions the reader is referred to the works of Lasia[58], [59].

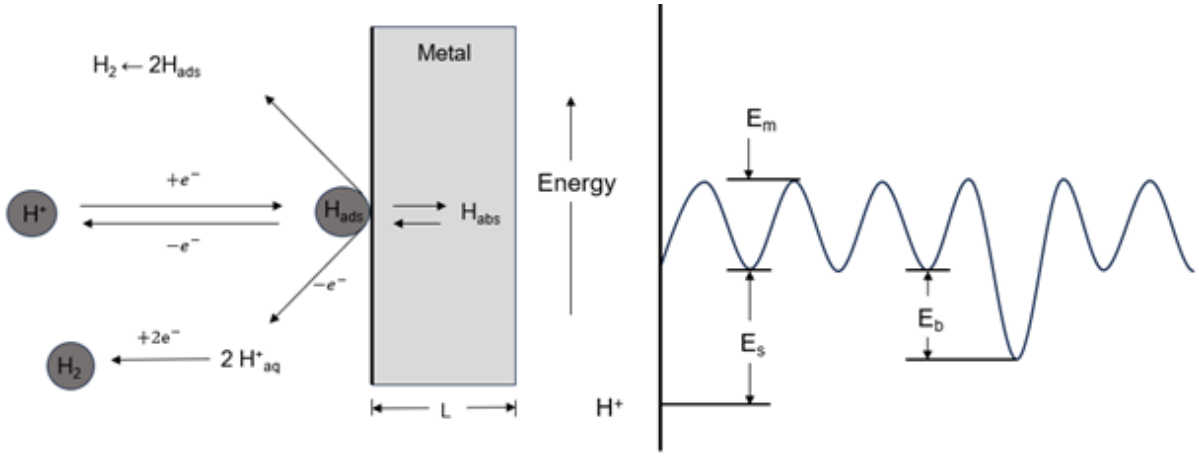


Figure 2.8: Schematic diagram of hydrogen adsorption on metal surface and hydrogen absorption inside the metal. Energies of hydrogen in H-metal equilibria: E_s, energy of solid solution; E_m, migration energy; E_b, trap binding energy. Adapted from [26], [60].

2.3.2 Hydrogen trapping and kinetics

Absorbed hydrogen atoms, due to their significantly smaller size, locate at regular interstitial sites. For an ideal crystal, they are preferentially at BCC tetrahedral (such as in tungsten) or FCC octahedral(such as austenitic steel or the Cantor alloy) interstitial sites. As will be discussed further on, HEAs possess a degree of lattice distortion and complexity of chemical environment which affects the positions of the interstitial sites which leads to non-equivalent hydrogen behaviour compared with traditional FCC alloys (Figure 2.9). It is important to note that hydrogen atoms in solid solution, i.e., at interstitial sites of the regular lattice, are only part of the total hydrogen atoms in most cases at thermal equilibrium. Actual metallic materials contain some lattice imperfections that are introduced during the manufacturing process i.e., "intrinsic defects", such as dislocations, vacancies, impurities and grain boundaries as illustrated in Figure 2.10 . In additive manufacturing, defects include cracks, voids, gas pores, keyhole pores, fusion lines, etc. These defects have been shown to act as trapping sites for hydrogen[61]–[63]. However, interstitial sites dominate in number and control the transport and partition of hydrogen at various trap sites.

Hydrogen diffusion behaviour is a critical parameter that describes hydrogen migration and influences the HE of the alloys. At medium temperatures, the diffusion of hydrogen atoms in a metal is a sequence of random jumps between neighbouring interstitial positions. To do this, a hydrogen atom must gain an additional energy E_m (Figure 2.8, which is referred to as the *activation energy for lattice diffusion* or migration energy. In the case of classical diffusion in

the intermediate temperature region (steady-state), the diffusive flux J in atoms/m^{2}s follows Fick's first law:

$$J_\infty = -D_H \nabla C \tag{2.8}$$

where:

- C is the local concentration of solute hydrogen and,
- D_H is the hydrogen diffusion coefficient in m^2/s

The diffusivity also has an Arrhenius-like temperature-dependence given by:

$$D = D_0 \exp(-\frac{E_a}{RT}) \tag{2.9}$$

where:

- D_0 is the pre-exponential factor,
- E_a is the activation energy for hydrogen diffusion,
- R is the gas constant and
- T is the absolute temperature

Moreover, the equation describing the evolution of the hydrogen concentration profile with time is given by Fick's second law:

$$\frac{\partial C}{\partial t} = D_H \nabla^2 C \tag{2.10}$$

For one dimensional (1-D) diffusion, Equation 2.10 reduces to:

$$\frac{\partial C}{\partial t} = D_H \frac{\partial^2 C}{\partial x^2} \tag{2.11}$$

where

- C is the hydrogen concentration,
- t is the time,
- D_H is the diffusion coefficient and
- x is the position

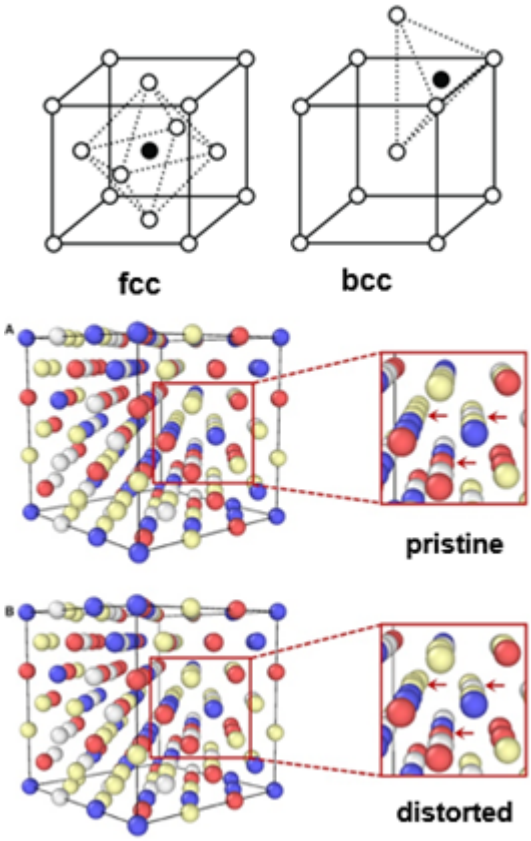


Figure 2.9: Octahedral and tetrahedral interstitial sites in fcc and bcc lattices (shaded circles) and illustration of the lattice distortion in FCC high entropy alloy. Reproduced from [56], [64]

Equations 2.8 to 2.10 apply to single crystals with perfect or defect-free lattices. Realistically, however, hydrogen atoms interact with lattice defects in metals such as point defects, dislocations, grain boundaries, etc. during migration in the lattice. The potential energy of a hydrogen atom varies by its sites, and the hydrogen atom preferentially stays, i.e. **trapped**, at sites close to defects where the potential energy is lower than that at interstitial sites in the regular lattice. The binding energy of hydrogen, E_b, with a type of defect is the energy difference between the trapped site and the regular lattice, as shown in Figure 2.11. The trapping of hydrogen is tighter at sites of higher E_b, making the location more stable. These are known as irreversible traps ($E_b > 60\ kJ/mol$) which includes carbides, inclusions and incoherent precipitates.

Interstitial sites, grain boundaries, lath boundaries, dislocations and coherent precipitates are classified as reversible traps ($E_b < 60\ kJ/mol$). For these kinds of traps, heating at a relatively lower temperature range of 100°C to 410°C promotes hydrogen desorption which is related to the amount of *diffusible hydrogen* in the lattice. Hence, the dynamics of hydrogen transport and trapping are described by first, the solute hydrogen which occupies interstitial positions in the

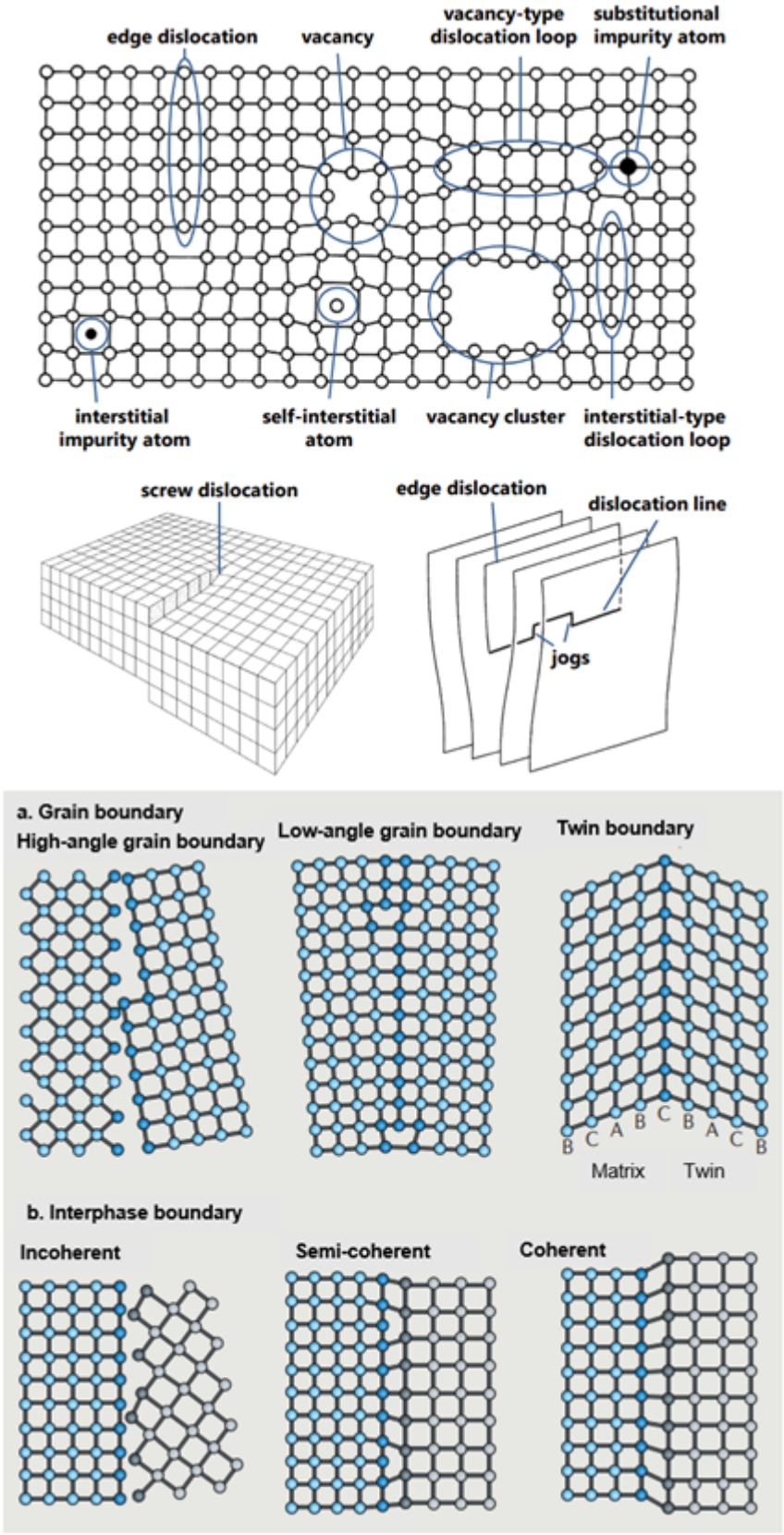


Figure 2.10: Various types of lattice defects in metals(adapted from [65], [66])

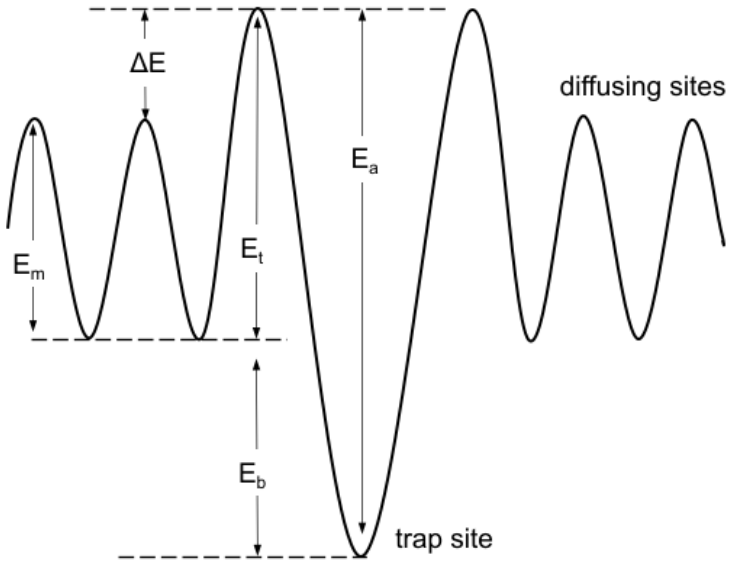


Figure 2.11: Schematic illustration of energy states of hydrogen in lattice and trap sites in metals.

lattice and travels via thermally activated diffusion and second, the trapped hydrogen, i.e., the hydrogen located in various kinds of trapping sites. Solute hydrogen can become trapped by entering trapping sites and can be released from them via thermally activated de-trapping. A general formulation of diffusion accompanying trapping and de-trapping processes is given by McNabb and Foster by adding a term accounting for the interchange of hydrogen atoms between diffusing and trapped states to Equation 2.11. It is given by:

$$\frac{\partial C}{\partial t} + \sum_i N_i \frac{\partial \theta_i}{\partial t} = D_L \widetilde{N}^2 C_L \tag{2.12}$$

with

$$\frac{\partial \theta_i}{\partial t} = k_i C_L \left(1 - \theta_i\right) - p_i \theta_i \tag{2.13}$$

where θ denotes the fraction of available normal lattice and traps occupied by hydrogen, C_L is the lattice hydrogen concentration, k and p are trapping and de-trapping rate parameters and N is the number of trapping sites. The physics and derivation of diffusion is out of the scope of the present investigation and the reader is invited to the works of Crank and Nagumo[67]–[69].

Although the kinetics of hydrogen mobility is more complex than we currently know, there is consistent evidence to purport that strongly trapped hydrogen do not play a signficant role in embrittlement. However, diffusible hydrogen does and this is due to its ability to move and concentrate on critical stress zones where failure is most likely to initiate.

2.3.3 Mechanisms of hydrogen embrittlement

The extent of hydrogen embrittlement is affected by several crucial factors: hydrogen pressure (concentration), temperature, alloy composition, processing and post-processing such as heat-treatment, surface finish, grain directions and other microstructural features. A high hydrogen pressure increases the amount of atomic hydrogen per unit volume and thus augmenting local hydrogen environment embrittlement (HEE) effects on surface defects or tips of advancing cracks. At lower temperature, hydrogen diffuses slowly due to lack of kinetic energy, hence, hydrogen trapping by certain microstructural features such as grain boundaries is enhanced. Increasing the temperature reduces trapping as hydrogen atoms become more mobile and can possibly diffuse externally. This explains why hydrogen embrittlement is most severe at lower temperatures,e.g. room temperature. For the same reason, slow strain rate tests (SSRT) are conducted to ensure a hydrogen environment on a propagating crack despite its sluggish movement. For example, many conventionally manufactured Fe-Ni-Cr austenitic steels are mostly embrittled by hydrogen at a temperature range of -150°C to 150°C and strain rates are often in the order of 10^{-6} s^{-1}. These two- *dependence on strain rate and temperature*- are known to be the key features of HE.

Surface finish is also important, as surface microcracks can grow to internal cracks undetected when exposed to hydrogen and can cause catastrophic failure. The product form, processing technique, alloy compositions and heat treatment can drastically affect HE properties, especially for alloys with complex microstructures. Structures with fine grains and discontinuous phases and precipitates might resist HE while larger grains and continuous intergranular precipitates may provide a path for fracture and facilitating embrittlement[19]. This is significant in LPBF where the part produced has a complex, hierarchical microstructure with poor as-printed surface quality and often needs heat-treatment to reduce defects and porosity and improve consolidation.

After sufficient hydrogenation, the alloys are typically macroscopically embrittled. Hydrogen assisted cracking could commence followed by ductile, mixed ductile-brittle, or completely brittle

fracture mode. In terms of fracture micromechanisms, hydrogen can change microscopic fracture modes from pure ductile (dimpled) mode due to microvoid coalescence to mixed quasi-cleavage or brittle cleavage, transgranular or intergranular fracture[70].

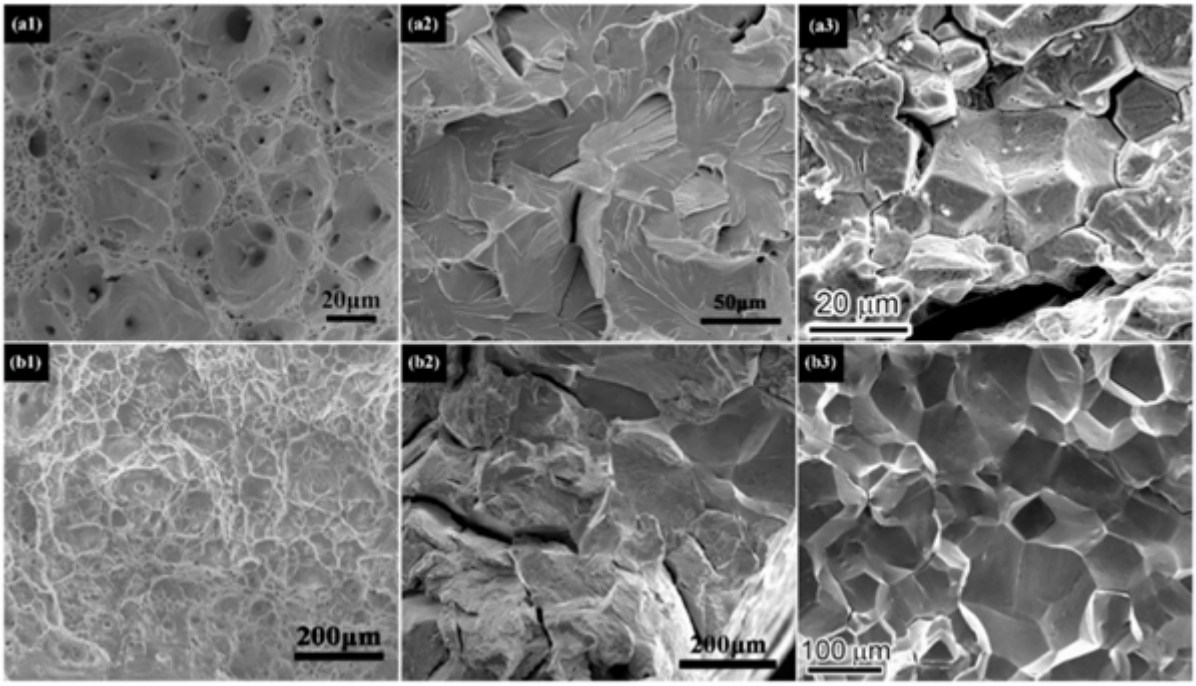


Figure 2.12: Examples of fracture surfaces for different fracture modes. Dimples characteristic of microvoid coalescence (a1,b1) suggest ductile fracture in the absence of hydrogen. Brittle fracture due to hydrogen includes cleavage (a2), intergranular cracking (a3,b3) and quasi-cleavage(b2)(adapted from Wang,et.al., Martin, et.al., and Wada, et.al.[71]–[73])

Although HE of alloys has been studied for one and a half centuries, there are still disputes over its nature and mechanisms because first, it is highly interdisciplinary and as such would need intensive requirements for a comprehensive understanding and secondly, hydrogen mobility and trapping, with hydrogen being the smallest and lightest element, is extremely challenging to study directly[26]. One must have information on the nature of the source of atomic hydrogen and how it interacts with the surface of the specimen, how it enters the metal through the crystal structure or grain boundaries and interacts with and trapped by microstructural features, moves with dislocations and induces different fracture modes. Despite the challenges, several HE mechanisms have been proposed and they include[55]:

- high hydrogen pressure bubble or void,
- hydrogen-induced reduction in surface energy,
- hydrogen enhanced dislocation ejection from the surface or near-surface region,
- hydrogen induced reduction in cohesive strength (HEDE),

- hydrogen enhanced localised plasticity (HELP),
- hydrogen and deformation assisted vacancy production,
- hydrogen and strain induced phase transformations and,
- nanovoid growth, nucleation and coalescence (NVC)

According to Koyama, *et.al.*(2017):

> *"...the main challenge in identifying the governing mechanisms behind hydrogen embrittlement lies in mapping hydrogen trapping and kinetics with microstructural sensitivity[74]"*

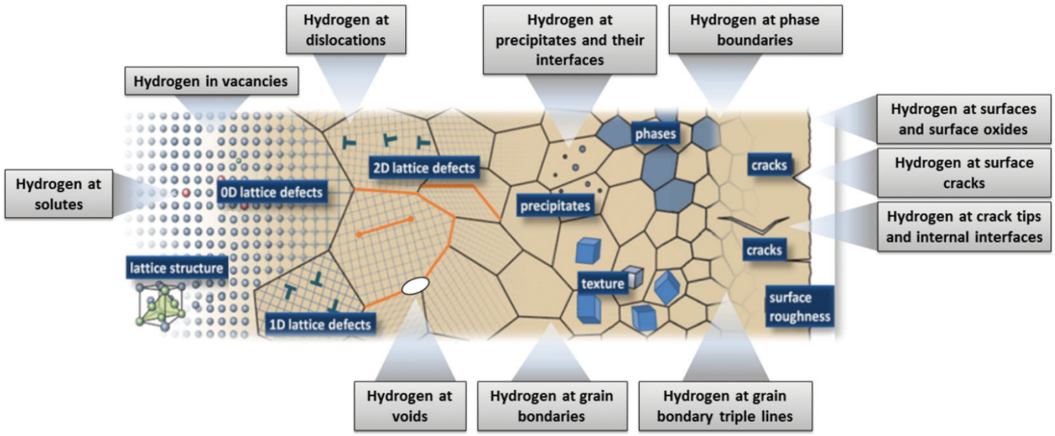


Figure 2.13: Schematic diagram showing interaction of lattice defects such as vacancies and certain solutes, dislocations, grain boundaries, phase interfaces, triple points, precipitates, micro- and nano-cracks, surface steps, voids, and surface oxide layers. Adapted from Koyama, *et.al.* 2017.

The mechanisms at work depend on the material, nature of hydrogen source and the load applied. However, for conventionally and additively manufactured CoCrFeMnNi HEA, the most cited mechanism in literature is the hydrogen enhanced decohesion (HEDE) and hydrogen enhanced localised plasticity (HELP). On one hand, hydrogen enhanced decohesion occurs when the presence of hydrogen in the crystal lattice reduces the bond strength and therefore leads to breakage at lower threshold. For this, grain boundary character such as angles, symmetry, tilts, twinning and misorientations play an important role. **HEDE** is mainly characterised by an intergranular (IG) brittle fracture mode or IG cracking, indicating that grain boundaries are the weakest paths for hydrogen-assisted crack initiation and propagation. On the other hand, **HELP** asserts that the presence of hydrogen accelerates the generation and movement of

dislocations, i.e. higher dislocation velocity, irrespective of dislocation type and crystal structure. The hydrogen modifies the environment of dislocations (or defects to which it is attached) such that in some areas, stress fields are reduced, lowering the energy barrier that must be overcome for dislocations to move. This is characterised by the presence of ductile features in hydrogen-assisted fracture surfaces such as tear-ridges and slip bands as illustrated in Figure 2.14. These features were observed in numerous alloys, including the cast, equimolar FeNiCoCr, which is a derivative of the Cantor alloy[75]. This mechanism provides the basis as to why hydrogen embrittlement has a strong dependence on a narrow temperature, slow strain rates and normal loads. When the strain rate and stress is high, dislocation velocity increases and dislocations can move away from a hydrogen environment. At elevated temperatures, hydrogen will not remain bound to the dislocation environment and modify stress fields around it and instead act as a strengthening agent that impedes dislocation motion. However, it is widely agreed that while these mechanisms can all be operative in the HE process, no single mechanism can completely explain all the associated fracture features. For instance, Wang, *et.al.* (2014), Martin *et.al.* (2011,2012) and Djukic *et.al.* (2019) proposed and described how the two aforementioned mechanisms can work in synergy in the so-called HELP+HEDE mechanism or HELP-mediated HEDE[71], [72], [76], [77]. This model suggests that hydrogen interacts with dislocations, promoting the formation of local dislocations during the deformation. Simultaneously, hydrogen migration towards grain boundaries can be accomplished through enhanced dislocation movement due to the HELP mechanism activity. As mobile dislocations encounter the grain boundaries, the dislocations are piled up at the site, and hydrogen is deposited, leading to stress concentration and hydrogen enrichment. When the critical hydrogen concentration is reached, **intergranular-like** cracking occurs.

This synergistic mechanism reclassified hydrogen assisted-fracture into two groups: pure brittle intergranular (IG) and plasticity-mediated integranular-like (IG-like) fractures. Pure brittle IG fracture appears at locally high hydrogen concentrations while IG-like fracture is characterised by reduced hydrogen concentration[70].

2.3.4 Quantifying and mapping hydrogen-metal interactions

Aside from evaluating the operative mechanisms, formulating a clear understanding of fundamental hydrogen-material interactions such as uptake, trapping and diffusion are crucial to the

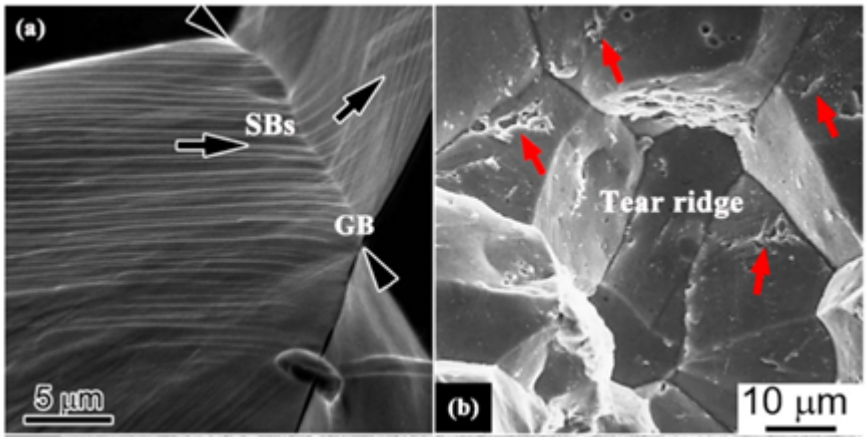


Figure 2.14: Plastic slip bands at hydrogen-assisted integranular fracture facet in Ni alloy (a); tear ridges on grain boundary facets of Cd-plated steel (b). Reproduced from Martin, *et.al.*, (2012) and Lynch, (2019) [72], [78].

study of material degradation due to hydrogen embrittlement. For one, the mechanism of Stage II crack growth as illustrated in Figure 2.15 (a) common with hydrogen-assisted cracking has been shown to have a linear relationship with changes in hydrogen diffusivity[81]–[83]. Second, diffusible hydrogen is a critical parameter that correlates with the threshold stress intensity factor for hydrogen-assisted cracking[84]–[86] and third, studies have revealed that the addition of strong trapping sites such as carbides by microstructural tailoring, alloying, etc. increases the HE resistance by decreasing the amount of diffusible hydrogen in a closed system[87], [88]

Two general approaches exist for analysing hydrogen-metal interactions: (1) quantification of hydrogen content (both diffusible and trapped) and trapping parameters, and (2) spatially resolving and microstructure-sensitive mapping. In the former category, the two most common methods are permeation and thermal desorption. On one hand, permeation involves two solution environments separated by metal of interest acting as a membrane. Hydrogen atoms are generated on one side, absorbed thru the metal (membrane) and effuses to the other side. The source of hydrogen can be gaseous or electrochemical. Permeation experiments are outside the scope of this study but is extensively reported by the works of Boes and Züchner (1976) and Subramanyan (1981)[89], [90] . On the other, thermal desorption-based methods typically use specimens that have been pre-charged with hydrogen, which are then placed in a vacuum chamber and heated according to a pre-programmed temperature vs time profile. Thermal desorption spectroscopy analysis (TDA) is a quantitative method for determining the hydrogen content at specific microstructural constituents with a characteristic trapping depth such as dislocations. Although this method does not provide spatially resolving mapping, hydrogen desorption rate

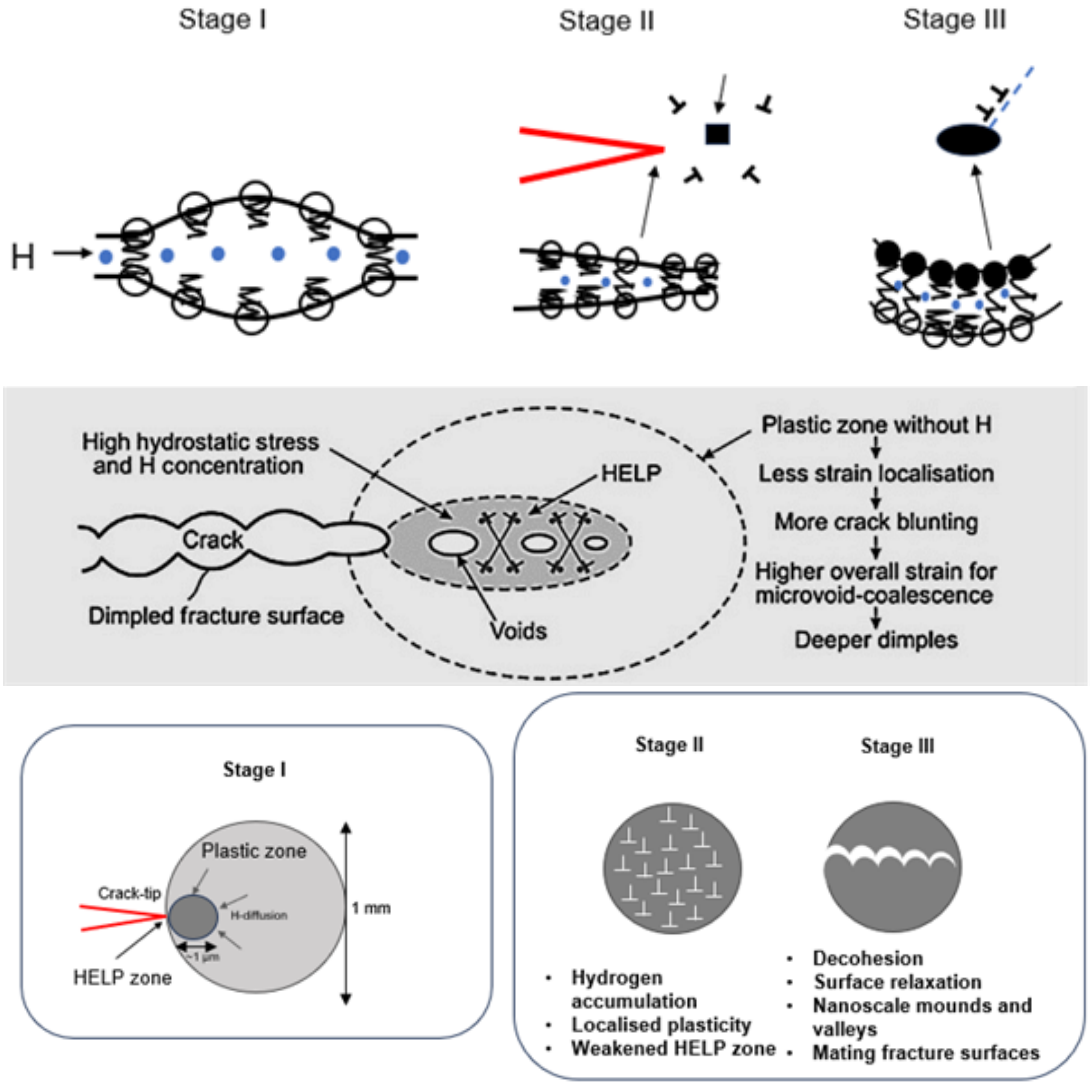


Figure 2.15: Schematic illustrations of the three dominant mechanisms of hydrogen embrittlement, HEDE (top), HELP (middle) and HELP+HEDE (bottom) [79], [80].

profiles detected by TDA are microstructure-sensitive (see Figure 2.16). For one, the global hydrogen content can be quantified by TDA. Specifically, TDA measurements conducted at different heating rates enable the determination of the activation energy of de-trapping from each type of lattice defect by analysing the resulting hydrogen desorption profiles. Accordingly, the cumulative hydrogen content associated with each of the TDS peaks that is characterised by a specific activation energy E_a, of the underlying trapping mechanism gives the local hydrogen content at each of these lattice defect traps[68], [74]. However, interpretation of experimental TDS spectra, i.e., relating TDS ouput to trapping characteristics remains a challenge. The three most common theoretical framework that approach this problem are proposed by first, McNabb and Foster which I briefly mentioned in Section 2.3.2, second by Oriani and lastly by Kissinger

(also known by Choo-Lee). As mentioned, McNabb and Foster's model provides a generalised treatment that explicitly includes hydrogen trapping and detrapping kinetics in the treatment of hydrogen diffusion[91]. This approach is complex and solutions are generally difficult. Hence, Oriani simplified the model by assuming a *local equilibrium* between trap sites and the lattice, reducing it to a single equation[92] while Kissinger assumes a detrapping (dissociation) dominated mechanism where diffusion is fast which also simplified the model to a single solution to calculate trap binding energies[93], [94]. Kissinger's approach, although the most straightforward, has a very narrow applicability within a small TDS heating rate range, sufficiently thin samples and high-diffusivity materials such as BCC crystals. Hence, Oriani's approach is often considered to be the most appropriate to model H-diffusion in FCC materials because of the significantly lower diffusivities. Oriani assumed that trap kinetics (trapping-detrapping) occur faster than lattice diffusion[1]. Such an assumption implies that the chemical potentials of the hydrogen in lattice sites and in trap sites are equal, what we refer to as *local equilibrium*. This is a crucial requirement in the correct application of Oriani's equations and the methods employed in this study were designed to achieve this criterion.

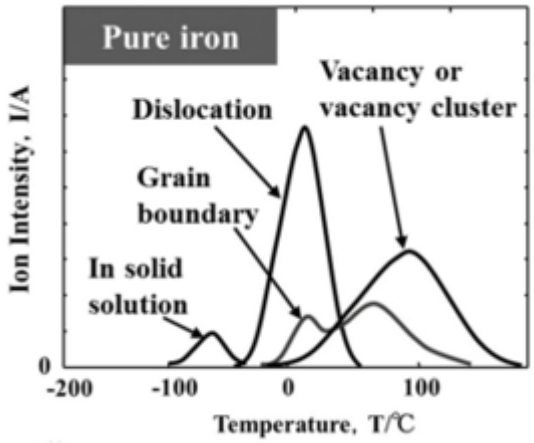


Figure 2.16: Schematic of a hydrogen desorption profile together with indication of the corresponding trap sites. Reproduced from Abe,at.al.(2011)[95]

Spatially resolving and microstructure-sensitive mapping techniques include autoradiography, scanning photoelectrochemical microscopy, scanning electrochemical microscopy, secondary ion mass spectroscopy (SIMS), silver reduction and decoration, the hydrogen microprint technique, scanning Kelvin probe force microscopy, atom probe tomography (APT), prompt γ activation analysis, proton-proton scattering, and neutron radiography. Among all these techniques,

[1]this implies that the rate-limiting step is the diffusion of hydrogen through the lattice

the maximum attainable spatial and chemical resolution for resolving the position of hydrogen can be achieved by atom probe tomography (APT). Moreover, the high spatial resolution (∼0.1 nm to 0.3 nm in depth and 0.3-0.5 nm laterally) and high chemical sensitivity(<10 ppm) is well-suited for HEAs with complex chemical compositions composed of local atomic configurations and nano-sized microstructural features. The analysis volume of APT typically measures tens of nanometers in diameter and hundreds of nanometers in depth. When combined with site-specific specimen preparation using focused ion beam, APT facilitates detailed investigations of the chemistry of strengthening phases at the microscale, including their interfaces in HEAs[96]. APT combines well-controlled evaporation and ionisation of surface atoms layer-wise from a tip-shaped specimen in combination with time-of-flight mass-to-charge spectroscopy and a position sensitive detector. The time-of-flight serves for chemical analysis through mass-to-charge spectroscopy and the impact regions on the position-sensitive multi-channel detector serve for the determination of the original position of the field-evaporated ions within the sample. A three-dimensional map can thus be reconstructed from the collected data. Typical dimensions of the analysed volume can comprise up to one billion atoms on current state of the art instruments[74]. However, since hydrogen is ubiquitous in any ultra-high vacuum system, APT experiments are conducted using deuterium charging. Atom probe tomography is utilised in this study as a supplemental characterisation technique to analyse the microstructure and possibly map hydrogen distribution in a microstructural feature. Hence a comprehensive discussion on the physics of atom probe tomography, particularly of field evaporation, is beyond the scope of the study and the reader is directed to the work of Gault, et.al.[97]–[99].

2.3.5 Hydrogen embrittlement in CoCrFeMnNi HEA

Several studies on the conventionally manufactured Cantor alloy showed that it has superior hydrogen embrittlement resistance as evidenced by the very low reduction in ductility due to hydrogen charging compared to 304 and 316L stainless steels. Fractographic analysis shows similar mode of ductile fracture for charged and uncharged samples, supporting that hydrogen does not induce ductile-to-brittle fracture in the HEA. It was reasoned that gaseous H-charging fails to embrittle the alloy because the hydrogen content is below the threshold required for triggering HELP[23]. It was even reported that rather than being detrimental to the mechanical properties as it is in most other alloys, hydrogen was rather observed to enhance strengthening

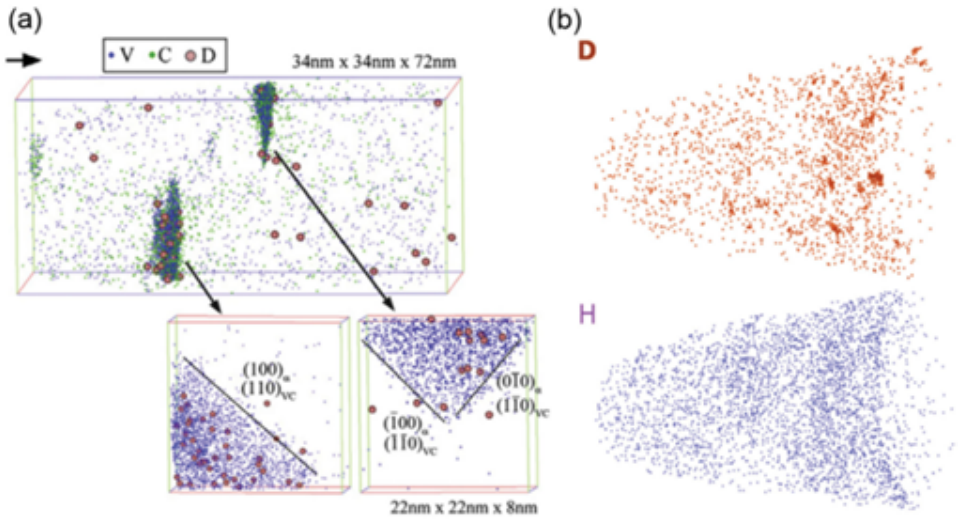


Figure 2.17: (a) APT revealing the deuterium distribution at a vanadium carbide precipitate. (b) Comparison of deuterium and hydrogen distributions in Ag, revealing that deuterium is more indicative when aiming to reveal microstructure-related effects. Reproduced from Koyama,et.al.2017[74].

and toughening mechanisms. This was attributed to hydrogen reducing the stacking fault energy (SFE) and therefore the phase stability of the alloy, *i.e.*, hydrogen alloying decreases the stability of the FCC lattice structure matrix, triggering more intense nanotwinning upon loading, thereby improving the strain-hardening of the alloy. It is worth noting that the diffusible hydrogen concentration in the sample with the highest increase in ultimate tensile strength (UTS) and ductility is 8.01 wt.ppm, and increasing the hydrogen concentration shows slightly reduced increments in the two measured properties suggesting that induced hydrogen alloying, promoting both stress and ductility assumes certain saturation states[100]. Furthermore, because the alloy is reported to possess superior mechanical properties at cryogenic temperatures[5], it has been demonstrated that the damage tolerant property can be maintained even when exposing the Cantor alloy to hydrogen at 77 K, also attributed to the aforementioned reduction in SFE. The formation of deformation twins and a very slow diffusion rate of atomic hydrogen at this temperature prevents hydrogen from an effective enrichment and therefore has minor effect on the ductility of the material. Moreover, compared to nickel, and other stainless steels with FCC crystal structure, the Cantor alloy exhibits the most solubility of hydrogen because of the higher Cr and Mn content which contribute to a higher trap density[24].[2] These reports seem to imply that the classical Cantor alloy belongs to the group of metals that are essentially immune

[2]Note that solubility and diffusivity of hydrogen in austenitic vs ferritic alloys are inversely related. For instance, γ-iron has a higher solubility but very low diffusivity while α-iron has a low solubility but higher diffusivity.

to hydrogen embrittlement. However, the contrary has been demonstrated upon charging at a significantly higher hydrogen pressure of 120 MPa for 160 hours. The samples failed at a significantly slower strain rate (10^{-6} s^{-1} compared to 10^{-4} s^{-1}) with an integranular fracture mode[25]. In addition, studies show that hydrogen can either increase or decrease the yield strength or doesn't affect it at all, inducing both strengthening or softening. These conflicting findings can be attributed to the difference in strain rate, hydrogen content and the type of hydrogen charging. Even so, it is well known that the conventionally manufactured CoCrFeMnNi shows much lower HE susceptibility than type 304 and 316 stainless steels[28].

Aside from the strain rate, temperature and method of hydrogen charging used, there are other special considerations that affect HE in high entropy alloys, namely:

- **Hydrogen dissolution, diffusion behaviour and trapping**. HEAs are found to have higher hydrogen storage capacity than traditional alloys. This is due to the variation of the chemical environment and lattice symmetry distortion to an extent not present in traditional alloys causing the hydrogen behaviour to be non-uniform, i.e., all the octahedral and tetrahedral sites are no longer equivalent.

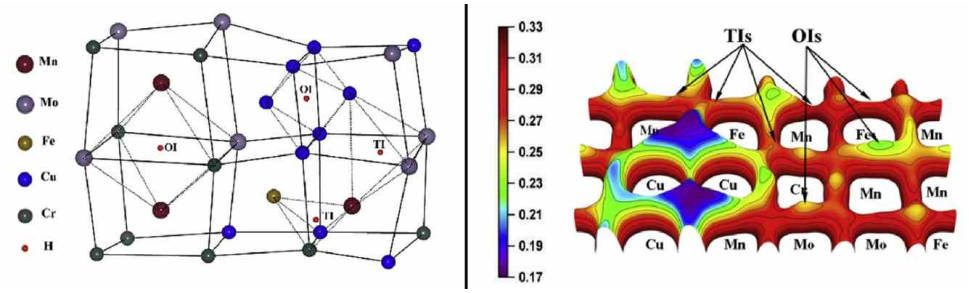


Figure 2.18: Schematic of the lattice distortion in example HEA and 3D isosurface of electronic density. Reproduced from Ren, *et.al.* (2019)[101].

For FCC CoCrFeMnNi, hydrogen atoms preferentially reside at octahedral interstitial sites which has a lower average dissolution energy compared to tetrahedral sites. The higher relative amounts of Cr and Mn provides more of these interstitial sites which leads to increased H-trapping. Hydrogen diffusion in HEAs can be described as sluggish compared to pure metals, for several reasons. Migration of H across the lattice are blocked by unstable interstitial positions, irregular barrier energies along pathways and lattice potential fluctuations. Cr having more valence electrons that interact with H stabilises lattice hydrogen, leading to more trapping and decreased mobility. Temperature also affects diffusion as hydrogen gains more mobility and thermal energy introduces additional changes in lattice

structures and energies. Comprehensive information on peak temperatures, types of strong hydrogen traps and its effects on the mechanical properties of HEAs are still lacking to date. One prevailing hypothesis is that the introduction of strong H-traps can enhance resistance to HE by hindering diffusion and/or desorption. The extent of hydrogen diffusion is dependent on the diffusion coefficient, D_H. For the conventionally manufactured Cantor alloy, machine learning model calculations have found that D_H can be expressed as a function of the atomic ratios of each components as[102]:

$$log(D_H) = 0.096Fe\ -0.47Co\ +3.05Ni\ -1.01Cr\ -1.66Mn\ -15.05 \tag{2.14}$$

In another study, the temperature dependence of D_H for equiatomic CoCrFeMnNi is expressed as[29]:

$$D = 4.3 \times 10^{-7}\ exp(\frac{-51.7kJmol^{-1}}{RT}) \tag{2.15}$$

Typical values from literature for conventionally manufactured Cantor alloy range from $1.4 - 3.7 \times 10^{-16}\ m^2/s$ at room temperature[28], [29]. However, studies on hydrogen diffusion for additively manufactured Cantor alloy or HEAs in general are limited due to the complexity of the microstructure[103]. A report by Lin, *et.al.* (2022) estimated the diffusivity coefficient to be $1.1 \times 10^{-15}\ m^2/s$ for the as-printed Cantor alloy and $1.8 \times 10^{-15}\ m^2/s$ for annealed through cathodic charging and fitting of Fick's law assuming 1-D diffusion[104]. Although the results show great correspondence, low charging times and thicker samples do not guarantee a homogeneous distribution of hydrogen in the specimens which is necessary for the assumption of Fick's diffusion laws. Furthermore, a description of the nature of trapping in relation to the microstructure has not been put forward.

- **Hydrogen concentration**. Low hydrogen concentration has an effect of reducing the stacking fault energy and promotes the formation of twins that enhance the strength and plasticity by creating new surfaces and reducing the mean path of dislocations, aka twin boundary strengthening[75], [100]. On the other hand, high hydrogen concentrations often achieved thru very high gas pressures of >100 MPa and electrochemical hydrogen charging decreases the cohesive strength of potential cracking sites like grain and phase boundaries or interfaces promoting decreased plasticity and brittle fracture (HEDE mechanism). Also, whether hydrogen affects the yield strength or not depends on the hydrogen concentration and a critical value that denotes a significant transition point is yet to be determined.

- **Alloying elements affect hydrogen diffusivity, twin formation and grain boundary cohesion**. For example, the presence of relatively higher amounts of Cr in the Cantor alloy introduces more H-traps. Moreover, the removal of Mn has been shown to increase HE resistance although the underlying mechanism remains unknown, and the addition of Mo to CoCrNi increases HE resistance due to solid solution strengthening and increase in grain boundary cohesion[105], [106].

- **Microstructure**. Reducing dislocation density along grain boundaries has been shown to improve HE resistance. Grain refinement also tends to do the same effect by decreasing local hydrogen segregation. However, studies on annealed CoCrFeMnNi at 700°C reported the formation of a tetragonal σ-phase precipitates with composition 46.5Cr-16.6Fe-17.6Co-12.7Mn-6.6Ni atomic percent that act as cracking sites for HE[107]. Although the phenomenon might be expected to be similar, the effect of precipitates on the HE properties of LPBF CoCrFeMnNi have not been extensively investigated.

Earlier reports on LPBF CoCrFeMnNi show a great resistance to HE owing to the high solubility of hydrogen resulting from nanoscale heterogeneity and easy formation of twins. Moreover, after gaseous pre-charging at 15 MPa, the yield strength was even improved and the strain at break only decreased slightly[27]. As pointed out before for conventionally manufactured HEA, such behaviour often occurs at lower gas pressures and higher strain rates. Hence, most of the subsequent studies have used electrochemical hydrogen charging which introduces more H into the sample. In addition, a number of these studies have adopted *in-situ* charging, i.e., the samples are charged simultaneously with mechanical testing[28], [49], [107]. This is in contrast to *pre-charging* where the samples are often immersed in liquid nitrogen after charging to prevent outgassing prior to the mechanical testing, e.g. uniaxial tension tests. The former is meant to induce external HE while pre-charging intends to induce internal HE.

As described previously, cellular structures made from walls of high density dislocations are observed in LPBF CoCrFeMnNi. Studies have shown that there can be a local variation in hydrogen diffusion coefficients in different microstructural features such as the ones found in AM HEA and these can promote cracking in hydrogen-dense regions. In fact, it was reported that as-printed CoCrFeMnNi is embrittled when electrochemically pre-charged with hydrogen and showed intergranular crack propagation. These results point to the possibility that hydrogen gathering at the dislocation cellular structures could promote the increase of boundary misori-

entation and lead to cracking. However, this conjecture needs further validation. Nevertheless, there is evidence to conclude that modification of the cellular structure by well-controlled annealing improved the HE resistance of the alloy. After annealing at 900°C for 1 hour, many completely recrystallised equiaxial grains were formed due to the easing of local residual strain. Also, annealing reduced the density of dislocations while maintaining the outline of the cellular structures. For these annealed samples, a deformation area decorated with dislocation structures and nanotwins formed near the surface where plastic deformation preferentially occured initially thru hydrogen enhanced localised plasticity (HELP). This mechanism also allowed H-atoms to diffuse to the interior of the now thinner-walled cell structures, decreasing H-concentration in the grain boundaries. When cracking does occur, slip bands and dislocation cells form from the grain boundaries being able to capture more hydrogen, blocking the propagation of HE cracks[28].

Local hydrogen concentration at microstructural features unique to AM HEAs can be investigated further using atom probe tomography. As briefly mentioned in the preceding chapter, the high spatial resolution and chemical sensitivity in APT has already allowed for the investigation of grain boundary segregation and interfacial phase transformation in conventionally manufactured HEAs where it is revealed that Ni and Mn co-segregate to some grain boundary regions with the depletion of Fe, Co, Cr, while Cr is enriched in other regions of the grain boundaries where Mn and Ni are depleted[108]. The technique has been applied to AM HEAs as well such as LPBF AlCoCrFeNi and CoCrFeNi where it was used to reveal a more homogenous phase without Fe-Cr and Al-Ni enrichment and fluctuating Cr concentration for AlCoCrFeNi and a mechanism of hot-cracking in CoCrFeNi[109], [110]. However, to the best of our knowledge, there are no reports on the spatial mapping of hydrogen for the AM Cantor alloy. The closest in terms of composition and crystal structure are APT analyses of hydrogen in steels where the study focuses on H-trapping in semi-coherent and incoherent second-phase precipitates and phase boundaries[111]. Although the findings of these studies provide insights into the science of hydrogen-defect interaction for alloys in general, the unique chemistry of the classical equiatomic CoCrFeMnNi combined with the microstructure evolution in LPBF necessitates a separate investigation. The lack thereof means that identification of the challenges to APT sample preparation and subsequent analysis are lacking, which is important in proper interpretation of APT data.

2.4 Summary

As promised, I have discussed the relevant background behind studies on the hydrogen embrittlement of alloys, particularly the CoCrFeMnNi (Cantor) alloy. Aside from laying out the fundamental aspects of the phenomenon, I have also identified issues in the field such as: (1) conflicting observations of embrittlement or ductilisation and the roles of microstructural features such as dislocation cells, (2) unvalidated or insufficient assumptions in the analysis and interpretation of thermal desorption spectroscopy data that arise from the methodology such as low charging times and non-homogeneous hydrogen concentration and (3) the lack of information on the challenges of conducting atom probe tomography analysis for detecting hydrogen on the alloy. Thus, I have solidified the need to conduct this study and I am ready to proceed to the discussion of the means in which I achieve the stated aim.

Chapter 3

Experimental Methods and Characterisation Techniques

In Chapter 1 I have laid out the aim of the current investigation and in the preceding chapter, I have fleshed out the relevant background that led to the formulation of this aim. In this Chapter, I discuss the steps that were carried out towards the attainment of this aim and briefly provide an overview of the methods involved in these steps, including theory and relevant literature. I recall from the first chapter that this study aims to provide a detailed description of the effects of hydrogen on an additively manufactured CoCrFeMnNi high entropy alloy at as-printed and annealed conditions. In order to attain this aim, I had to:

- fabricate a well-consolidated Cantor alloy (equiatomic CoCrFeMnNi) by selective laser melting, a laser powder bed fusion technique, and characterise its physical properties.
- investigate the microstructural evolution of the alloy after annealing at 900°C for 2 hours *in air* and relate this to the observed changes in mechanical properties including hydrogen embrittlement.
- quantify the amount of hydrogen in the alloy and calculate the hydrogen trapping and diffusion parameters using thermal desorption analysis (TDA).
- identify challenges in the site-specific detection and description of the presence of hydrogen such as in grain boundaries using atom probe tomography.

The following sections describe the specific procedures within these steps.

3.1 Powder Analysis

This study uses gas-atomised pre-alloyed powders provided by H.C. Starck GmbH with the following nominal powder composition:

Table 3.1: Elemental composition of the HEA powder

	Co	**Cr**	**Fe**	**Mn**	**Ni**	**O**	**H**	**C**	**N**
Conc (wt%)	23.2	18.2	19.5	17.9	21.2	0.077	0.0015	0.007	Bal

The prints were made using once-recycled powders.[1] They were sieved before addition to the powder bed and analysed using SEM for morphology and EDS for elemental composition with

[1]The concentration of the five principal elements come from the as-received virgin powders but since they have been once-used, the C, H and O concentrations are determined as well to assess powder quality. The levels are very low and should not be a concern for LPBF.

a Zeiss Ultra SEM and ThermoScientific Phenom ParticleX Steel Desktop SEM, respectively. Particle size distribution was obtained using a Horiba LA-920 Laser Scattering Particle Size Distribution Analyser.

3.2 Additive Manufacturing

The powders were fed to a ProX® 200 Direct Metal Printer (DMP). A parametric study was done to determine the printing parameters that would lead to a maximum consolidation of the printed specimens. A central composite design was used having a total of 20 rectangular builds with dimensions 10 mm x 10 mm x 5 mm (See Appendix A). The levels of the parameters were based on references [12]–[15], [47], [112], [113]. The as-built samples were cut from the build plate using an Excetek V440G EDM. Afterwards, the relative density was evaluated using the Archimedes principle. Image J software was used to evaluate porosity by SEM image analysis. A theoretical density of 8.05 g/cm^3 was used for all relative density measurements of the as-printed specimens[114]. The printing parameters of the sample with the highest density is used to print blocks with dimensions 80 mm x 16 mm x 20 mm. After printing, some blocks were placed in a tube furnace and annealed in air for a holding time of 2 hours at 900°C set temperature with a temperature ramp of 5°C/min followed by furnace cooling at a rate of 10°C/min.

3.3 Phase Determination and Elemental Analysis

To identify the phases present, representative samples (as-received powders and LPBF parts) were machined from the sample blocks, polished, characterised by X-ray diffraction (XRD) using a Bruker D8 Advance X-ray diffractometer with CuKα radiation (λ=0.14 nm) with $9^\circ < 2\theta < 99^\circ$ for a total scan time of 1 hour. Elemental composition of both as-received powders and AM builds were evaluated via SEM-EDX using a Zeiss Ultra SEM equipped with an 80 mm^2 Oxford Instruments EDX detector.

3.4 Metallurgical Sample Preparation

Sample coordinates are defined as Z being the build direction (**BD**) and transverse directions **TD1** and **TD2** being orthogonal to Z. Samples were cut from the as-built parts on the longitudinal and transverse planes with respect to the build direction as indicated in Figure 3.1. They were then mounted on a conductive phenolic SEM resin and ground using P600 and P1200 SiC papers and subsequently polished with 3 μm diamond suspension for an average of 10 minutes. Final polishing was done with 50 nm colloidal silica until a mirror finish was achieved with an average duration of 10 to 15 minutes. For EBSD analysis, final polishing is prolonged until there are almost no visible scratches under the light microscope. Ultrasonic cleaning was used to remove further contaminants on the surface.

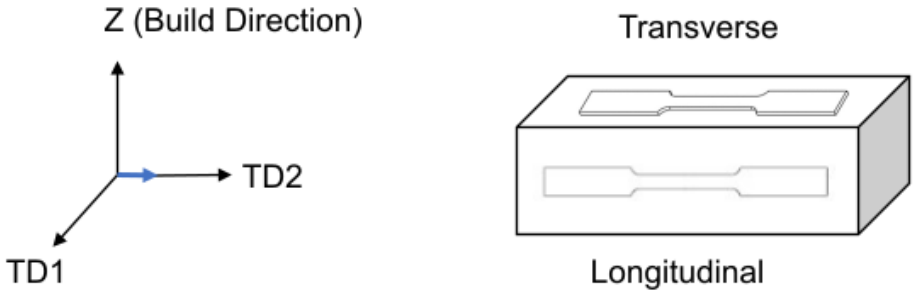


Figure 3.1: Coordinate system and schematic of sample cut direction.

3.5 Mechanical Testing

Flat dog-bone tensile samples were EDM-cut from the printed rectangular blocks according to ASTM sample standards as shown in Figure 3.2[115]. The samples were subjected to uniaxial tests in an Instron 3366 tensile tester equipped with an extensometer. The engineering strain vs engineering stress curves were plotted and the yield stress (σ_y), ultimate tensile stress (σ_t) and strain at break (%) were recorded. The fracture surface was then analysed using a Zeiss Ultra scanning electron microscope (SEM).

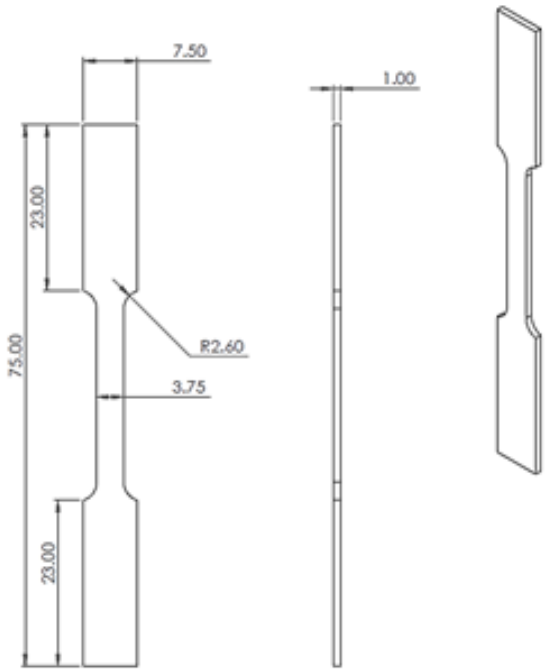


Figure 3.2: Tensile specimens. Thicknesses of 0.5 mm, 1 mm and 2 mm were used in the study.

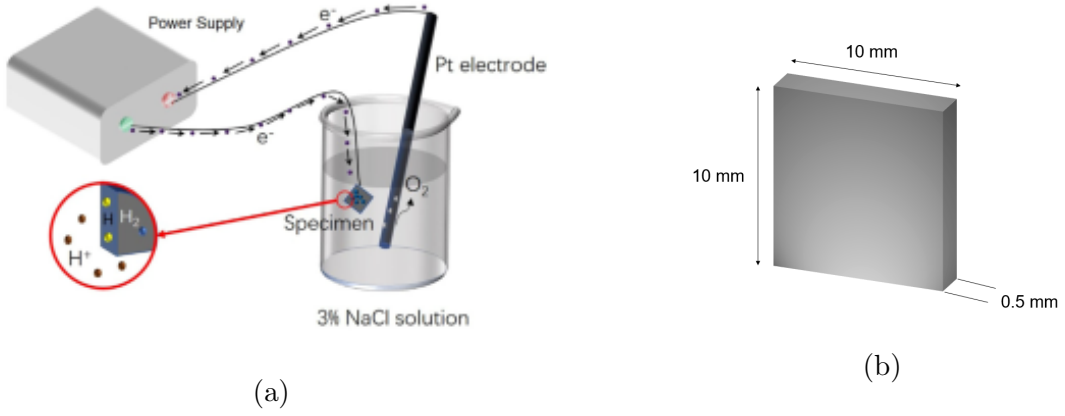
3.6 Microstructure Characterisation and Fractography

To reveal the microstructure, electrolytic etching was done on polished samples using 10% oxalic acid for ∼90 seconds. The samples were washed with deionised water and then ultrasonically cleaned with ethanol. The etched samples were then viewed under the optical microscope for initial examination and then under the Zeiss Ultra SEM which was also used for fractography. Electron backscatter diffraction (EBSD) and Electron Channeling Contrast Imaging (ECCI) was used to analyse the phases, grain size, texture and image dislocation cells with a Zeiss Supra SEM and Zeiss Merlin I equipped with a high-resolution EBSD detector at 15-20 kV acceleration voltage.

3.7 Hydrogen charging

Both tensile and TDS specimens (with dimensions in Figure 3.3 (b)) were electrochemically pre-charged with hydrogen in a Gamry three-electrode electrochemical cell filled with 3 wt% NaCl solution at 80°C for 7 days. The choice of charging time and temperature was informed by a prior optimisation experiment detailed in Appendix C and is also discussed in further detail in

Chapter 5. The counter electrode consisted of a platinum rod that worked as the anode and the specimen itself was the cathode. A saturated calomel reference electrode (SCE) was employed to monitor the electrochemical potential of the sample during the charge. Hydrogen was generated by imposing a cathodic current density, J_C, of 5 mA/cm^2 by means of a TTi-PLH120 DC power supply. The solution was deaerated with nitrogen gas for at least 1 hour before starting the hydrogen charge and N_2 bubbling was maintained until the end of the experiment. Figure 3.3 (a) shows a schematic diagram of the electrochemical cell set-up used in this work.



(a) (b)

Figure 3.3: (a)The electrochemical hydrogen charging set-up. Reproduced from Zafra, *et.al.* (2022)[116] (b) Dimensions of the specimens used for TDS.

3.8 Thermal Desorption Spectroscopy

Analyses of the desorption of adsorbed hydrogen from the metal surface under a controlled temperature ramp provide information on various parameters such as the number and populations of adsorbing phases, and the activation energy of desorption. The desorption-rate profile against temperature in thermal desorption spectroscopy is affected not just by hydrogen states in the metal but also experimental parameters such as specimen size and the temperature-ramp rate. In thermal desorption analysis, the measured quantity is the desorption rate of lattice hydrogen that diffuses out through the material undergoing trapping and detrapping processes. TDS measurements are usually performed in an ultrahigh vacuum chamber. The measurement system consists of a mass spectrometer and a heating device. The sample temperature is often measured by a thermocouple attached to the sample and is sometimes controlled by a feedback system to be linearly increased. A differentially pumped quadruple mass spectrometer (QMS) with a shield shown in Figure 3.4 is used for this measurement [117].

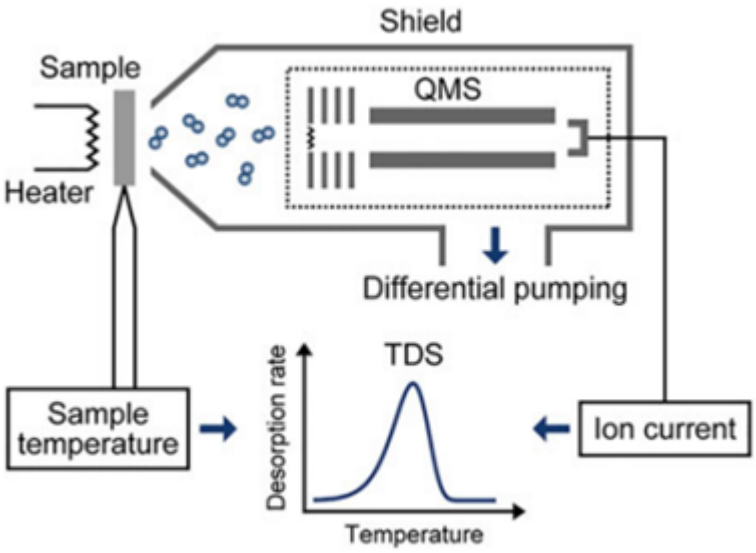


Figure 3.4: Schematic setup of the TDS measurement. A shielded and differentially pumped quadropole mass spectrometer preferentially detects desorbing gas from the front side of the heated sample. Reproduced from Ogura, et.al.(2018)[117].

All desorption-based experiments were completed using a dedicated thermal desorption spectroscopy (TDS) system capable of achieving heat rates as fast as 60°C/min. The system consists of a dedicated analysis chamber, which was maintained at a vacuum pressure of 10^{-9} mbar using a turbomolecular pump, and a small sample loading chamber designed to minimise the time required to reach vacuum levels comparable to the analysis chamber. An ultra-high vacuum thermal desorption system, which utilises a regularly calibrated Hiden Analytical RC PIC quadruple mass spectrometer with a detection resolution of 4.4 x 10^{-6} wppm/s was used to separate the desorption of hydrogen from that of other atomic or molecular species. In this system, four ceramic rods extend to press the sample against an aluminium nitride (AlN) sheet, which aims to maximise the conduction and ensure the homogeneous heating of the specimen (Figure 3.5). Afterwards, the desorption experiment is initiated using a pre-programmed temperature vs time sequence. Two types of TDS experiments were conducted in this study:

- Constant heating rate desorption tests, during which a pre-selected linear temperature ramp is imposed on the sample and hydrogen desorption rate (wppm/s) is recorded versus time. These tests are used to determine the total hydrogen concentration in the sample after charging and to characterise hydrogen trapping.

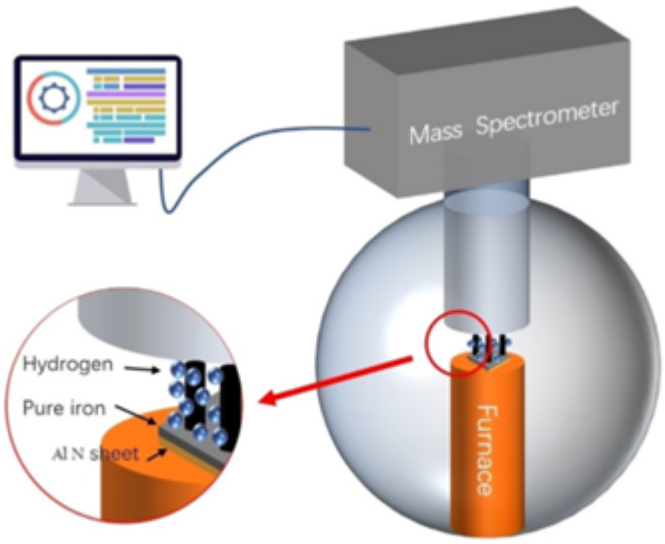


Figure 3.5: Schematic representation of the thermal desorption spectrometer used in this work. Reproduced from Zafra, et.al. (2022) [116].

- Isothermal TDS (ITDS) experiments, during which the sample is maintained at a fixed temperature and hydrogen desorption rate is recorded versus time. With the appropriate fitting procedure, these curves can provide the hydrogen diffusion coefficient at a given temperature.

For quantification of the hydrogen desorbed in the tensile samples, three TDS squares of thickness 1 mm for every microstructural condition (LPBF-AP, LPBF-Ann and W-HEA) were hydrogen charged in the same electrochemical cell and tested using a constant heating rate desorption test. The TDS specimens have a thickness of 1 mm so it will be the same as the thickness of the hydrogen charged tensile samples.

For determination of the hydrogen diffusion coefficients, 4 samples of less than 0.5 mm per microstructural condition were tested corresponding to 22°C,100°C,200°C, and 300°C isothermal temperatures and 2 TDS samples for each microstructural condition were tested for constant heating rate desorption tests at 10°C for trapping and binding energy analysis. Because these measurements are independent of the tensile tests, the thicknesses have been reduced to 0.5 mm or less to ensure that the hydrogen has penetrated into the entire thickness of the specimen as informed by a prior experimental run detailed in Appendix C.

The testing parameters are discussed in greater detail in Chapter 5.

3.9 Atom Probe Tomography

An APT experiment requires a high-positive voltage (V) applied to a very sharp needle-shaped specimen (with a tip radius less than 100 nm) in an ultra-high vacuum (UHV, $< 10^{-9}$ Pa) analysis chamber. An intense electrostatic field (F) is thus generated at the apex of the tip given by

$$F = \frac{V}{k_f R} \tag{3.1}$$

where

- V is the applied voltage,
- R is the tip radius, and
- k_f is the field factor with a value between 2 and 4 which accounts for the reduction of the actual field from the theoretical value due to the geometry of the tip and the local electrostatic environment.

By applying either ultra-fast high voltage (voltage mode) or laser pulses (laser mode), the field at the tip reaches a critical value and the tip atoms are layer-wise field-evaporated and leave the specimen with a positive charge. These ions are then projected toward a position-sensitive digital detector that records their time-of-flight and impact positions which provide the positions of evaporated ions in the original sample. The time of flight of the ion is defined as the time between the application of the pulse that triggers the field evaporation and the moment when the resulting impact is measured by the detection system. It is directly related to kinetic energy and from the time of flight, the mass-to-charge ratio of the ion (in Daltons, Da) is obtained which enables the identification of its elemental nature. Thus, a three-dimensional elemental map can be reconstructed from the collected data, applying an inverse projection of the detector coordinates to the tip surface. Depth-scaling is done considering the sequence and volume of detected atoms[74], [111], [118], [119]. It is crucial to take note that the residual gas in the APT UHV analysis chamber is mainly composed of hydrogen. In the presence of residual H, molecules of H_2 adsorb onto the tip and its shank during APT experiments at cryogenic temperatures

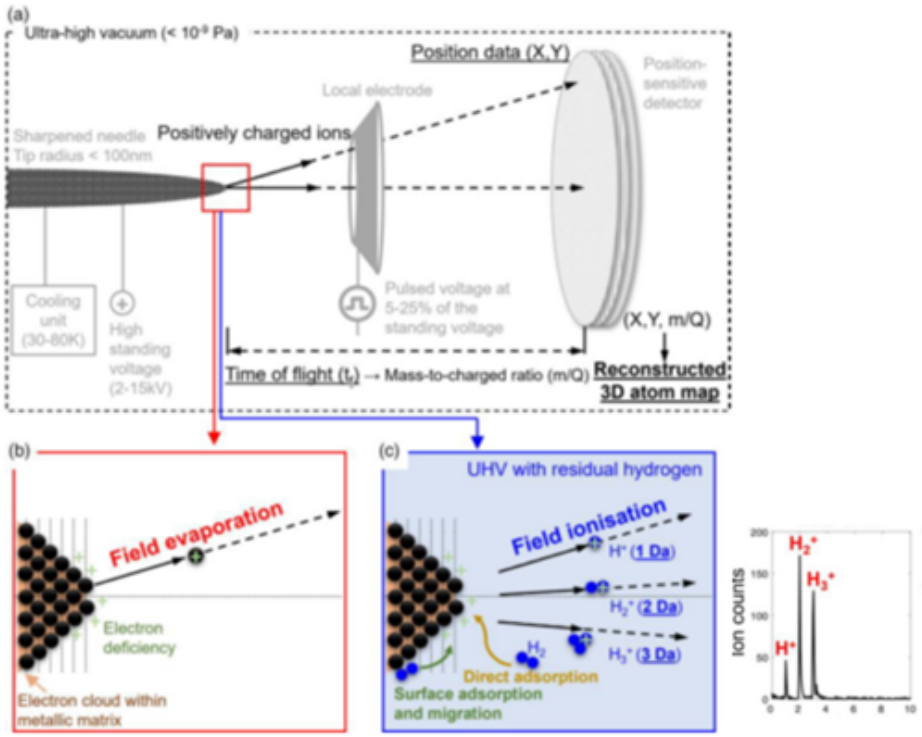


Figure 3.6: Schematic diagram of the mechanism underlying APT measurements. Reproduced from Chen, et.al. (2023)[111]

and are ionised from the tip under the electrostatic field. This can result in the detection of H^+, H^{2+}, and H^{3+} as 1, 2, and 3 daltons (Da) in APT mass-to-charge spectra. Given these artefacts and complexity in the mass-to-charge spectra peak interpretation, a strategy that has been adopted is to use deuterium (^2H or D) as a surrogate for H (protium). Deuterium is an isotope of hydrogen with a 0.015% natural abundancy and has a larger atomic mass but a very similar reactivity and behaviour, including diffusivity at the atom probe length-scale. The mechanisms of hydrogen isotopes formation together with the rationale of using deuterium is more comprehensively discussed by Chen, *et.al.* (2020)[120].

3.10 Summary

A general discussion of the methods employed in this study has been provided in this chapter. These methods were employed to accomplish the steps needed to achieve the aim of this work. To produce well-consolidated AM CoCrFeMnNi, I characterised the powders and conducted an optimisation run prior to additive manufacturing followed by examination and characterisation of the resulting build. To investigate the microstructural evolution of the alloy, a post-processing

heat treatment in the form of air-annealing was done and characterisation techniques such as electron microscopy were used. In quantifying hydrogen uptake and describing trapping parameters, thermal desorption analysis was employed, and finally, atom probe tomography was used to identify challenges in the direct detection of hydrogen in the additively manufactured Cantor alloy. In the succeeding chapters, I present the relevant results and discussion that were produced following these methods.

Chapter 4

Microstructure and properties of an equiatomic CoCrFeMnNi high entropy alloy manufactured by laser powder bed fusion

4.1 Introduction

Additive manufacturing of the CoCrFeMnNi high-entropy alloy (also known as Cantor alloy) has gained attention in recent years since its printability was demonstrated with laser powder bed fusion (LPBF) in 2018[15]. From an initial consolidation of 98%, optimisation of process parameters in laser powder bed fusion has increased the consolidation up to 99.8%[12], [14], [15], [47]. Furthermore, the 3D-printed alloy has been shown to possess a single-phase FCC crystal structure with superior mechanical properties such as a yield strength of up to 700 MPa at room temperature and 1 GPa at cryogenic temperatures which is attributed to the different strengthening mechanisms most notably grain refinement, grain boundary strengthening and the Hall-Petch effect, precipitation strengthening (tetragonal σ-phase), oxides and deformation twinning. These properties can be attributed to laser powder bed fusion as a manufacturing process. The rapid solidification in LPBF suppresses the formation of brittle intermetallics and promotes the formation of a hierarchical microstructure including melt pools, columnar grains, sub-micron cellular and dendritic structures and dislocations[13]. Despite these promising mechanical and functional properties, the production of defect-free parts with LPBF has remained a challenge. Pores, voids and cracks at macro to sub-micrometer scale are ubiquitous, as well as high-angle grain boundaries and massive dislocation pile-ups. The presence of pores, voids, and cracks (from solidification and liquation) serve as local stress concentrators and the stochastic nature of these defects affect the consistency of mechanical properties of a printed build. Moreover, high-angle grain boundaries are preferred sites for fracture owing to segregation of embrittling phases or elements, or some alloying elements at boundaries such as manganese in the case of the Cantor HEA[14], [121]. At even smaller length scales, cellular and dendritic structures have been reported to contribute remarkably to the enhanced strength through dislocation hardening. Furthermore, the role of dislocation structures such as dislocation cells found in AM HEA or LPBF alloys in general in the plasticity and other properties of the material are still not fully understood. LPBF alloys are also shown to possess a high residual stress due to the highly localised heat source, its motion and the relatively slow heat conduction that induce large thermal gradients, which can lead to distortion of the build and unexpected changes in the mechanical properties[122]. Annealing and other post process heat treatments such as hot isostatic pressing (HIP) have been employed to reduce residual stresses and dislocation density and decrease the amount of pores and voids by promoting recrystallisation and grain growth.

This in turn increases their plasticity and impact toughness, which helps improve the reliability of parts in service[121]. Thus, the microstructure evolution of AM alloys, including the characterisation of the defects at different length scales are important in predicting their properties and performance. For instance, the current study examines the susceptibility to embrittlement of the alloy when exposed to hydrogen. Hydrogen embrittlement (HE) is caused by the uptake of hydrogen atoms into the metal lattice and subsequent segregation into microstructural features and defects. The result is a degradation of the alloy's mechanical properties such as ductility and fracture toughness. Thus, HE is a serious concern for alloys in direct contact with hydrogen-rich environments such as during production, storage, transport, or service. These applications have gained ever increasing attention due to the promise of hydrogen as a sustainable source of energy. Being the first mainstream high-entropy alloy, the HE and microstructure relationship of conventionally manufactured CoCrFeMnNi HEA has been well-studied and the alloy is demonstrated to exhibit resistance to HE. Depending on the charging method, strain rate and testing temperature, CoCrFeMnNi HEA resists HE by virtue of its unique chemical composition such as the presence of high amounts of Cr and Mn which can act as strong traps for hydrogen and/or increased tendency for nanotwinning upon deformation leading to the dynamic Hall-Petch effect. The dominant mechanisms for HE in these alloys are the so-called hydrogen enhanced decohesion (HEDE) and hydrogen enhanced local plasticity. The former posits that hydrogen segregates along the grain boundaries and decreases the boundary bond strength which makes it preferential sites for crack propagation. With this, the role of grain boundary character such as degree of misorientation, etc. are important to examine. The latter on the other hand deals with the role of hydrogen in lowering the stress level to initiate dislocation movement thereby increasing the alloy's plasticity. In this case, the role of dislocation structure is a focus of investigation. Grain boundary character and dislocation structure are just two of the myriad of microstructural features that are a direct result of the type of manufacturing process and that significantly affect its HE susceptibility. Moreover, with the popularity of additive manufacturing as a route to manufacture advanced materials, the same investigations should be extended to AM CoCrFeMnNi HEA. In this chapter, I commence the investigation of the HE susceptibility of the CoCrFeMnNi HEA by examining its most defining microstructural features relevant to the study of hydrogen embrittlement. Two different microstructural conditions will be compared, as-printed and air-annealed at 900°C for 2 hours followed by furnace cooling. The

results in these chapter inform our analysis of hydrogen diffusion and trapping in the subsequent chapter and provides insight into the microstructure evolution of air annealed AM samples.

4.2 Experimental Methods

Figure 4.1 shows the particles and particle size analysis of the equiatomic CoCrFeMnNi HEA powder used for the LPBF process. Table 3.1 lists the elemental composition including the amounts of oxygen, hydrogen and carbon. Pre-alloyed powder with purity greater than 99.9% was used and its shape is spherical. The average particle diameter of the initial powder was 17.5 μm. The powders were fed to a ProX® 200 DMP and blocks with dimensions 80 mm x 60 mm x 20 mm were printed in an argon atmosphere. A standard set of printing parameters obtained from an optimisation run (see Appendix A) were used and summarized in Table 4.1.

Table 4.1: Parameters used for printing in the ProX® 200 DMP obtained from parametric study detailed in Appendix A

Laser Power, W	**Hatch Spacing, um**	**Scan Speed, mm/s**	**Scan Strategy**	**Volumetric Energy Density (VED), J/mm^3**
200	50	1400	Normal, norm, back and forth with 67° rotation	95.2

It is important to note that the laser power indicated here is nominal. The actual laser power during printing is lower by about 10%, the attenuation is expected and is machine-dependent. Therefore, the actual VED is lower.

4.2.1 Microstructural Characterisation

To identify the phases present, representative samples (powders, as-printed and annealed) were machined from sample blocks, polished and analysed by XRD (see Chapter 3 3.4). The as-printed samples designated as LPBF-AP were heat-treated at 900°C for 2 hours **in air** followed by furnace cooling and designated as LPBF-Ann. Due to the oxidizing nature of the gases inside the furnace, a thin layer of oxide scale (typically up to several microns owing to the protective nature of a large concentration in the alloy) formed on the block surface during annealing[123]. This is removed by grinding and samples were obtained from the interior of

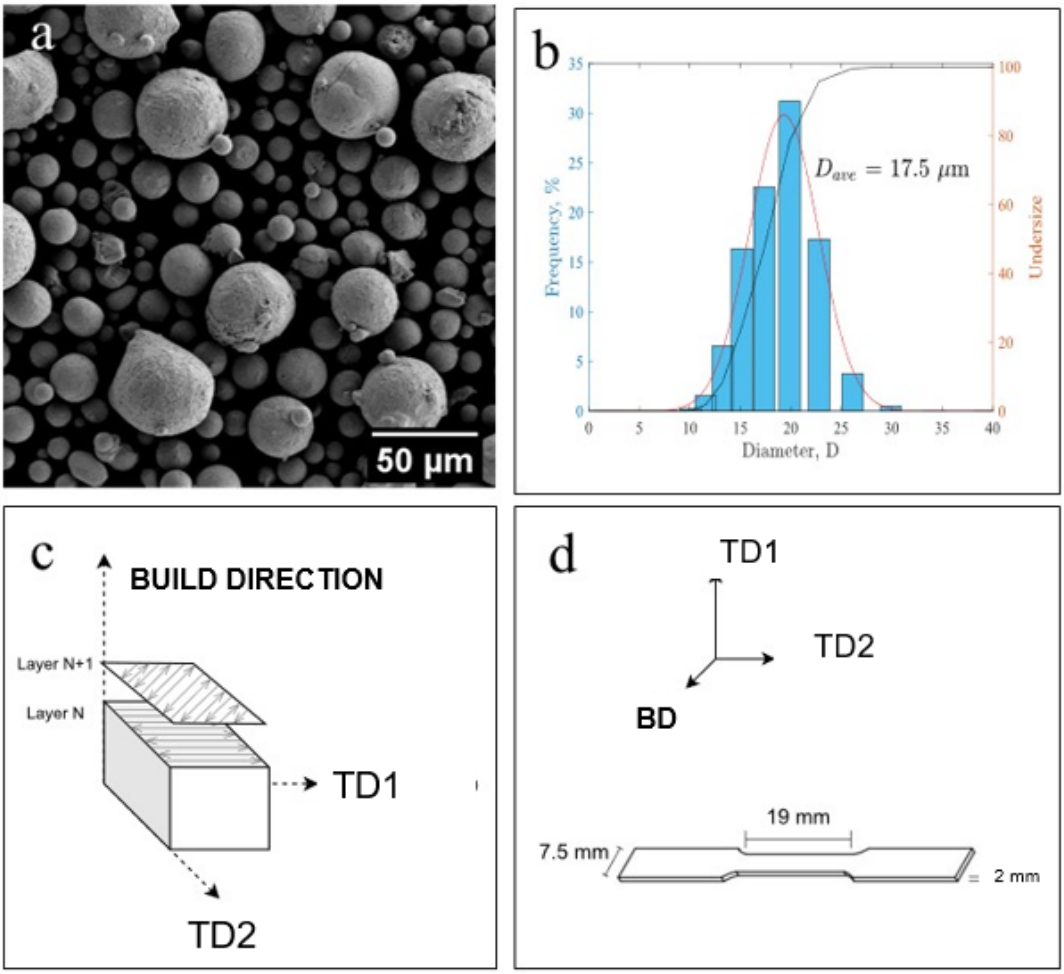


Figure 4.1: Powder feedstock used for printing SLM CoCrFeMnNi (a), with the average particle size of 17.5 μm (b), the scanning strategy employed when printing is normal, back and forth with interlayer rotation of 67° (c), Tensile specimens were extracted parallel to the build as indicated, dog-bone tensile specimens have dimensions specified in (d).

the block. Moreover, wrought CoCrFeMnNi samples were produced from vacuum arc-melting , homogenisation and hot rolling and was also examined to aid the discussion. They are designated as HEA-W. Elemental and microstructural characterisation were done as with Chapter 33.6. Flat tensile samples with other dimensions shown in Figure 3.2 were machined with thicknesses 2 mm (transverse and longitudinal) and 1 mm (longitudinal) and along the rolling direction for wrought samples. Tensile specimens were ground with SiC papers up to P4000 and samples for microstructure characterisation were ground up to P1000, diamond-polished with 3μm followed by oxide polishing (OPS) as described in Chapter 3 3.4.

4.2.2 Mechanical Testing

Tensile samples with dimensions specified in 4.2 were machined by EDM from printed blocks. The dimensions with thickness of 2 mm are proportional with the smallest specimen dimensions for flat samples found in ASTM E8. The reduction is necessary due to the size limitations in the printer used. Compliance to ASTM E8 allows for comparison of the tensile properties in this study to that found in literature. Moreover, for comparison of annealed and as-printed samples, a thickness of 1 mm is used due to sample constraints. Slow strain rate tests (SSRT) were conducted at a strain rate of 1×10^{-6} s^{-1} in an Instron 8801 equipped with an extensometer. An SSRT was used in order to be consistent with the rest of the tensile tests in this work. The strain reported in the flow curves was determined by the extensometer measurement.

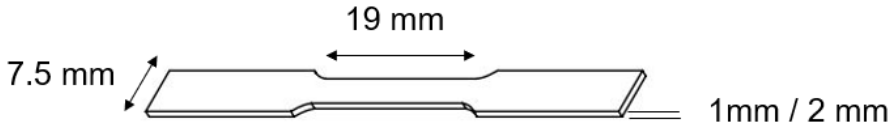


Figure 4.2: Dimensions of the tensile specimens that were used for the mechanical testing for this chapter.

4.3 Results

4.3.1 Physical Characteristics of the build

Figure 4.3 shows a tiled optical microscope image of the first prints (using the default printing parameters of the ProX 200 DMP). The calculated porosity based on the analysis of this micrograph is 5.27%. The associated SEM image of one of the many ever-present voids show unmelted powders indicating that the natire of the porosity is due to lack of fusion. This can be attributed to insufficient laser power, very high scan speed, or inappropriate scan strategy. The parametric study done using the previous printing results as baseline for the factors and levels listed in Appendix A indicated that the relative density of the builds increase with increasing energy density, until a point where further increase in the latter doesn't improve relative density

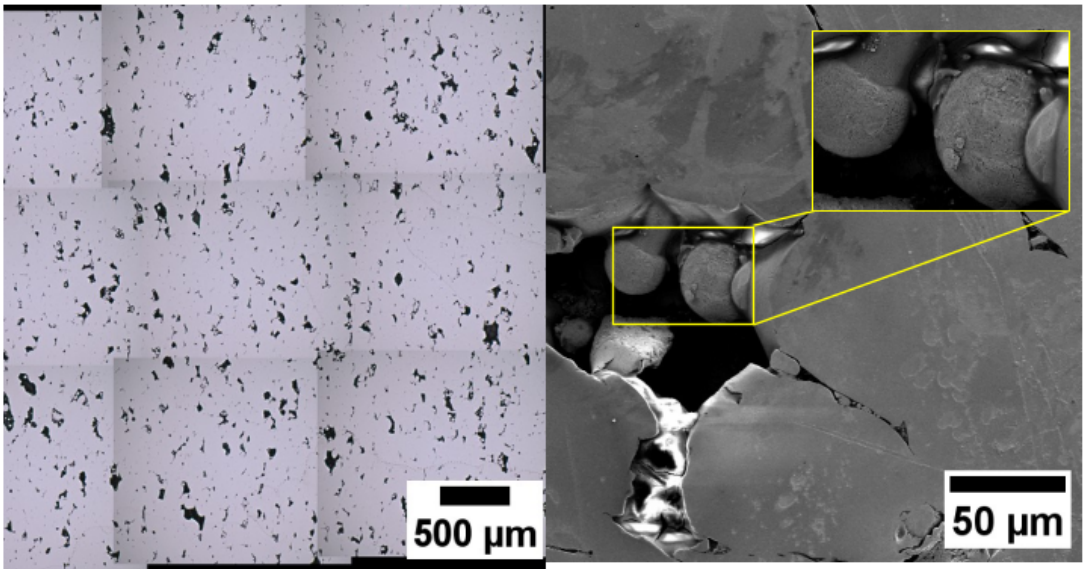


Figure 4.3: Defects and lack of fusion in the preliminary build

anymore. The maximum relative density at 99.2% using the Archimedes method was achieved with the printing parameters shown in Table 4.1. From these optimal parameters, tensile blocks were printed in which sections were examined under the optical microscope (OM). From Figure 4.4 it can be seen that this time, the as-printed builds show significant reduction of defects compared to the first prints in Figure 4.3. This is also true for the annealed specimens (Figure 4.4 b).

4.3.2 Microstructure of AM CoCrFeMnNi HEA

Phase and elemental composition analysis

The XRD spectra in Figure 4.5 of the powder and LPBF-AP samples show only a single FCC phase in both pre-alloyed powder and printed builds, which indicate that the AM process did not produce additional phases. The powder and first-print XRD spectra are identical, confirming the prevalence of unmelted powders in the latter due to lack of fusion. Compared to the tensile builds, the annealed samples also have a single-phase FCC crystal structure but the peaks have a slight shift towards higher 2θ, indicating a decrease in the crystallite size or a contraction of the unit cell (see inset). Moreover, this can also indicate alleviation of the residual stress present in the LPBF-AP samples due to heat-treatment. Comparison of the full-width at half maximum (FWHM) of the curves suggests that the peaks of LPBF-AP are broader than LPBF-Ann specimens which indicates a greater dislocation density in the former. This suggests that

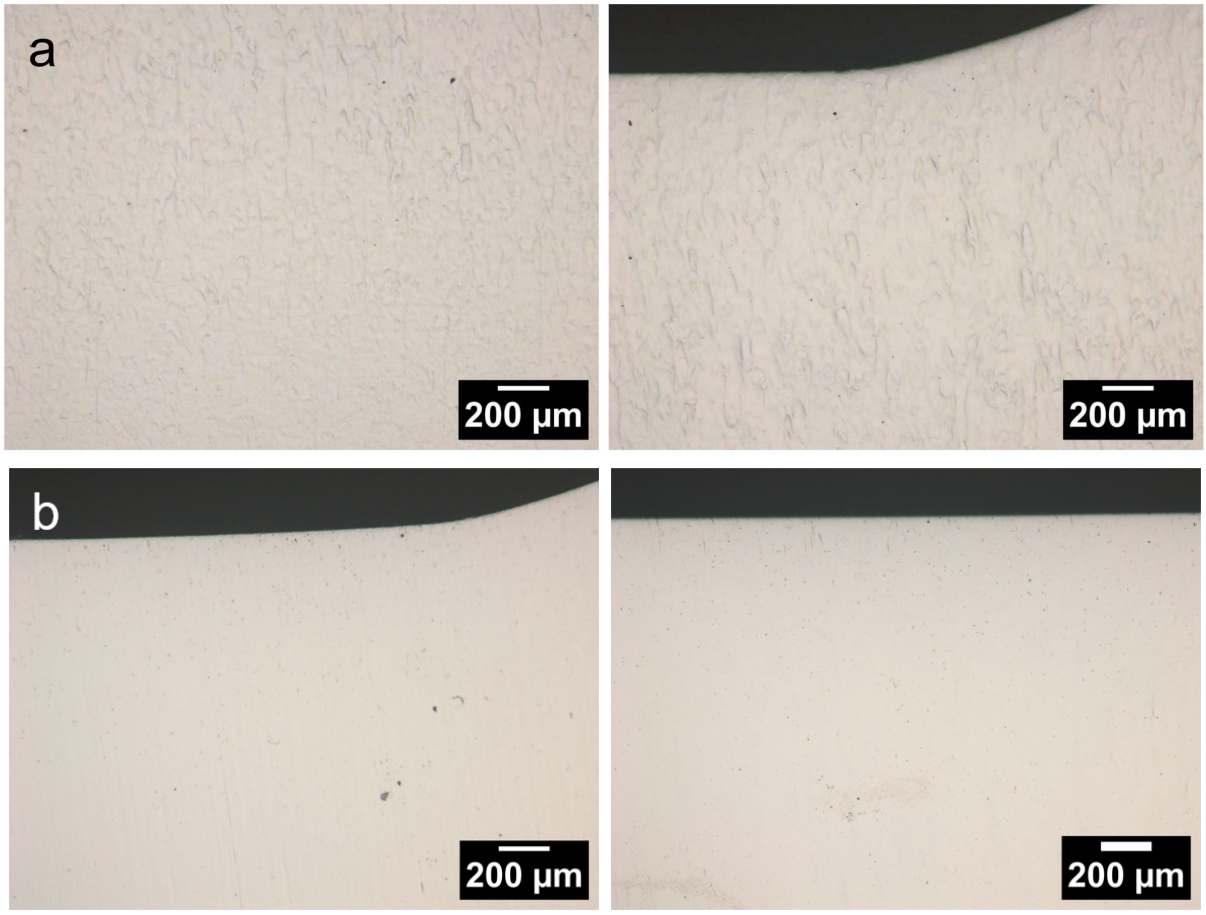


Figure 4.4: Optical microscope images of the polished surfaces for (a) as-printed samples and (b) annealed specimen

annealing has decreased the dislocation density of the as-printed alloy[124]. Using the XRD spectra, the dislocation density can be estimated using the Multiple Whole Profile method (see Appendix B). The estimated dislocation density for the as-printed specimen is 2.13 $\times 10^{15}$ m^{-2} whereas after annealing at 900°C for 2 hours the estimated dislocation density has been reduced to 7.69 $\times 10^{13}$ m^{-2}. Furthermore, the XRD spectra reveals a decrease in the lattice parameter **a** for the FCC crystal from (3.593 ± 0.004) Åto (3.584 ± 0.002)Åwith an increase in density from 8.03±0.03 g/cm^3 to 8.09±0.01 g/cm^3 when annealed. As shown in Figure 4.6 EDS maps of the as-printed build revealed an even distribution of Co, Cr, Fe, Mn and Ni in the material with a near equimolar concentration close to 20 at.% each [1] suggesting no macrosegregation in the bulk sample. The phase analysed using EBSD shows only a single austenite FCC structure consistent with the XRD results.

[1] the only real useful information here are amounts of principal elements relative to each other as EDS quant does not provide accurate concentration values

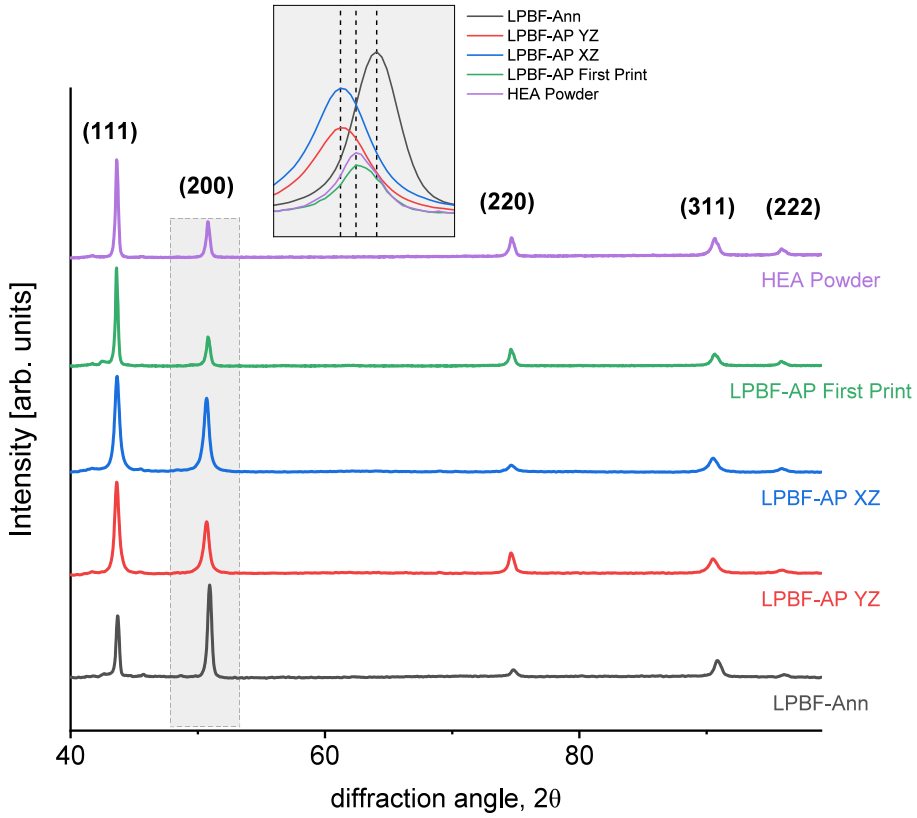
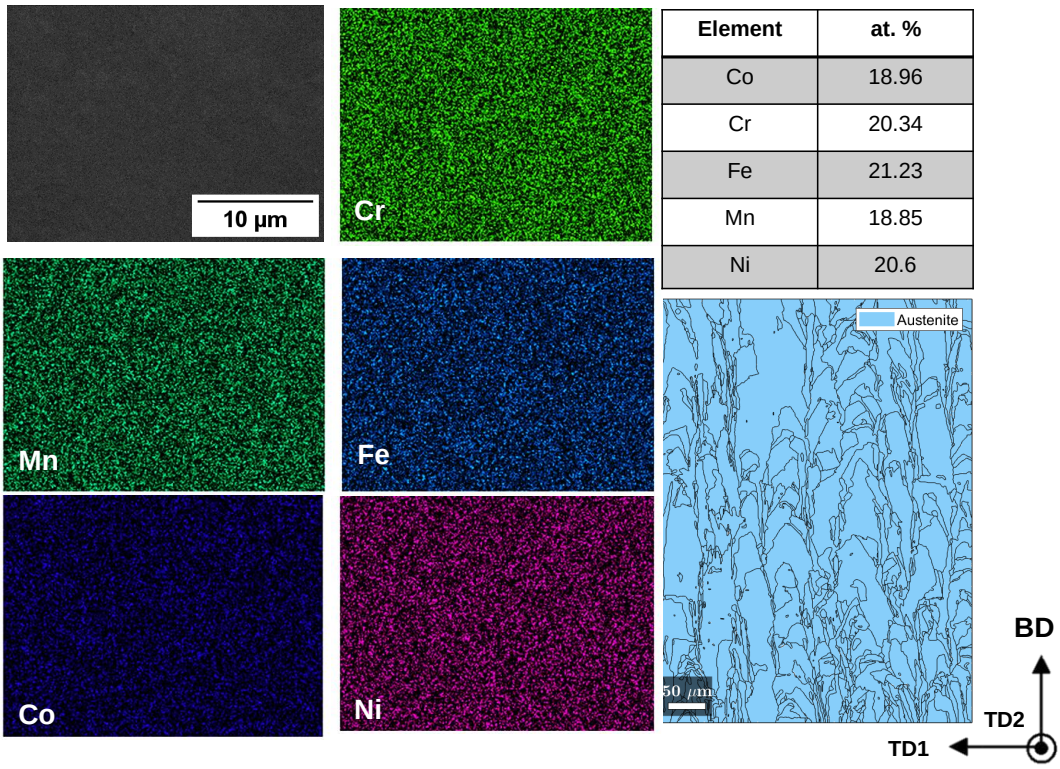


Figure 4.5: XRD spectra of the powder and printed builds.

LPBF microstructure and dislocation network

From the typical EBSD pole figures (IPF-Z) maps shown in Figure 4.8, it can be shown that the grain structure of the as-printed HEA alloy differs considerably between the transverse and longitudinal sections. Annealing at 900°C for 2 hours did not change the columnar grain shape with a slight grain growth (Figure 4.7). The angle between consecutive layers, in this case 67° plays a key role in the epitaxial growth in additive manufacturing, as it sets the orientation of the new heat flux with respect to existing cells.

To get the detailed information about the grain orientation, stereographic projection known as the EBSD pole figure was employed to analyse the effect of annealing at 900°C. In a pole figure shown in 4.9, a unit cell is considered to be the centre point of a huge sphere, and different faces of the unit cell can be presented as points of the sphere. These points of intersection of the plane normal with the sphere are also known as poles. For example, the (001) pole represents the projection of the (001) plane which is parallel to the (001) plane of the unit cell and the pole 001 is at the centre of the basic circle. Therefore, different planes can be represented as dots on



Element	at. %
Co	18.96
Cr	20.34
Fe	21.23
Mn	18.85
Ni	20.6

Figure 4.6: SEM image with the elemental distribution map, elemental composition and EBSD phase map.

the circle by stereographic projection. When taking all the grains into consideration and overlap all the pole figure of different grains in the same circle, it can be indicated that the material is textured if the points are clustered together, or random if they are distributed[125]. Texture data obtained from the EBSD maps show that the 67° rotation scanning strategy induces a relatively random texture with some grains strongly oriented at all $< 100 >$, $< 110 >$ and $< 111 >$ directions, as shown in the pole figures[2]. However, annealing suggests an increase in the texture favoring $< 001 >$ orientation of the grains.

The etched surface of the as-printed sample reveals a typical "fish scale" microstructure associated with the presence of fusion lines in Figure formed from the variations in chemical composition and solidification microstructure[14]. Figure shows that the meltpool consists of columnar cells growing epitaxially preceded by a brief planar growth in the fusion line for as short growth distance which breaks down into a cell array. This is also observed in LPBF SS 316L and high speed electron beam welding of Fe-Ni-Cr alloys[16], [126], [127].

[2]Pole figures are used instead of the inverse pole figure maps which require at least two map orientations to determine texture

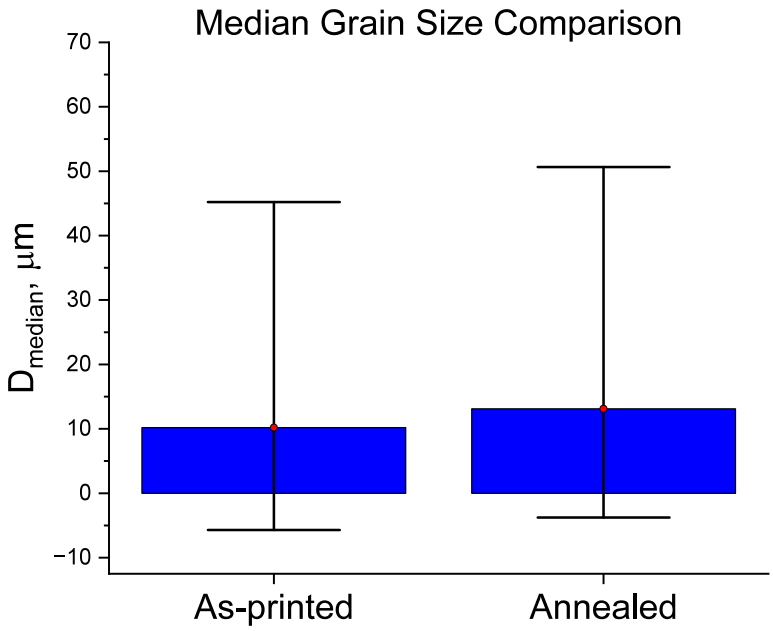


Figure 4.7: Grain size comparison for two specimens at different microstructural conditions. The median is used as a measure of central tendency to reduce the influence of extreme values.

The columnar cells, depending on the sampling direction can be rod-like, with an average diameter ranging from 200 nm to 400 nm (Figure). Defects such as gas pores and microcracks that run along the cell boundaries are observed.

After annealing at 900°C , as seen in the optical microscope images in Figure 4.4 b, the polished surface is almost similar to the as-printed specimen. However, at higher magnification under the SEM, the surface is decorated by dot-like structures that are hypothesized to be pores, inclusions or precipitates as seen in Figure 4.11 a and b.

This is supported by the etched surface showing a greater amount of pitting, indicating the presence of inclusions, fine particles or pores where regions etch differently than the bulk sample. Interestingly, these pits are often found along fusion and grain boundaries. It is tricky to ascertain what these dot-like structures are but based on a corrosion study by Ren, *et.al.* (2019) [17] on LPBF HEA, it is logical to suggest that these are micropores that can be found in higher densities in annealed samples in contrast to as-printed samples. This is also corroborated by other studies on the oxidation of HEAs which will be discussed in the next section. Aside from the presence of these etch pits, annealing changed the morphology of the microstructure with the reduction of the overlaying fish scale microstructure and the reduced prominence of the

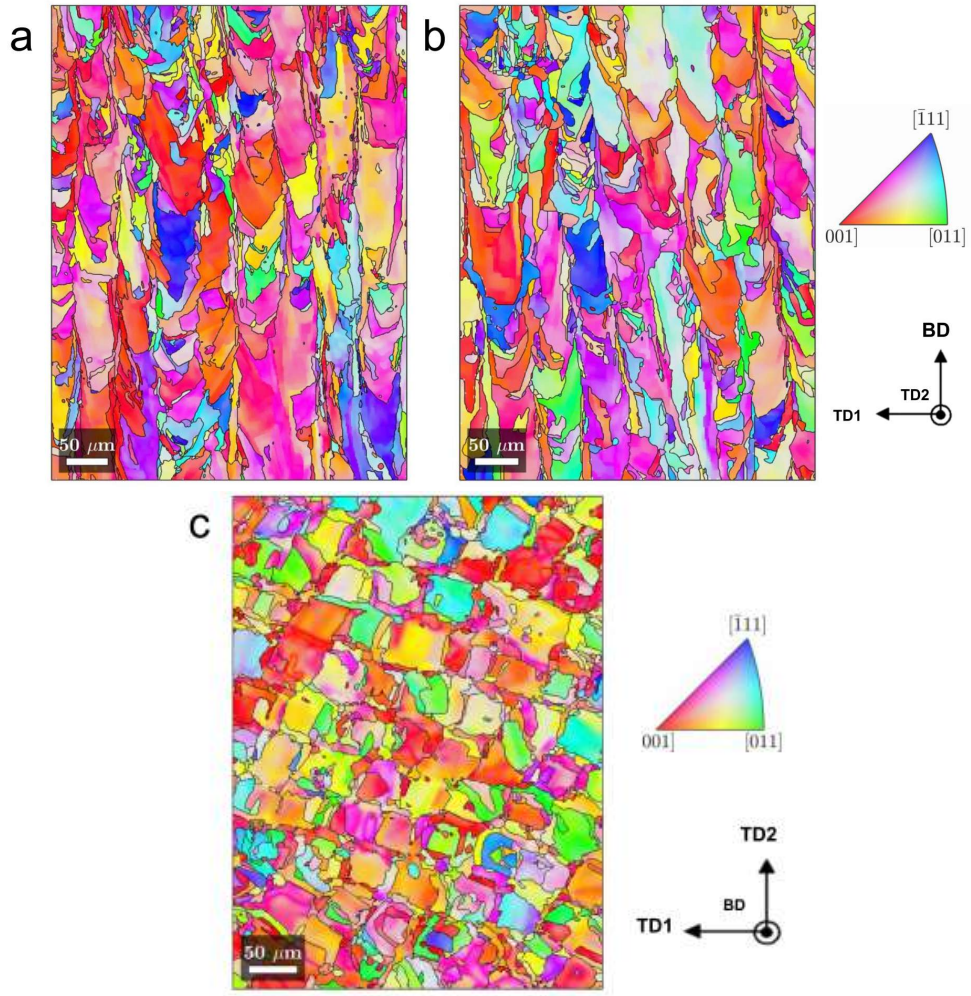


Figure 4.8: EBSD IPF-Z maps showing grain structure of (a,c) LPBF-AP and (b) LPBF-Ann samples

fusion lines. The cellular structure is also reduced, as seen from a comparison of SEM images of large pores in Figure 4.12. This is also observed in LPBF CoCrFeNi[121].

From the electron channeling contrast (ECC) images in Figure 4.13 of the as-printed sample, a dislocation network is revealed composed of cells that have mostly dislocation-free interiors while the cell walls have high dislocation densities. This dislocation network is found almost everywhere in the as-printed sample. Fine particles with an average size of less than 100 nm are observed in the cell interiors as well as in cell and grain boundaries, as indicated by arrows. These were identified as oxides whose composition was revealed by atom probe tomography and is discussed in the next subsection. Interestingly, this dislocation network is shown to be less prevalent in the annealed sample, with more regions where the dislocation network is disintegrated Figure 4.13 b.

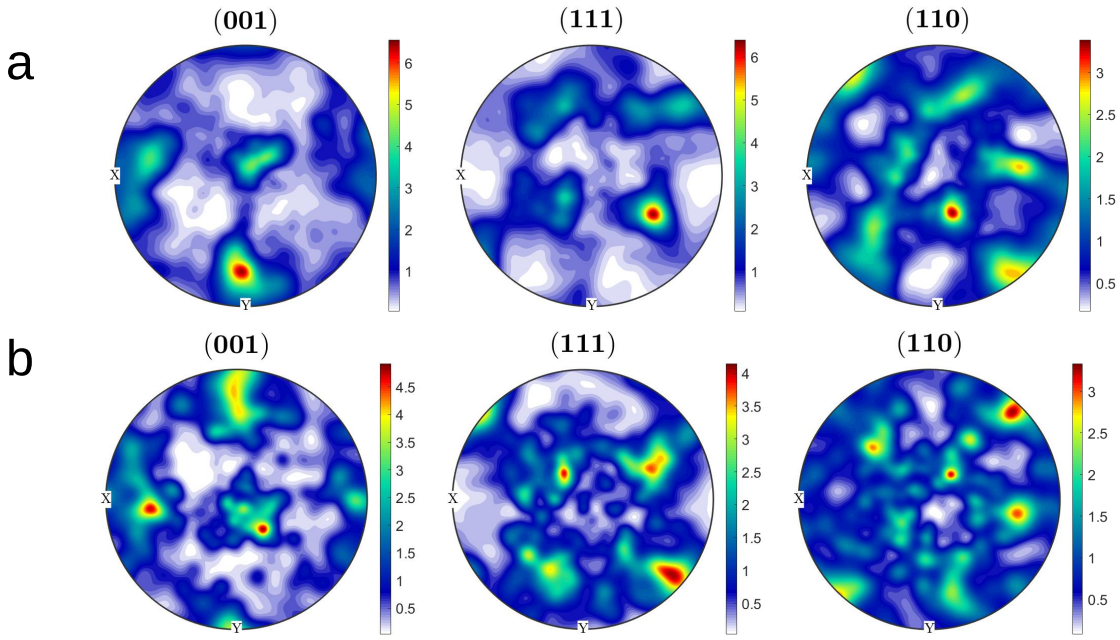


Figure 4.9: Pole figures associated with the (a) LPBF-AP and (b) LPBF-Ann specimens.

Furthermore, conventional EBSD can be used to estimate the dislocation density after annealing at 900°C. The dislocation density is related to the local misorientation or the degree of lattice mismatch between neighbouring grain and sub-grain structures. The degree of local misorientation in the as-printed sample is high as shown in Figure4.14. Annealing at 900°C did not significantly change the local misorientation. Similar findings are observed in LPBF FeCoCrNi wherein only annealing at temperatures above 900°C eliminated the local misorientation due to grain recrystallisation[121].

As typical with LPBF, numerous dislocations exist in the as-printed specimen. Dislocation strengthening is one of the most common strengthening mechanisms in AM alloys. During deformation, strength is increased because dislocation movement is hindered by either the formation of *statistically stored dislocations* (SSDs) from dislocation entanglement or the strain gradient at internal interfaces such as grain boundaries which are adjusted by *geometrically necessary dislocations* (GNDs). The proportion of SSDs in AM alloys is very small owing to the absence of deformation during rapid solidification. However, GNDs are numerous due to the high degree of lattice mismatch and thus GNDs are the primary form of dislocations in undeformed LPBF specimens. Quantitavely analysing the dislocation density helps to understand the specific contribution of not just the mechanical properties such as yield strength and tensile strength, but also the role of dislocations in the alloy's response to hydrogen[28], [79], [107]. From the orien-

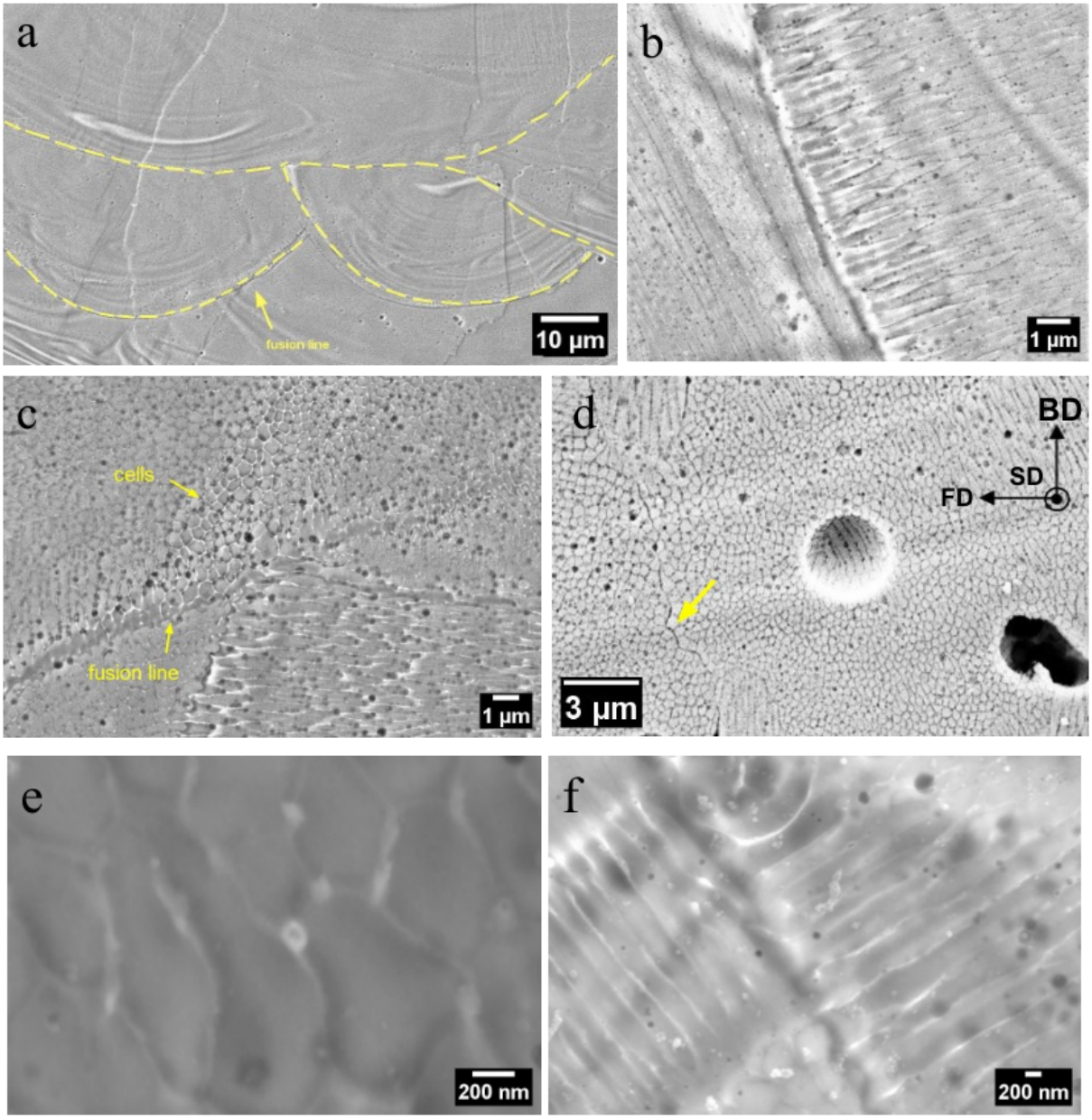


Figure 4.10: Etched microstructure of the as-printed specimen

tation differences between neighbouring points, the lattice curvature and-if elastic stresses are neglected- the dislocation density tensor can be derived. This procedure is conveniently done using MTEX[128]. From Figure 4.15, the GND density for as-printed is very high and decreased slightly after annealing at 900° C for 2 hours. This is also observed in LPBF FeCoCrNi and CoCrFeMnNi from previous studies[28], [104], [121].

As seen in Figure 4.16 most of the grain boundaries in both as-printed and annealed samples are high-angle grain boundaries (HAGBs) and there is a slight decrease in the density of the low-angle grain boundaries (LAGBs) for the annealed sample, which is consistent with the

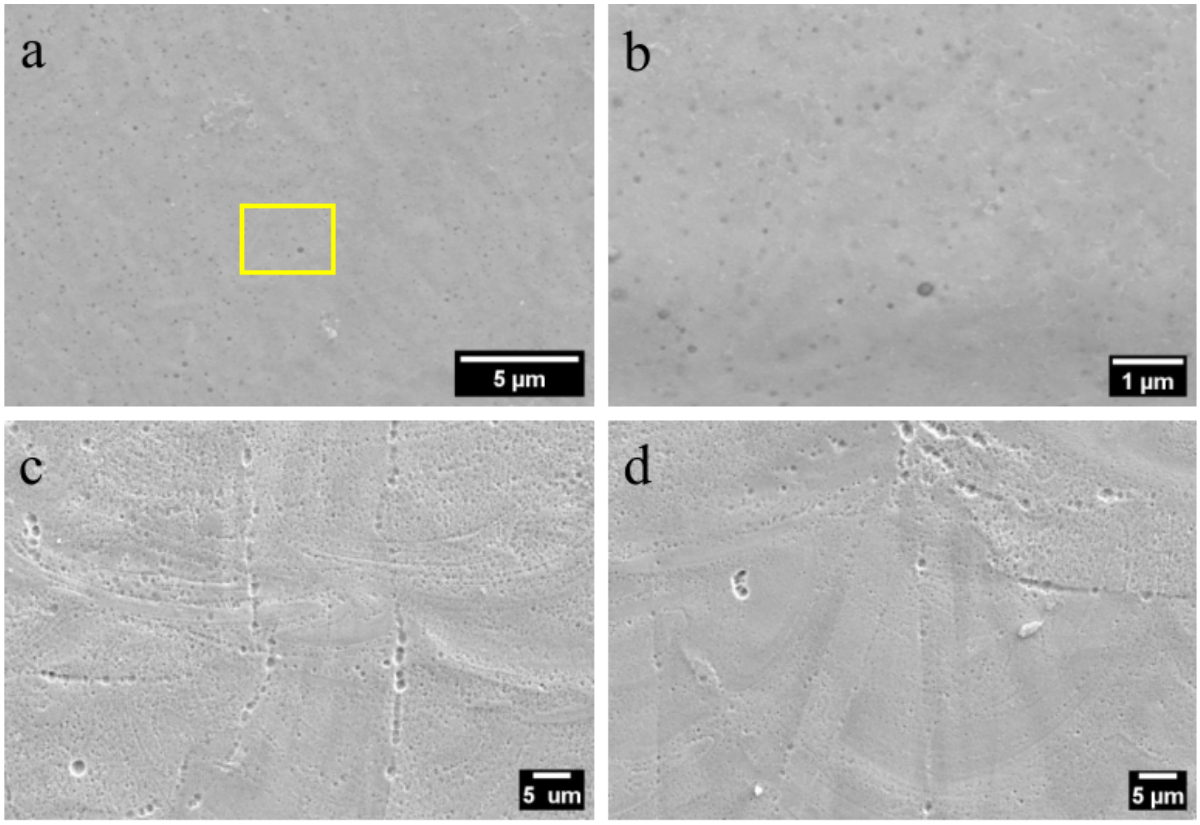
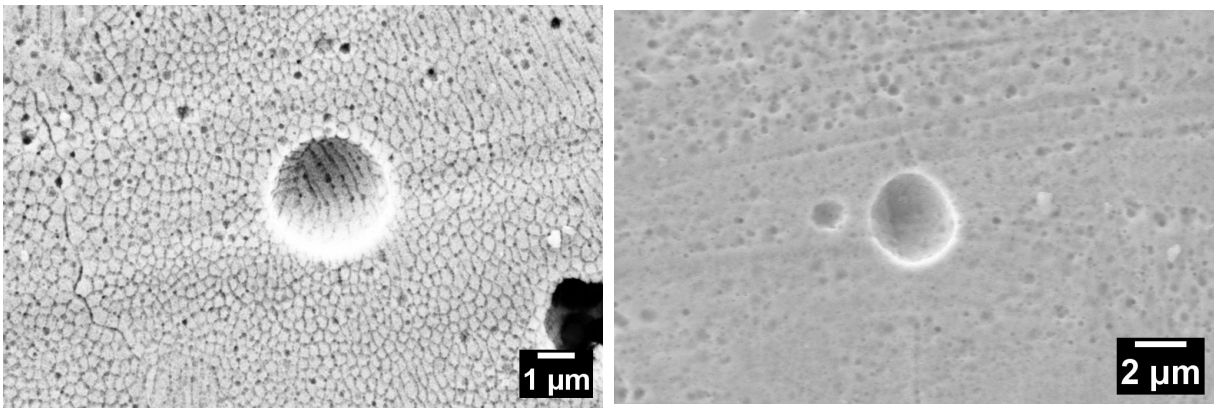


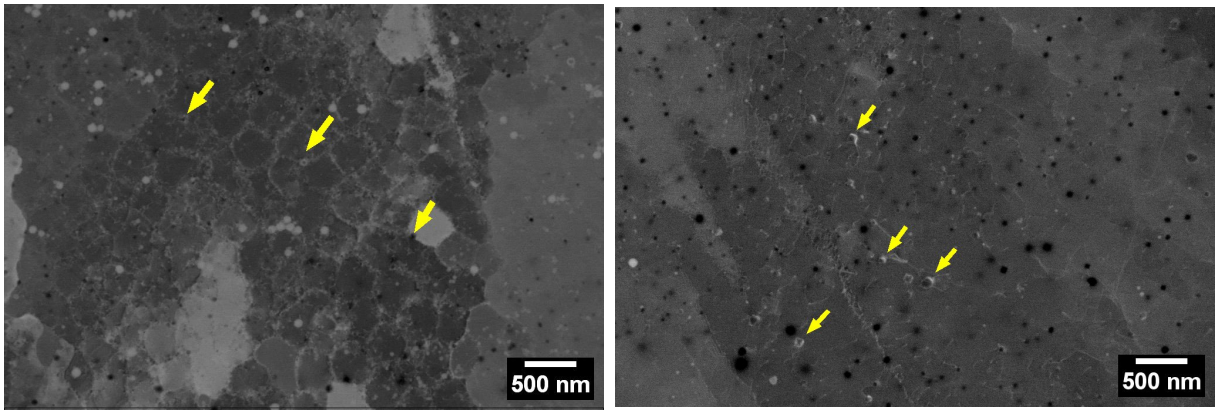
Figure 4.11: (a,b) Surface of as-polished LPBF-Ann specimen as seen under the SEM. (c,d) Etched microstructure of the LPBF-Ann specimen showing numerous etch pits. Fusion boundaries are less pronounced.



(a) (b)

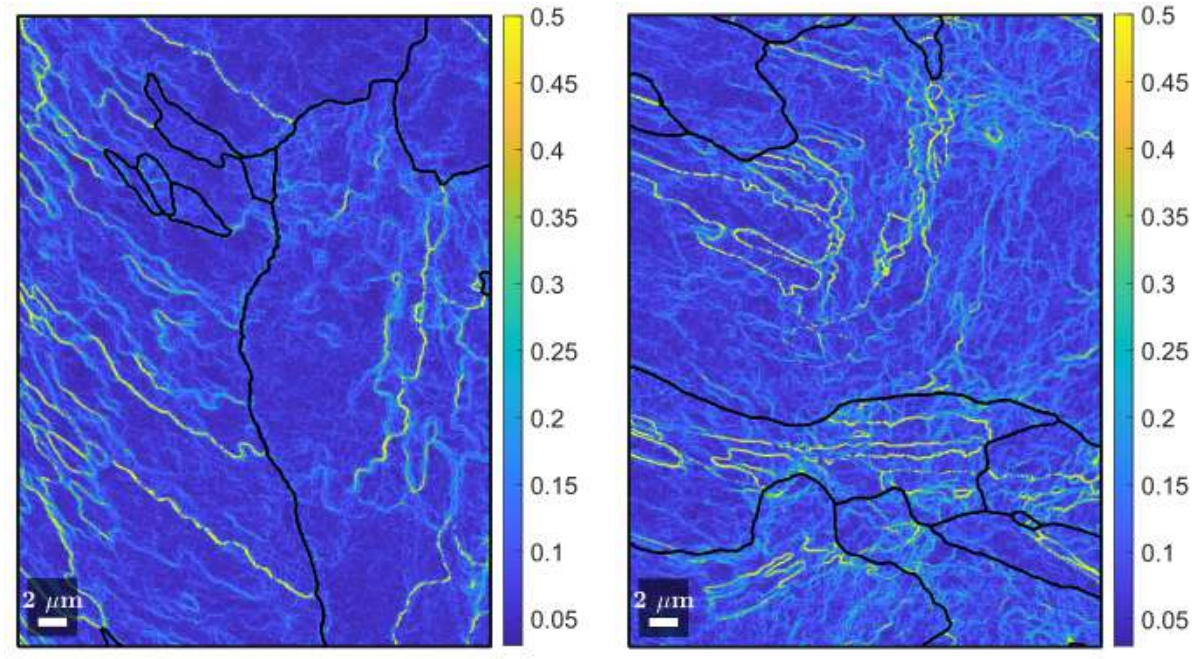
Figure 4.12: Comparison of SEM images of pores in (a) LPBF-AP and (b) LPBF-Ann specimens.

observation that the density of dislocations have been reduced to a small extent after annealing at 900°C for 2 hours.



(a) (b)

Figure 4.13: Electron channeling contrast (ECC) images showing the dislocation network in (a) LPBF-AP and (b) LPBF-Ann specimens. The yellow arrows indicate nano-oxides.



(a) (b)

Figure 4.14: Kernel Average Misorientation (KAM) maps of (a) LPBF-AP and (b) LPBF-Ann specimens Step size: 50 nm.

Atom Probe Tomography

APT can serve as an invaluable tool in determining the composition and the spatial resolution of the fine particles in the samples. For the as-printed sample, these fine particles are mostly manganese-rich nano-oxides formed during the LPBF process as shown in previous studies[14], [124]. Moreover the nano-oxides present in the annealed samples contain a much higher amount

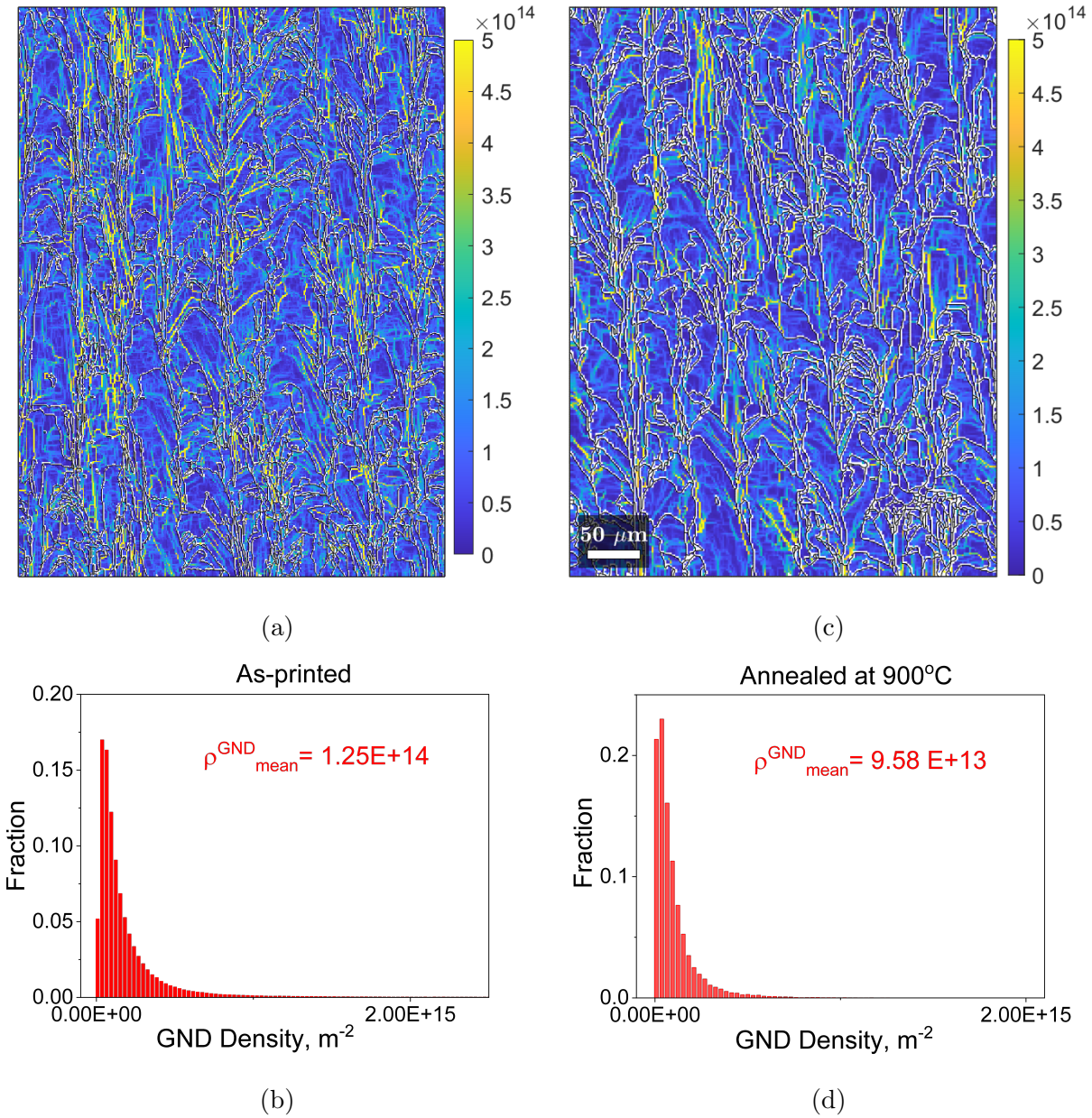


Figure 4.15: Geometrically necessary dislocation (GND) maps of (a) LPBF-AP sample with the GND density distribution (b) and (c) LPBF-Ann sample with its associated GND density distribution (d)

of oxygen compared to the as-printed sample. Again, this can be attributed to the oxygen-rich amosphere during annealing in air at 900°C.

Moreover, site-specific atom probe tomography revealed the segregation of nickel and to some extent chromium in the as-printed sample. This confirms the microsegregation previously revealed using STEM-EDX [11], [47], [129].

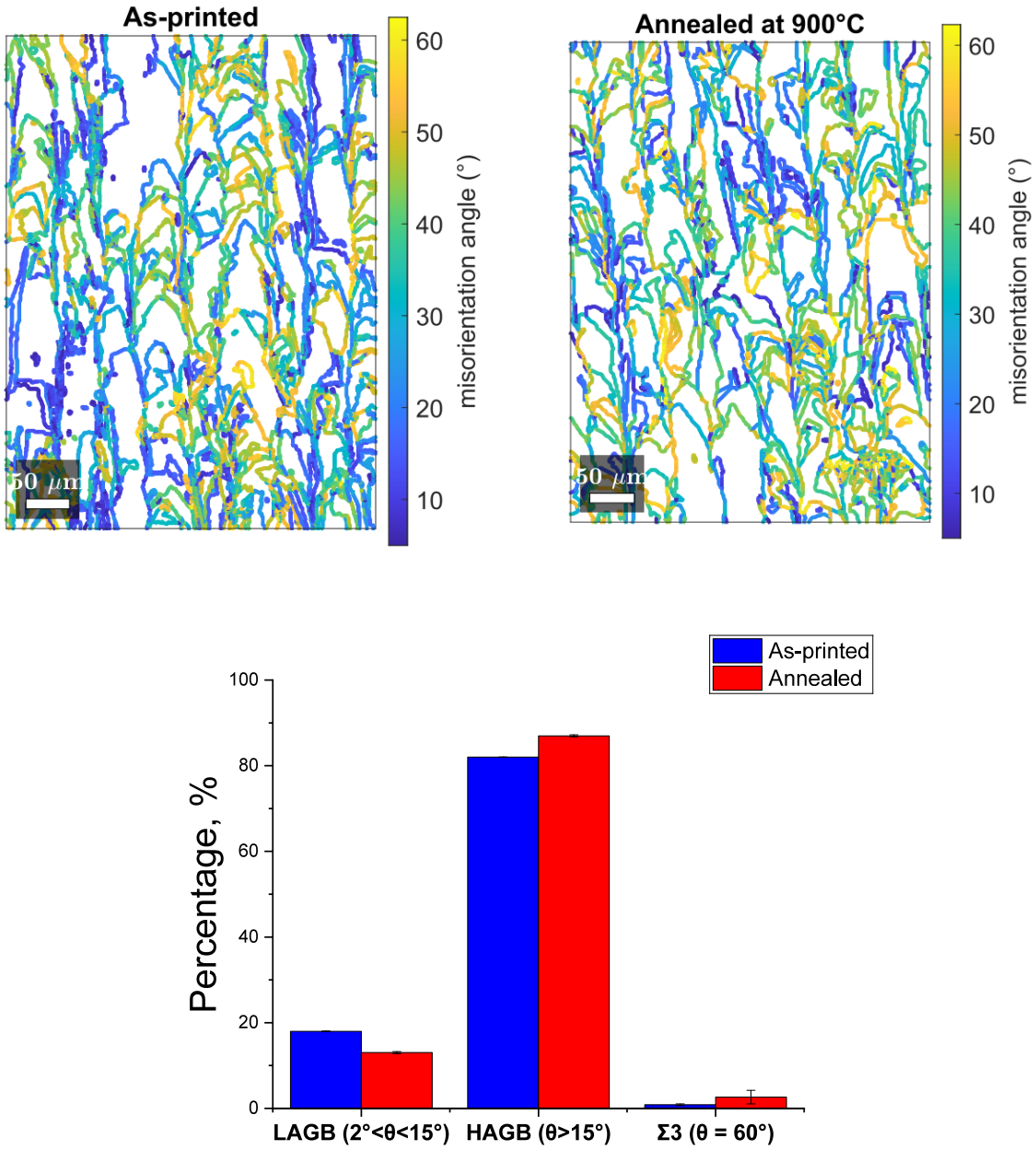
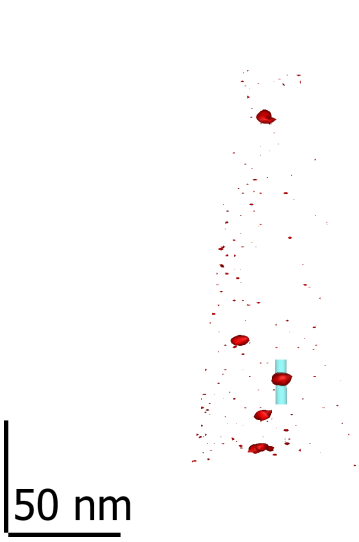


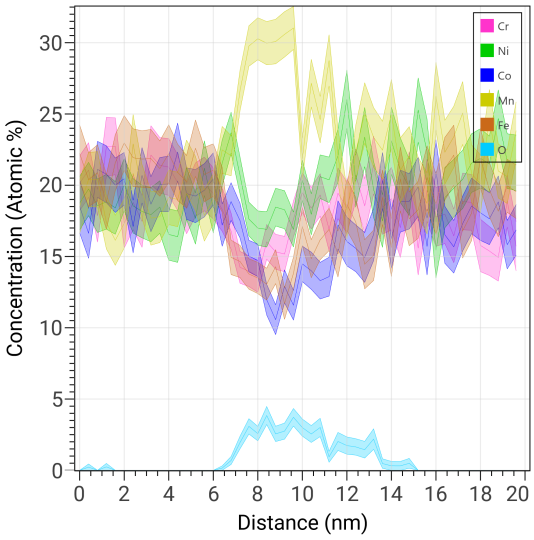
Figure 4.16: Summary of the grain boundary character of the LPBF-AP and LPBF-Ann specimens.

Tensile Tests and Fractography

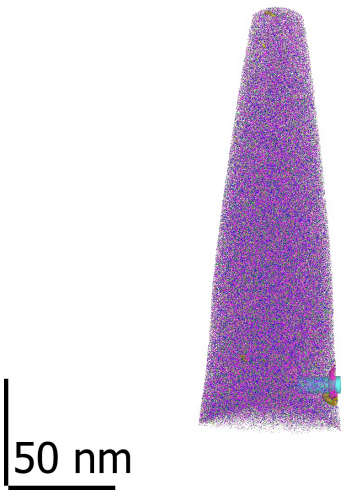
To evaluate the alloy's behaviour in tension, tensile stress-strain curves of 2-mm thick, flat specimens were obtained from the transverse and longitudinal directions (opposite and parallel to the build direction). The test was done in duplicates to ensure reproducibility. The total strain is around 30%. The difference in magnitude of the yield stress and tensile stress of the two specimens cut from different sections suggest anisotropy of the printed build, with the transverse



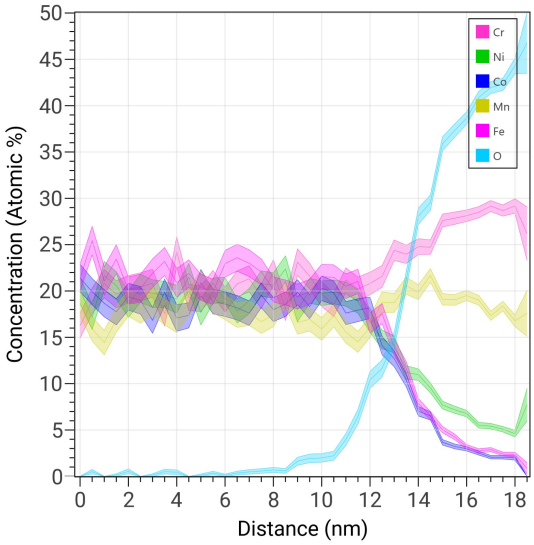
(a)



(b)



(c)



(d)

Figure 4.17: Atom probe tomography reconstructed maps of the (a) bulk as-printed sample at 30 at.% Mn isoconenctration surface showing fine particles with region of interest indicated by cylinder (b) 1-D concentration profile of selected nanoparticle along the longitudinal axis of the cylinder (c) LPBF-Ann reconstructed map of the bulk sample showing region with nanoparticle and (d) 1-D concentration profile of selected particle along the long axis of the cylinder as region of interest.

section having a higher strength and ductility overall, consistent with previous reports on the anisotropy of AM alloys[14], [43], [124].

As listed in Table 4.2, the yield stress of the CoCrFeMnNi HEA manufactured by LPBF in this study is consistent with that of a previous LPBF report and is significantly higher than those manufactured by other processes. The ultimate tensile strength is >20% higher compared to those manufactured by spark plasma sintering(SPS) and vacuum arc remelting

(VAR). Moreover, the yield strength and tensile strength are superior comapred to other lased-based additive manufacturing processes such as Laser Engineered Net Shaping (LENS), Direct Energy Deposition (DED) and Electron Beam Melting (EBM)[8], [14], [45], [46], [130]–[133].

Table 4.2: Tensile properties of the CoCrFeMnNi high-entropy alloy used in this study vs those reported in previous studies. Values for this study are averaged over duplicate samples.

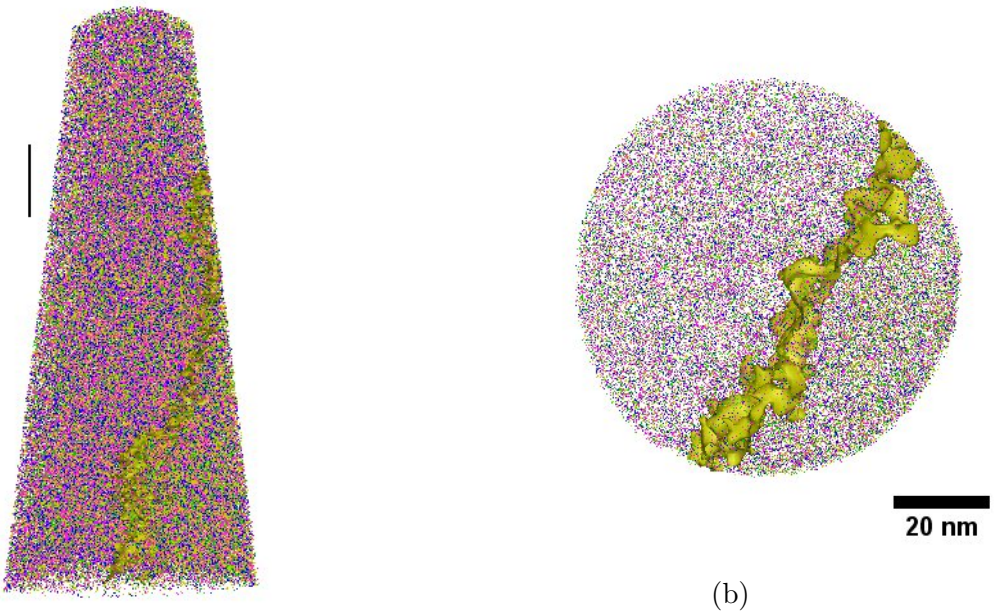
	Yield Stress (0.2% offset), MPa	**UTS**, MPa	**Strain at break**, %	**Reference**
LPBF (transverse)	386±42	626±53	30.6±1.8	This study
LPBF(longitudinal)	503±54	748±59	31.1±1.9	This study
LPBF(X-direction)	530±20	783±7	23±1	[14]
LENS	517		26	[130]
DED	424	651.3	47.9	[131]
EBM	205±3	497±2	63±1	[8]
VAR + drop casting	210	590	42	[8], [132]
	205±5	493±2	61.7	
SPS	237-312	571-613	27-37	[46]
Rotary swaging	265±10	740	31	[45]

To compare the mechanical properties of the annealed specimen, 1 mm thick flat tensile **longitudinal** samples were used as previously mentioned in the Methods section. This comparison is independent of the The reduction in thickness from The test was performed in duplicate for reproducibility. The values are summarised in Table 4.3.

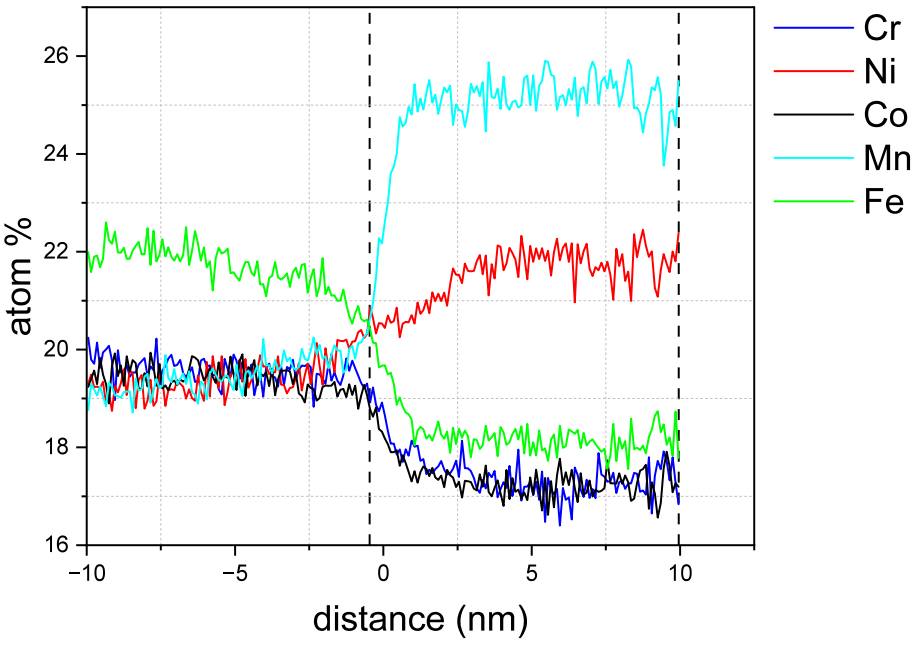
Table 4.3: Summary of the mechanical properties of the 1mm-thick as-printed and annealed tensile specimens

	LPBF-AP	**LPBF-Ann**
E, GPa	176 ± 8	175 ± 8
σ_y, MPa	555 ± 2	434 ± 1
σ_T, MPa	591 ± 49	634 ± 6
Elongation, %	23.2 ± 1.7	32.5 ± 2.1
% RA	46.2 ± 1.3	51.4 ± 0.6

As expected, annealing exemplified the strength-ductility trade-off typical of metals. Ductility increased by ∼54% with a reduction of the yield strength by ∼21%. Here, reduction in area as a measure of ductility is introduced, where the samples both exhibited almost ∼50% reduction in area in the gauge region as a consequence of necking phenomenon characteristic of ductile fracture. This is revealed in the fracture surfaces of the tensile specimens in both as-printed and annealed, showing a dimpled appearance characterised by cup-like depressions called microvoids. Fracture is transgranular and is facilitated by microvoid coalescence which is typical for ductile metals, after annealing, the size of the microvoids have relatively increased and visible on the dimple walls are slip traces. The increase in the dimple size and formation of slip bands in the dimple walls that look like surface steps (arrow in Figure 4.21) indicate a more ductile fracture which is a consequence of improved ductility after annealing[28], [134], [135].



(a) (b)



(c)

Figure 4.18: Atom probe tomography reconstructed maps of the LPBF-AP specimen showing (a) all major distribution of ions overlaid on a manganese isosurface showing region of elemental segregation (b) top view of the specimen tip (c) proxigram of a cylinder constructed across the region of elemental segregation showing enrichment of Mn and Ni.

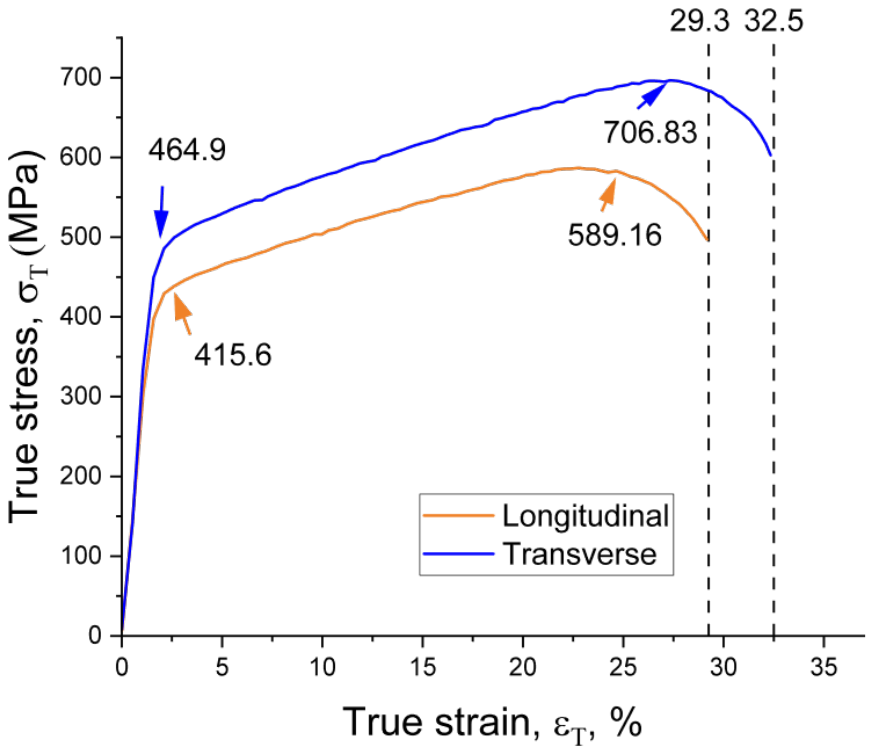


Figure 4.19: True stress-strain curves of 2 mm-thick as-printed samples. 2-mm thick samples were used in conformance to a modified ASTM-E8 standard for better comparison with other studies in Table 4.2

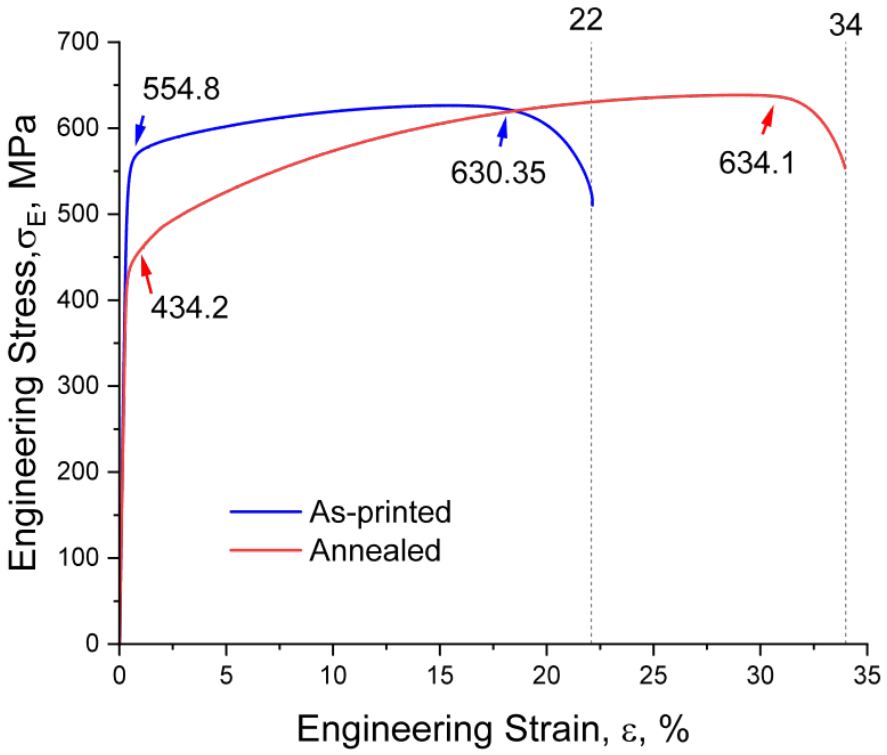


Figure 4.20: Representative stress-strain curves for the as-printed and annealed specimen (1 mm thickness)

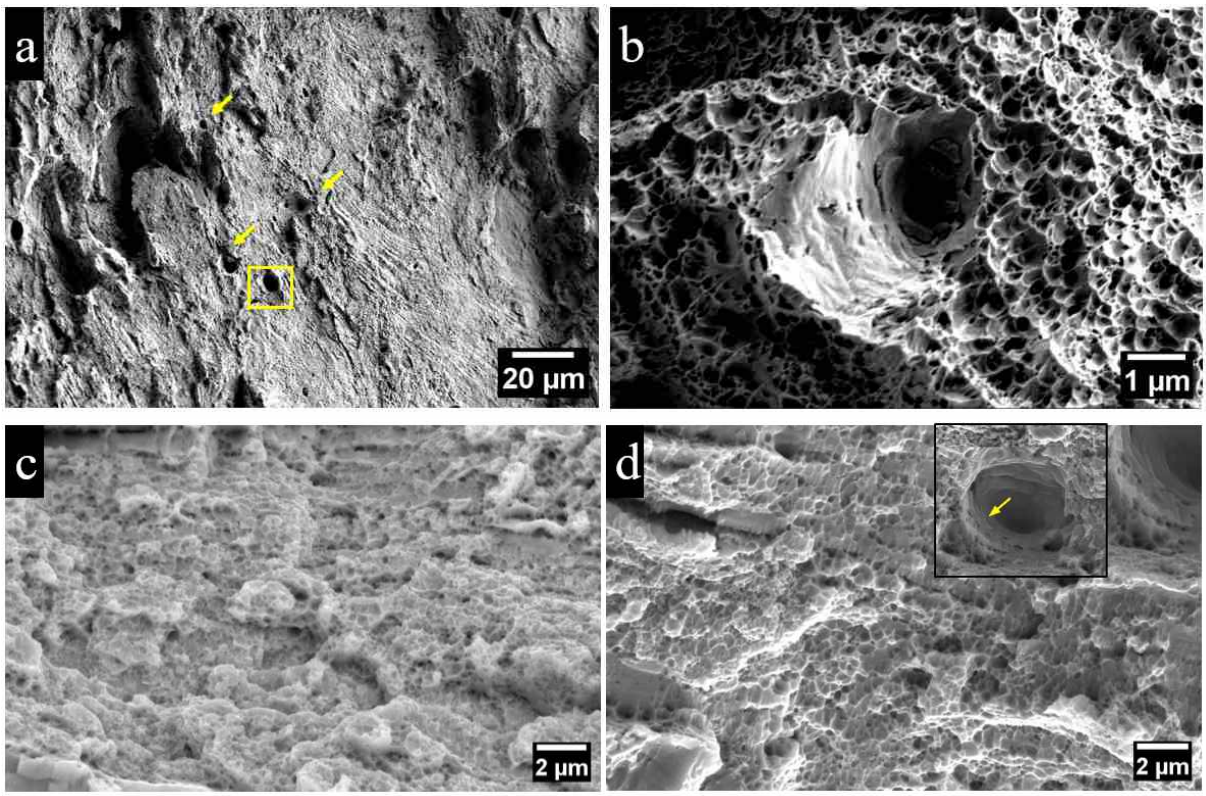


Figure 4.21: Fractured surfaces of the as-printed specimen (a,b). Comparison of dimples for as-printed (c) and annealed (d) fractured surfaces at 5000x magnification.

4.3.3 Discussion

Annealing and oxidation effects

The results obtained indicate the relative thermal stability of the AM CoCrFeMnNi HEA after annealing at 900°C for 2 hours. The thermodynamic transition from the dominant configurational entropy of mixing at high temperature is expected to cause the precipitation of intermetallic phases in the FCC matrix such as the chromium enriched BCC σ-phase as shown in previous reports for annealing at lower temperatures from 773-973[136]. However, when the configurational entropy of mixing becomes dominant at 1173K, experimental data obtained after 2 hours of annealing at 900°C indicate that the alloy remained as a single-phase FCC solid solution, consistent with CALPHAD[3] predictions for the alloy at high temperatures[29], [129]. The decrease in the lattice parameter is expected to occur after annealing. This can be attributed to the removal of manganese from the lattice structure which has an atomic radius of 1.35Å, greater than that of the other components(1.24Å-1.26Å). This depletion of Mn in the bulk HEA due to the formation of manganese oxides and the fact that manganese has been demonstrated to evaporate readily in comparison to other transition metals is shown in the relative percentage compositions of the principal elements in the annealed sample(Figure). This Mn evaporation can also occur during the LPBF process itself in addition to during annealing. In general, metal vaporisation influences the flow behaviour of the melt pool and the shielding gas (in this case argon) and is directly related to the formation of porosity, spatter and powder denudation. This is because when the metal vapor condenses into fume consisting of small particles. It blocks the propagation of laser radiation causing attenuation of the laser energy. This reduced laser power on the powder bed causes unstable melting and a surge of formation defects such as pores and voids[137]–[139]. Moreover, annealing in air results to thermal oxidation of the alloy in which the continuous reaction between air and the surface of the alloys at high-temperature forms an oxide scale. Practically, the alloy can be de-scaled and the oxides removed, to reveal the base alloy underneath. The depth of the scale depends on several factors, including the diffusivity of oxygen in the alloy, and its composition and microstructure. Internal oxidation can occur forming intermetallics, typically along the grain boundaries (intergranular oxidation) as well as the formation of pores in the oxide scale, in the oxide scale/base metal interface and the base metal itself. During thermal oxidation, pores form due to the coalescence of vacancies left

[3]CALculation of PHAse Diagrams

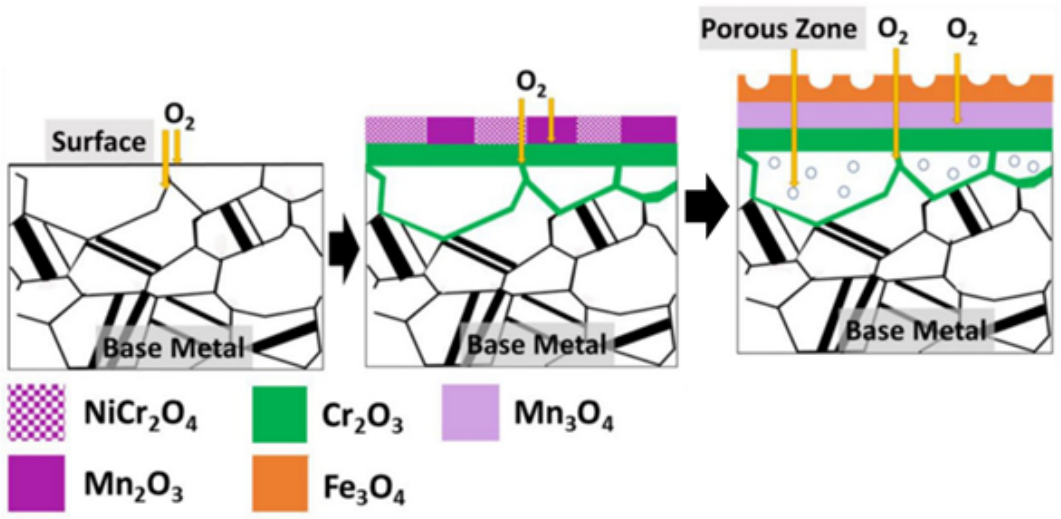


Figure 4.22: Illustration of the oxidation mechanism of equiatomic CoCrFeMnNi. Reproduced from Agustianingrum, *et.al.* (2020)[140].

behind by the outward migation of metal atoms. The conventionally manufactured equiatomic CoCrFeMnNi HEA produces a thinner oxide scale compared to HEAs and MEAs with higher Fe content. In addition, internal oxidation is not observed and there is little to no pores formed in the base alloy[140]. However, there are certain chemical and microstructural characteristics of AM alloys that might support the contrary. This includes chemical composition and its homogeneity, the microstructure, surface roughness, the residual stresses and characteristic defects. Open porosity and surface roughness as well as unmelted powder particles and other metallurgical defects could acts as diffusion channels that can promote rapid outward diffusion of volatile components such as Mn and Cr reacting with inward diffusing oxygen[141], [142]. This may explain the presence of the dot-like features in Figure 4.11 (a,b) indicative of a relatively increased internal oxidation and vacancy to pore formation in the AM specimen. This also suggests that the specimen examined was cut from the region of the rectangular block close to the surface exposed to the oxidising atmosphere[141], [143]. Another indication that these are not secondary phases or precipitates is the decrease in yield strength and increase in ductility after annealing in air as indicated by the flow stress curves in Fig 4.15. Secondary phases or oxides dispersed in the HEA matrix including *in situ* second phases has been demonstrated to significantly increase the yield strength of the CoCrFeMnNi HEA by up to 30% and incoherent BCC oxides such as MnO and MnO_2 contributes to a significant decrease in elongation to fracture[144]–[146]. Strength is increased due to the several ways in which these particles can act to retard dislocation motion. They can act as strong impenetrable particles through which

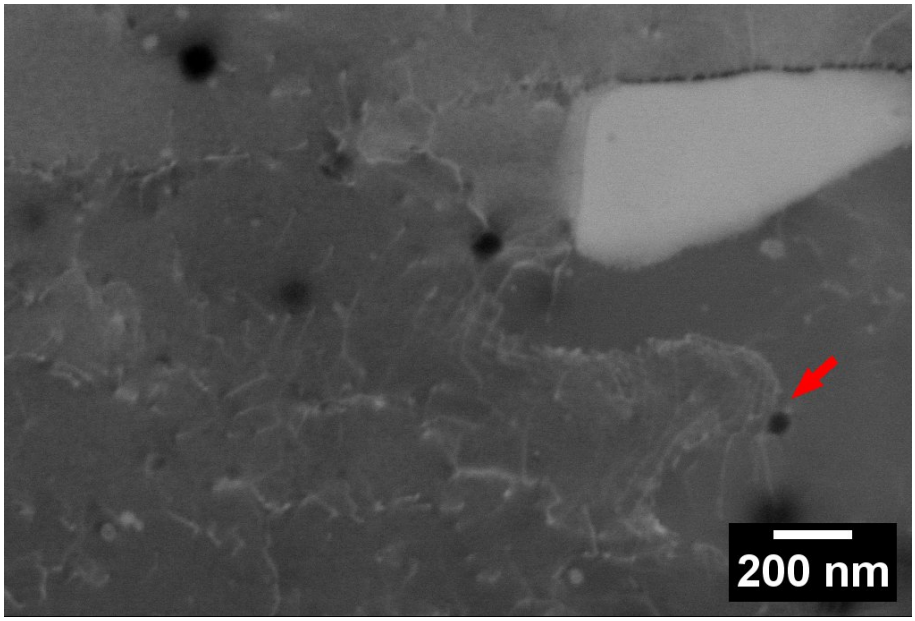


Figure 4.23: Interaction of dislocations with a nano-oxide.

dislocations can move only by sharp changes in curvature of the dislocation line or as coherent particles through which dislocations can pass but at much greater stress compared to dislocation motion through the matrix alone[147] as shown in Figure 4.23.

This effect is demonstrated by the increase in yield strength of the LPBF CoCrFeMnNi compared to the wrought counterpart (as detailed in Table 4.2) due to the contribution of Orowan strengthening via nanosized Cr-rich and Mn-rich oxides in the matyrix as seen in Figure 4.11.[124], [148]. Moreover, these nanosized oxides will exert a retarding force or pressure on LAGBs and HAGBs which may have a considerable effect on the process of recovery, recrystallisation and grain growth[149]. This "pinning effect" contributes to the retarded grain growth during annealing. Lastly, the most definitive proof of these porosities in the specimens close to the oxide scale surface is the annealed etched microstructure. Oxalic acid acts as a corrosive substance that reacts on the surface of the of the specimen depending on its reactivity. Porosities are obvious preferential sites for etching forming distinct etch pits that are more pronounced than the ones found in the as-printed sample. This was also demonstrated by Melia *et.al.* (2019) in annealed DED processed CoCrFeMnNi[131].

Formation mechanism of the dislocation network

Aside from Orowan strengthening, dislocation strengthening is one of the most common strengthening mechanisms in additive manufacturing . Dislocations are formed when vacancies in the molten state are not filled during solidification. Usually, there is an abundance in the molten state where vacancy energy is low and they are gradually filled during solidification where the vacancy energy is high. Due to the rapid solidification in LPBF coupled with sluggish diffusion, one of the four core properties of HEAs, these vacancies remain unfilled and they coalesce, resulting into massive dislocations[121]. Two types of dislocations are described in the dislocation model of deformation proposed by Ashby: statistically stored dislocations (SSDs) and geometrically necessary dislocations (GNDs). Based on this model, when a polycrystalline material deforms, the disassembling of constituent grains and subsequent slip generates SSDs. This in turn generates overlaps and voids between grains and corrected by the introduction of GNDs until the grains fit again and reassemble[147], [150]. In LPBF, it is generally assumed that solidification occurs without deformation so the proportion of SSDs in the as-printed material is minimal or nearly absent. Conversely, GNDs are abundant due to significant lattice mismatches at interfaces (e.g. grain boundaries) following rapid solidification (Figure). These mistmatches at interfaces influence strain gradients near the interfaces in a manner similar to the effects of dislocation entanglement caused by non-uniform deformation. High GND regions can acts as stress concentrators, influencing crack initiation and propagation. Fig 4.12 shows that these high GND regions are along the grain boundaries which is significant in studying intergranular failure mechanisms such as corrosion or hydrogen embrittlement.

Within a single grain, there is a substructure morphology as revealed by the etched microstructures in Figure 4.10. The preferential reaction of the etchant suggests interdendritic microsegregation in the HEA where Mn and to a lesser extent Ni segregate to the cell boundaries as previously reported[11], [47], [129] and revealed by atom probe tomography in this study. These sub-micron cellular structures are decorated by cell walls of high density dislocations and relatively dislocation-free (clean) interiors, as shown in the ECC images in Figure, forming a distinct dislocation network, i.e., dislocation structures exhibited the same spacing and orientation as dendrites. This is very common in LPBF HEAs and 316 L stainless steels, but the formation mechanism of this dislocation structure is not fully understood. Even so, several mechanisms have been proposed to explain the formation of this dislocation network in AM metals[33],

[151]–[157]. In a recent study Bertsch, et.al. (2020) showed that constitutional stresses[4] due to microsegregation, coherency strains due to precipitation networks and misorientations between dendrites are not the main sources of dislocation structures. Instead, the primary source of dislocations in AM materials is deformation induced by thermal expansion or shrinkage in a constrained medium. That is, the dislocation density and structure are determined by the residual stresses and strains developed after solidification[158]. It follows that these dislocations structures are inherently metastable and that elimination/reduction of the residual stresses and strains by post-processing heat treatments may result to its decomposition. At lower annealing temperatures(<500 K) it has been shown that this substructural morphology is not altered[121]. However, from the representative etched microstructure in Figure and ECC images in Figure, these substructures became less distinct and the associated dislocation network either partially annihilated and decomposed or experienced a reduction in the density of dislocations in the cell walls. This is consistent with previous findings on LPBF CoCrFeMnNi and other AM alloys with dislocation cells[28], [121].

Effects of annealing on the microstructure and mechanical properties

It is well established that annealing AM alloys at higher temperatures, particularly at or above 900°C (1173 K) past the recovery stage induces recrystallisation followed by grain growth. Recrystallisation facilitates the nucleation and growth of new, strain-free grains with significant reduction in dislocation density. Grain morphology tends to change from columnar to equiaxed and numerous annealing twins are also produced. The prospect of annealing at temperatures above the recrystallisation temperature but below the melting point to induce recrystallisation can be beneficial to AM alloys but in a way defeats the purpose of the fabrication route. Reaping the benefits of post-processing heat treatment at the same time exploiting the inherent microstructure in AM is an enticing goal. This is the basis for choosing the annealing temperature and holding time used in this study. As shown, although there is inconclusive evidence to suggest a significant reduction in dislocation density, it is unequivocal that annealing has altered the dislocation network and the density of the dislocation walls have been reduced. Moreover, the grains did not experience significant grain growth and grain boundary character only exhibited a slight change with very little twinning involved. This suggests that the main driver of

[4]stresses that develop within a material due to inhomogeneities in its composition, microstructure or thermal history

the strengthening and softening mechanisms in the AM HEA, aside from Orowan strengthening, is the dislocation network. As shown in Figure 4.24 the deformed sample exhibited the same morphology of the dislocation network, suggesting that it is mostly not composed of mobile dislocations. The fixed dislocation network acts as a barrier to dislocation motion and results to

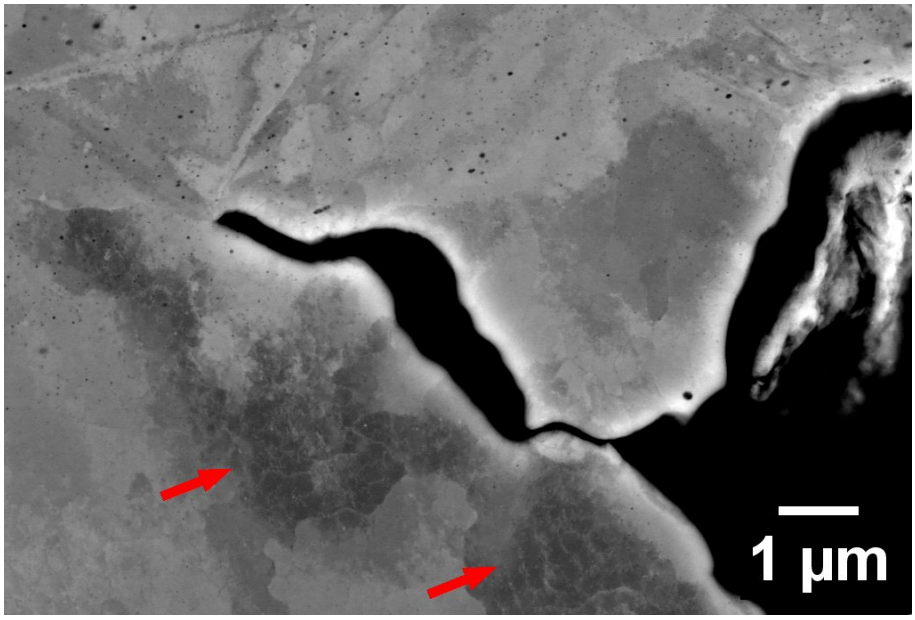


Figure 4.24: Deformed sample showing the intact dislocation network in the vicinity of a crack.

a dislocation pile-up within the network. This pile-up further hinders the passage of subsequent dislocations, thereby strengthening the material. After annealing, the yield strength decreased while the elongation to failure increased. This is common for work-hardened samples with high dislocation densities, similar to the as-printed specimens. The presence of suspected porosities due to vacancy coalescence described previously may be detrimental to the mechanical properties of the alloy but the relatively high increase in ductility suggests that their contribution is overshadowed by another factor. Typically, annealing especially at higher temperatures reduces the dislocation density as it gives vacancies the opportunity to be filled and relocate, thereby decreasing its strengthening effect. Thus, the observed decomposition of the dislocation network after annealing might be the significant contributing factor to explain the decrease in yield strength. Consequently, because the dislocations are less restricted, they can move and interact more easily accommodating more plastic strain allowing more deformation before fracture, resulting in higher ductility. Because the usual obstacles to dislocation movements such as coarser grain, dislocation density and precipitates remain relatively unchanged, it can be suggested that the significant increase in ductility at 50% is mostly due to the decomposition of the rigid dislocation network alone. However, annealing did not significantly change the ultimate tensile stress

(UTS) of both specimens. The tensile strength is typically related to the amount of residual stress in the sample, whereby relieving the latter contributes to an increase in the former. This is because the reduction in residual stress leads to the release of the local stress during deformation thus increasing the tensile stress. In this case, the contribution of the decomposed dislocation network has superseded the effect of the reduction of the residual stress, hence the UTS remains the same.

4.4 Summary

A well-consolidated, highly dense LPBF-built equiatomic CoCrFeMnNi HEA was confirmed to have single FCC structure, compositional homogeneity and relative phase stability at 900°C. The as-printed specimen has a hierarchichal microstructure composed of columnar grains with dendritic cellular substructures which are mostly retained after annealing in air at 900°C for 2 hours followed by furnace cooling. The network of substructures are decorated by walls of relatively dense dislocations with mostly dislocation-free interior. This dislocation network was shown to be mostly immobile. Fine oxides with a diameter of a few tens of nanometers are dispersed in the FCC matrix too small to be detected by XRD. However, atom probe tomography revealed that these oxides are mostly Mn-rich and Cr-rich, with high oxygen content oxides found in the annealed samples. The nanoscale oxides contributed to the higher yield strength of the as-printed AM specimen compared to the wrought one. After annealing in air, migration of Mn and Cr to the surface to form an oxide film creates vacancies that coalesce into pores in the region of the base metal closer to the surface. This migration is exacerbated by the fact that AM materials contain more defects such as random pores compared to their conventionally manufactured counterpart. This is also supported by the decrease in lattice parameter after annealing. Although it is inconclusive whether the annealing conditions significantly decreased the dislocation density, there is evidence to suggest that the heat treatment caused the decomposition of the unique cellular dislocation network. Consequently, dislocation strengthening is considerably reduced resulting to a decrease in yield strength and increased plasticity of the specimen as evidenced by the increased elongation to fracture. Grain size and grain boundary character remained mainly unchanged after the heat-treatment. This suggests that the contribution of the changes in grain size, grain boundary character and nano-oxides were not significant in the softening of the alloy after annealing. Therefore, the findings reflect that modification of the

cellular dislocation network alone can impart significant changes in the mechanical properties of the alloy. In the current landscape, heat-treatment conditions that aim to modify the grain structure of the AM alloy is usually the norm and these are almost always done under an inert atmosphere. In this work, I have shown a significant alteration of the mechanical properties by dislocation network modification alone. This supports the idea that retaining the inherent AM microstructure, without undergoing recrystallisation and grain growth by further annealing at much higher temperatures and longer holding times even without a protective atmosphere is a viable strategy in tailoring the mechanical response of the AM Cantor alloy. This approach to the best of my knowledge has not been discussed in greater detail prior to this work. However,it is highly recommended to investigate further the role of porosities due to oxidation and its role in the mechanical properties of the alloy to understand the behaviour of the alloy during annealing in air.

Chapter 5

Evaluation of hydrogen diffusion, trapping and embrittlement in an additively manufactured CoCrFeMnNi high entropy alloy

5.1 Introduction

The first single-phase FCC HEA discovered, CoCrFeMnNi, has been reported to possess higher resistance to hydrogen embrittlement [24], even showing increased ductility after hydrogen charging, which can be attributed to the enhancement of deformation twin formation by lowering the stacking fault energy (SFE) and thus the phase stability of the alloy[159], [160]. These interesting responses to hydrogen have helped to increase the attention to research on high-entropy alloys as potential hydrogen-resistant materials. However, most of these studies focus on HEAs manufactured by vacuum arc melting and other conventional manufacturing processes. Although findings from these studies prove to be invaluable in advancing the study of HEAs, the advent of additive manufacturing (AM) has provided new opportunities for fabricating geometrically complex HEAs with the capability of developing products of high geometrical complexities and in situ tailoring of their microstructures.

In Chapter 4 an equimolar CoCrFeMnNi HEA have been successfully fabricated by additive manufacturing, specifically by selective laser melting, a laser powder bed fusion technique. The microstructural evolution of the alloy after annealing in air at 900°C for 2 hours and the ensuing mechanical properties suggested its promise in the applications I enumerated in Chapter 1, especially with exposure to hydrogen-rich environments have been investigated as well. As discussed previously, hydrogen is detrimental to high-strength metals in that it causes hydrogen embrittlement, compromising its mechanical properties that may lead to catastrophic failure. This process begins with the ingress of hydrogen into the crystal structure of the alloy and understanding the processes that occur from hydrogen diffusion to the interaction of hydrogen with the alloy's microstructure, such as sites that trap hydrogen, is key to the development of hydrogen-resistant CoCrFeMnNi HEA.

However, despite the current interest in these class of AM alloys, there are only a handful of investigations on its response towards hydrogen diffusion and trapping. Moreover, the findings are often conflicting and depends heavily on test methodology. This is expected because analysis of the diffusivity and trapping for alloys with complex microstructures is not straightforward. For example, one of these studies reported that LPBF-built CoCrFeMnNi HEA strengthened by in-situ nanoscale oxides exhibited an excellent hydrogen embrittlement resistance due to the high hydrogen solubility and easy deformation twin formation[27]. From the analysis of fractured sur-

faces, they found that nano-oxides may induce quasi-cleavage fracture in the alloy and that the fractographies are similar for hydrogen charged and uncharged samples. This early work represented an initial attempt to relate AM microstructure to hydrogen embrittlement. Subsequently, Fu, et.al reported that reduction of the dislocation density by simple annealing increases the HE resistance of the alloy. Dislocation cells, as discussed in Chapter 4 are common microstructural features in AM alloys and thus merits investigation. They proposed that dislocation cells acted as fast diffusion channels for hydrogen and enhanced hydrogen segregation towards the grain boundaries, contributing to increased intergranular cracking and consequently, HE susceptibility [28]. This was corroborated by Lin, et.al. where they showed that the reduction of the density of dislocation cells and the resulting low hydrogen concentration at the dislocation cell walls contributed to a deformation twin- strengthened surface which retarded the onset of fracture by plastic localisation, leading to hydrogen-induced ductilisation in an annealed sample[104]. The contributions of these findings to elucidating the role of dislocation structures and in general, the microstructure of AM CoCrFeMnNi HEA in its hydrogen response are crucial, but short charging durations, low hydrogen penetration and non-homogeneous H-distribution in the specimens limit a comprehensive analysis of hydrogen trapping and diffusion and consequently, the embrittlement response. This is exemplified by the few reports on the value of the hydrogen diffusivity, D_H, of the CoCrFeMnNi HEA in literature, for both conventional and additive manufactured samples[103]. Hence, in this chapter I presented calculations of the hydrogen diffusivity based on samples where hydrogen has penetrated through the entire thickness of the specimens, providing a detailed analysis of hydrogen trapping and diffusion in the AM alloy. Moreover, actual exposure to hydrogen in real world applications are often prolonged. Thus, I also reported the hydrogen response of the alloy after longer charging times particularly in the annealed condition where ductilisation was previously observed[28] and described the fracture and embrittlement mechanisms. This provides an opportunity to look at HE behaviour and hydrogen trapping under relatively severe conditions and offer insights into engineering HE resistant additively manufactured CoCrFeMnNi.

5.2 Methods

In order to achieve our aim of quantifying the amount of hydrogen in the sample and calculate hydrogen diffusion and trapping parameters, samples were charged electrochemically and

analysed using thermal desorption spectroscopy (TDS). Tensile tests were done followed by fractography and microstructure examination. I also employed the *TDS Simulator* software, a Matlab® app developed by my collaborators at the University of Oxford and Imperial College London, which is a recent development that allows the calculation of trapping parameters using only a single TDS analysis as input data. The details of these methods are discussed in the following sections.

5.2.1 Hydrogen charging

Both tensile tests and TDS specimens (with dimensions shown in 5.1 were electrochemically pre-charged with hydrogen in a Gamry three-electrode electrochemical cell filled with 3 wt.% NaCl solution.

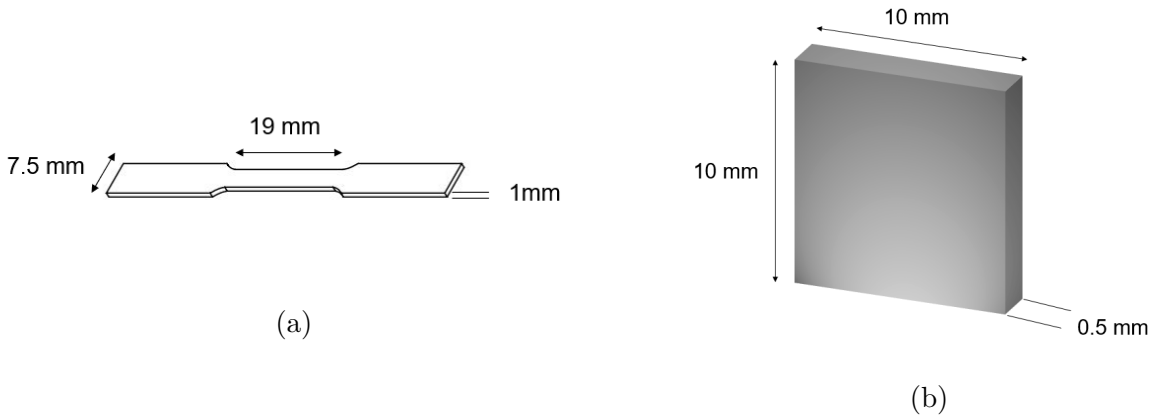


Figure 5.1: Dimensions of the (a)Tensile specimens (b) TDS specimens used for this chapter.

The counter electrode (CE) consisted of a platinum rod, that worked as the anode and the specimen itself was the cathode. A saturated calomel reference electrode (SCE) was employed to monitor the electrochemical potential of the sample during the charge. Hydrogen was generated by imposing a cathodic current density, J_C, of 5 $mA\ cm^{-2}$ by means of a TTi-PLH120DC power supply. The solution was deaerated with nitrogen gas for at least 1 hour before starting the hydrogen charge and N_2 bubbling was maintained until the end of the experiment. Figure 3 shows a schematic diagram of the electrochemical cell set-up used in this work[116].

Due to the insufficient diffusivity data of AM CoCrFeMnNi HEA reported, an initial experiment involving 0.5 mm thick TDS squares were conducted to assess the suitable duration of hydrogen charging to attain hydrogen ingress into the entire thickness of the sample. Using avail-

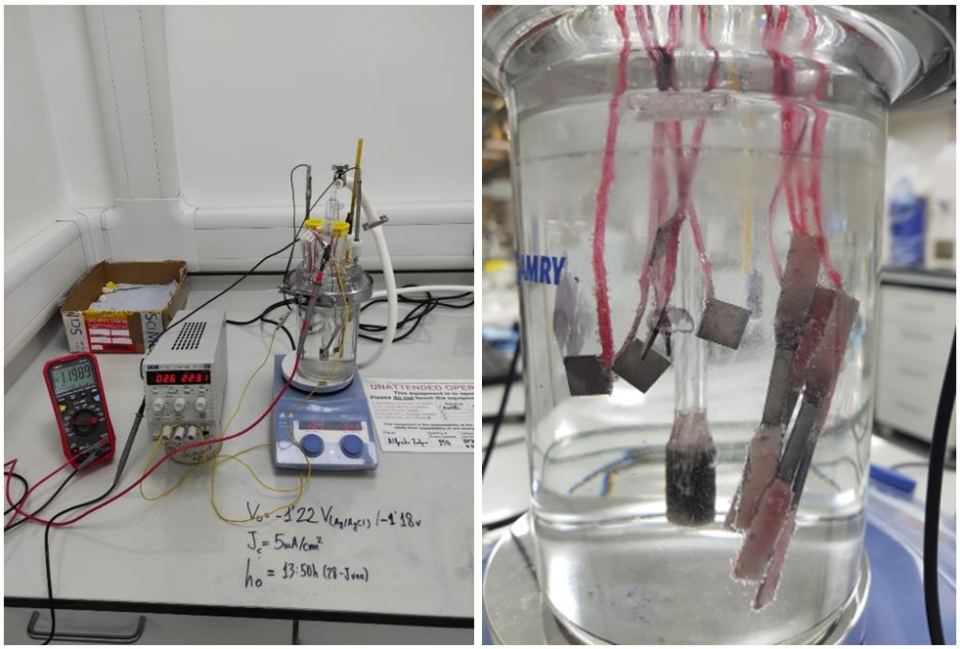


Figure 5.2: The electrochemical hydrogen charging set-up

able literature data for the hydrogen diffusivity of conventionally manufactured CoCrFeMnNi HEA which is 3.7 $\times 10^{-6}$ $m^2 s^{-1}$ [30], a 0.5 mm thick sample would require around 21 days of charging to be saturated with hydrogen. It is important to note that measuring uniformity of H-concentration is beyond the scope of this study. However, when the specimens are saturated with hydrogen, and has been held in such a state for a significant amount of time, the H concentration can be assumed to be uniform, meaning no significant diffusion gradients exist and that local equilibrium[1] is likely achieved[161]. Attainment of local equilibrium is a necessary condition in the correct application of Fick's diffusion laws to describe hydrogen diffusion in alloys using the Oriani approach as mentioned in Chapter 2 Section 2.3.4. Details of this initial run can be found in Appendix C. In order to reduce the charging times and considering the exponential evolution of the diffusivity with temperature (Arrhenius relationship), the charge was conducted at 80°C by placing the cell onto a programmable hotplate that is able to regulate and keep the temperature of the solution constant (±1°C) during the test. At this temperature, the diffusivity of the as-cast CoCrFeMnNi is theoretically higher by an order of magnitude so homogenous H-content is expected at shorter times. From the results of the experiments involving the 0.5 mm thick samples charged for 7 days, the obtained H-diffusivity showed that the hydrogen was able to penetrate the sample thickness within 3 days at the specified charging

[1]Local equilibrium means that at every point in the material, the chemical potential of hydrogen is uniform, and phase boundaries, defects, or interfaces are in equilibrium with the surrounding hydrogen environment.

conditions. Therefore, the 1 mm thick specimens were pre-charged for 7 days. During this time, the solution was regularly checked and small amounts of new solution (hot and deaerated) were added to the cell when required to ensure constant charging conditions. Immediately after the completion of the electrochemical charge all samples were soaked in liquid nitrogen, where they remained until the moment of testing to avoid hydrogen escape.

5.2.2 TDS measurements

An ultra high vacuum thermal desorption system, which utilised a regularly calibrated Hiden Analytical RC PIC quadruple mass spectrometer to separate the desorption of hydrogen from that of other atomic or molecular species was used in this work. For each TDS measurement, the sample was first electrochemically pre-charged with hydrogen following the procedure described above, rinsed with acetone and distilled water and carefully dried. Then, it was loaded into the transfer chamber of the TDS (which was pumped down to $\sim 10^{-7}$ mbar and finally transferred to the analysis chamber for hydrogen detection. The dwell time between the end of the hydrogen charge and rthe beginning of the analysis was 30 minutes. The background pressure for all desorption measurements was less than 2×10^{-8}mbar, which provided a detection resolution of 4.4×10^{-6}wppm/s. Two types of TDS experiments were conducted in this study:

- Constant heating rate desorption tests, during which a pre-selected linear temperature ramp is imposed on the sample and hydrogen desorption rate in wppm/s is recorded versus time. These tests are used to determine the total hydrogen concentration in the sample after charging and to characterise hydrogen trapping.
- Isothermal TDS (ITDS) experiments, during which the sample is maintained at a fixed temperature and hydrogen desorption rate is recorded versus time. With the appropriate fitting procedure, these curves can provide the hydrogen diffusion coefficient at a given temperature.

Trapping Measurements

The total hydrogen content introduced in 10 x 10 x (0.3-0.4) mm^3 and 10 x 10 x 1 mm^3 samples during the cathodic charge was calculated via integration of the desorption spectra obtained

when heating the sample from 25°C to 850°C at a heating rate of 10∘C per minute. The hydrogen concentration as well as in uncharged sample was measured in order to obtain the hydrogen desorption curve (wppm/s vs elapsed time) for each condition. To calculate trapping parameters such as trap binding energy, E_b and the trap density, N_t, two methods were used: first is the method of Choo[94] based on a simplification of the work of Kissinger, which requires performing TDS runs at different heating rates and second, by fitting the output of numerical TDS experiments based on Oriani's trapping model–which assumes local equilibrium between hydrogen in the lattice and microstructural sites–to the experimental TDS desorption curves using the Matlab® App *TDS Simulator*. *TDS Simulator* is a new software tool to rigorously model thermal desorption spectroscopy (TDS) experiments. It can produce hydrogen desorption curves for arbitrary choices of material parameters, number of traps and hydrogen trap characteristics, using the primary hydrogen diffusion and trapping models (Oriani, McNabb-Foster). Moreover, it contains a specific functionality for loading experimental TDS data and conducting the inverse calibration of a selected transport model, providing automatic estimates of the density and binding energy of each hydrogen trap type in the material[162], [163]. The key assumptions for which the *TDS Simulator* is based is McNabb and Foster's model which provides a generalized treatment that explicitly includes hydrogen trapping and detrapping kinetics in the treatment of hydrogen diffusion. Oriani sought to simplify McNabb and Foster's framework by assuming a local equilibrium between trap sites and the lattice, which reduces the McNabb and Foster framework to a single equation. The Oriani and McNabb–Foster models are commonly used to analyze TDS (Thermal Desorption Spectroscopy) spectra; however, they typically require numerical tools that are not widely accessible within the hydrogen research community. The *TDS Simulator* addresses that gap by introducing the first comprehensive framework for analyzing TDS data, incorporating both Oriani and McNabb–Foster approaches for any number of trap sites. Additionally, it presents the first standalone software tool for performing virtual TDS experiments. A thorough explanation of the theory behind the model used in the program can be read from [162]. Despite being fairly recent in its deployment, it has been used in a newly published study in Nature in 2024 to analyse the hydrogen trapping behaviour of additively manufactured Inconel 718 [164] and is currently being utitlised by ongoing parallel studies by Mechanics of Materials research group in Oxford University and Imperial College London, including this work.

Diffusivity measurements

Isothermal desorption (ITDS) experiments have been deemed suitable for metals with low hydrogen diffusivities such as the Cantor alloy. Most ITDS experiments use an ultra high vacuum where it is necessary to reach an appropriate value before starting the test. The low diffusivity in FCC metals minimizes the hydrogen that diffuses out of the specimen during this time, making the measurements relatively reliable[165]. Thus, ITDS experiments were performed at 22°C,100°C,200°C, and 300°C on less than 0.5 mm thick samples pre-charged with hydrogen according to the process described in Section 3.8. From the initial run on 0.5 mm thick samples, these ITDS samples are most likely to have a nominally uniform hydrogen concentration after 7 days of charging. Duplicate tests were conducted to evaluate the repetitiveness of the measurements. By integrating the isothermal desorption profile (wppm/elapsed time) it is possible to determine the diffusible hydrogen content at a given temperature, C_{iso}. In addition, after the completion of each isothermal experiment, the specimen was immediately heated to 850°C at 30° C/min to extract the remaining trapped hydrogen content, $C_{trapped}$. The apparent hydrogen diffusion coefficient, D_{app}, was determined by fitting the output of a 1-D finite element (FE) simulation of hydrogen transport (diffusion described by Fick's second law) to the experimental ITDS profile. The sample was discretised in 200 elements with decreasing size towards the free surface. A homogeneous hydrogen concentration across the specimen's thickness was assumed as initial condition (i.e., $C = C_{0iso}$ at $t = 0$) and a hydrogen concentration was prescribed at the free surface of the specimen during the whole desorption process (i.e.,$C = 0$ at $x = \pm 1/2$). In the ITDS performed at 22°C and given that the heater stage of the TDS was not used, the diffusivity, $D_{22°C}$ was determined in a single step analysis by iteratively changing the C_{0iso} and $D_{22°C}$ values until finding the best fit to the experimental curve. On the other hand, the diffusivity at higher temperatures say 90°C, $D_{90°C}$ was determined by means of a two-step simulation in which hydrogen desorption takes place first at room temperature (∼30 minutes resting period plus the necessary time to reach the targeted temperature) and then at the desired isothermal temperature of 90°C. The previously determined $D_{22°C}$ was used to simulate the first step and C_{0iso} and $D_{90°C}$ were then adjusted to fit the desorption curve at high temperature. FE calculations were conducted using the commercial package COMSOL® Multiphysics. The Livelink tool was employed to integrate COMSOL® with Matlab®, where a

routine parameter optimisation based on the curve fit function *lsqurvefit* (Levenberg-Marquadt algorithm for least square minimisation) was used for the fitting.

5.2.3 Tensile tests

Slow strain-rate tests (SSRT) were conducted at a strain rate of $1 \times 10^{-6}\ s^{-1}$ in an Instron 8801 equipped with an extensometer. Moreover, as-printed and annealed samples were also tested at a faster strain rate of $1 \times 10^{-4}\ s^{-1}$. The strain reported in the tensile curves was determined by the extensometer measurement. The final elongation of the sample, e_f, was calculated with the difference between its final and initial calibrated length. The reduction in area, RA, yield strength σ_y, and ultimate tensile strength σ_T, was also determined from the flow stress data. Tensile tests were done twice for reproducibility. As the effect of hydrogen on mechanical properties of alloys is primarily reflected in plasticity loss, the HE index (%HEI) of the samples are assessed by the percent reduction in area, which can be described as:

$$\%HEI = \frac{\varphi_{noH} - \varphi_H}{\varphi_{noH}} \times 100 \tag{5.1}$$

where φ_{noH} and φ_H are values of the area of the cross section of the gauge length before and after tensile testing for both charged and hydrogen pre-charged samples. Equation 5.1 can also be used for other tensile property values aforementioned. SEM using a Zeiss Ultra was used to examine the fracture surface and identify failure modes.

5.2.4 Atom Probe Tomography

An FEI Helios Nanolab 600i dual-beam FIB/SEM was used for preparing specimens for atom probe tomography (APT). APT experiments were conducted on either a LEAP 5108 XR instrument (CAMECA Instruments Inc. Madison, WI, USA) in laser pulsing acquisition mode at a set point temperature of 50 K, 0.5 % detection rate, laser power of 50 picoJoules, and 125 kHz pulse frequency. These levels were previously identified for austenitic materials including HEAs. For the cryogenic transfer workflows, the facilities developed within the framework of the Laplace Project at the Max Planck Institute for Sustainable Materials (MPISusMat) was used. The deuterium charging was done in the ReactHub Module (RHM) equipped with a laser and

hydrogen/deuterium gas flow so as to perform charging at selected temperatures while the sample is held on a cryo-stage to enable fast quenching. Site-specific APT specimens were prepared by using the lift-out procedure with the gallium Focused Ion Beam[37]. It was transferred into the LEAP 5108 XR loadlock where it was subjected to an outgassing heat treatment at 150°C and 10^{-7} mbar pressure for approximately 4 hours in order to desorb the hydrogen previously trapped within the material, as suggested in Ref. [20]. This short heat treatment is not expected to substantially modify the microstructure but help desorb some of the trapped H within the specimen's microstructure arising from the initial specimen preparation. The specimen was subsequently transferred into the analysis chamber and an APT analysis was started in order to clean the specimen's surface up to a voltage of 3–4 kV. Then it was transferred to the RHM for charging through the ultra-high vacuum (UHV) suitcase. Deuterium gas charging was carried out in the RHM at a pressure of 250 mbar for 6 hours at 200°C, followed by an immediate quench down to 45 K on the cryo-stage of the RHM. The specimen was then transferred back into the LEAP 5108 XR for further measurement through the pre-cooled UHV suitcase. The actual equipment used are shown in Figure 5.3 as part of the Laplace Project in MPI-SusMat. Further information on the equipment set-up can be found in Ref. [166].

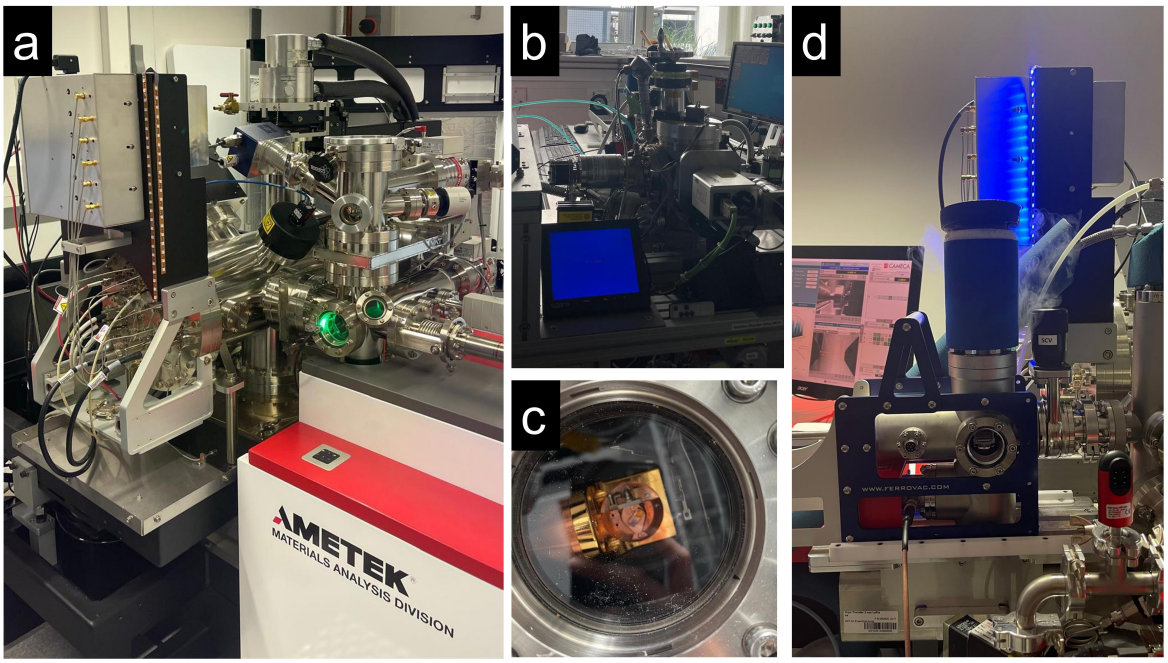


Figure 5.3: The atom probe tomography set-up within the Laplace Project at the Max Planck Institut für Nachhaltige Materialien (Max Planck Institute for Sustainable Materials) in Düsseldorf, Germany comprising of the (a) CAMECA LEAP R5108 XR, (b) the React Hub Module showing the specimen puck (c) inside the chamber for deuterium charging and (d) the pre-cooled UHV suitcase that allows for the transfer of the specimen to the atom probe.

5.3 Results

Initially, TDS experiments were done on 0.5 mm thick samples to determine the sufficient charging time to ensure hydrogen diffusion throughout the entire thickness of the sample. Due to the lack of literature around H diffusivity of AM Cantor alloy, a predicted concentration profile was calculated based on the parameters in Table 5.1 for the wrought equiatomic alloy which has a diffusivity of $9.6 \times 10^{-15}\ m^2 s^{-1}$ at room temperature (RT)[103]. This is done using Equation 5.2 [67]:

$$\frac{C - C_0}{C_{abs} - C_0} = 1 - \frac{4}{\pi} \sum_{n=0}^{\infty} \frac{\frac{(-1)^n}{2n+1} \exp\left\{-\frac{D_{abs}(2n+1)^2 \pi^2 t}{4L^2}\right\} \cos((2n+1)\pi x)}{2L} \tag{5.2}$$

where

- C is the hydrogen concentration at position x after a certain absorption time t,
- C_0 is the initial uniformly distributed hydrogen concentration (measured in uncharged samples at $t = 0$) and
- C_{abs} is the hydrogen concentration at the surface of the specimen which corresponds to the stable hydrogen concentration measured at large charging times.

Table 5.1: Diffusivity parameters used for predicted concentration profile.

Parameters	
Charging time	7 days (604,800 s)
Specimen thickness	0.50 mm
Temperature	80°C
Pre-exponential factor, D_0	4.3×10^{-7}
Activation energy, E_a	51.7 kJ/mol

Furthermore, the samples were charged at an elevated temperature of 80°C because higher temperature increases hydrogen mobility, so hydrogen can diffuse more easily and quickly into the metal lattice. This also enhances the electrochemical reaction kinetics and increases the rate of hydrogen generation due to thermal activation. The results from this initial run show that the AM specimen has a hydrogen diffusivity which is two orders of magnitude higher than the one used for prediction calculations and that samples were saturated with hydrogen after charging for 3 days or longer. More details can be found in Appendix C. Following this, charging the specimens for 7 days would sufficiently introduce hydrogen into the sample that can satisfy the

assumption of local equilibrium. The choice of 7 days is only chosen to provide a wide margin of confidence that the 0.5 mm samples are saturated with hydrogen. This does not imply that doubling the number of days of charging will also saturate the 1 mm samples as seemingly suggested by Fick's second law, since diffusion in this system follows a more complicated model as will be demonstrated and explained later on.

This assumption of local euilibrium which is often neglected in literature becomes particularly important for the assessment of hydrogen trapping using Kissinger's approach or Oriani's and McNabb and Foster's trapping models, since uniform H concentration at the beginning of the desorption stage is a necessary condition in all of them[161], [167]. Without satisfying this condition, the calculated binding energies and density of trapping sites would be erroneous.

Plots of hydrogen desorption rate vs temperature are shown in Figure 5.4 for wrought and as printed samples at the same heating rate of 10°C. As discussed in Chapter 2 the number of trapping sites is related to the number of desorption peaks in the desorption spectra present in the two kinds of specimens. The plot was approximated with a Gaussian function where the best fit was obtained by deconvoluting the TDS spectrum into two Gaussian curves. This indicates that the total desorption curve is actually a convolution of two peaks at two different temperatures, which can be interpreted as coming from two different kinds of hydrogen trap sites with a fairly low binding energy from the temperature values, indicating that these traps are reversible and contribute to the diffusible hydrogen concentration.

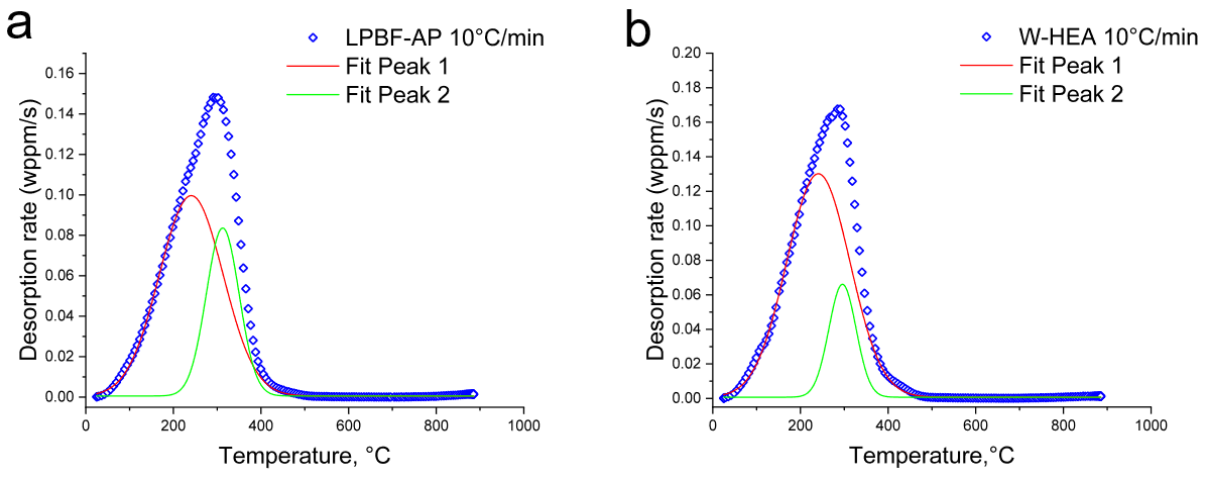


Figure 5.4: Fitted TDS spectra of (a) as-printed LPBF and (b) wrought CoCrFeMnNi HEA. The TDS samples have thicknesses of less than 0.5 mm. Note that these samples are assumed to be saturated with hydrogen after 7 days of charging.

The desorption curves are consistent with that observed in studies by Luo, et.al. and Koyama, et.al. [100], [168]. From the figure, it can be deduced that additive manufacturing did not significantly change the position of the hydrogen desorption peaks, especially the low temperature peak. The shift in the values of the low temperature peak has been observed in the wrought alloy as a consequence of grain refinement[168]. Since additive manufacturing produces more refined microstructure with the presence of cellular substructures, the higher 2nd peak temperatures might be attributed to this. The peak temperatures from the TDS spectra of the saturated specimens are shown in Table 5.2 below.

Table 5.2: Peak temperature and total hydrogen concentration for the wrought, as-printed and annealed LPBF samples.

	T_{p1},°C	T_{p2},°C	C_H (ave), wppm
HEA-W	241.3	295.8	182.5 ± 8.2
LPBF-AP	241.3	313.05	513.8 ± 32.0
LPBF-Ann	230.7	304.3	172.22 ±38.0

Because the peak temperature difference for three samples is reasonably less than 15-20°C, it is reasonable to suggest that the traps may have similar binding energies[169]. Data obtained from varying the heating rates show that the average hydrogen desorbed is maximum for the as-printed sample, which is 180% higher than the wrought specimen. This observation has been reported several times in other additively manufactured alloys such as SS 316L indicating that the traps present in each condition might have similar binding energies but different densities, with the as-printed sample having the highest. It is important to note that sample variability in terms of compositional homogeneity, sample dimensions, surface conditions, to name a few, can greatly affect the amount of hydrogen desorbed. Moreover, the desorption temperatures are relatively low, which is a further indication that the hydrogen diffusion is diffusion-controlled rather than dissociation-controlled. This will be relevant in the succeeding section where the appropriate model to use in determining trapping parameters are discussed.

Next, the TDS spectra for different heating rates of the as-printed sample and the annealed specimens of 1-mm thickness as shown in Figure 5.5 are examined. The area under these curves represent the total hydrogen desorbed and even from visual inspection alone, it is confirmed that the total amount of hydrogen desorbed for the LPBF-AP sample is much higher (Table 5.3. This can be attributed to the increase of the volume fraction of the cell and grain boundary coupled

with the high density of dislocations, and this is augmented by the presence of manufacturing defects such as porosities and voids. It is noteworthy that the specimen annealed in air at 900°C for 2 hours has a lower amount of hydrogen desorbed. Normally for annealed samples, this can be attributed to the grain growth due to annealing and the effect of recrystallisation, however, it was established in the preceding chapter that grain growth is virtually negligible and that there are essentially no recrystallised grains. Hence, this can be attributed to the minimisation of manufacturing defects due to the decrease in residual stress after annealing and the reduction of lattice defects such as disintegration of the dislocation network and reduced dislocation density.

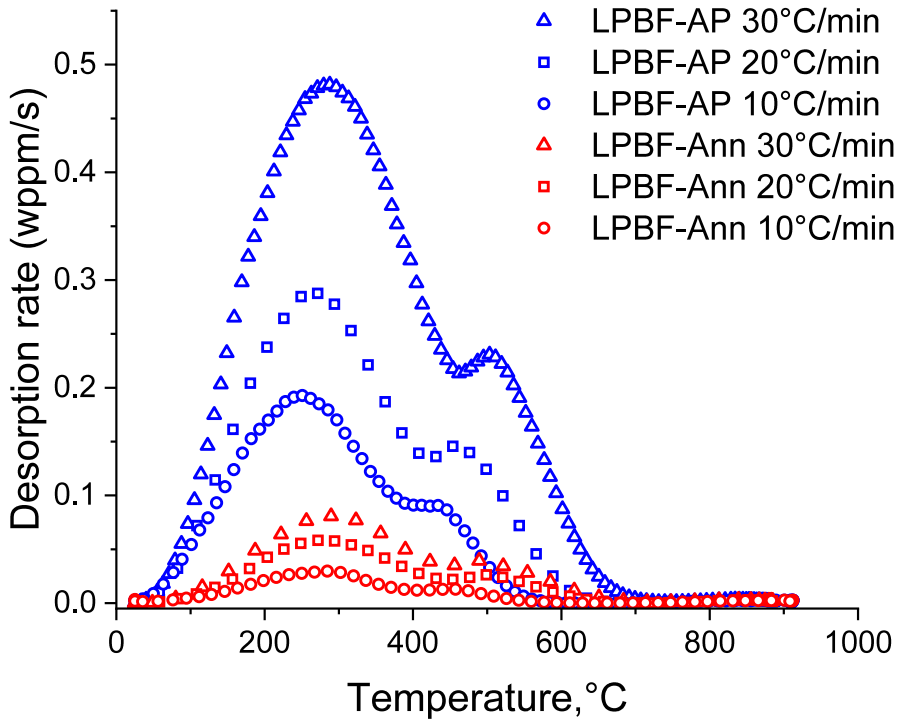


Figure 5.5: Comparison of the TDS spectra of 1-mm thick as-printed vs annealed LPBF samples.

Table 5.3: Total hydrogen desorbed for the as-printed and annealed 1-mm LPBF samples.

	C_H,ave
LPBF-AP	152.0 ± 16.3
LPBF-Ann	25.3 ±1.2

The existence of the 2nd peak at higher temperature is notable in all of the spectra and is attributed to the desorption of hydrogen from high-energy traps. It is also evident that this peak gradually shifts to the right as the heating rate is increased. I note that the total hydrogen

concentration values from Column 4 of Table 5.2 are higher versus that of Table 5.3 because of the influence of among other things, specimen thickness (0.5 mm vs 1 mm), the trends are similar (i.e., LPBF-AP having higher hydrogen content). Another difference is the presence of defined shoulder peaks at higher temperatures in the 1-mm thick samples compared to the 0.5 mm samples. This is an indication of a sample with a non-homogeneous H concentration which is expected for a thicker sample. Usually, in order to find the de-trapping activation energy of the different hydrogen traps present in each material and associate them with the specific microstructural features of this material, one is tempted to use the well-known method based on the work of Lee,et.al. Equation 5.3 is a simplification of the original formula of Kissinger[69], [93], [170]–[172] on this TDS data:

$$\frac{d\ln\left(\frac{\varphi}{T_p^2}\right)}{d\left(\frac{1}{T_p}\right)} = -\frac{E_a}{R} \tag{5.3}$$

where ψ is the heating rate ($^{\circ}C/h$), T_p is the TDS peak temperature in Kelvin, E_a is the activation energy in J/mol of the specific trap associated with the corresponding peak temperature and R is the universal gas constant, 8.3145 J/mol-K. After TDS measurements using different heating rates, deconvolution of these results and plotting of $ln(\psi/(T_P)^2$ vs $1/T_p$ for each peak temperature , the activation energy corresponding to that specific trap is obtained from the slope E_a/R. Figure 5.6 shows the linear fitting of the Kissinger formula and Table 5.4 shows the peak temperatures and relevant quantities for the as-printed sample at different heating rates. The same procedure was done with the wrought and LPBF-Ann samples which is summarized in Table 5.5.

The activation energies obtained from this approach can be used to gain insight into the mechanism of desorption that is dominant. From the activation energy, the trap binding energy, E_b can be derived. Trap binding energy, E_b is equal to $E_a - E_m$ where E_a is the trap activation energy or the energy needed to escape from the trap site to the normal lattice site and E_m is

Table 5.4: Calculated parameters for Kissinger's formula of the as-printed sample using 0.5 mm thick, hydrogen saturated TDS samples.

	Peak 1				**Peak 2**			
ϕ [°C/min]	T_{p1}[K]	${T_{p1}}^2$	$1/T_{p1}$	$\ln\left(\phi/{T_{p1}}^2\right)$	T_{p2}[K]	${T_{p2}}^2$	$1/T_{p2}$	$\ln\left(\phi/{T_{p2}}^2\right)$
5	435.0	189216	0.002	-10.5	521.1	271567	0.00192	-10.9
10	514.4	264627	0.002	-10.2	586.2	343630	0.00171	-10.4
25	524.9	275478	0.002	-9.3	672.1	451718	0.00148	-9.8

Table 5.5: Activation energies of the peaks identified as trap sites in the TDS spectra of the specimens.

	Activation energy, kJ/mol	
Sample	Peak 1	Peak 2
LPBF-AP	19.03	21.23
LPBF-Ann	26.74	5.45
wrought	61.19	9.61

the activation energy of hydrogen diffusion in the lattice. Two issues arise from the application of the Kissinger approach in this instance: one is that the goodness-of-fit given by R^2 is low and inconsistent for the specimen and trap type,and the other is that if we consider an E_m of 53.07 kJ/mol (a value obtained from austenitic stainless steels)[173], then E_m is very large relative to the E_a values shown in Table 5.5. This means that the desorption mechanism is diffusion-controlled and that Kissinger's approach is insufficient in characterising trapping.

For diffusion-controlled desorption, TDS analysis is done using McNabb and Foster or Oriani's approach. For this instance, the results of fitting using Oriani's model assuming two kinds of trapping sites using the Matlab® App *TDS Simulator* replotted with plotting software Origin® Lab is shown in Figure 5.7. It is also possible to calculate the density of trap sites associated with these peaks. The total number of trapped hydrogen atoms is the product of the number of sites and the fractional occupancy by hydrogen, and the binding energies with traps determine the distribution of hydrogen atoms. Some details on the *TDS Simulator* software can be found in Appendix E. The lattice hydrogen concentration is given by:

$$C_L = \theta_L \beta N_L \tag{5.4}$$

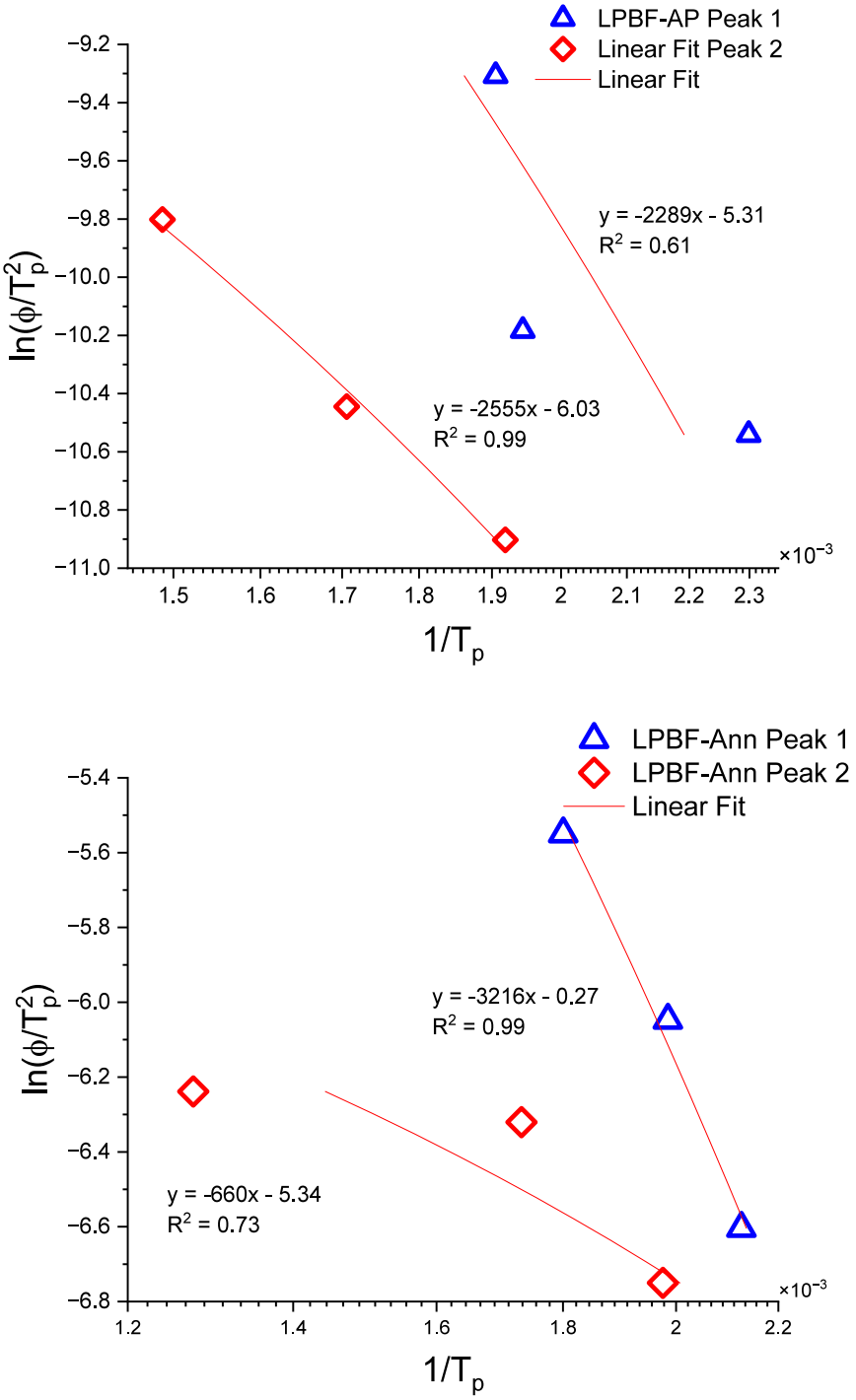


Figure 5.6: Linear fit of Kissinger's formula for the LPBF-AP and LPBF-Ann specimens.

and the trapped hydrogen concentration is given by:

$$C_T = \theta_T \alpha N_T \tag{5.5}$$

where θ_L is the occupancy ratio of lattice sites, β is the number of interstitial sites per lattice atom, N_L is the number of lattice sites per unit volume. Similarly, θ_T is the occupancy ratio of trapping sites, α is the number of hydrogen atom sites per trap and N_T is the number of trapping sites per unit volume. The relationship between θ_T and θ_L is given by the Oriani equation:

$$\frac{\theta_T}{1-\theta_T} = K\frac{\theta_L}{1-\theta_L} \tag{5.6}$$

where

$$K = \exp\left(\frac{-\Delta H}{RT}\right) \tag{5.7}$$

and where ΔH is the trap binding energy.

A detailed discussion of how these equations are incorporated in the software algorithm can be found in [162]. The average E_b and density of trap sites, N_t are also shown in Table 5.6. The single TDS peak at a certain temperature in both specimens support the assumption that desorption is lattice diffusion-controlled.

Usually, for pure lattice diffusion-controlled desorption this peak is at the lower temperature range of 200-400 K[26]. For the additively manufactured specimen, the shift of this single peak at a slightly higher temperature and the degree of asymmetry indicates the influence of weak or reversible traps. In fact, this single peak can be deconvoluted into two Gaussian peaks both at temperatures below 400°C. From the results of the simulator, the first peak of the as-printed specimen can be interpreted to be mainly the effect of trap 1, the weaker trap with the higher trap density as supported by the peak height, although the difference compared to the second peak in terms of temperature and height is very small. They also have very similar binding energies and are classified as reversible traps. The microstructural features associated with these trapping parameters are grain boundaries and dislocations. Grain boundaries and dislocations are normally challenging to resolve because they are very similar in energies[94], [174], [175]. However, the first trap can be attributed to dislocations due to the increased dislocation density in AM alloys. Hence, the second trap with a slightly higher binding energy are attributed to grain boundaries. For the annealed sample, the binding energies of the two traps are similar to the as-

printed specimen except that the density of traps are lower. The reduction in dislocation density further supports the suggestion that the traps are due to dislocations and grain boundaries.

Table 5.6: Average binding energies, E_b, and densities, N_t, of the two main trapping sites of LPBF-AP and LPBF-Ann specimens obtained from the *TDS Simulator* App.

Condition	**Trap 1**		**Trap 2**	
	E_b, kJ/mol	N_t, m^{-3}	E_b, kJ/mol	N_t, m^{-3}
LPBF-AP	-19.2	5.35 x 10^{24}	-19.0	5.35 x 10^{24}
LPBF-Ann	-20.0	9.76 x 10^{23}	-21.9	8.64 x 10^{23}

5.3.1 Hydrogen diffusivity

Hydrogen atoms occupy normal insterstitial sites (NILS) and additionally can reside at trapping sites such as interfaces and dislocations. The total hydrogen concentration is the sum of the lattice hydrogen concentration and trapped hydrogen concentration. Now, the lattice concentration $C_L(x,t)$ in space x and time t is dictated by Fick's law for pure lattice site diffusion. However, in the presence of traps, hydrogen diffusion is modified by both trapping and de-trapping of hydrogen atoms. The hydrogen diffusivity of LPBF-AP and LPBF-Ann samples was calculated from the isothermal TDS experiments conducted at 22, 90, 200 and 300 °C on samples electrochemically pre-charged with hydrogen for 7 days. Table 5.7 shows the average diffusivity obtained in all the isothermal TDS experiments conducted for the LPBF-AP and LPBF-Ann specimens, and the value for HEA-W is also included for reference. The results of the fitting for 22 and 200 degrees Celsius are given in Figure D.4. More information on the fitted experimental curves can be found in Appendix D.

Table 5.7: Hydrogen diffusivity, D, obtained from isothermal TDS at different temperatures for as-printed, annealed and wrought specimens.

Condition	**Temperature, °C**			
	22	**100**	**200**	**300**
LPBF-AP	2.52 x 10^{-14}	3.53 x 10^{-13}	7.40 x 10^{-12}	3.98 x 10^{-11}
LPBF-Ann	1.24 x 10^{-15}	not tested	5.69 x 10^{-12}	4.50 x 10^{-11}
HEA-W	8.05 x 10^{-16}	4.63 x 10^{-13}	4.63 x 10^{-12}	1.10 x 10^{-11}

The fitting with finite element calculations in COMSOL®-Matlab® produced a good fit for all the experimental data sets across all temperatures with an R^2 greater than 0.95 for all specimens. The diffusivity is highest with the as-printed sample which is especially evident at 22°C where trapping effects are more pronounced. The diffusivity of the annealed sample is one magnitude lower at10^{-15} and the specimen with the lowest diffusivity is the wrought sample. This is corroborated by the result of the total hydrogen desorbed where the as-printed sample has higher hydrogen content among the three samples. The diffusivity is in good agreement with literature as shown and summarised in Table 5.8.

The calculation of the diffusivities at different isothermal temperatures is especially helpful in the determination of the pre-exponential factor, D_0. Recall that, the diffusivity also has an Arrhenius-like temperature-dependence given by:

$$D = D_0 \exp(-\frac{E_a}{RT}) \tag{5.8}$$

where:

- D_0 is the pre-exponential factor,
- E_a is the activation energy for hydrogen diffusion,
- R is the gas constant and
- T is the absolute temperature

As shown in Figure 5.9, plotting $1/T$ vs $ln\ D$ allows for the calculation of the activation energy from the slope $-E_a/R$ and the pre-exponential factor from the intercept, $ln\ D_0$. The complete expression of the Arrhenius relation allows for the calculation of the diffusivity coefficient at any temperature.

It is also worth highlighting from Table 5.8 that there is a lack of studies on the hydrogen diffusion parameters such as the pre-exponential factor and activation energies, especially for the additively manufactured CoCrFeMnNi alloy.

5.3.2 Effect of hydrogen charging on tensile properties

Engineering stress-strain curves of hydrogen pre-charged samples and uncharged CoCrFeMnNi in as-printed and annealed conditions are shown in Figure. The as-printed specimens pre-charged

with hydrogen for 7 days before tensile testing exhibited a drastic decrease in ductility with up to 90% difference in the breaking strain between the two samples. This is also supported by the highest HEI in terms of reduction in area among the three kinds of samples which is evident even by visual examination of the fractured dogbones in Figure 5.11. The uncharged as-printed specimen exhibited a typical cup-and-cone fracture which is more pronounced in the uncharged annealed specimen. The as-printed samples exhibited virtually no necking after H-charging, while a closer look at the charged samples in Figure 5.12showed a degree of necking with the annealed specimen. Moreover, the annealed specimen in this figure exhibited step-wise surface cracks that are characteristic of hydrogen-induced cracking. Interestingly, this is not observed to the same extent in the as-printed samples. This can be attributed to the severe embrittlement in the as-printed specimen. Because the specimen immediately fractured, there is no chance for numerous cracks to form along the length of the gauge length distal to the fractured region. In fact, this supports the increased plasticity of the annealed sample.

The stress-strain curves in Figure 5.10 indicate that the as-printed samples were severely embrittled after hydrogen charging. Also, the as-printed samples showed a slight decrease in yield strength after H-charging while annealed samples remained the same. Although several studies reported an increase in yield strength after charging due to the solid-solution strengthening effect of hydrogen, they have employed a shorter hydrogen charging time than this study (e.g. 46 hours vs 7 days)[167]. The results in this case might be due to the relatively higher hydrogen concentration introduced into the sample which made the unfavourable mechanisms triggered by high hydrogen content more dominant compared to the beneficial nano-twinning induced hydrogen strengthening. Moreover, most of these studies used gaseous hydrogen charging[23], [100], [176] in contrast to electrochemical charging employed in this study. High H-concentration in the surface as a result of electrochemical charging can cause initial surface cracks that reduce the overall ductility and strength of the sample which explains why there is a very little difference in yield strength and ultimate tensile strength after charging.

Annealing at 900°C for 2 hours increased the ductility of the as-printed samples by as much as 43% with a slight decrease in yield strength, consistent with the strength-ductility trade-off in most alloys. This can be attributed to the enlargement of grains after annealing which decreased the contribution of grain boundary strengthening as predicted by the Hall-Petch relation. Moreover, this suggests that annealing may have decreased the density of defects in

the sample, particularly the density of dislocations, allowing for a lower critical shear stress for slip to occur. Together with the lowering of the yield strength is the increase in strain-hardening rate of the annealed samples. This is consistent with the presence of dispersed nano-sized oxide particles in the HEA matrix. Dislocations accumulate in tangles around these fne particles during its motion. This promotes slip systems, and loops around particles tend to make them comform, by elastic deformation, to the plastic deformation of the matrix. As a result, high elastic strains are developed in the particles capable of supporting a large fraction of the total load[147]. This is supported by the disappearance of the dislocation cell network as shown in the ECC images in Figure 4.13.

Moreover, hydrogen charging reduced the ductility by up to 67%. However, although the train at break for charged samples is significantly lower than the uncharged ones, they do show some recovery of ductility which suggests that even simple annealing in air can impart hydrogen embrittlement resistance to the AM HEA. The average reduction in area of the 1-mm thick as-printed and annealed specimens and their respective mechanical properties obtained from the stress-strain curves are summarized in Table 5.9.

5.3.3 Fractography

SEM images of the fracture surfaces of representative samples are shown in Figure, respectively. The fracture surface of the as-printed and annealed uncharged samples show a mechanism of microvoid coalescence shown by the presence of dimples and voids, typical of ductile fracture. By contrast, that of the pre-charged samples showed two distinct fracture surfaces. These regions show an area of brittle fracture around the perimeter which is directly related to the extent of hydrogen ingress into the specimen (hydrogen affected region and an area of ductile fracture in the middle). A closer look at the fracture surface shows a characteristic dimpled rupture due to microvoid coalescence in the ductile region and cleavage with integranular fracture in the hydrogen affected zone.

The brittle zone area fraction (BZAF) in percentage was quantified using ImageJ and the brittle zone depth was calculated as an average of the penetration depth of both sides of the specimen. It is worth noting that the brittle zone depth of the two kinds of samples differ

significantly, with hydrogen penetrating further in as-printed samples compared to the annealed ones. Moreover, the area is more uniform on both sides for SLM-AP. Whereas in some regions of the annealed samples, the brittle zone depth is significantly shorter. This suggests that the hydrogen ingress is slower and more non-uniform across the surface in the annealed samples which is consistent with the observed recovery of ductility mentioned previously. A summary of the brittle zone parameters are shown in Table 3.

The amount of hydrogen in the samples after H-charging for 7 days were obtained from desorption experiments with 1 mm-thick samples shown in the desorption curves (wppm/s vs. temperature) in Figure 7. The experiments were performed using different heating rates.

The presence of a pronounced shoulder peak at higher temperature in these TDS curves indicate that the samples do not have a uniform hydrogen distribution after charging for 7 days, in contrast to the 0.5 mm samples. Figure 8 shows a closer look at the fracture surface reveals a penetration depth of 250 µm and 200 µm for as-printed and annealed samples respectively, which suggests a relatively higher extent of hydrogen ingress in as-printed samples. Integration of the desorption curves confirm a significantly higher desorbed hydrogen concentration in as-printed samples as listed in Table 4.

Fracture surface examination reveals that the hydrogen pre-charged tensile samples have two distinct fracture surfaces. They hydrogen affected zone shows a characteristic intergranular/quasi-cleavage fracture as described in Section 3.5. It is also interesting to note that the fracture seems to be along the interdendritic regions due to the resemblance of the fracture lines to the etched microstructure as shown in a magnified SEM image in Figure 9. Intergranular fracture have been reported to have "brittle" striations perpendicular to the local crack growth direction in AISI 4340 steel . Also, the regularity of the fracture surface pattern suggests that fracture occurs following the layer thickness of the build (or it could be the fusion lines of the fishscale microstructure)..

EBSD scan of the crack on the fracture surface point to the hydrogen enhanced decohesion (HEDE) mechanism as the dominant mechanism at work.

After annealing at 900°C, the same kind of intergranular, interdentritic cleavage fracture in the brittle region of the specimen can be observed which suggests that the hydrogen embrittlement resistance of the annealed sample may not be due largely to a change in the grain size or

dendritic microstructure after annealing. However, a comparison of the fracture surface of the as-printed and annealed specimens at much higher magnification shows a difference.

5.3.4 Challenges in the direct detection and mapping of hydrogen using atom probe tomography

So far, thermal desorption analysis which is a microstructure sensitive approach to relate hydrogen trapping parameters to microstructural features such as grain boundaries and dislocations was successfully employed. This is key to understanding the design of hydrogen resistant CoCrFeMnNi. However, another key strategy is to design atomic-scale microstructural traps to limit hydrogen diffusion and mitigate hydrogen embrittlement. For example, the incorporation of finely dispersed nanoscaled carbides within the 10 nm range such as vanadium carbides limit deleterious hydrogen effects by acting as strong traps that retain hydrogen and prevent diffusion and thus hydrogen assisted-cracking. Although these approaches sound viable, there are very few direct experimental information that exist on the interaction of hydrogen with such strong traps due to the technical difficulty of directly detecting and observing hydrogen atoms[177], [178]. I have detailed in Chapter 1 how atom probe tomography is able to provide a solution for this dilemma. However, the sample preparation for this technique is not straightfoward and several workflows have been investigated to establish the best practices from specimen lift-out, tip sharpening, deuterium charging, to sample transfer [179]. Here I discuss the challenges in the application of this technique to a highly alloyed system such as the CoCrFeMnNi high-entropy alloy.

First of these challenges is the preparation of the specimen tip. In order to be of considerable research interest, a site-specific sample preparation was done on the bulk specimen, targeting precipitates, grain boundaries, chemical segregation sites, or dislocations to which can act as microstructural traps. Because the specimen tip must not exceed 100 nm in diameter (often in the range of 50 nm) this objective is often difficult to achieve within the allotted time frame. Moreover, after sample preparation with Gallium FIB, this route is sometimes supplemented by transmission Kikuchi diffraction (TKD) to facilitate the positioning of this specific site of choice, e.g., an intrinsic defect or phase, sufficiently close to the tip apex. However, irradiating the specimen with energetic electrons and ions can lead to the generation of vacancies and even amorphisation of the specimen. As an example of a region of interest, a region of nickel

segregation is shown in Figure 5.18 a and b for the LPBF-AP sample. However, the mass spectra shows no deuteration in the sample which can indicate that the segregation region is not a strong trap for deuterium or that the gas charging is insufficient for deuterium ingress into the sample, or that deuterium ingress is hindered by an ionic coating that resulted from the sample preparation.

The phenomenon is also observed in the LPBF-Ann sample in Figure 5.19 where the mass spectra showed no sign of deuterium in the sample. It is interesting to note that there is an increased concentration of oxygen in the specimen tip forming an "oxygen cap." This might be due to the increased oxidation of the annealed sample. The role of oxygen and how it affects the gas charging process or field evaporation remains unclear but I theorise that oxygen may have played a role in hindering the detection of deuterium during field evaporation.

Out of all samples prepared, only the wrought sample showed a small peak at mass number = 2 Daltons and 3 Daltons, the corresponding mass number for deuterium ion and hydrogen bonded to a deuterium ion, respectively in the wrought specimen. This is evidence of a successful deuteration of the sample. However, this peak may be an artifact and would require reconstruction of the specimen tip to verify. Hence,the combined hydrogen and deuterium distribution in the reconstructed tip is shown in Figure 5.20 d.

It can be seen from Figure 5.20 c that there is a relatively denser distribution of hydrogen in the region that corresponds to a change in the voltage profile of the specimen, indicating a region of higher field evaporation. It is difficult to assess whether this is an interface or a boundary but Figure 5.20 d shows clusters of H/D of the same region viewed from the top, indicating deuterium enriched voids similar to those observed in previous reports using the same sample preparation workflow [180], [181]. These voids are likely formed due to the aggregation of vacancies generated by sub-surface cascades caused by ion irradiation or indirectly by electron irradiation. Since vacancies serve as strong traps for H/D [182], the voids exhibit significant D enrichment[183].

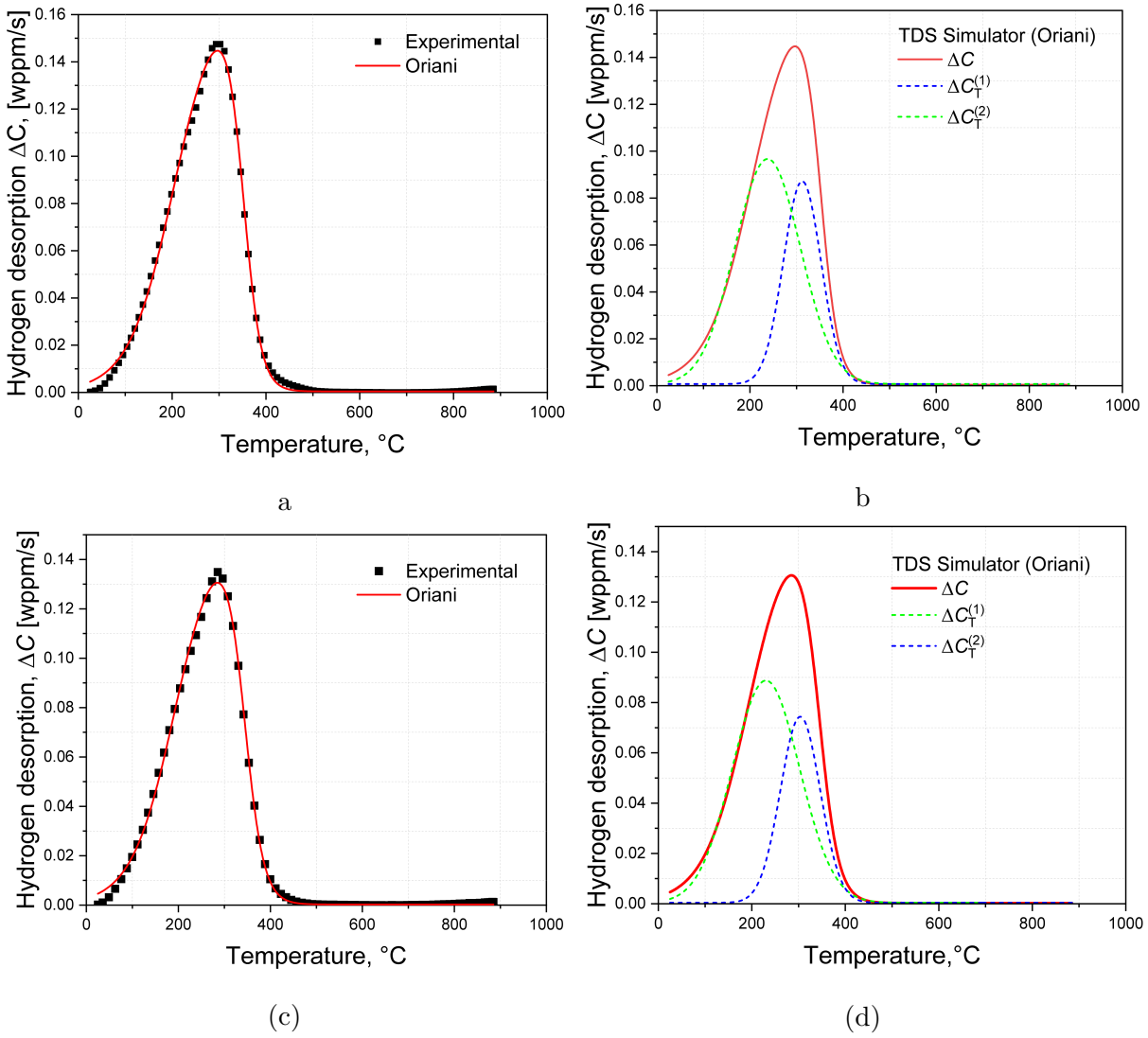
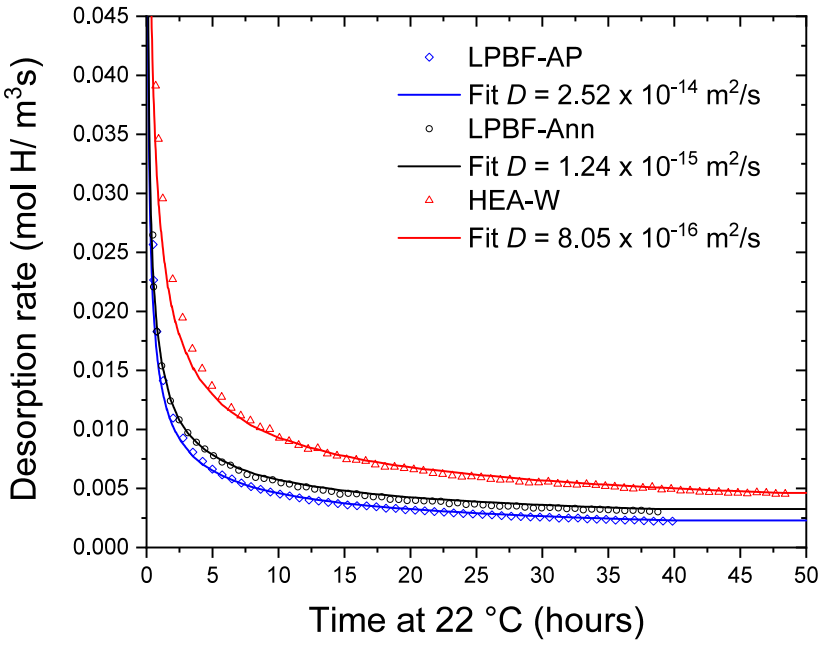
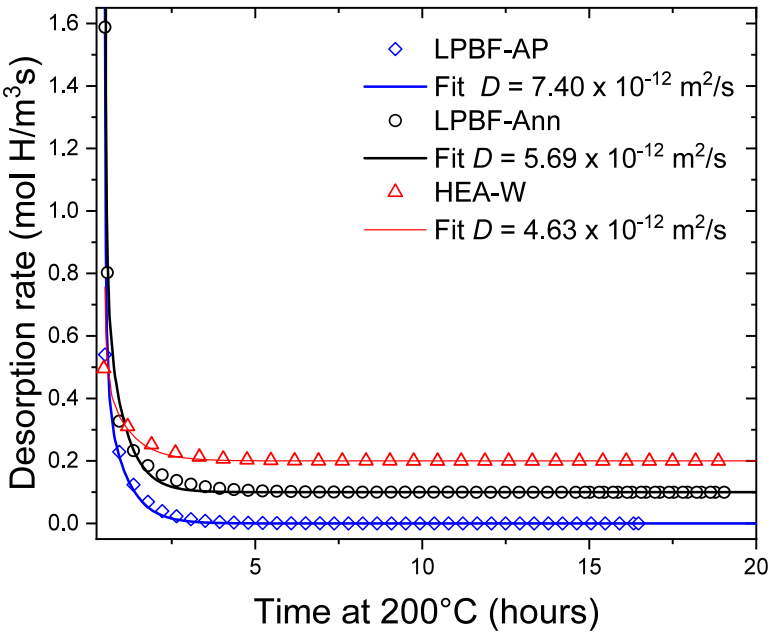


Figure 5.7: Using the inference fitting capabilities of *TDS Simulator* to gain insight into the trapping characteristics of an AM Cantor alloy: experimental and simulated desorption curves, with the latter being obtained using TDS Simulator's optimization algorithm, and contribution of each relevant type, as determined by *TDS Simulator* for (a,b) LPBF-AP and (c,d) LPBF-Ann. In (b and d), traps are ordered from smaller to larger absolute binding energy, $\Delta H = E_b$. Goodness of fit measured by coefficient of determination (adjusted R^2): (a) 0.9981 (c)0.9984



(a)



(b)

Figure 5.8: Isothermal TDS and numerical fitting for diffusivity calculations. Isothermal TDS (ITDS) experiments performed at (a) 22°C and (b) 200°C and the best fit to 1-D hydrogen transport FE simulations.

Table 5.8: Comparison of hydrogen diffusivity values in literature for the CoCrFeMnNi HEA. Note the agreement of the calculated D_0 values in this work to previous work which validates ITDS as a viable method for calculating the diffusivity.

	Condition	D_{eff}	D_0	E_a, **kJ/mol**	T_{range}	**Method**
Reference						
Lin, et.al. (2022)	SLM-as-printed	1.1 x 10^{-15}			RT	natural aging test, TDA
	SLM-annealed	1.8 x 10^{-15}			RT	
	CHRA	6.9 x 10^{-15}			RT	
Feng et.al. (2022)	HR+SA at 1000°C	1.4-1.7 x 10^{-16}			RT	diffusion distance
Marques, et.al. (2021)	VAR	3.7 x 10^{-16}	4.3 x 10^{-7}	-51.7	RT	Permeation
Belo, et.al. (2020)	VAR	0.9 x 10^{-11}			300°C	Permeation
This work	LPBF-as-printed	2.52 x 10^{-14}	1.02 x 10^{-7}	-37.8	22-300°C	Isothermal TDS
	LPBF annealed at 900°C	1.24 x 10^{-15}	4.12 x 10^{-6}	-53.6		
	wrought	8.05 x 10^{-16}	7.37 x 10^{-7}	-49.7		

Note: CHRA- casting, homogenisation, cold rolling and annealing; HR+SA- hot-rolled and solution annealed; VAR- Vacuum Arc Remelting

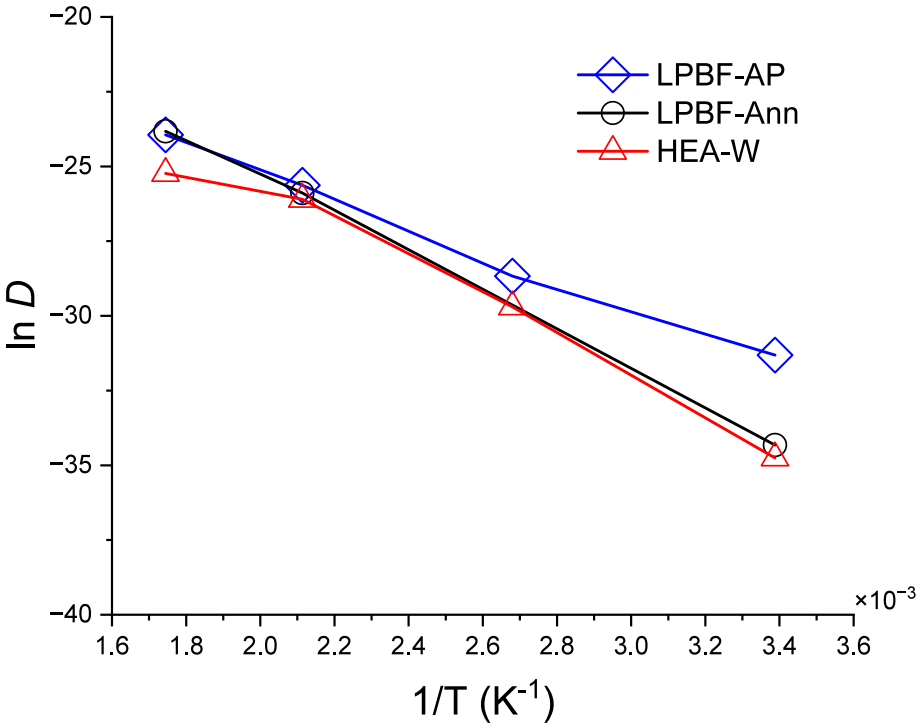


Figure 5.9: Hydrogen diffusivity at different temperatures fitted to the Arrhenius relationship D = D_0exp(-E_a/RT) where D_0 is the pre-exponential factor and E_a is the activation energy for diffusion.

Table 5.9: Mechanical properties of hydrogen pre-charged and uncharged 1-mm thick tensile samples of additively manufactured specimens

Material	**Charging duration**	**Tensile strength, σ_T (MPa)**	**Yield strength, σ_y, (MPa)**	**Strain at break (%)**	**Reduction in Area (%)**	**HEI (%)**
LPBF-AP	0 h	630 ± 6	555±2	23±2	46±1	90.9
	7 days	546±2	538±3	2±0.1	4±1	
LPBF-Ann	0 h	634±5	434±1	33±2	51±1	64.5
	7 days	540±2	430±3	11±3	16±3	

Table 5.10: Brittle zone depth and brittle zone area fraction (BZAF) of hydrogen charged AM CoCrFeMnNi

	LPBF-AP	LPBF-Ann
Brittle zone depth, μm	314.2 ± 35.2	190.0 ± 45
Brittle zone area fraction (BZAF)	62.8 %	38.0%

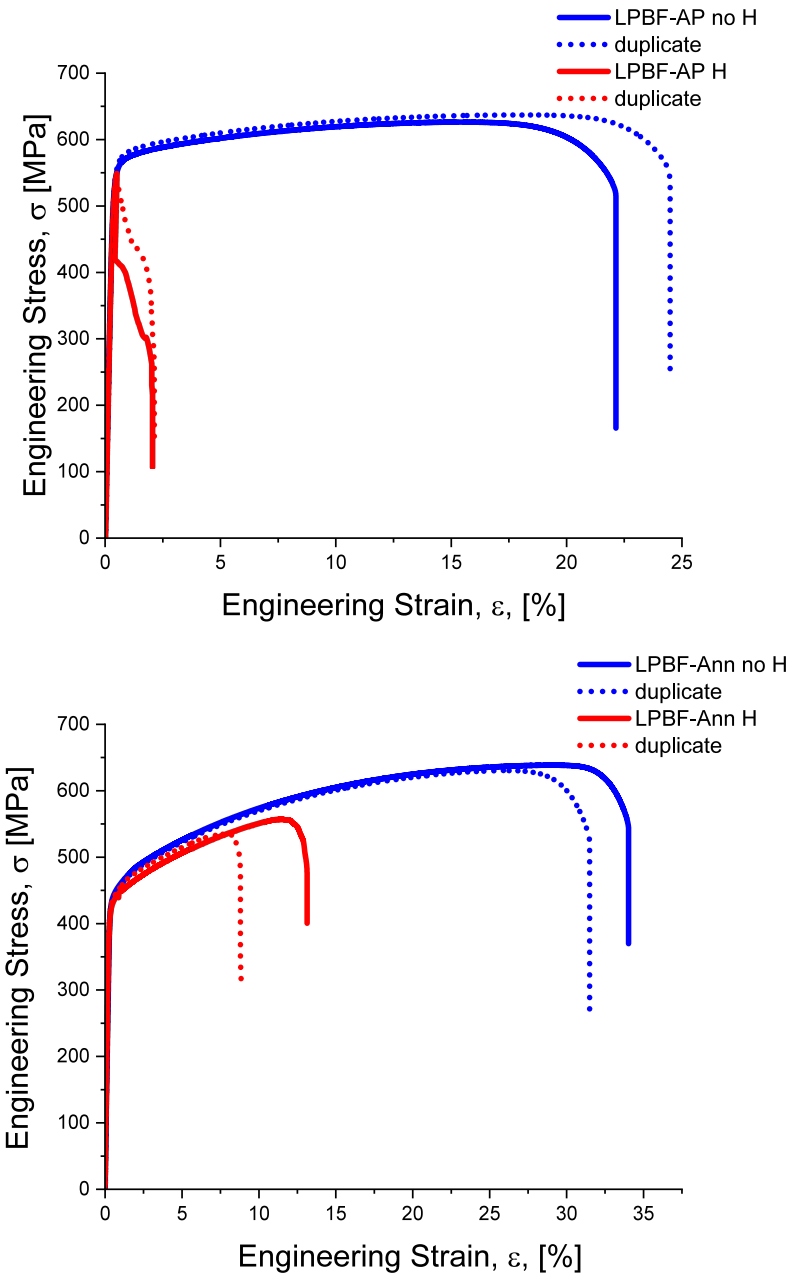


Figure 5.10: Engineering stress-strain curves of hydrogen pre- charged and uncharged tensile samples: as-printed and annealed. The dashed lines represent replicates.

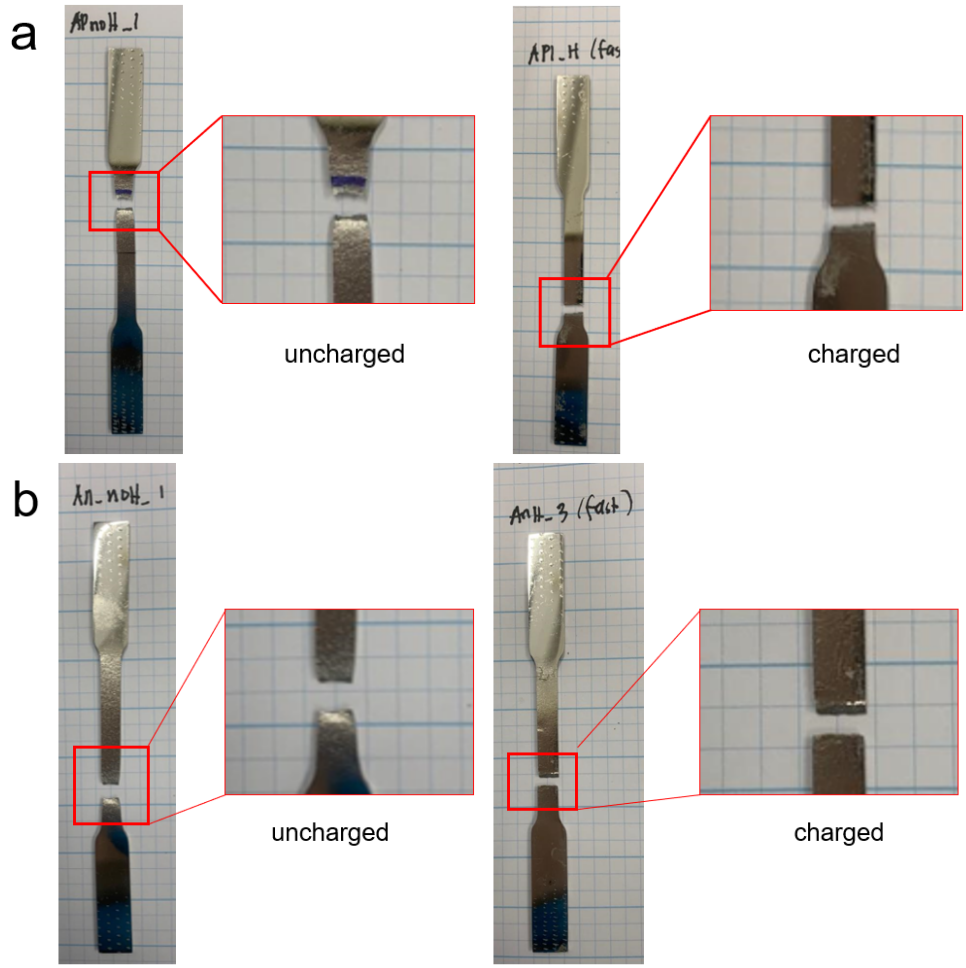
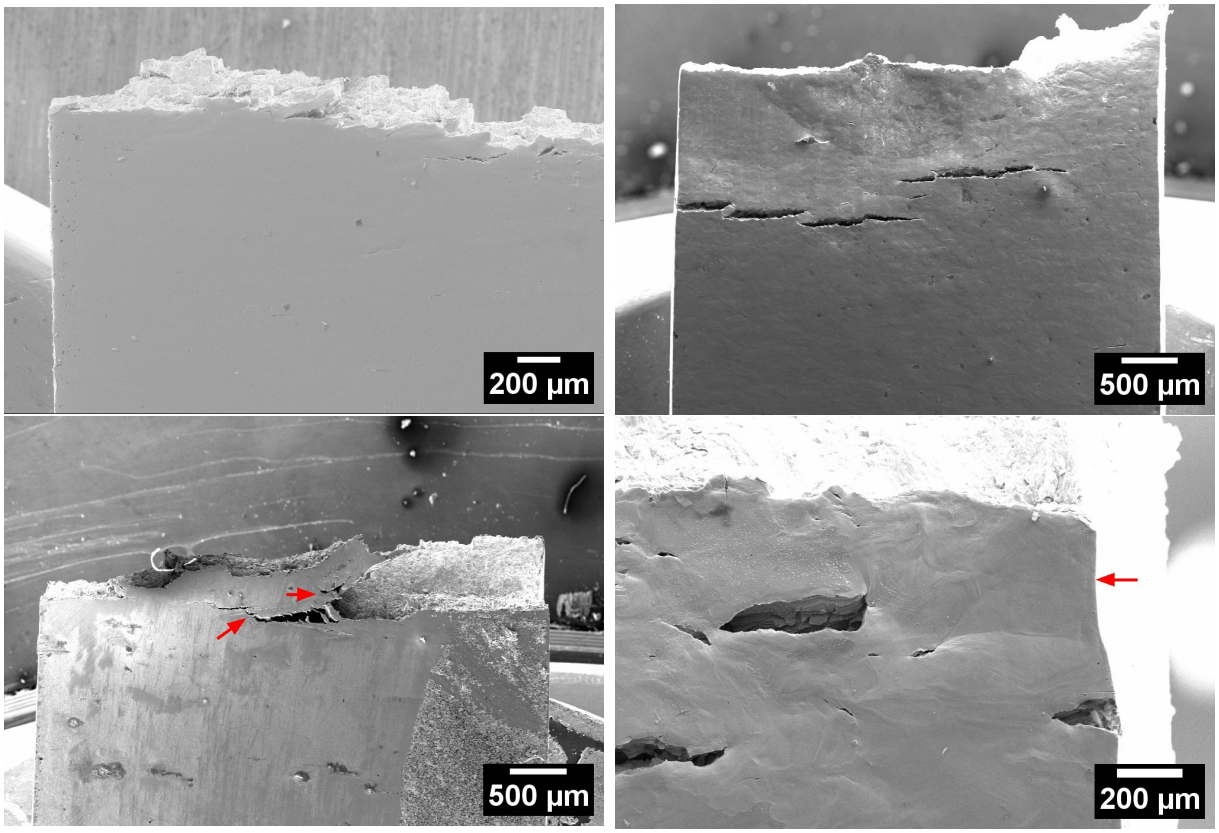


Figure 5.11: Necking observed in fractured tensile specimens: (a) LPBF-AP (b) LPBF-Ann



(a) (b)

Figure 5.12: SEM micrographs of the neck region in the fractured tensile specimens for (a) as printed and (b) annealed.

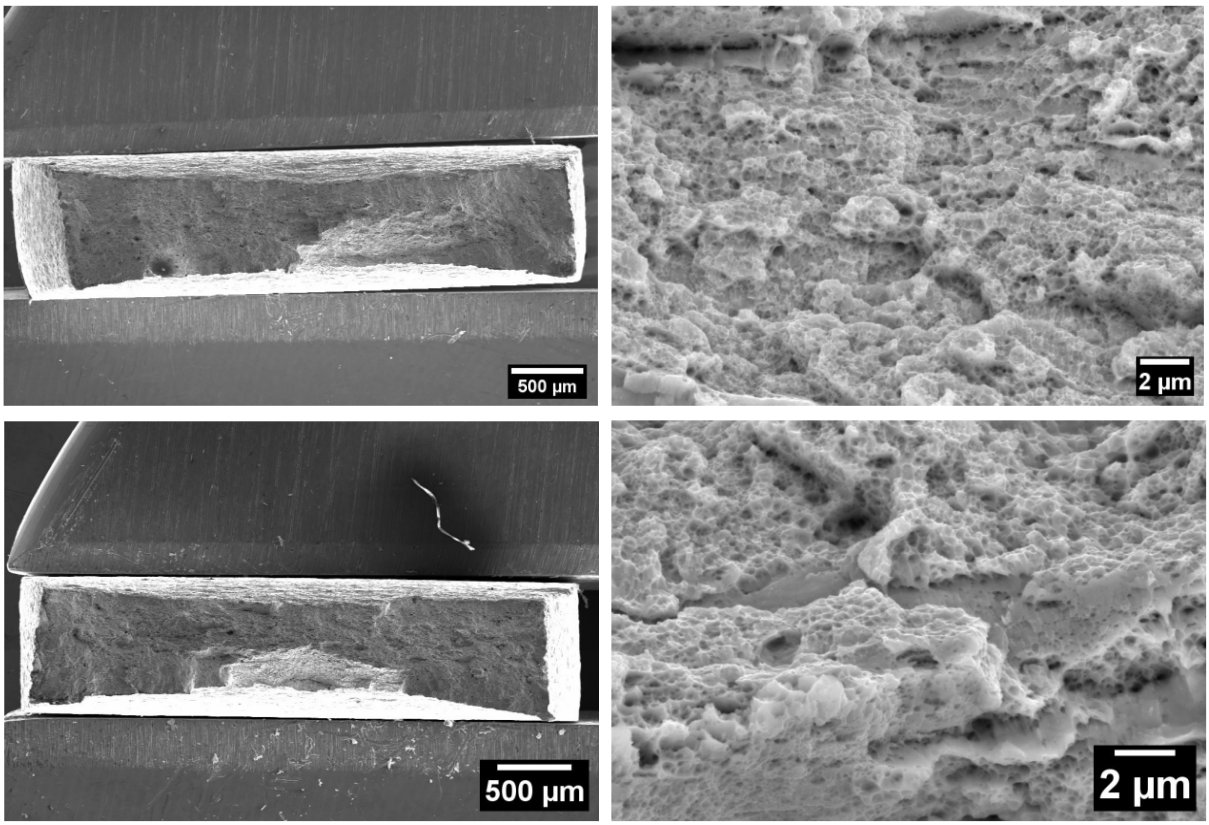


Figure 5.13: Caption

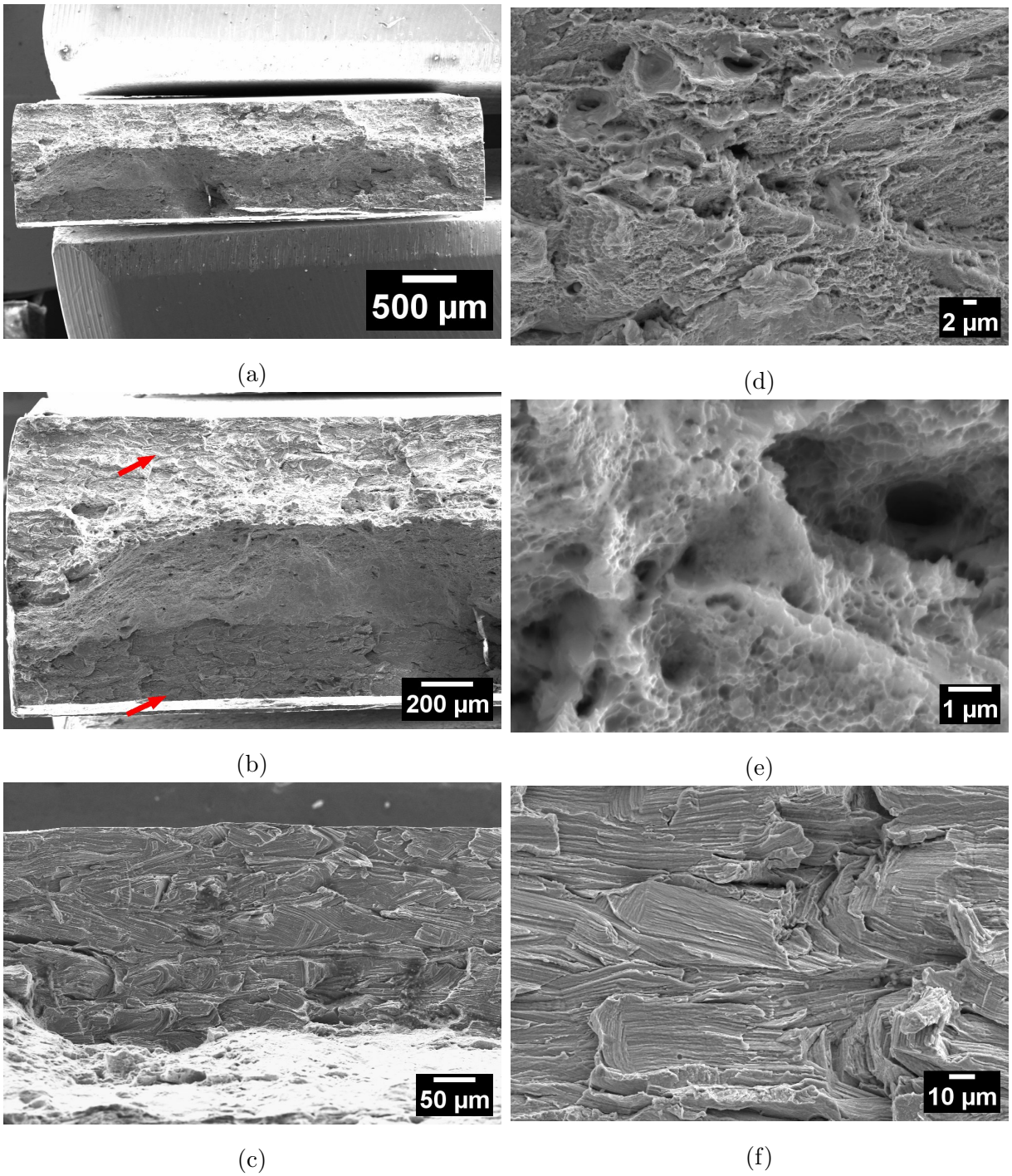


Figure 5.14: SEM micrographs of fracture surfaces of LPBF-AP specimen showing (a) step-wise cracking (b) hydrogen-affected zones (c) magnified image of ductile region in the middle of the fracture surface (d) magnified brittle region showing intergranular fracture with quasi-cleavage like features.

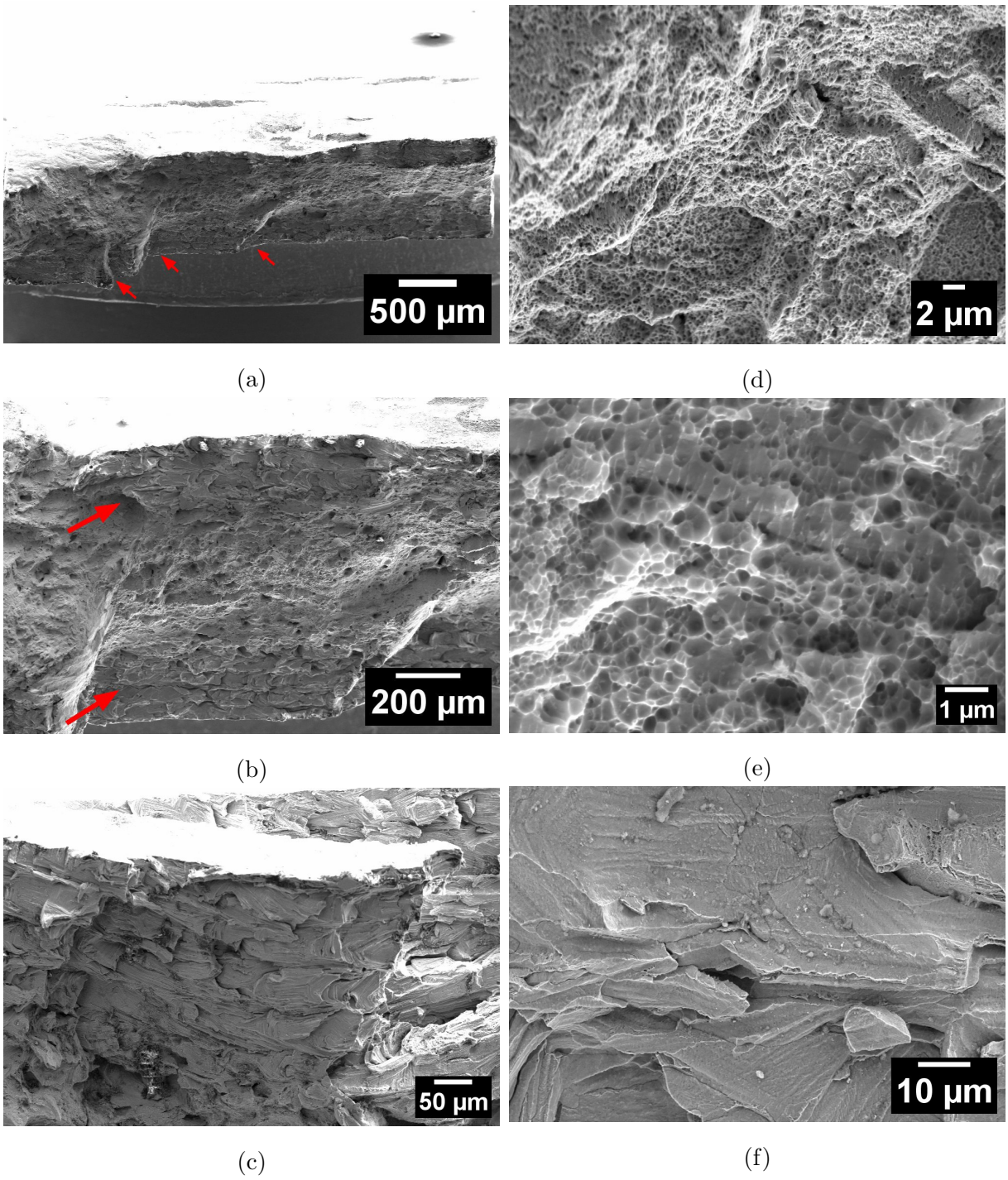


Figure 5.15: SEM micrographs of fracture surfaces of LPBF-Ann specimen showing (a) step-wise cracking (b) hydrogen-affected zones (c) magnified image of ductile region in the middle of the fracture surface (d) magnified brittle region showing intergranular fracture with quasi-cleavage like features.

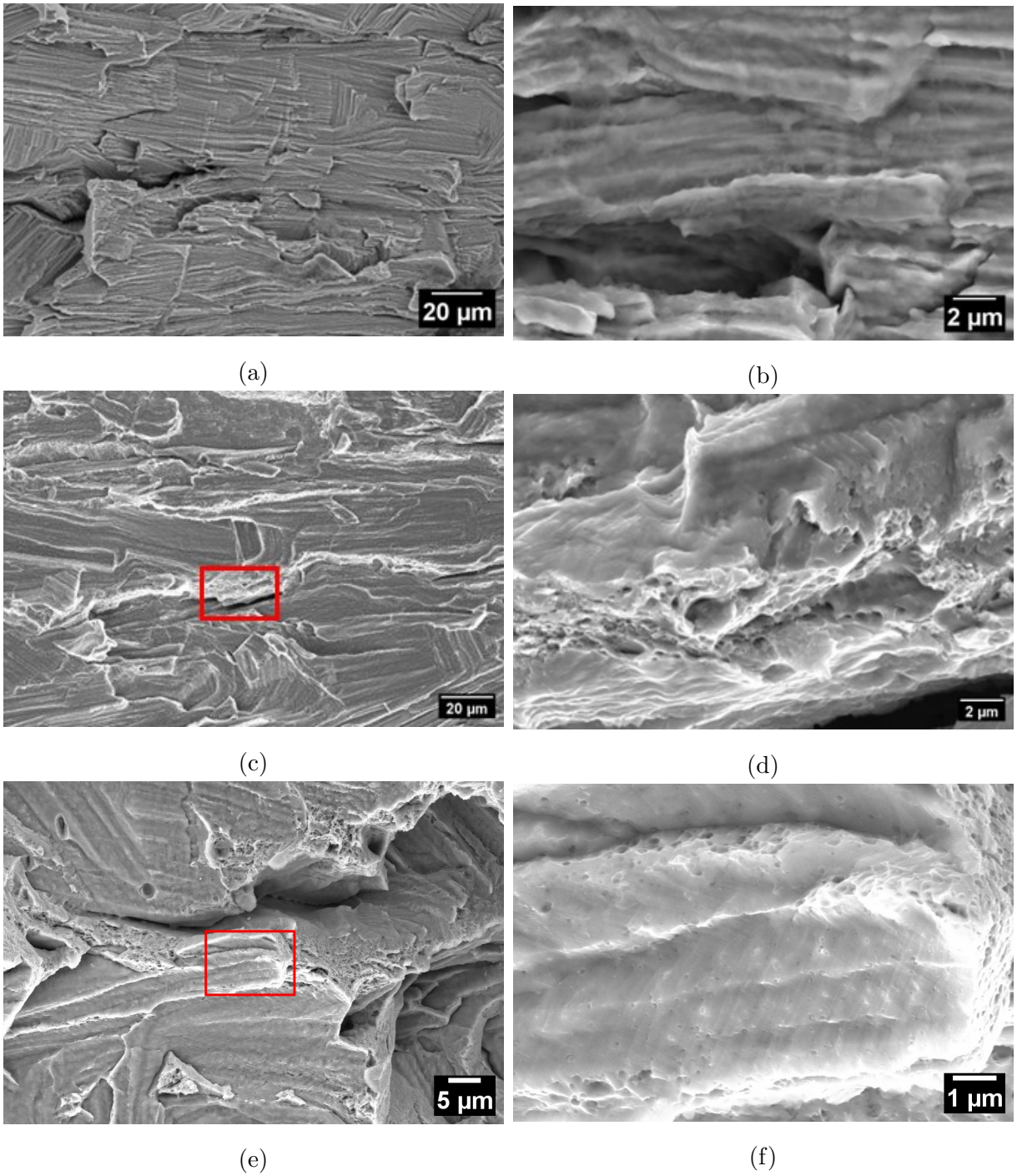
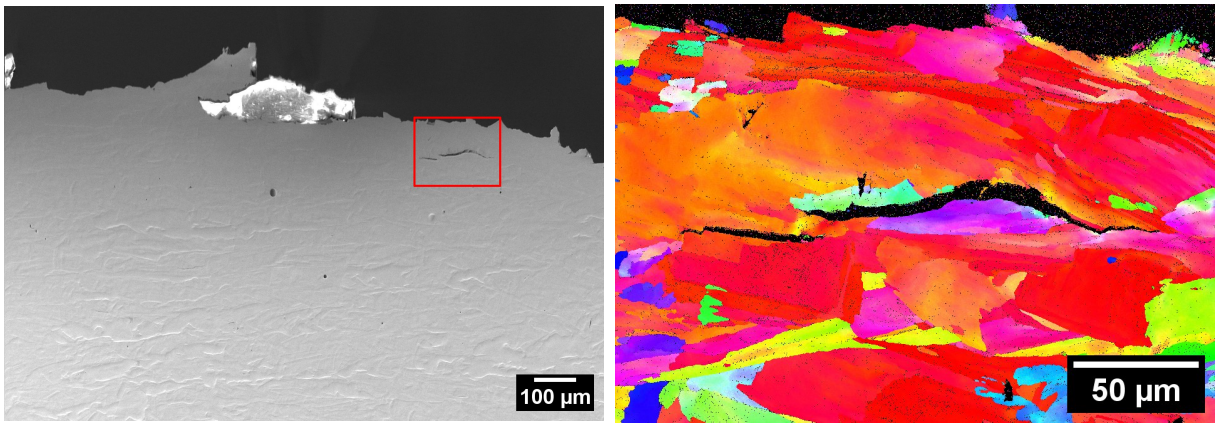


Figure 5.16: LPBF-AP vs LPBF-Ann fracture surfaces. LPBF-AP(top) shows uniform, flat surface ridges, while LPBF-Ann(bottom) shows the presence of microvoids on the edges of surfaces (tear ridges). Also at higher magnification, slip bands on the cleavage facets are visible. All these point to 'plasticity-mediated' HEDE mechanism.



(a) (b)

Figure 5.17: Electron back-scattered diffraction image of a step-wise crack on the surface of a charged fracture specimen showing intergranular decohesion both at grains with large and small misorientation.

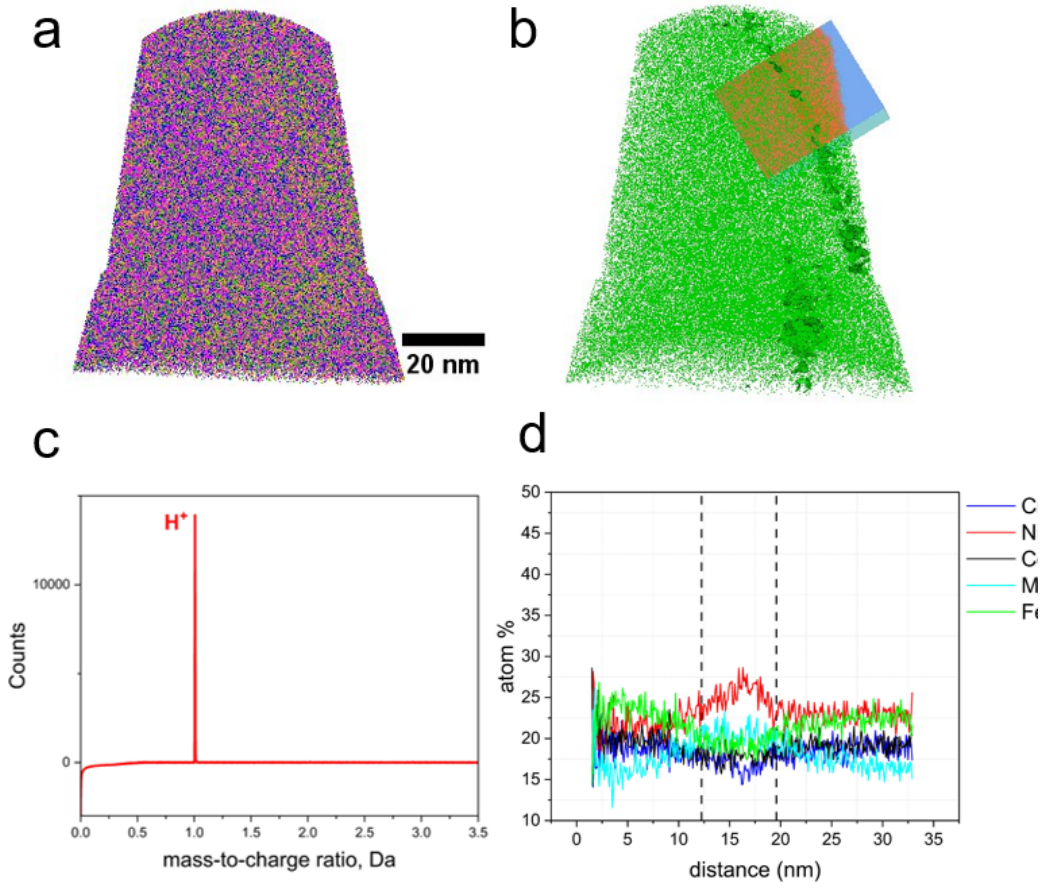


Figure 5.18: Atom probe tomography reconstruction of the LPBF-AP specimen showing (a) all major distribution of ions, (b) Nickel distribution and cylinder for 1-D concentration profile (c) mass spectra (d) proxigram of all major elements between bulk sample and region of interest.

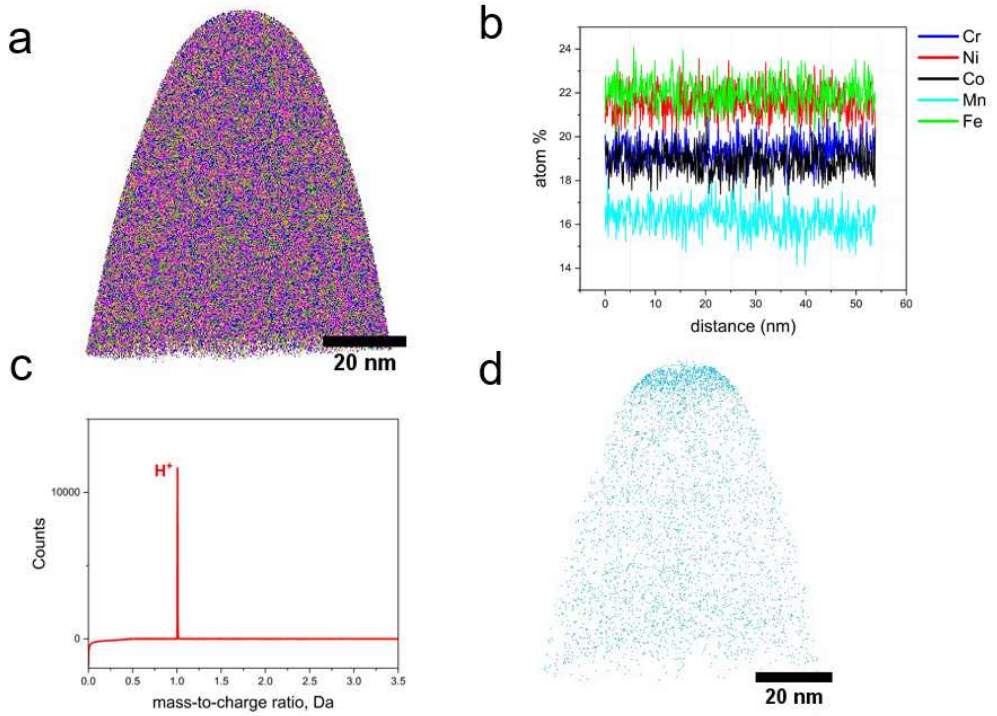


Figure 5.19: Atom probe tomography reconstruction of the LPBF-Ann specimen showing (a) all major distribution of ions,(b) 1-D concentration profile along the z-axis showing significant Mn depletion supporting the previous report of Mn evaporation (c) mass spectra showing no peak corresponding to Deuterium and (c) distribution of oxygen in the specimen.

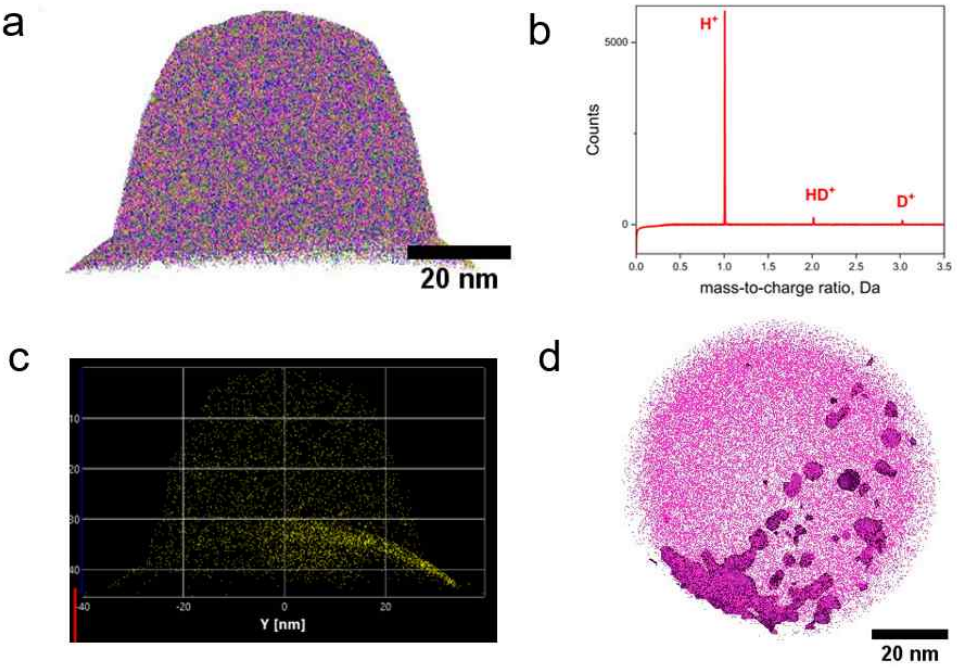


Figure 5.20: Atom probe tomography reconstruction of the HEA-W specimen showing (a) all major ion distributions, (b) the mass spectra with peaks corresponding to deuterium, (c) the total distribution of H/D in the sample and (d) top view isosurface showing H/D clusters

5.4 Discussion

5.4.1 Effect of specimen thickness on hydrogen diffusion and trapping

From the aforementioned results, the TDS peak shapes of less than 0.5 mm thick specimens such as those seen in Figure 5.4 differs with that of the peak shapes found in thicker samples in Fig 5.5. As supplemented by the analysis of experimental and numerically simulated data it became obvious that the differences in the profile of hydrogen concentration in the specimen after charging leads to the differences in the TDS peak shape. Thicker samples have more complex diffusion peak shapes and is attributed to the specific hydrogen release when there is an inhomogeneous distribution profile of hydrogen in the specimen. Even though the desorption is lattice diffusion dominated, the relative thickness of the specimen cause redistribution of hydrogen between lattice and trapping sites during the TDS experiment. This effect is further compounded by the fact that FCC metals like the Cantor alloy have very low diffusivities and must be taken into account when analysing their TDS data. [184].

The magnitude of the wppm of H in LPBF-AP found in Table 5.2 which is substantially large compared to LPBF-Ann and HEA-W is consistent with that observed by Yang, et.al. (2021) which reported around 423 wppm after 25 hours of charging at 40°C [185]. Furthermore, the much thinner samples used in this measurements (0.3 mm-0.4 mm) are expected to have a higher concentration of hydrogen desorbed than the 1 mm thick samples found in Table 5.3 . This is because in "thick" specimens, frequent trapping and de-trapping events happen during diffusion through the specimen. On the other hand, in "thin" specimens, lattice hydrogen diffuses out readily and trapping and detrapping events take place independently[26]. This same influence of sample thickness on hydrogen desorption was also observed by Perez-Escobar, et.al for high-strength steels [186]. I posit that the mitigation of trapping and de-trapping processes by sufficiently decreasing the thicknesses of the specimens subjected to TDS tests allows for the assumption of local equilibrium between lattice and trap diffusing states as well as a relatively homogeneous hydrogen distribution. This is further supported by the deficiency of the Kissinger's approach in consistently predicting the activation energies of the microstructural traps. The Kissinger's approach assumes a trap dissociation dominated desorption such as what can be expected of the 1-mm thick specimens under the same charging conditions. This means that applying the Kissinger or Choo-Lee equation, Equation 5.3, would be more suited to the

TDS data in Figure 5.5 as we've seen in supplementary calculations not included here for which the reader can verify themselves. This is mainly due to the fact that even from visual inspection, the two peaks in Figure 5.5 are shifted regularly with increasing heating rates.

5.4.2 Isothermal TDS measurements and H-diffusivity

The suitability of isothermal TDS tests in estimating the apparent or effective hydrogen diffusivity has been demonstrated in literature only fairly recently [116], [187]. The success of the method relies on the fact that FCC metals have very low hydrogen diffusivities in the order of $10^{-16}\ m^2 s^{-1}$ and as a consequence of lattice-dominated desorption, the diffusion can be assumed to be independent of hydrogen concentration. This assumption is valid mostly for pure metals and part of the previously perceived limited applicability of the isothermal TDS approach in calculating hydrogen diffusivities pertain to the complexity of highly alloyed metals. This difference is exemplified not just by diffusivity but also with solubility. In effect, the solubility of hydrogen in steels is substantially altered by alloying. For example, in austenitic stainless steels, the heat of solution of hydrogen is about 16 kJ/mol much less than that of pure γ-iron. Higher solubilities in austenitic steels than those in ferritic stainless steels are due not only to the crystal structures but also to alloying elements such as Ni and Cr [26]. Meanwhile, diffusivity for austenitic steels is lower than ferritic steels. This interplay between solubility and diffusivity can be explained by the presence of preferential trapping sites in both crystal structures as discussed in Chapter 2. For the CoCrFeMnNi HEA, with an FCC phase, the increased Ni and Cr concentration that can act as trap sites can increase solubility which explains the relatively high concentration of hydrogen in all three specimens in Table 5.2. In comparison, it follows that the as-printed sample, with its increased dislocation density and complex microstructure would have a higher amount of hydrogen desorbed. Despite these complications, the values of effective hydrogen diffusivities, including the pre-exponential factor and activation energy obtained from fitting isothermal TDS curves are very consistent with the observed desorption data and mechanical testing as well as previous reports in literature, most notably agreeing very well to the *ab-initio* calculations of the mentioned parameters in Table 5.8.

5.4.3 Quantifying and mapping hydrogen

The TDS spectra indicated reversible traps that have very close energies. Due to the small difference in energies, the *TDS Simulator* has identified this as a single peak that can be deconvoluted into two Gaussian peaks that can be interpreted as the contribution of two closely related traps. The two traps can be attributed to grain boundaries and dislocations which have very close energies and possibly coherent precipitates. However, further proof of the coherency of the precipitates is needed. If this is the case then more weak traps in the as-printed state should be expected because it has more grain boundaries and relatively higher dislocation density, which is what has been observed.

The study also suggests the crucial role of not just dislocation density but the geometry of the dislocation network itself in facilitating hydrogen embrittlement. It is important to mention that the calculation of dislocation density employed in this study is not conclusive. Analysis of the XRD spectra mentioned in Chapter 4 using the Continuous Whole Profile Method (CWMP) showed a significant decrease in dislocation density while calculation of GNDs using more localised high-resolution EBSD maps show no significant difference. CWMP, although having the advantage of a wide sample area and potentially suitable for bulk average data, is an indirect approach, and suffers from reduced spatial resolution. On the other hand, the EBSD approach using analysis of lattice curvature is a direct approach but may not be representative of the entire specimen. However, there is reason to theorise that while the dislocation density can act as effective trapping sites for hydrogen [164], the regular arrangement of the dislocation network allows for the unencumbered mobility of hydrogen throughout the alloy during the slow-strain rate tensile tests and thus facilitating hydrogen assisted-cracking. This is evident in the EBSD scan of a long crack in the LPBF-AP specimen in Figure 5.21 where the occurrence of transgranular cracks are prevalent as indicated by the black arrows, possibly propagating along the dislocation network as compared to the annealed sample where intergranular cracking is mostly observed.

Morever, a scan on an intergranular crack shows the relatively high misorientation along the dislocation network suggesting a possible path for crack propagation.

Atom probe tomography would have revealed the relatively increased presence of hydrogen in dislocation dense sites in the sample if not for the aforementioned challenges in the sample

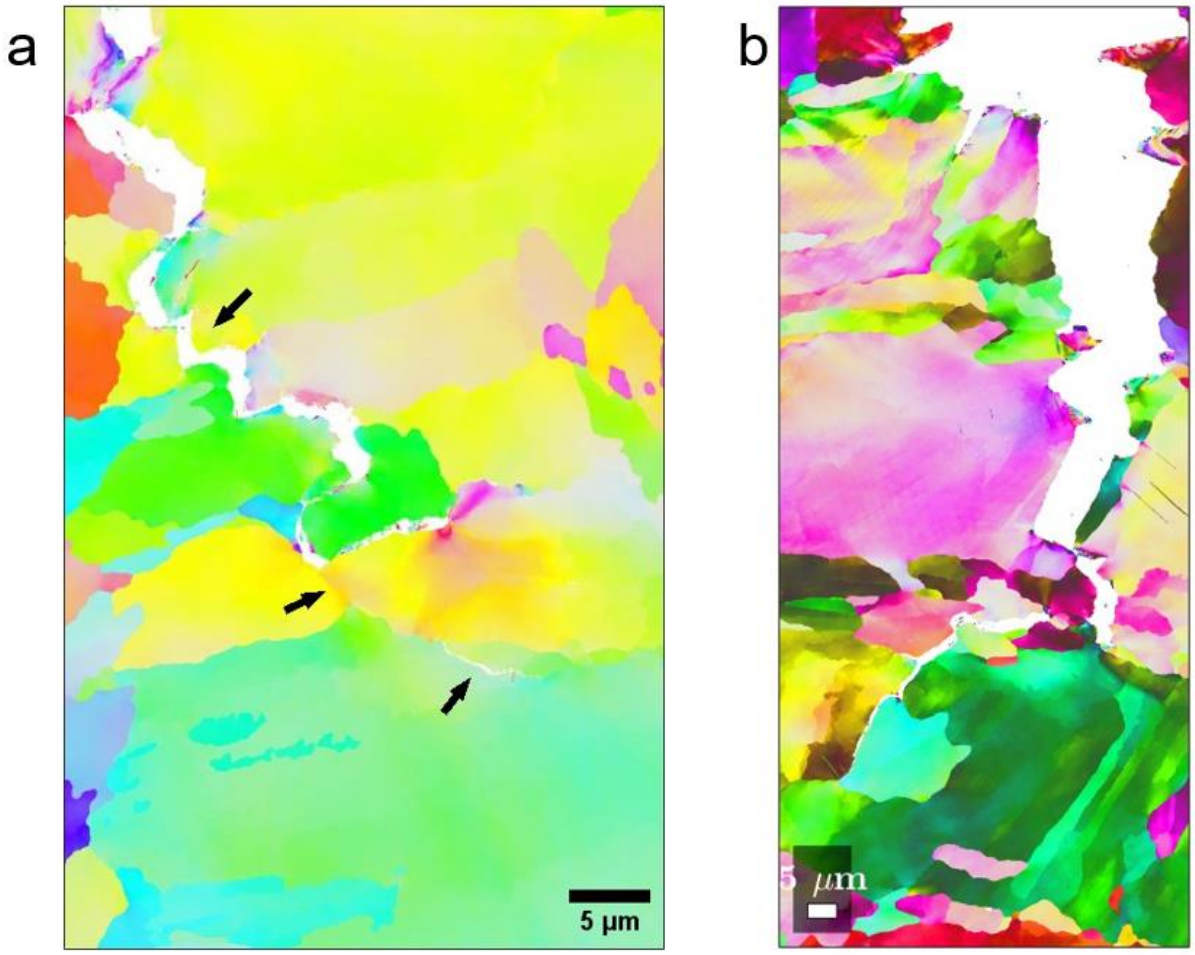


Figure 5.21: EBSD scan of a long crack propagating along the gauge area of the tensile specimen (a) LPBF-AP (b) LPBF-Ann

preparation of APT tips. However, gallium implantation even with platinum protection as performed by Saksena, et.al. [181] together with the vulnerability of austenitic alloys for phase transformation and ionisation induced damage [188] may have created voids and other hydrogen trap sites that are not inherent to the material. Thus it is difficult to relate the mapped hydrogen locations to the actual hydrogen embrittlement behaviour. The relatively short period of time dedicated to the technique did not allow for subsequent investigations to resolve the issues regarding sample preparation. However, the APT results have been insightful in confirming the local concentration changes at the nano-scale for these alloys, which are relevant in the domain of hydrogen-microstructure interactions.

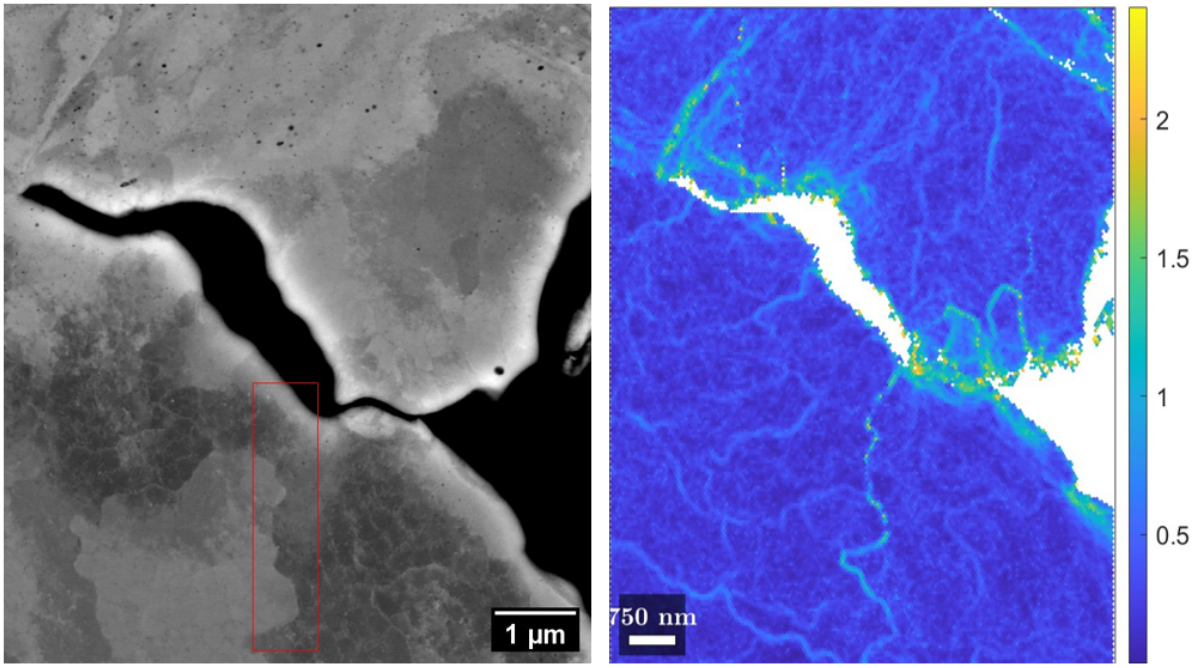


Figure 5.22: ECC image and corresponding Kernel Average Misorientation map of a crack in the LPBF-AP sample showing a possible path for crack propagation following dislocation cells network.

5.4.4 Influence of dislocation cells in hydrogen embrittlement mechanism

It is rational to some extent that hydrogen-assisted IG fracture is attributed to the HEDE mechanism. However, the HEDE mechanism cannot explain plastic features, such as slip bands or tear ridges, etc. on the grain facets in the case of IG-like fracture such as those seen in the LPBF-Ann samples. Therefore, the classification of hydrogen-assisted IG fracture into two groups, i.e. IG and IG-like fractures were recently proposed to distinguish pure brittle IG and plasticity-mediated IG-like fractures. In a study on tempered lath martensitic steel, it was concluded that pure brittle IG fracture appears at locally high hydrogen concentrations while IG-like fracture is characterized by reduced hydrogen concentration [70], [189]. This is consistent with the results for the LPBF-Ann and LPBF-AP samples. The lower amount of hydrogen desorbed in the LPBF-Ann sample compared to the LPBF-Ann sample suggests a higher probability of locally high hydrogen concentration particularly in dense dislocation populated regions following the geometry of the dislocation network. Upon annealing, this dislocation network has disintegrated, reducing possible regions of hydrogen accumulation. The increase in ductility of the LPBF-Ann specimens in conjunction with the plastic features of intergranular-like cracking points to the HELP assisted HEDE mechanism at work, with dislocation density and dislocation

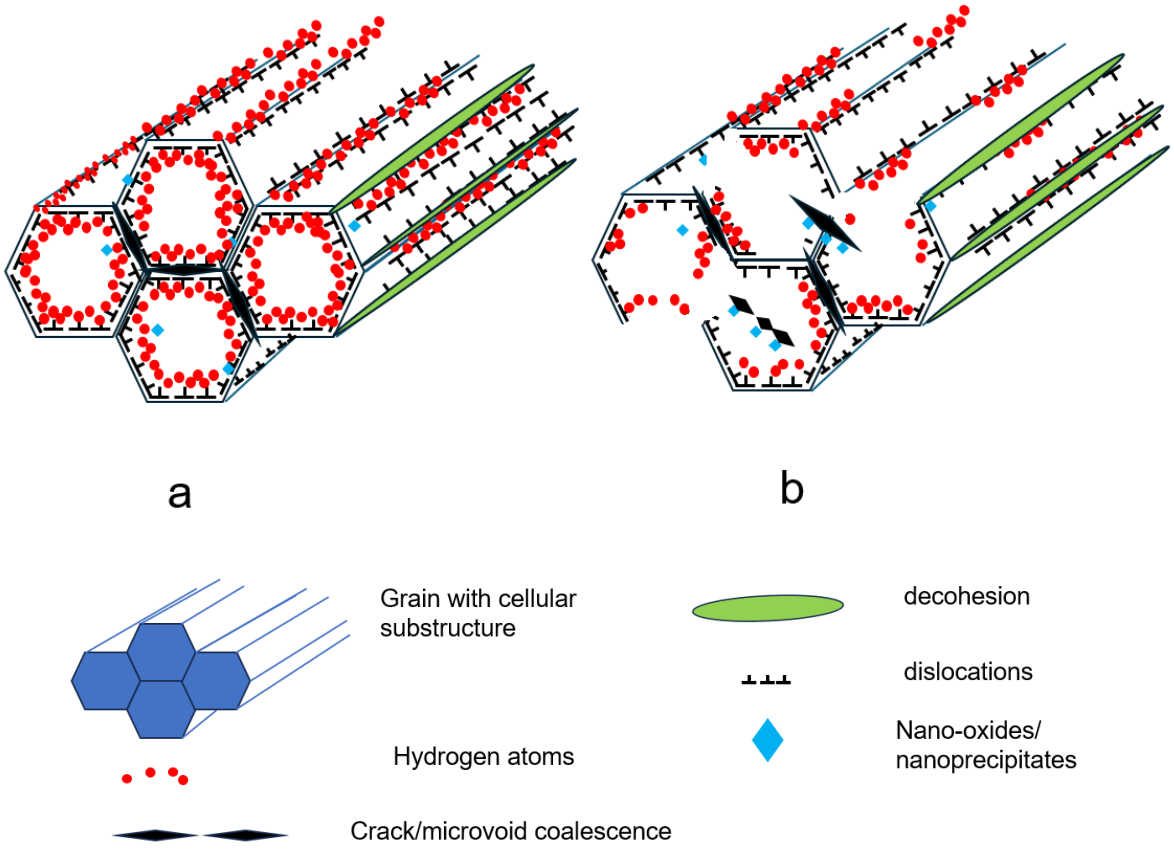
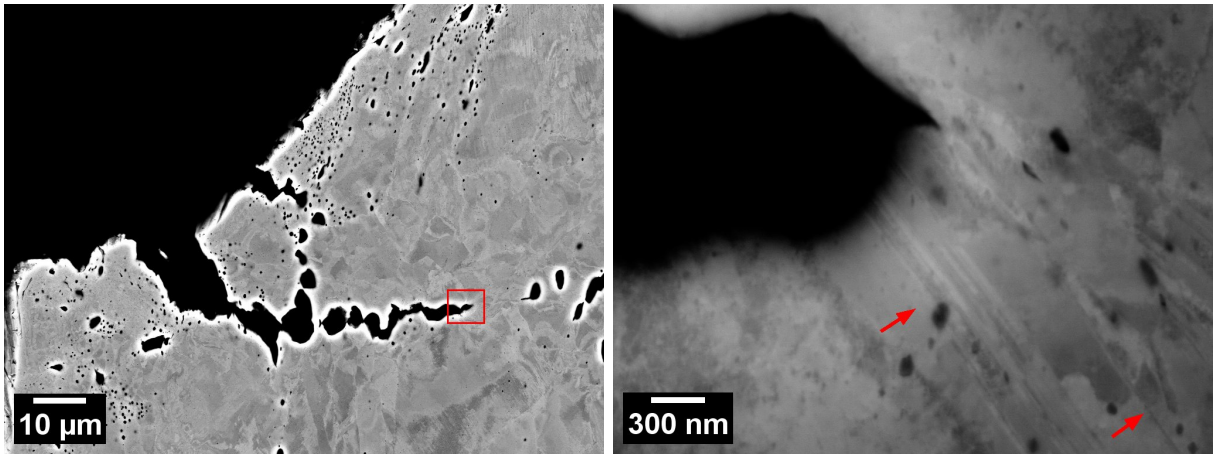


Figure 5.23: Schematic illustration of the hydrogen embrittlement mechanism of (a) LPBF-AP specimen showing dense dislocation network and possible path of hydrogen-assisted cracking along the cellular interdenditic regions and grain boundary decohesion (HEDE) and (b) LPBF-Ann where dislocation density is reduced and dislocation network has disintegrated owing to reduced hydrogen decoration in the cell walls giving rise to possible microvoid coalescence and other plastic features signifying plasticity (HELP) mediated HEDE.

network playing a crucial role as diffusion channels for hydrogen. A schematic illustration of the mechanism highlighting the role of dislocation cells in the crack initiation and propagation in as-printed and annealed specimens is shown in Figure 5.23. In the LPBF-AP samples, grain boundary decohesion leading to IG cracking and quasi-cleavage features both in grain boundaries and interdendritic regions are highly assisted by hydrogen and is mobilised by the interconnected dislocation network allowing for greater mobility along cell boundaries. On the other hand, due to reduced density of dislocation in cell walls, local hydrogen content is lowered, and coupled with the disintegration of the network itself, cracks can form due to microvoid coalescence on fine particles which might explain the appearance of fine dimples and other plastic features in the LPBF-Ann samples.



(a) (b)

Figure 5.24: Deformation nanotwins in proximity to a crack in LPBF-Ann samples.

Moreover, the annealed samples show deformation nanotwins as in Figure 5.24 which also contributes to the plasticity-mediated mechanism. It has been theorised that hydrogen can trigger nanotwinning in the Cantor alloy upon reaching a critical value [70], [160], [190] by reducing the stacking fault energy. Thus it can be suggested that the very high hydrogen concentration in LPBF-AP samples could have been more than the threshold necessary to trigger nanotwinning. The disintegration of the dislocation network allowed for a reduced number of hydrogen traps and combined with the significantly lower diffusion coefficient decreased the hydrogen content in the LPBF-Ann sample enough for hydrogen to exhibit its stacking fault energy lowering effect and thus promote twinning upon deformation.

5.5 Summary

In this chapter I have presented details on the examination of hydrogen embrittlement susceptibility of the additively manufactured CoCrFeMnNi high-entropy alloy in as-printed and annealed microstructural conditions. Several established and novel techniques have been employed to describe hydrogen absorption and diffusion and mechanical properties and relate them to the microstructure. The study highlighted the following:

- Decrease in hydrogen absorption of annealed samples. Simple annealing in air has significantly reduced the hydrogen diffusivity coefficient of the additively manufactured CoCrFeMnNi HEA and together with a decrease in the number of traps due to the disintegration

of the dislocation network and reduction of dislocation density, hydrogen absorption is reduced in the annealed sample. This reduction allowed the hydrogen concentration to be within the window of hydrogen concentration that triggers nano-twinning by lowering the stacking fault energy of the atoms which ultimately leads to the annealed specimen exhibiting superior hydrogen embrittlement resistance compared to the as-printed specimen.

- Application of diffusion models under valid assumptions. The analysis and calculation of hydrogen trapping parameters such as trap density, activation energies and the pre-exponential factor were done with specimens that have been saturated with hydrogen, leading to a valid assumption of local equilibrium between lattice and trap sites. This allows for the application of the Oriani and McNabb and Foster models, in contrast to Kissinger or Choo-Lee approach. Satisfying these conditions justify the use of the *TDS Simulator* app which allows modelling of TDS data and obtaining trapping parameters using only a single sample and removes the need to conduct TDS measurements at several heating rates such as that of the Kissinger approach.

- Suitability of isothermal TDS technique to calculate hydrogen diffusivity. Owing to the low hydrogen diffusivities of FCC alloys, the methodology in isothermal TDS experiments have been demonstrated to be effective in determining the apparent hydrogen diffusivity in the Cantor alloy, both in additively manufactured (as-printed and annealed) and wrought conditions. This is evidenced by the close agreement of the experimentally obtained D_H to that of first-principles calculations.

- The role of dislocation density and dislocation network in the hydrogen embrittlement response of the Cantor HEA. Hydrogen-induced cracking behaves differently in the two specimens. On one hand, the arrangement of a network of cells with walls decorated with dense dislocations allows for greater hydrogen mobility on top of the grain boundary decohesion, allowing for cracks to propagate along dislocation cells. This leads to more brittle trans-granular cracks in addition to brittle intergranular cracks between grain boundaries. On the other hand, the disintegration of the dislocation network and reduced hydrogen concentration allowed for microvoid coalescence in the LPBF-Ann samples, with hydrogen increasing the mobility of dislocations instead of the other way around (dislocations increasing mobility of hydrogen). This dislocation mobility increases plasticity and thus

the annealed samples exhibited a relatively greater ductility compared to the as-printed samples after hydrogen charging. This leads to:

- The difference in HE mechanisms in as-printed and annealed conditions. The dominant mechanism in the LPBF-AP samples is hydrogen enhanced decohesion (HEDE) while a synergistic mechanism of plasticity mediated HEDE is observed in the LPBF-Ann samples.
- The use of gallium FIB and associated workflow can introduce voids into the APT specimen making it difficult to prepare samples with purely inherent defects that act as traps. Also, it was shown that deuterium gas ingress into the additively manufactured samples is difficult and needs to be further investigated.

To conclude, this study ushers in an understanding of the hydrogen embrittlement response of the Cantor high-entropy alloy from a microstructural perspective and demonstrated the application of suitable modelling techniques based on validated assumptions that allow for greater accuracy in determining diffusion and trapping parameters both crucial to the strategies needed to design hydrogen-resistant Cantor alloy manufactured by laser powder bed fusion. Specifically, this study has determined a value of the hydrogen diffusion coefficient that is obtained from samples that have fulfilled the requirements of local equilibrium which is often neglected in previous studies. This value reflects hydrogen behaviour in CoCrFeMnNi more accurately and subsequently, alloy design against hydrogen embrittlement. Moreover,the results of the trapping analysis in this work further adds to the credence of the *TDS Simulator* in modelling based on Oriani and McNabb-Foster's approach, as its use in the CoCrFeMnNi alloy both wrought and additvely manufactured has never been demonstrated before. Finally, the HELP+HEDE mechanism has just recently resurfaced in the hydrogen community as an ubiquitous mechanism for HE. In this work, I have shown a definitive proof of the mechanism in AM CoCrFeMnNi which has never been depicted before.

Chapter 6

Conclusions and outlook

The aim of this thesis is to provide a detailed description of the hydrogen effects on an additively manufactured CoCrFeMnNi high entropy alloy that addresses the issues related to low hydrogen ingress into the sample, lack of trapping and diffusion analysis with validated assumptions, lack of understanding on the role of AM microstructure in hydrogen trapping and embrittlement and lack of identifying the challenges in mapping hydrogen-alloy interaction using atom probe tomography. For this, CoCrFeMnNi HEA was manufactured by laser powder bed fusion and wrought HEA were prepared by vacuum arc melting. To introduce hydrogen into representative specimens, electrochemical hydrogen charging was used and the samples were charged for 7 days at a temperature of 80°C. Slow-strain rate tests were conducted to determine the mechanical properties of uncharged and hydrogen pre-charged tensile specimens. Optical and electron microscopy (SEM, EBSD, ECCI) were utilised to examine the microstructure evolution of the alloy and investigate fracture mechanisms. Thermal desorption spectroscopy and atom probe tomography were used in quantifying and mapping hydrogen content with microstructural characteristics. It was found that by charging "thin" specimens with thickness of less than 0.5 mm with the described hydrogen charging conditions, hydrogen ingress into the sample is optimised, penetrating into the entire thickness. For 1 mm thick samples, fractographic analysis reveals that hydrogen ingress is extensive and to the best of our knowledge, is the maximum among previous literature. With this amount of hydrogen, hydrogen embrittlement is severe and thus, no hydrogen induced ductilisation, where hydrogen charged samples become more ductile than uncharged ones, was observed.

This method of hydrogen charging leads to specimens saturated with hydrogen which is a solid ground in which it can be posited that hydrogen concentration is homogeneous across the "thin" sample validating the simplifying assumptions of significant trap occupancy and local equilibrium between lattice and trapping sites. By virtue of this, the hydrogen trapping parameters such as density of traps and trap binding energy were calculated from TDS analysis using the *TDS Simulator* that correctly applies Oriani's approach for lattice-dominated desorption instead of using the Kissinger's approach. It was found that the alloy, regardless of additively manufactured or wrought, have mostly reversible traps associated with grain boundaries and dislocations and possibly coherent oxides/nanoprecipitates. Moreover, the trap density is highest with the additively manufactured samples, particularly with the as-printed samples, and was reduced after annealing in air at 900°C for 2 hours. The hydrogen diffusivity obtained from isothermal TDS tests are well-aligned with the values previously reported in literature, with as-printed samples having the highest hydrogen diffusivity which is reduced by an order of magnitude by annealing.

With annealing, it was revealed that the dislocation network together with the dislocation density plays a crucial role in the hydrogen embrittlement response. For as-printed AM samples with high dislocation density and intact dislocation network, electrochemical hydrogen exposure led to severe hydrogen embrittlement while annealed AM samples, with disintegrated dislocation network and lower dislocation density, there is a recovery of ductility of almost 30%. The numerous, interconnected dislocation network acted as diffusion channels to increase hdyrogen mobility for hydrogen-assisted cracking. On the other hand, with reduced dislocation density, hydrogen took the opposite role and mobilised the dislocations, leading to hydrogen enhanced plasticity, and since the hydrogen concentration is high enough to trigger decohesion, the resulting mechanism, as supported by fractographic analysis, is a synergistic effect of hydrogen enhanced localised plasticity (HELP)-mediated hydrogen enhanced decohesion (HEDE).

Finally, mapping of hydrogen at certain microstructural features such as grain boundaries and dislocation cells were attempted and it was found that sample preparation (gallium FIB and energetic electrons from Transmission Kikuchi Diffraction) introduced voids into the specimen tip, making it impossible to differentiate between inherent microstructural traps from sample preparation artifacts. Gas charging with deuterium also was not successful for additively man-

ufactured samples which can point to a cause unique to AM alloys such as the presence of an oxide cap on the specimen tip, etc.

In this thesis, it has been demonstrated that substantial changes in the mechanical properties can be achieved solely through modification of the dislocation network. This finding supports the feasibility of preserving the inherent microstructure of additively manufactured (AM) alloys without inducing recrystallisation and grain growth via subsequent high-temperature annealing and extended holding times, even in the absence of a protective atmosphere. Such an approach to microstructural retention and mechanical property tailoring in the AM Cantor alloy has, to the best of my knowledge, not been comprehensively addressed in prior literature.

Moreover, this work presents a hydrogen diffusion coefficient derived from specimens that satisfy the condition of local equilibrium—an essential criterion often neglected in earlier studies. The resulting value offers a more accurate representation of hydrogen transport behaviour in CoCrFeMnNi, with important implications for alloy design strategies aimed at mitigating hydrogen embrittlement.

The trapping analysis conducted herein also reinforces the credibility of the *TDS Simulator*, which is based on the Oriani and McNabb-Foster models. Its successful application to both wrought and additively manufactured forms of the CoCrFeMnNi alloy is demonstrated for the first time.

Finally, while the combined HELP+HEDE mechanism has only recently re-emerged in the literature as a widely applicable explanation for hydrogen embrittlement, this thesis provides the first conclusive evidence of its operation in the AM CoCrFeMnNi system.

With the above, I have successfully addressed our aim mentioned in Chapter 1 Section 1.3, that is, I have provided a detailed description, bound by the study scope and limitations, of the hydrogen diffusion, trapping and embrittlement of an additively manufactured CoCrFeMnNi high entropy alloy. I have also enumerated the novel aspects of this work how the findings in this thesis addressed the gaps in the literature.

The results presented here highlight several research topics that can be investigated in the future such as:

- The influence of surface conditions on hydrogen diffusion which is a major limitation of this study. In relation to this, the influence of surface treatments for additively manufactured samples such as shot-peening that may hinder hydrogen ingress into the sample would be interesting to look at.

- Further use of the *TDS Simulator* and isothermal TDS analysis on other kinds of compositionally complex alloys. The suitability of these approaches in this study begs application to other alloys as well, and will eliminate the difficulty of running multiple TDS experiments for trapping analysis.

- Hydrogen embrittlement behaviour of annealed AM samples at higher temperatures and/or longer holding time to produce fully recrystallised grains in the AM sample. This will complete the picture in relating hydrogen behaviour to microstructure evolution in AM CoCrFeMnNi.

- In-situ hydrogen charging and mechanical testing.

- Influence of in-situ and post heat-treatment nano-oxides and nanoprecipitates as hydrogen traps, including characterisation of their coherency.

- Determination of an appropriate workflow for APT sample preparation to minimise ion and electron beam defects in a highly-alloyed austenitic system like CoCrFeMnNi HEA.

- Influence of HE on fatigue strength. Hydrogen embrittlement can have a profound impact on the fatigue strength of metallic components, often reducing their service life by promoting the initiation and rapid propagation of microcracks under cyclic loading. When hydrogen atoms diffuse into a metal's crystal lattice—whether from electrochemical reactions, high-pressure hydrogen environments, or corrosion processes—they weaken interatomic bonds and facilitate localized plasticity and brittle fracture mechanisms. As a result, materials that might otherwise exhibit robust endurance limits under repeated stress can experience premature fatigue failure at significantly lower stress amplitudes. To date, the impact or synergistic effect of HE on the low-cycle and high-cycle fatigue life of AM CoCrFeMnNi HEAs has not been investigated in detail and with the alloy's prospects as service parts, research in this direction is highly recommended.

- Other post-processing heat treatments. Other than annealing, several post-processing techniques can significantly reduce hydrogen embrittlement (HE) susceptibility in addi-

tively manufactured (AM) alloys by addressing microstructural defects, residual stresses, and surface conditions such as 1) hot isostatic pressing (HIP). HIP Densifies the material by eliminating internal porosity and lack-of-fusion defects. As a result, it reduces hydrogen trapping sites and stress concentrators, improving resistance to hydrogen-assisted cracking. 2) Surface mechanical treatments like shot or ultrasonic peening which can induce compressive residual surface stresses and refine surface grain structure and thus inhibit crack initiation and slows hydrogen diffusion at the surface. 3)laser surface remelting which can refine surface microstructure, closes micro-cracks, and homogenizes chemical composition 4) coatings and surface barriers such as nitriding, aluminizing which can impede hydrogen ingress through physical and chemical barriers.

Bibliography

[1] B. Cantor, "Multicomponent and high entropy alloys," *Entropy*, vol. 16, no. 9, pp. 4749–4768, 2014, ISSN: 10994300. DOI: 10.3390/e16094749.

[2] K. Biswas, J. W. Yeh, P. P. Bhattacharjee, and J. T. M. DeHosson, "High entropy alloys: Key issues under passionate debate," *Scripta Materialia*, vol. 188, pp. 54–58, Nov. 2020, ISSN: 1359-6462. DOI: 10.1016/J.SCRIPTAMAT.2020.07.010.

[3] E. George, W. Curtin, and C. Tasan, "High entropy alloys: A focused review of mechanical properties and deformation mechanisms," *Acta Materialia*, vol. 188, pp. 435–474, Apr. 2020, ISSN: 13596454. DOI: 10.1016/j.actamat.2019.12.015. [Online]. Available: https://linkinghub.elsevier.com/retrieve/pii/S1359645419308444.

[4] B. Cantor, "Multicomponent high-entropy Cantor alloys," *Progress in Materials Science*, no. October, p. 100 754, 2020, ISSN: 00796425. DOI: 10.1016/j.pmatsci.2020.100754. [Online]. Available: https://doi.org/10.1016/j.pmatsci.2020.100754.

[5] B. Gludovatz, A. Hohenwarter, D. Catoor, E. H. Chang, E. P. George, and R. O. Ritchie, "A fracture-resistant high-entropy alloy for cryogenic applications," *Science*, vol. 345, no. 6201, pp. 1153–1158, 2014, ISSN: 10959203. DOI: 10.1126/science.1254581.

[6] Y. Brif, M. Thomas, and I. Todd, "The use of high-entropy alloys in additive manufacturing," *Scripta Materialia*, vol. 99, pp. 93–96, 2015, ISSN: 13596462. DOI: 10.1016/j.scriptamat.2014.11.037. [Online]. Available: http://dx.doi.org/10.1016/j.scriptamat.2014.11.037.

[7] A. Ostovari Moghaddam, N. A. Shaburova, M. N. Samodurova, A. Abdollahzadeh, and E. A. Trofimov, "Additive manufacturing of high entropy alloys: A practical review," *Journal of Materials Science and Technology*, vol. 77, pp. 131–162, 2021, ISSN: 10050302.

DOI: 10.1016/j.jmst.2020.11.029. [Online]. Available: https://doi.org/10.1016/j.jmst.2020.11.029.

[8] P. Wang, P. Huang, F. L. Ng, *et al.*, "Additively manufactured CoCrFeNiMn high-entropy alloy via pre-alloyed powder," *Materials and Design*, vol. 168, p. 107 576, 2019, ISSN: 18734197. DOI: 10.1016/j.matdes.2018.107576. [Online]. Available: https://doi.org/10.1016/j.matdes.2018.107576.

[9] I. Gibson, D. Rosen, and B. Stucker, *Additive Manufacturing Technologies*. New York, NY: Springer New York, 2015, vol. 100, pp. 4–7, ISBN: 978-1-4939-2112-6. DOI: 10.1007/978-1-4939-2113-3. [Online]. Available: https://link.springer.com/10.1007/978-1-4939-2113-3.

[10] K. G. Pradeep, C. C. Tasan, M. J. Yao, Y. Deng, H. Springer, and D. Raabe, "Non-equiatomic high entropy alloys: Approach towards rapid alloy screening and property-oriented design," *Materials Science and Engineering: A*, vol. 648, pp. 183–192, 2015, ISSN: 09215093. DOI: 10.1016/j.msea.2015.09.010. [Online]. Available: http://dx.doi.org/10.1016/j.msea.2015.09.010.

[11] C. Haase, F. Tang, M. B. Wilms, A. Weisheit, and B. Hallstedt, "Combining thermodynamic modeling and 3D printing of elemental powder blends for high-throughput investigation of high-entropy alloys – Towards rapid alloy screening and design," *Materials Science and Engineering A*, vol. 688, no. January, pp. 180–189, 2017, ISSN: 09215093. DOI: 10.1016/j.msea.2017.01.099. [Online]. Available: http://dx.doi.org/10.1016/j.msea.2017.01.099.

[12] R. Li, P. Niu, T. Yuan, P. Cao, C. Chen, and K. Zhou, "Selective laser melting of an equiatomic CoCrFeMnNi high-entropy alloy: Processability, non-equilibrium microstructure and mechanical property," *Journal of Alloys and Compounds*, vol. 746, pp. 125–134, May 2018, ISSN: 09258388. DOI: 10.1016/j.jallcom.2018.02.298.

[13] Z. G. Zhu, Q. B. Nguyen, F. L. Ng, *et al.*, "Hierarchical microstructure and strengthening mechanisms of a CoCrFeNiMn high entropy alloy additively manufactured by selective laser melting," *Scripta Materialia*, vol. 154, pp. 20–24, Sep. 2018, ISSN: 13596462. DOI: 10.1016/j.scriptamat.2018.05.015.

[14] B. Dovgyy, A. Piglione, P. A. Hooper, and M. S. Pham, "Comprehensive assessment of the printability of CoNiCrFeMn in Laser Powder Bed Fusion," *Materials and Design*, vol. 194, p. 108 845, Sep. 2020, ISSN: 18734197. DOI: 10.1016/j.matdes.2020.108845.

[15] A. Piglione, B. Dovgyy, C. Liu, C. M. Gourlay, P. A. Hooper, and M. S. Pham, "Printability and microstructure of the CoCrFeMnNi high-entropy alloy fabricated by laser powder bed fusion," *Materials Letters*, vol. 224, pp. 22–25, 2018, ISSN: 18734979. DOI: 10.1016/j.matlet.2018.04.052. [Online]. Available: https://doi.org/10.1016/j.matlet.2018.04.052.

[16] M.-S. Pham, B. Dovgyy, P. A. Hooper, C. M. Gourlay, and A. Piglione, "The role of side-branching in microstructure development in laser powder-bed fusion," 2020. DOI: 10.1038/s41467-020-14453-3. [Online]. Available: https://doi.org/10.1038/s41467-020-14453-3.

[17] J. Ren, C. Mahajan, L. Liu, D. Follette, W. Chen, and S. Mukherjee, "Corrosion behavior of selectively laser melted CoCrFeMnNi high entropy alloy," *Metals*, vol. 9, no. 10, 2019, ISSN: 20754701. DOI: 10.3390/met9101029.

[18] Q. Xu, H. Q. Guan, Z. H. Zhong, S. S. Huang, and J. J. Zhao, "Irradiation resistance mechanism of the CoCrFeMnNi equiatomic high-entropy alloy," *Scientific Reports 2021 11:1*, vol. 11, no. 1, pp. 1–8, Jan. 2021, ISSN: 2045-2322. DOI: 10.1038/s41598-020-79775-0. [Online]. Available: https://www.nature.com/articles/s41598-020-79775-0.

[19] J. Lee, "Hydrogen embrittlement," *Shreir's Corrosion*, no. April, pp. 902–922, 2010. DOI: 10.1016/B978-044452787-5.00200-6.

[20] D. Rogers, *Fear of Failure: Why bolts on London's Cheesegrater tower began to break*, 2015. [Online]. Available: https://www.globalconstructionreview.com/fear-failure-why-bolts-londons-che8es8e8gr8a8t8er/.

[21] T. Langill, *Lessons Learned from the Bay Bridge Bolt Failure*, 2017. [Online]. Available: https://www.structuremag.org/article/lessons-learned-from-the-bay-bridge-bolt-failure/#:~:text=The%20results%20of%20this%20study%20indicate%20the%20Bay,perfect%20environment%20to%20introduce%20hydrogen%20into%20the%20steel..

[22] Creos, DESFA, Elering, *et al.*, *Extending the European Hydrogen Backbone: A EUROPEAN HYDROGEN INFRASTRUCTURE VISION COVERING 21 COUNTRIES*, 2021. [Online]. Available: https://www.ehb.eu/page/publications.

[23] Y. Zhao, D. H. Lee, M. Y. Seok, *et al.*, "Resistance of CoCrFeMnNi high-entropy alloy to gaseous hydrogen embrittlement," *Scripta Materialia*, vol. 135, no. October, pp. 54–58, 2017, ISSN: 13596462. DOI: 10.1016/j.scriptamat.2017.03.029. [Online]. Available: http://dx.doi.org/10.1016/j.scriptamat.2017.03.029.

[24] Z. Pu, Y. Chen, and L. H. Dai, "Strong resistance to hydrogen embrittlement of high-entropy alloy," *Materials Science and Engineering A*, vol. 736, no. August, pp. 156–166, 2018, ISSN: 09215093. DOI: 10.1016/j.msea.2018.08.101.

[25] K. E. Nygren, K. M. Bertsch, S. Wang, H. Bei, A. Nagao, and I. M. Robertson, "Hydrogen embrittlement in compositionally complex FeNiCoCrMn FCC solid solution alloy," *Current Opinion in Solid State and Materials Science*, vol. 22, no. 1, pp. 1–7, 2018, ISSN: 13590286. DOI: 10.1016/j.cossms.2017.11.002. [Online]. Available: https://doi.org/10.1016/j.cossms.2017.11.002.

[26] M. Nagumo, *Fundamentals of hydrogen embrittlement*. 2016, pp. 1–239, ISBN: 9789811001611. DOI: 10.1007/978-981-10-0161-1.

[27] Y. K. Kim, J. Y. Suh, and K. A. Lee, "Effect of gaseous hydrogen embrittlement on the mechanical properties of additively manufactured CrMnFeCoNi high-entropy alloy strengthened by in-situ formed oxide," *Materials Science and Engineering A*, vol. 796, no. March, p. 140 039, 2020, ISSN: 09215093. DOI: 10.1016/j.msea.2020.140039. [Online]. Available: https://doi.org/10.1016/j.msea.2020.140039.

[28] Z. Fu, B. Yang, K. Gan, *et al.*, "Improving the hydrogen embrittlement resistance of a selective laser melted high-entropy alloy via modifying the cellular structures," *Corrosion Science*, vol. 190, no. July, p. 109 695, 2021, ISSN: 0010938X. DOI: 10.1016/j.corsci.2021.109695. [Online]. Available: https://doi.org/10.1016/j.corsci.2021.109695.

[29] S. C. Marques, A. V. Castilho, and D. S. dos Santos, "Effect of alloying elements on the hydrogen diffusion and trapping in high entropy alloys," *Scripta Materialia*, vol. 201, p. 113 957, 2021, ISSN: 13596462. DOI: 10.1016/j.scriptamat.2021.113957. [Online]. Available: https://doi.org/10.1016/j.scriptamat.2021.113957.

[30] J. S. Belo, S. C. Marques, A. V. Castilho, L. M. de Oliveira, R. A. Simão, and D. S. dos Santos, "Hydrogen diffusivity and interaction with Fe20Mn20Ni20Co20Cr20 and Fe22Mn40Ni30Co6Cr2 high-entropy alloys," *Journal of Alloys and Compounds*, vol. 815, p. 152 314, Jan. 2020, ISSN: 0925-8388. DOI: 10.1016/J.JALLCOM.2019.152314.

[31] L. Claeys, M. B. Rizi, K. Verbeken, and T. Depover, "Hydrogen interaction with FCC CoCrFeMnNi high entropy alloy," in *Procedia Structural Integrity*, vol. 54, Elsevier B.V., 2024, pp. 250–255. DOI: 10.1016/j.prostr.2024.01.080.

[32] H. G. Nelson, J. E. Stein, M. Fieid, and C. .94035, "N A S A T E C H N I C A L N O T E NASA TN 0-7265 m GAS-PHASE HYDROGEN PERMEATION THROUGH ALPHA IRON, 4130 STEEL, AND 304 STAINLESS STEEL FROM LESS THAN looo C TO NEAR 6000 C Ames Reseurch Center," Tech. Rep.

[33] S. Gorsse, C. Hutchinson, M. Gouné, and R. Banerjee, "Additive manufacturing of metals: a brief review of the characteristic microstructures and properties of steels, Ti-6Al-4V and high-entropy alloys," *Science and Technology of Advanced Materials*, vol. 18, no. 1, pp. 584–610, 2017, ISSN: 18785514. DOI: 10.1080/14686996.2017.1361305. [Online]. Available: http://doi.org/10.1080/14686996.2017.1361305.

[34] L. Valdevit, K. Bertoldi, J. Guest, and C. Spadaccini, "ARCHITECTED MATERIALS: SYNTHESIS, CHARACTERIZATION, MODELING, AND OPTIMAL DESIGN," *Journal of Materials Research*, vol. 33, no. 3, pp. 241–246, 2018, ISSN: 20445326. DOI: 10.1557/jmr.2018.18.

[35] S. Franchitti, R. Borrelli, C. Pirozzi, *et al.*, "Investigation on Electron Beam Melting: Dimensional accuracy and process repeatability," *Vacuum*, vol. 157, no. July, pp. 340–348, 2018, ISSN: 0042207X. DOI: 10.1016/j.vacuum.2018.09.007. [Online]. Available: https://doi.org/10.1016/j.vacuum.2018.09.007.

[36] M. Grasso and B. M. Colosimo, "Process defects and in situ monitoring methods in metal powder bed fusion: A review," *Measurement Science and Technology*, vol. 28, no. 4, 2017, ISSN: 13616501. DOI: 10.1088/1361-6501/aa5c4f.

[37] C. Y. Yap, C. K. Chua, Z. L. Dong, *et al.*, "Review of selective laser melting: Materials and applications," *Applied Physics Reviews*, vol. 2, no. 4, 2015, ISSN: 19319401. DOI: 10.1063/1.4935926. [Online]. Available: http://dx.doi.org/10.1063/1.4935926.

[38] S. A. David, J. A. Siefert, and Z. Feng, *Welding and weldability of candidate ferritic alloys for future advanced ultrasupercritical fossil power plants*, Nov. 2013. DOI: 10.1179/1362171813Y.0000000152.

[39] A. Sola and A. Nouri, "Microstructural porosity in additive manufacturing: The formation and detection of pores in metal parts fabricated by powder bed fusion," *Journal of Advanced Manufacturing and Processing*, vol. 1, no. 3, pp. 1–21, 2019, ISSN: 2637-403X. DOI: 10.1002/amp2.10021.

[40] S. A. Khairallah, A. T. Anderson, A. Rubenchik, and W. E. King, "Laser powder-bed fusion additive manufacturing: Physics of complex melt flow and formation mechanisms of pores, spatter, and denudation zones," *Acta Materialia*, vol. 108, pp. 36–45, 2016, ISSN: 13596454. DOI: 10.1016/j.actamat.2016.02.014. [Online]. Available: http://dx.doi.org/10.1016/j.actamat.2016.02.014.

[41] H. E. Sabzi, S. Maeng, X. Liang, M. Simonelli, N. T. Aboulkhair, and P. E. Rivera-Díaz-del-Castillo, "Controlling crack formation and porosity in laser powder bed fusion: Alloy design and process optimisation," *Additive Manufacturing*, vol. 34, no. June, p. 101 360, 2020, ISSN: 22148604. DOI: 10.1016/j.addma.2020.101360. [Online]. Available: https://doi.org/10.1016/j.addma.2020.101360.

[42] J. Robinson and M. Scott, "Liquation cracking during the welding of austenitic stainless steels and nickel alloys," *Philosophical Transactions of the Royal Society of London. Series A, Mathematical and Physical Sciences*, vol. 295, no. 1413, pp. 105–117, 1980, ISSN: 0080-4614. DOI: 10.1098/rsta.1980.0079.

[43] I. Tolosa, F. Garciandía, F. Zubiri, F. Zapirain, and A. Esnaola, "Study of mechanical properties of AISI 316 stainless steel processed by "selective laser melting", following different manufacturing strategies," DOI: 10.1007/s00170-010-2631-5. [Online]. Available: www.lortek.es.

[44] W. R. Wang, W. L. Wang, and J. W. Yeh, "Phases, microstructure and mechanical properties of AlxCoCrFeNi high-entropy alloys at elevated temperatures," *Journal of Alloys and Compounds*, vol. 589, pp. 143–152, 2014, ISSN: 09258388. DOI: 10.1016/j.jallcom.2013.11.084. [Online]. Available: http://dx.doi.org/10.1016/j.jallcom.2013.11.084.

[45] G. Laplanche, O. Horst, F. Otto, G. Eggeler, and E. P. George, "Microstructural evolution of a CoCrFeMnNi high-entropy alloy after swaging and annealing," *Journal of Alloys and Compounds*, vol. 647, pp. 548–557, 2015, ISSN: 09258388. DOI: 10.1016/j.jallcom.2015.05.129. [Online]. Available: http://dx.doi.org/10.1016/j.jallcom.2015.05.129.

[46] N. Eißmann, B. Klöden, T. Weißgärber, and B. Kieback, "High-entropy alloy CoCrFeMnNi produced by powder metallurgy," *Powder Metallurgy*, vol. 60, no. 3, pp. 184–197, 2017, ISSN: 17432901. DOI: 10.1080/00325899.2017.1318480.

[47] M. Jin, A. Piglione, B. Dovgyy, *et al.*, "Cyclic plasticity and fatigue damage of CrMnFeCoNi high entropy alloy fabricated by laser powder-bed fusion," 2020. DOI: 10.1016/j.addma.2020.101584. [Online]. Available: https://doi.org/10.1016/j.addma.2020.101584.

[48] J. Fiocchi, C. A. Biffi, M. Elnemr, J. Shipley, A. Tuissi, and R. Casati, "Hot isostatic pressing and heat treatments of LPBFed CoCuFeMnNiTi0.13 high-entropy alloy: microstructure and mechanical properties," *Journal of Materials Research and Technology*, vol. 26, pp. 9127–9138, 2023, ISSN: 22387854. DOI: 10.1016/j.jmrt.2023.09.223. [Online]. Available: https://doi.org/10.1016/j.jmrt.2023.09.223.

[49] S. Feng, Z. Ai, J. He, B. Yang, G. Gou, and L. Han, "Effect of Annealing and Hot Isostatic Pressing on the Structure and Hydrogen Embrittlement Resistance of Powder-Bed Fusion-Printed CoCrFeNiMn High-Entropy Alloys," *Metals*, vol. 13, no. 3, 2023, ISSN: 20754701. DOI: 10.3390/met13030630.

[50] X. Tan, Z. Wang, H. Chen, *et al.*, "Effects of Heat Treatment on the Microstructure and Mechanical Properties of a Dual-Phase High-Entropy Alloy Fabricated via Laser Beam Power Bed Fusion," *Micromachines*, vol. 15, no. 4, 2024, ISSN: 2072666X. DOI: 10.3390/mi15040471.

[51] C. Zhang, J. Zhu, H. Zheng, H. Li, S. Liu, and G. J. Cheng, "A review on microstructures and properties of high entropy alloys manufactured by selective laser melting," *International Journal of Extreme Manufacturing*, vol. 2, no. 3, 2020, ISSN: 26317990. DOI: 10.1088/2631-7990/ab9ead.

[52] S. Qu, L. Wang, J. Ding, Y. Lu, and X. Song, "Influence of Heat Treatment on the Microstructure and Mechanical Properties of Pure Copper Components Fabricated via

Micro-Laser Powder Bed Fusion," *Materials*, vol. 17, no. 24, 2024, ISSN: 19961944. DOI: 10.3390/ma17246270.

[53] J. M. Torralba and M. Campos, "High entropy alloys manufactured by additive manufacturing," *Metals*, vol. 10, no. 5, pp. 1–15, 2020, ISSN: 20754701. DOI: 10.3390/met10050639.

[54] W. H. Johnson, "On some remarkable changes produced in iron and steel by the action of hydrogen and acids," *Nature*, vol. 11, no. 281, p. 393, 1875, ISSN: 00280836. DOI: 10.1038/011393A0.

[55] I. M. Robertson, P. Sofronis, A. Nagao, *et al.*, "Hydrogen Embrittlement Understood," *Edward DeMille Campbell Memorial Lecture ASM Internatinal*, 2014. DOI: 10.1007/s11663-015-0325-y.

[56] M. Zibrov, "The Influence of Radiation, Mechanical, and Plasma-Induced Damage on Deuterium Retention in Tungsten," Tech. Rep.

[57] J. Venezuela, C. Tapia-Bastidas, Q. Zhou, *et al.*, "Determination of the equivalent hydrogen fugacity during electrochemical charging of 3.5NiCrMoV steel," *Corrosion Science*, vol. 132, pp. 90–106, Mar. 2018, ISSN: 0010938X. DOI: 10.1016/j.corsci.2017.12.018.

[58] A. Lasia and D. Grégoire, "General Model of Electrochemical Hydrogen Absorption into Metals," *Journal of The Electrochemical Society*, vol. 142, no. 10, pp. 3393–3399, Oct. 1995, ISSN: 0013-4651. DOI: 10.1149/1.2050267. [Online]. Available: https://iopscience.iop.org/article/10.1149/1.2050267.

[59] A. Lasia, "Mechanism and kinetics of the hydrogen evolution reaction," *International Journal of Hydrogen Energy*, vol. 44, no. 36, pp. 19 484–19 518, Jul. 2019, ISSN: 03603199. DOI: 10.1016/j.ijhydene.2019.05.183. [Online]. Available: https://doi.org/10.1016/j.ijhydene.2019.05.183%20https://linkinghub.elsevier.com/retrieve/pii/S0360319919320981.

[60] M. Zielinski, "Positive and Negative Aspects of Electrode Reactions of Hydrogen Evolution and the Influence of a Constant Magnetic Field," *Journal of Advanced Chemical Engineering*, vol. 4, no. 2, 2016. DOI: 10.4172/2090-4568.1000106.

[61] M. A. Pick and K. Sonnenberg, "A MODEL FOR ATOMIC
DROGEN-PETAL IN

iON

-APPLICATION TO RECYCLING, RECOMBINATION AND PERMEATION," Tech. Rep., 1985.

[62] S. M. Myers, P. M. Richards, W. R. Wampler, and F. Besenbacher, "ION-BEAM STUDIES OF HYDROGEN-METAL INTERACTIONS," Tech. Rep., 1989, pp. 9–64.

[63] Y. W. You, X. S. Kong, X. B. Wu, *et al.*, "Dissolving, trapping and detrapping mechanisms of hydrogen in bcc and fcc transition metals," *AIP Advances*, vol. 3, no. 1, Jan. 2013, ISSN: 21583226. DOI: 10.1063/1.4789547.

[64] Q. He and Y. Yang, *On lattice distortion in high entropy alloys*, Jul. 2018. DOI: 10.3389/fmats.2018.00042.

[65] J. William D. Callister and D. G. Rethwisch, *Materias Science and Engineering: An Introduction*, 9th. Wiley & Sons, Inc., 2013, ISBN: 9783642209420.

[66] K. Lu, *Stabilizing nanostructures in metals using grain and twin boundary architectures*, Mar. 2016. DOI: 10.1038/natrevmats.2016.19.

[67] J. Crank, *The mathematics of diffusion*, p. 414, ISBN: 0198533446.

[68] M. Nagumo, "Hydrogen Trapping and Its Direct Detection," in *Fundamentals of Hydrogen Embrittlement*, Springer Nature Singapore, 2023, pp. 11–40. DOI: 10.1007/978-981-99-0992-6{_}2.

[69] M. Nagumo, "Diffusion and Transport of Hydrogen," in *Fundamentals of Hydrogen Embrittlement*, Springer Nature Singapore, 2023, pp. 77–93. DOI: 10.1007/978-981-99-0992-6{_}4.

[70] X. Li, J. Zhang, Y. Cui, M. B. Djukic, H. Feng, and Y. Wang, *Review of the hydrogen embrittlement and interactions between hydrogen and microstructural interfaces in metallic alloys: Grain boundary, twin boundary, and nano-precipitate*, Jun. 2024. DOI: 10.1016/j.ijhydene.2024.05.257.

[71] S. Wang, M. L. Martin, P. Sofronis, S. Ohnuki, N. Hashimoto, and I. M. Robertson, "Hydrogen-induced intergranular failure of iron," *Acta Materialia*, vol. 69, pp. 275–282, 2014, ISSN: 13596454. DOI: 10.1016/j.actamat.2014.01.060.

[72] M. L. Martin, B. P. Somerday, R. O. Ritchie, P. Sofronis, and I. M. Robertson, "Hydrogen-induced intergranular failure in nickel revisited," *Acta Materialia*, vol. 60, no. 6-7, pp. 2739–2745, Apr. 2012, ISSN: 13596454. DOI: 10.1016/j.actamat.2012.01.040.

[73] K. Wada, C. Shibata, H. Enoki, T. Iijima, and J. Yamabe, "Hydrogen-induced intergranular cracking of pure nickel under various strain rates and temperatures in gaseous hydrogen environment," *Materials Science and Engineering: A*, vol. 873, May 2023, ISSN: 09215093. DOI: 10.1016/j.msea.2023.145040.

[74] M. Koyama, M. Rohwerder, C. Tasan, *et al.*, "Materials Science and Technology Recent progress in microstructural hydrogen mapping in steels: quantification, kinetic analysis, and multi-scale characterisation," 2017, ISSN: 1743-2847. DOI: 10.1080/02670836.2017.1299276. [Online]. Available: https://www.tandfonline.com/action/journalInformation?journalCode=ymst20.

[75] K. E. Nygren, S. Wang, K. M. Bertsch, H. Bei, A. Nagao, and I. M. Robertson, "Hydrogen embrittlement of the equi-molar FeNiCoCr alloy," *Acta Materialia*, vol. 157, pp. 218–227, Sep. 2018, ISSN: 13596454. DOI: 10.1016/j.actamat.2018.07.032.

[76] M. L. Martin, I. M. Robertson, and P. Sofronis, "Interpreting hydrogen-induced fracture surfaces in terms of deformation processes: A new approach," *Acta Materialia*, vol. 59, no. 9, pp. 3680–3687, 2011, ISSN: 13596454. DOI: 10.1016/j.actamat.2011.03.002. [Online]. Available: http://dx.doi.org/10.1016/j.actamat.2011.03.002.

[77] M. B. Djukic, G. M. Bakic, V. Sijacki Zeravcic, A. Sedmak, and B. Rajicic, *The synergistic action and interplay of hydrogen embrittlement mechanisms in steels and iron: Localized plasticity and decohesion*, Jul. 2019. DOI: 10.1016/j.engfracmech.2019.106528.

[78] S. Lynch, *A review of underlying reasons for intergranular cracking for a variety of failure modes and materials and examples of case histories*, Jun. 2019. DOI: 10.1016/j.engfailanal.2019.02.027.

[79] X. Li, X. Ma, J. Zhang, E. Akiyama, Y. Wang, and X. Song, *Review of Hydrogen Embrittlement in Metals: Hydrogen Diffusion, Hydrogen Characterization, Hydrogen Embrittlement Mechanism and Prevention*, Jun. 2020. DOI: 10.1007/s40195-020-01039-7.

[80] T. Neeraj, R. Srinivasan, and J. Li, "Hydrogen embrittlement of ferritic steels: Observations on deformation microstructure, nanoscale dimples and failure by nanovoiding,"

Acta Materialia, vol. 60, no. 13-14, pp. 5160–5171, Aug. 2012, ISSN: 1359-6454. DOI: 10.1016/J.ACTAMAT.2012.06.014.

[81] R. P. Gangloff, "Critical issues in hydrogen assisted cracking of structural alloys," *Environment-Induced Cracking of Materials*, pp. 141–165, Jan. 2008. DOI: 10.1016/B978-008044635-6.50015-7.

[82] E. Martínez-Pañeda, C. F. Niordson, and R. P. Gangloff, "Strain gradient plasticity-based modeling of hydrogen environment assisted cracking," *Acta Materialia*, vol. 117, pp. 321–332, Sep. 2016, ISSN: 13596454. DOI: 10.1016/J.ACTAMAT.2016.07.022.

[83] Z. D. Harris, E. M. Dubas, A. S. Popernack, B. P. Somerday, and J. T. Burns, "Elucidating the loading rate dependence of hydrogen environment-assisted cracking in a Ni-Cu superalloy," *Theoretical and Applied Fracture Mechanics*, vol. 111, Feb. 2021, ISSN: 01678442. DOI: 10.1016/J.TAFMEC.2020.102846.

[84] K. N. Akhurst and T. J. Baker, "Threshold Stress Intensity for Hydrogen-Induced Crack Growth.," *Metallurgical transactions. A, Physical metallurgy and materials science*, vol. 12 A, no. 6, pp. 1059–1070, 1981, ISSN: 03602133. DOI: 10.1007/BF02643487.

[85] R. P. Gangloff, "H-Enhanced Deformation and Fracture in the Crack Tip Process Zone," in *International Hydrogen Conference (IHC 2016): Materials Performance in Hydrogen Environments*, B. P. Somerday and P. Sofronis, Eds., ASME Press, Oct. 2017, p. 0, ISBN: 9780791861387. DOI: 10.1115/1.861387{_}ch1. [Online]. Available: https://doi.org/10.1115/1.861387_ch1.

[86] E. Martínez-Pañeda, A. Golahmar, and C. F. Niordson, "A phase field formulation for hydrogen assisted cracking," *Computer Methods in Applied Mechanics and Engineering*, vol. 342, pp. 742–761, 2018, ISSN: 00457825. DOI: 10.1016/j.cma.2018.07.021.

[87] H.K.D.H. Bhadeshia, "Prevention of Hydrogen Embrittlement in Steels," *ISIJ International*, vol. 56, no. 1, pp. 24–36, 2016.

[88] R. Fernández-Sousa, C. Betegón, and E. Martínez-Pañeda, "Analysis of the influence of microstructural traps on hydrogen assisted fatigue," *Acta Materialia*, vol. 199, pp. 253–263, Oct. 2020, ISSN: 13596454. DOI: 10.1016/j.actamat.2020.08.030.

[89] N. Boes and H. Züchner, "Electrochemical methods for studying diffusion, permeation and solubility of hydrogen in metals," *Journal of The Less-Common Metals*, vol. 49, no. C, pp. 223–240, 1976, ISSN: 00225088. DOI: 10.1016/0022-5088(76)90037-0.

[90] P. K. Subramanyan, "Electrochemical Aspects of Hydrogen in Metals," in *Electrochemical Materials Science*, 962, vol. STP, Boston, MA: Springer US, Jan. 1981, pp. 411–462. DOI: 10.1007/978-1-4757-4825-3{_}8. [Online]. Available: https://asmedigitalcollection.asme.org/astm-ebooks/book/1604/chapter/27823801/Electrochemical-Aspects-of-Hydrogen-in-Metals%20http://link.springer.com/10.1007/978-1-4757-4825-3_8.

[91] A. McNabb and P. K. Foster, *Institute of Metals Division - A New Analysis of the Diffusion of Hydrogen in Iron and Ferritic Steels*, 1963.

[92] R. Oriani, "The diffusion and trapping of hydrogen in steel," *Acta Metallurgica*, vol. 18, no. 1, pp. 147–157, Jan. 1970, ISSN: 00016160. DOI: 10.1016/0001-6160(70)90078-7. [Online]. Available: https://linkinghub.elsevier.com/retrieve/pii/0001616070900787.

[93] H. E. Kissinger, "Variation of Peak Temperature With Heating Rate In Differential Thermal Analysis," Tech. Rep. 4, 1956.

[94] W. Y. Choo and J. Y. Lee, "Thermal Analysis of Trapped Hydrogen in Pure Iron," Tech. Rep.

[95] N. Abe, H. Suzuki, K. Takai, N. Ishikawa, and H. Sueyoshi, "Identification of hydrogen trapping sites, binding energies, and occupation ratios at vacancies, dislocations and grain boundaries in iron of varying carbon content," vol. 2, pp. 1277–1284, 2011.

[96] R. Hu, S. Jin, and G. Sha, "Application of atom probe tomography in understanding high entropy alloys: 3D local chemical compositions in atomic scale analysis," *Progress in Materials Science*, vol. 123, p. 100 854, Jan. 2022, ISSN: 00796425. DOI: 10.1016/j.pmatsci.2021.100854.

[97] B. Gault, M. P. Moody, J. M. Cairney, and S. P. Ringer, *Atom Probe Microscopy* (Springer Series in Materials Science). New York, NY: Springer New York, 2012, vol. 160, pp. 3–7, ISBN: 978-1-4614-3435-1. DOI: 10.1007/978-1-4614-3436-8. [Online]. Available: https://link.springer.com/10.1007/978-1-4614-3436-8_1%20https://link.springer.com/10.1007/978-1-4614-3436-8.

[98] B. Gault, A. Chiaramonti, O. Cojocaru-Mirédin, *et al.*, *Atom probe tomography*, Dec. 2021. DOI: 10.1038/s43586-021-00047-w.

[99] B. Gault, M. P. Moody, F. De Geuser, *et al.*, "Spatial resolution in atom probe tomography," *Microscopy and Microanalysis*, vol. 16, no. 1, pp. 99–110, Feb. 2010, ISSN: 14319276. DOI: 10.1017/S1431927609991267.

[100] H. Luo, Z. Li, W. Lu, D. Ponge, and D. Raabe, "Hydrogen embrittlement of an interstitial equimolar high-entropy alloy," *Corrosion Science*, vol. 136, no. September 2017, pp. 403–408, 2018, ISSN: 0010938X. DOI: 10.1016/j.corsci.2018.03.040. [Online]. Available: https://doi.org/10.1016/j.corsci.2018.03.040.

[101] X. L. Ren, P. H. Shi, W. W. Zhang, X. Y. Wu, Q. Xu, and Y. X. Wang, "Swamps of hydrogen in equiatomic FeCuCrMnMo alloys: First-principles calculations," *Acta Materialia*, vol. 180, pp. 189–198, 2019, ISSN: 13596454. DOI: 10.1016/j.actamat.2019.09.014.

[102] X. Y. Zhou, J. H. Zhu, Y. Wu, X. S. Yang, T. Lookman, and H. H. Wu, "Machine learning assisted design of FeCoNiCrMn high-entropy alloys with ultra-low hydrogen diffusion coefficients," *Acta Materialia*, vol. 224, Feb. 2022, ISSN: 13596454. DOI: 10.1016/j.actamat.2021.117535.

[103] D. Wan, S. Guan, D. Wang, X. Lu, and J. Ma, "Hydrogen embrittlement of additively manufactured AlCoCrFeNi2.1 eutectic high-entropy alloy," *Corrosion Science*, vol. 195, Feb. 2022, ISSN: 0010938X. DOI: 10.1016/j.corsci.2021.110007.

[104] Y. T. Lin, X. An, Z. Zhu, M. L. S. Nai, C. W. Tsai, and H. W. Yen, "Effect of cell wall on hydrogen response in CoCrFeMnNi high-entropy alloy additively manufactured by selective laser melting," *Journal of Alloys and Compounds*, vol. 925, p. 166 735, 2022, ISSN: 09258388. DOI: 10.1016/j.jallcom.2022.166735. [Online]. Available: https://doi.org/10.1016/j.jallcom.2022.166735.

[105] J. Yi, X. Zhuang, J. He, M. He, W. Liu, and S. Wang, "Effect of Mo doping on the gaseous hydrogen embrittlement of a CoCrNi medium-entropy alloy," *Corrosion Science*, vol. 189, Aug. 2021, ISSN: 0010938X. DOI: 10.1016/j.corsci.2021.109628.

[106] M. Koyama, H. Wang, V. K. Verma, K. Tsuzaki, and E. Akiyama, "Effects of Mn Content and Grain Size on Hydrogen Embrittlement Susceptibility of Face-Centered Cubic High-Entropy Alloys," *Metallurgical and Materials Transactions A: Physical Metallurgy and Materials Science*, vol. 51, no. 11, pp. 5612–5616, Nov. 2020, ISSN: 10735623. DOI: 10.1007/s11661-020-05966-z.

[107] H. Wang, M. Koyama, T. Hojo, and E. Akiyama, "Hydrogen embrittlement and associated surface crack growth in fine-grained equiatomic CoCrFeMnNi high-entropy alloys with different annealing temperatures evaluated by tensile testing under in situ hydrogen charging," *International Journal of Hydrogen Energy*, vol. 46, no. 65, pp. 33 028–33 038, 2021, ISSN: 03603199. DOI: 10.1016/j.ijhydene.2021.07.136. [Online]. Available: https://doi.org/10.1016/j.ijhydene.2021.07.136.

[108] A. Hariharan, L. Lu, J. Risse, *et al.*, "Misorientation-dependent solute enrichment at interfaces and its contribution to defect formation mechanisms during laser additive manufacturing of superalloys," *Physical Review Materials*, vol. 3, no. 12, Dec. 2019, ISSN: 24759953. DOI: 10.1103/PhysRevMaterials.3.123602.

[109] Z. Sun, X. P. Tan, M. Descoins, D. Mangelinck, S. B. Tor, and C. S. Lim, "Revealing hot tearing mechanism for an additively manufactured high-entropy alloy via selective laser melting," *Scripta Materialia*, vol. 168, pp. 129–133, Jul. 2019, ISSN: 13596462. DOI: 10.1016/j.scriptamat.2019.04.036.

[110] D. Karlsson, A. Marshal, F. Johansson, *et al.*, "Elemental segregation in an AlCoCrFeNi high-entropy alloy – A comparison between selective laser melting and induction melting," *Journal of Alloys and Compounds*, vol. 784, pp. 195–203, May 2019, ISSN: 09258388. DOI: 10.1016/j.jallcom.2018.12.267.

[111] Y. S. Chen, P. Y. Liu, R. Niu, *et al.*, *Atom Probe Tomography for the Observation of Hydrogen in Materials: A Review*, Feb. 2023. DOI: 10.1093/micmic/ozac005.

[112] Z. Xu, H. Zhang, W. Li, *et al.*, "Microstructure and nanoindentation creep behavior of CoCrFeMnNi high-entropy alloy fabricated by selective laser melting," *Additive Manufacturing*, vol. 28, pp. 766–771, Aug. 2019, ISSN: 22148604. DOI: 10.1016/j.addma.2019.06.012.

[113] L. P. Dowling, "Development of localised process parameter control for repeatability in metal additive manufacturing," no. February, 2021.

[114] ICDD, "© 2014 International Centre for Diffraction Data. All rights reserved.," *00-050-1439 Cd0.6Zn0.4Te*, no. I, p. 2014, 2014.

[115] ASTM E8, "ASTM E8/E8M standard test methods for tension testing of metallic materials 1," *Annual Book of ASTM Standards 4*, no. C, pp. 1–27, 2010. DOI: 10.1520/E0008.

[116] A. Zafra, Z. Harris, C. Sun, and E. Martínez-Pañeda, "Comparison of hydrogen diffusivities measured by electrochemical permeation and temperature-programmed desorption in cold-rolled pure iron," *Journal of Natural Gas Science and Engineering*, vol. 98, Feb. 2022, ISSN: 18755100. DOI: 10.1016/J.JNGSE.2021.104365.

[117] S. Ogura and K. Fukutani, "Thermal Desorption Spectroscopy," in *Compendium of Surface and Interface Analysis*, Springer Singapore, 2018, pp. 719–724. DOI: 10.1007/978-981-10-6156-1{_}116.

[118] E. A. Marquis, P.-P. Choi, F. Danoix, *et al.*, "New Insights into the Atomic-Scale Structures and Behavior of Steels," *Microscopy Today*, vol. 20, no. 4, pp. 44–48, 2012, ISSN: 1551-9295. DOI: 10.1017/s1551929512000387.

[119] K. Hono, D. Raabe, S. P. Ringer, and D. N. Seidman, "Atom probe tomography of metallic nanostructures," *MRS Bulletin*, vol. 41, no. 1, pp. 23–29, 2016, ISSN: 08837694. DOI: 10.1557/mrs.2015.314.

[120] S. Chen, R. Murakami, K. Araki, and M. Owari, "Quantitative analysis of residual hydrogen on platinum surface by atom probe," *e-Journal of Surface Science and Nanotechnology*, vol. 18, pp. 127–132, 2020, ISSN: 13480391. DOI: 10.1380/EJSSNT.2020.127.

[121] D. Lin, L. Xu, H. Jing, Y. Han, L. Zhao, and F. Minami, "Effects of annealing on the structure and mechanical properties of FeCoCrNi high-entropy alloy fabricated via selective laser melting," *Additive Manufacturing*, vol. 32, no. October 2019, p. 101 058, Mar. 2020, ISSN: 22148604. DOI: 10.1016/j.addma.2020.101058. [Online]. Available: https://doi.org/10.1016/j.addma.2020.101058.

[122] P. C. Collins, D. A. Brice, P. Samimi, I. Ghamarian, and H. L. Fraser, "Microstructural Control of Additively Manufactured Metallic Materials," *Annual Review of Materials Research*, vol. 46, pp. 63–91, 2016, ISSN: 15317331. DOI: 10.1146/annurev-matsci-070115-031816.

[123] R. Y. Chen and W. Y. Yuen, "Review of the high-temperature oxidation of iron and carbon steels in air or oxygen," *Oxidation of Metals*, vol. 59, no. 5-6, pp. 433–468, 2003, ISSN: 0030770X. DOI: 10.1023/A:1023685905159.

[124] Y. K. Kim, J. Choe, and K. A. Lee, "Selective laser melted equiatomic CoCrFeMnNi high-entropy alloy: Microstructure, anisotropic mechanical response, and multiple strengthen-

ing mechanism," *Journal of Alloys and Compounds*, vol. 805, pp. 680–691, Oct. 2019, ISSN: 09258388. DOI: 10.1016/j.jallcom.2019.07.106.

[125] Q. Tang, T. He, K. Yu, *et al.*, "The effect of thickness on texture of Ge2Sb2Te5 phase-change films," *Journal of Materials Science: Materials in Electronics*, vol. 31, no. 8, pp. 5848–5853, 2020, ISSN: 1573482X. DOI: 10.1007/s10854-019-02645-7. [Online]. Available: https://doi.org/10.1007/s10854-019-02645-7.

[126] J. W. Elmer, "ICKL-5-W4 Distribution Oiosiorv LC-704 The Influence of Cooling Rate on the Microstructure of Stainless Steel Alloys," 1988.

[127] J. W. Elmer, S. M. Allen, and T. W. Eagar, "Microstructural development during solidification of stainless steel alloys," *Metallurgical Transactions A*, vol. 20, no. 10, pp. 2117–2131, 1989, ISSN: 03602133. DOI: 10.1007/BF02650298.

[128] W. Pantleon, "Resolving the geometrically necessary dislocation content by conventional electron backscattering diffraction," *Scripta Materialia*, vol. 58, no. 11, pp. 994–997, 2008, ISSN: 13596462. DOI: 10.1016/j.scriptamat.2008.01.050.

[129] G. Bracq, M. Laurent-Brocq, C. Varvenne, *et al.*, "Combining experiments and modeling to explore the solid solution strengthening of high and medium entropy alloys," *Acta Materialia*, vol. 177, pp. 266–279, 2019, ISSN: 13596454. DOI: 10.1016/j.actamat.2019.06.050.

[130] S. Guan, D. Wan, K. Solberg, *et al.*, "Additive manufacturing of fine-grained and dislocation-populated CrMnFeCoNi high entropy alloy by laser engineered net shaping," *Materials Science and Engineering A*, vol. 761, p. 138 056, Jul. 2019, ISSN: 09215093. DOI: 10.1016/j.msea.2019.138056.

[131] M. A. Melia, J. D. Carroll, S. R. Whetten, *et al.*, "Mechanical and Corrosion Properties of Additively Manufactured CoCrFeMnNi High Entropy Alloy," *Additive Manufacturing*, vol. 29, p. 100 833, Oct. 2019, ISSN: 22148604. DOI: 10.1016/j.addma.2019.100833.

[132] A. Gali and E. P. George, "Tensile properties of high- and medium-entropy alloys," *Intermetallics*, vol. 39, pp. 74–78, 2013, ISSN: 09669795. DOI: 10.1016/j.intermet.2013.03.018. [Online]. Available: http://dx.doi.org/10.1016/j.intermet.2013.03.018.

[133] J. Y. He, W. H. Liu, H. Wang, *et al.*, "Effects of Al addition on structural evolution and tensile properties of the FeCoNiCrMn high-entropy alloy system," *Acta Materialia*, vol. 62, no. 1, pp. 105–113, 2014, ISSN: 13596454. DOI: 10.1016/j.actamat.2013.09.037.

[134] P. Maruschak, I. Konovalenko, and A. Sorochak, "Methods for evaluating fracture patterns of polycrystalline materials based on the parameter analysis of ductile separation dimples: A review," *Engineering Failure Analysis*, vol. 153, no. July, p. 107 587, 2023, ISSN: 13506307. DOI: 10.1016/j.engfailanal.2023.107587. [Online]. Available: https://doi.org/10.1016/j.engfailanal.2023.107587.

[135] J. L. González-Velázquez, *Fractography and failure analysis*. 2018, vol. 3, pp. 1–165, ISBN: 9783319766508. DOI: 10.1007/978-3-319-76651-5{_}1.

[136] D. Y. Kovalev, A. S. Rogachev, N. A. Kochetov, and S. G. Vadchenko, "Evolution of the Phase Composition of the Cantor CoCrFeNiMn Alloy during Prolonged Annealing," *Physics of Metals and Metallography*, vol. 123, no. 11, pp. 1161–1170, 2022, ISSN: 15556190. DOI: 10.1134/S0031918X22601299.

[137] A. du Plessis, "Effects of process parameters on porosity in laser powder bed fusion revealed by X-ray tomography," *Additive Manufacturing*, vol. 30, no. September, p. 100 871, 2019, ISSN: 22148604. DOI: 10.1016/j.addma.2019.100871. [Online]. Available: https://doi.org/10.1016/j.addma.2019.100871.

[138] A. Ladewig, G. Schlick, M. Fisser, V. Schulze, and U. Glatzel, "Influence of the shielding gas flow on the removal of process by-products in the selective laser melting process," *Additive Manufacturing*, vol. 10, pp. 1–9, 2016, ISSN: 22148604. DOI: 10.1016/j.addma.2016.01.004. [Online]. Available: http://dx.doi.org/10.1016/j.addma.2016.01.004.

[139] J. Liu and P. Wen, "Metal vaporization and its influence during laser powder bed fusion process," *Materials and Design*, vol. 215, p. 110 505, 2022, ISSN: 18734197. DOI: 10.1016/j.matdes.2022.110505. [Online]. Available: https://doi.org/10.1016/j.matdes.2022.110505.

[140] M. P. Agustianingrum, F. H. Latief, N. Park, and U. Lee, "Thermal oxidation characteristics of Fex(CoCrMnNi)100-x medium and high-entropy alloys," *Intermetallics*, vol. 120, no. March, p. 106 757, 2020, ISSN: 09669795. DOI: 10.1016/j.intermet.2020.106757. [Online]. Available: https://doi.org/10.1016/j.intermet.2020.106757.

[141] J. L. Lee, A. C. Yeh, and H. Murakami, "Oxidation Properties of Additively Manufactured High Entropy Alloys: A Short Review," *High Temperature Corrosion of Materials*,

vol. 101, no. 6, pp. 1369–1379, 2024, ISSN: 27318400. DOI: 10.1007/s11085-024-10313-3. [Online]. Available: https://doi.org/10.1007/s11085-024-10313-3.

[142] D. Monceau and M. Vilasi, "High Temperature Oxidation of Additively Manufactured Structural Alloys," *Jom*, vol. 74, no. 4, pp. 1659–1667, 2022, ISSN: 15431851. DOI: 10.1007/s11837-022-05198-z. [Online]. Available: https://doi.org/10.1007/s11837-022-05198-z.

[143] Z. Tong, H. Liu, J. Jiao, W. Zhou, Y. Yang, and X. Ren, "Laser additive manufacturing of CrMnFeCoNi high entropy alloy: Microstructural evolution, high-temperature oxidation behavior and mechanism," *Optics and Laser Technology*, vol. 130, no. April, p. 106 326, 2020, ISSN: 00303992. DOI: 10.1016/j.optlastec.2020.106326. [Online]. Available: https://doi.org/10.1016/j.optlastec.2020.106326.

[144] Y. Song, S. Nam, Y. Kwon, K. Cho, K. A. Lee, and H. Choi, "Effect of multiple oxides on the mechanical properties of CoCrFeMnNi high-entropy alloy matrix composites," *Powder Metallurgy*, vol. 64, no. 3, pp. 166–172, 2021, ISSN: 17432901. DOI: 10.1080/00325899.2021.1892988. [Online]. Available: https://doi.org/10.1080/00325899.2021.1892988.

[145] H. Hadraba, Z. Chlup, A. Dlouhy, *et al.*, "Oxide dispersion strengthened CoCrFeNiMn high-entropy alloy," *Materials Science and Engineering: A*, vol. 689, no. December 2016, pp. 252–256, 2017, ISSN: 09215093. DOI: 10.1016/j.msea.2017.02.068. [Online]. Available: http://dx.doi.org/10.1016/j.msea.2017.02.068.

[146] J. L. Lee, C. C. Tsai, P. H. Chou, A. C. Yeh, and H. Murakami, "Development of oxidation-resistant L12-strengthened medium to high entropy alloys for additive manufacturing," *Journal of Alloys and Compounds*, vol. 1010, no. October 2024, p. 177 596, 2025, ISSN: 09258388. DOI: 10.1016/j.jallcom.2024.177596. [Online]. Available: https://doi.org/10.1016/j.jallcom.2024.177596.

[147] G. E. Dieter and D. J. Bacon, *Mechanical metallurgy*. McGraw-Hill, 1988, p. 751, ISBN: 007084187X.

[148] A. Sanaty-Zadeh, "Comparison between current models for the strength of particulate-reinforced metal matrix nanocomposites with emphasis on consideration of Hall-Petch effect," *Materials Science and Engineering: A*, vol. 531, pp. 112–118, 2012, ISSN: 09215093.

DOI: 10.1016/j.msea.2011.10.043. [Online]. Available: http://dx.doi.org/10.1016/j.msea.2011.10.043.

[149] F. Humphreys and M. Hatherly, "Chapter 4 THE STRUCTURE AND ENERGY OF GRAIN," *Recrystallization and Related Annealing Phenomena*, pp. 91–119, 2004.

[150] L. P. Evers, W. A. Brekelmans, and M. G. Geers, "Non-local crystal plasticity model with intrinsic SSD and GND effects," *Journal of the Mechanics and Physics of Solids*, vol. 52, no. 10, pp. 2379–2401, 2004, ISSN: 00225096. DOI: 10.1016/j.jmps.2004.03.007.

[151] A. J. Birnbaum, J. C. Steuben, E. J. Barrick, A. P. Iliopoulos, and J. G. Michopoulos, "Intrinsic strain aging, Σ3 boundaries, and origins of cellular substructure in additively manufactured 316L," *Additive Manufacturing*, vol. 29, no. April, p. 100 784, 2019, ISSN: 22148604. DOI: 10.1016/j.addma.2019.100784. [Online]. Available: https://doi.org/10.1016/j.addma.2019.100784.

[152] B. Barkia, P. Aubry, P. Haghi-Ashtiani, *et al.*, "On the origin of the high tensile strength and ductility of additively manufactured 316L stainless steel: Multiscale investigation," *Journal of Materials Science and Technology*, vol. 41, pp. 209–218, 2020, ISSN: 10050302. DOI: 10.1016/j.jmst.2019.09.017.

[153] A. Rukwied, A. W. Ruff, and W. A. Willard, "Study of the cellular solidification structure in a continuously cast high purity copper," *Metallurgical and Materials Transactions B*, vol. 2, no. 8, pp. 2105–2114, 1971, ISSN: 10735615. DOI: 10.1007/BF02917538.

[154] Y. S. J. Yoo, T. A. Book, M. D. Sangid, and J. Kacher, "Identifying strain localization and dislocation processes in fatigued Inconel 718 manufactured from selective laser melting," *Materials Science and Engineering: A*, vol. 724, no. April, pp. 444–451, 2018, ISSN: 09215093. DOI: 10.1016/j.msea.2018.03.127. [Online]. Available: https://doi.org/10.1016/j.msea.2018.03.127.

[155] L. Liu, Q. Ding, Y. Zhong, *et al.*, "Dislocation network in additive manufactured steel breaks strength–ductility trade-off," *Materials Today*, vol. 21, no. 4, pp. 354–361, 2018, ISSN: 18734103. DOI: 10.1016/j.mattod.2017.11.004. [Online]. Available: https://doi.org/10.1016/j.mattod.2017.11.004.

[156] D. A. Ramirez, L. E. Murr, E. Martinez, *et al.*, "Novel precipitate-microstructural architecture developed in the fabrication of solid copper components by additive manufacturing using electron beam melting," *Acta Materialia*, vol. 59, no. 10, pp. 4088–4099,

2011, ISSN: 13596454. DOI: 10.1016/j.actamat.2011.03.033. [Online]. Available: http://dx.doi.org/10.1016/j.actamat.2011.03.033.

[157] Z. Sun, X. Tan, S. B. Tor, and W. Y. Yeong, "Selective laser melting of stainless steel 316L with low porosity and high build rates," *Materials and Design*, vol. 104, pp. 197–204, 2016, ISSN: 18734197. DOI: 10.1016/j.matdes.2016.05.035. [Online]. Available: http://dx.doi.org/10.1016/j.matdes.2016.05.035.

[158] K. M. Bertsch, G. Meric de Bellefon, B. Kuehl, and D. J. Thoma, "Origin of dislocation structures in an additively manufactured austenitic stainless steel 316L," *Acta Materialia*, vol. 199, pp. 19–33, 2020, ISSN: 13596454. DOI: 10.1016/j.actamat.2020.07.063. [Online]. Available: https://doi.org/10.1016/j.actamat.2020.07.063.

[159] H. Luo, Z. Li, and D. Raabe, "Hydrogen enhances strength and ductility of an equiatomic high-entropy alloy," *Scientific Reports*, vol. 7, no. 1, pp. 1–7, 2017, ISSN: 20452322. DOI: 10.1038/s41598-017-10774-4. [Online]. Available: http://dx.doi.org/10.1038/s41598-017-10774-4.

[160] H. Luo, W. Lu, X. Fang, D. Ponge, Z. Li, and D. Raabe, "Beating hydrogen with its own weapon: Nano-twin gradients enhance embrittlement resistance of a high-entropy alloy," *Materials Today*, vol. 21, no. 10, pp. 1003–1009, 2018, ISSN: 18734103. DOI: 10.1016/j.mattod.2018.07.015. [Online]. Available: https://doi.org/10.1016/j.mattod.2018.07.015.

[161] A. Turnbull, *Hydrogen diffusion and trapping in metals*. Woodhead Publishing Limited, 2012, pp. 89–128, ISBN: 9780857095367. DOI: 10.1533/9780857095374.1.89. [Online]. Available: http://dx.doi.org/10.1533/9780857095374.1.89.

[162] E. Garcia-Maicas, Z. Harris, and E. Martinez-Paneda, "TDS Simulator: A MATLAB APP to model temperature-programmed hydrogen desorption,"

[163] *Home — TDS Simulator*. [Online]. Available: https://tdssimulator.web.ox.ac.uk/.

[164] C. Santos Maldonado, A. Zafra, E. M. Pañeda, P. Sandmann, R. Morana, and M.-S. Pham, "Influence of dislocation cells in the hydrogen diffusivity, trapping and embrittlement of wrought and additively manufactured Inconel 718," *Communications Materials*, 2024, ISSN: 2662-4443. DOI: 10.1038/s43246-024-00654-6. [Online]. Available: https://doi.org/10.21203/rs.3.rs-4217438/v1.

[165] D. Pérez Escobar, L. Duprez, A. Atrens, and K. Verbeken, "Influence of experimental parameters on thermal desorption spectroscopy measurements during evaluation of hydrogen trapping," *Journal of Nuclear Materials*, vol. 450, no. 1-3, pp. 32–41, Jul. 2014, ISSN: 0022-3115. DOI: 10.1016/J.JNUCMAT.2013.07.006.

[166] L. T. Stephenson, A. Szczepaniak, I. Mouton, *et al.*, "The Laplace project: an integrated suite for correlative atom probe tomography and electron microscopy under cryogenic and UHV conditions," pp. 1–13, 2018. [Online]. Available: http://arxiv.org/abs/1805.10836.

[167] X. Lu, T. Depover, and R. Johnsen, "Evaluation of hydrogen diffusion and trapping in nickel Alloy 625 by thermal desorption spectroscopy," *International Journal of Hydrogen Energy*, 2022, ISSN: 03603199. DOI: 10.1016/j.ijhydene.2022.07.094.

[168] M. Koyama, K. Ichii, and K. Tsuzaki, "Grain refinement effect on hydrogen embrittlement resistance of an equiatomic CoCrFeMnNi high-entropy alloy," *International Journal of Hydrogen Energy*, vol. 44, no. 31, pp. 17 163–17 167, Jun. 2019, ISSN: 03603199. DOI: 10.1016/j.ijhydene.2019.04.280.

[169] P. Redhead, "Thermal desorption of gases," *Vacuum*, vol. 12, no. 5, p. 274, 1962, ISSN: 0042207X. DOI: 10.1016/0042-207x(62)90543-2.

[170] J. Y. Lee and S. M. Lee, "Hydrogen trapping phenomena in metals with B.C.C. and F.C.C. crystals structures by the desorption thermal analysis technique," *Surface and Coatings Technology*, vol. 28, no. 3-4, pp. 301–314, 1986, ISSN: 02578972. DOI: 10.1016/0257-8972(86)90087-3.

[171] D. H. Lee, B. Sun, S. Lee, D. Ponge, E. A. Jägle, and D. Raabe, "Comparative study of hydrogen embrittlement resistance between additively and conventionally manufactured 304L austenitic stainless steels," *Materials Science and Engineering A*, vol. 803, no. August 2020, 2021, ISSN: 09215093. DOI: 10.1016/j.msea.2020.140499.

[172] A. Raina, V. S. Deshpande, and N. A. Fleck, "Analysis of thermal desorption of hydrogen in metallic alloys," Tech. Rep., 2017.

[173] Y. Yagodzinskyy, O. Todoshchenko, and S. Papula, "Hydrogen solubility and diffusion in austenitic stainless steels studied with thermal desorption spectroscopy," *Steel Research International*, vol. 82, no. 1, pp. 20–25, 2011, ISSN: 16113683. DOI: 10.1002/srin.201000227.

[174] B. Sun, W. Krieger, M. Rohwerder, D. Ponge, and D. Raabe, "Dependence of hydrogen embrittlement mechanisms on microstructure-driven hydrogen distribution in medium Mn steels," *Acta Materialia*, vol. 183, pp. 313–328, 2020, ISSN: 13596454. DOI: 10.1016/j.actamat.2019.11.029. [Online]. Available: https://doi.org/10.1016/j.actamat.2019.11.029.

[175] K. H. So, J. S. Kim, Y. S. Chun, K. T. Park, Y. K. Lee, and C. S. Lee, "Hydrogen delayed fracture properties and internal hydrogen behavior of a Fe-18Mn-1.5AI-0.6C TWIP steel," *ISIJ International*, vol. 49, no. 12, pp. 1952–1959, 2009, ISSN: 09151559. DOI: 10.2355/isijinternational.49.1952.

[176] Y. K. Kim, S. Yang, and K. A. Lee, "Superior Temperature-Dependent Mechanical Properties and Deformation Behavior of Equiatomic CoCrFeMnNi High-Entropy Alloy Additively Manufactured by Selective Laser Melting," *Scientific Reports*, vol. 10, no. 1, pp. 1–13, 2020, ISSN: 20452322. DOI: 10.1038/s41598-020-65073-2. [Online]. Available: http://dx.doi.org/10.1038/s41598-020-65073-2.

[177] Y. S. Chen, H. Lu, J. Liang, *et al.*, "Observation of hydrogen trapping at dislocations, grain boundaries, and precipitates," *Science*, vol. 367, no. 6474, pp. 171–175, 2020, ISSN: 10959203. DOI: 10.1126/science.aaz0122.

[178] Y. S. Chen, D. Haley, S. S. Gerstl, *et al.*, "Direct observation of individual hydrogen atoms at trapping sites in a ferritic steel," *Science*, vol. 355, no. 6330, pp. 1196–1199, 2017, ISSN: 10959203. DOI: 10.1126/science.aal2418.

[179] B. Gault, A. Saksena, X. Sauvage, *et al.*, "Towards establishing best practice in the analysis of hydrogen and deuterium by atom probe tomography," Tech. Rep.

[180] B. Gault, H. Khanchandani, T. S. Prithiv, S. Antonov, and T. B. Britton, "Transmission Kikuchi Diffraction Mapping Induces Structural Damage in Atom Probe Specimens," *Microscopy and Microanalysis*, vol. 29, no. 3, pp. 1026–1036, 2023, ISSN: 14358115. DOI: 10.1093/micmic/ozad029.

[181] A. Saksena, B. Sun, X. Dong, H. Khanchandani, D. Ponge, and B. Gault, "Optimizing site-specific specimen preparation for atom probe tomography by using hydrogen for visualizing radiation-induced damage," *International Journal of Hydrogen Energy*, vol. 50, pp. 165–174, 2024, ISSN: 03603199. DOI: 10.1016/j.ijhydene.2023.09.057. [Online]. Available: https://doi.org/10.1016/j.ijhydene.2023.09.057.

[182] R. Kirchheim, "Revisiting hydrogen embrittlement models and hydrogen-induced homogeneous nucleation of dislocations," *Scripta Materialia*, vol. 62, no. 2, pp. 67–70, 2010, ISSN: 13596462. DOI: 10.1016/j.scriptamat.2009.09.037. [Online]. Available: http://dx.doi.org/10.1016/j.scriptamat.2009.09.037.

[183] R. Nazarov, T. Hickel, and J. Neugebauer, "First-principles study of the thermodynamics of hydrogen-vacancy interaction in fcc iron," *Physical Review B - Condensed Matter and Materials Physics*, vol. 82, no. 22, pp. 1–11, 2010, ISSN: 10980121. DOI: 10.1103/PhysRevB.82.224104.

[184] O. Todoshchenko, Y. Yagodzinskyy, and H. Hänninen, "Thermal desorption of hydrogen from AISI 316L stainless steel and pure nickel," *Defect and Diffusion Forum*, vol. 344, pp. 71–77, Sep. 2013, ISSN: 16629507. DOI: 10.4028/www.scientific.net/DDF.344.71.

[185] X. Yang, Y. Yagodzinskyy, Y. Ge, *et al.*, "Hydrogen effects in equiatomic crfenimn alloy fabricated by laser powder bed fusion," *Metals*, vol. 11, no. 6, 2021, ISSN: 20754701. DOI: 10.3390/met11060872.

[186] D. Pérez Escobar, K. Verbeken, L. Duprez, and M. Verhaege, "Evaluation of hydrogen trapping in high strength steels by thermal desorption spectroscopy," *Materials Science and Engineering: A*, vol. 551, pp. 50–58, Aug. 2012, ISSN: 09215093. DOI: 10.1016/j.msea.2012.04.078.

[187] A. Zafra, L. B. Peral, J. Belzunce, and C. Rodríguez, "Effect of hydrogen on the tensile properties of 42CrMo4 steel quenched and tempered at different temperatures," *International Journal of Hydrogen Energy*, vol. 43, no. 18, pp. 9068–9082, May 2018, ISSN: 03603199. DOI: 10.1016/J.IJHYDENE.2018.03.158.

[188] R. P. Babu, S. Irukuvarghula, A. Harte, and M. Preuss, "Nature of gallium focused ion beam induced phase transformation in 316L austenitic stainless steel," *Acta Materialia*, vol. 120, pp. 391–402, 2016, ISSN: 13596454. DOI: 10.1016/j.actamat.2016.08.008. [Online]. Available: http://dx.doi.org/10.1016/j.actamat.2016.08.008.

[189] K. Ogawa, Y. Matsumoto, H. Suzuki, and K. Takai, "Hydrogen embrittlement susceptibility evaluation of tempered martensitic steels showing different fracture surface morphologies," *ISIJ International*, vol. 59, no. 9, pp. 1705–1714, 2019, ISSN: 09151559. DOI: 10.2355/isijinternational.ISIJINT-2019-130.

[190] S. Yan, Q. H. Qin, Z. Zhong -, *et al.*, "International Journal of Extreme Manufacturing TOPICAL REVIEW • OPEN ACCESS A review on microstructures and properties of high entropy alloys manufactured by selective laser melting You may also like On the real-time atomistic deformation of nano twinned," *IMMT International Journal of Extreme Manufacturing Int. J. Extrem. Manuf*, vol. 2, p. 21, 2020. DOI: 10.1088/2631-7990/ab9ead. [Online]. Available: https://doi.org/10.1088/2631-7990/ab9ead.

[191] G. Ribárik, Z. Horváth, and J. Lendvai, "Modeling of diffraction patterns based on microstructural properties," Tech. Rep.

Appendices

Appendix A

Design of Experiment

The design of experiment followed for the optimisation of the printing parameters was the Box-Wilson Central Composite Design (CCD). A schematic representation of the CCD is shown below

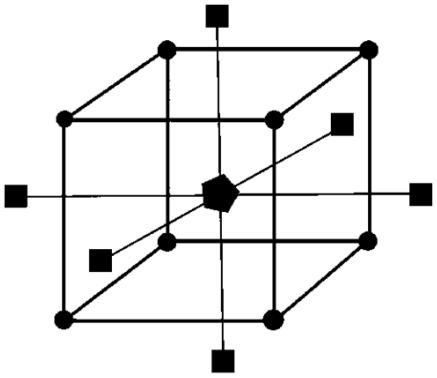


Figure A.1: A schematic representation of central composite design for a system with 3 parameters consisting of a centre point (pentagon), star(axial) points (squares), and fractional points(circles).

Table A.1: Parameters of the CCD design of experiment

Print Parameter Levels		
	lower	upper
laser power	180 W	200 W
hatch spacing	40μm	110μm
scan speed	800 mm/s	2500 mm/s
scan strategy	Normal, bi-directional, 67° rotation between layers	

The lower and upper values of the parameters in the above table were chosen according to the following: Laser power upper value and the scan strategy corresponds to the optimum laser power and scan strategy used in Reference [14], [15]. From the same references, the minimum

value is chosen as 60% of the maximum laser power of the ProX® 200 DMP to minimise lack of fusion defects. The hatch spacing upper value corresponds to the optimised hatch spacing value in the aforementioned reference and the lower value is the default lower value in the ProX® 200 DMP used by Reference [113]. For scan speed, the values are chosen based on the minimum and maximum scan speed values of the printer as in Reference [113]. In order to maximise information collected, the scanning strategies of some of the builds with identical parameters were modified into NormBi0, NormBi90, NormBi67, Concentric and Hexagons (Norm- Normal, Bi- bidirectional, 0,90 and 67- next layer angles). Based on an α of 1.68179 of the central composite design output from Minitab®, the table below summarizes the parameters of the different runs and their corresponding densities based on the Archimedes' principle.

Table A.2: Experimental design parameters and densities of the builds.

Sample ID	Scan Strategy	Laser Power	Hatch Spacing (μm)	Scan Speed (mm/s)	Layer thickness (μm)	VED (J/mm3)	ρ, Trial 1	ρ, Trial 2	ρ, Trial 3	ρ, Ave	Rel density, %
11	NormBi67	173.182	80	1100	30	65.60	7.8893	7.8895	7.8895	7.8894	98.00
12	NormBi67	190	80	1100	30	71.97	7.9384	7.9410	7.9410	7.9401	98.63
13	NormBi67	190	80	1605	30	49.34	7.5254	7.5115	7.5443	7.5271	93.50
14	NormBi67	206.818	80	1100	30	78.34	7.9809	7.9637	7.9637	7.9694	99.00
15	Hexagons	190	80	1100	30	71.97	7.9352	7.9559	7.9735	7.9549	98.82
21	NormBi0	190	80	1100	30	71.97	7.9264	7.9463	7.9463	7.9397	98.63
22	NormBi67	129	50	1400	30	61.43	7.6791	7.6818	7.6990	7.6866	95.49
23	NormBi90	190	80	1100	30	71.97	7.9513	7.9147	7.9318	7.9326	98.54
24	NormBi67	200	50	800	30	166.67	7.9710	7.9737	7.9371	7.9606	98.89
25	NormBi67	180	110	800	30	68.18	7.8356	7.8382	7.8358	7.8365	97.35
31	Concentric	190	80	1100	30	71.97	7.7478	7.7142	7.7310	7.7310	96.04
32	NormBi67	180	50	1400	30	85.71	7.9935	7.9760	7.9735	7.9810	99.14
33	NormBi67	200	110	1400	30	43.29	7.4076	7.2841	7.2950	7.3289	91.04
34	NormBi67	200	110	800	30	75.76	7.6031	7.6033	7.6033	7.6032	94.45
35	NormBi67	180	50	800	30	150.00	7.9810	7.9641	7.9641	7.9697	99.00
41	NormBi67	180	110	1400	30	38.96	7.3187	7.0628	7.0269	7.1361	88.65
42	NormBi67	200	50	1400	30	95.24	7.9861	7.9861	7.9861	7.9861	99.22
43	NormBi67	190	130	1100	30	44.13	7.3640	7.1841	7.1971	7.2484	90.04
44	NormBi67	190	40	2500	30	63.33	7.7199	7.6624	7.6624	7.6816	95.42
45	NormBi67	200	50	2000	30	66.67	7.8567	7.8742	7.8742	7.8684	97.74

Figure A.2 shows how the specimens were arranged on the build plate.

For reference, the Archimedes' principle states that a body immersed in a fluid experiences an upward buoyant force equal to the weight of the fluid it displaces. This principle underpins the hydrostatic weighing method commonly used to determine the relative density of solid materials wherein the weight of the sample is measured in air using a precision balance (W_{air}) and then the sample is suspended and weighed while fully submerged in a fluid of known density (distilled water with surfactant to prevent bubbles and improve wetting), yielding an apparent reduced

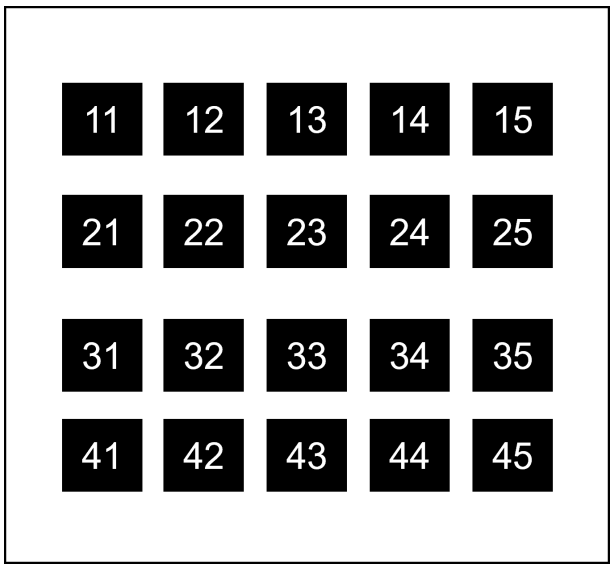


Figure A.2: Arrangement of specimens on the build plate

weight due to buoyancy (W_{fluid}). Using these values the relative density of the specimen is calculated as:

$$\rho_{\text{rel}} = \frac{W_{\text{air}}}{\frac{W_{\text{air}} - W_{\text{fluid}}}{\rho_{\text{theoretical}}}} \tag{A.1}$$

The theoretical density is taken to be 8.05 g/cm^3 as per Reference [114].

Appendix B

Indexing of XRD Data and Multiple Whole Profile Method

The Multiple Whole Profile Method is based on the method proposed by Ribarik [191]. It involves fitting the XRD spectra into either a Gauss + Levenberg-Marquadt or a Lorentz distribution. The area of the normalised intensity curve is β. From this, one can calculate the interplanar spacing, d as:

$$d = 1/\beta \tag{B.1}$$

and then,

$$\rho = \frac{2}{\pi(b_{burgers}d)^2} \tag{B.2}$$

where $b_{burgers}$ is the magnitude of the Burger's vector. For an FCC crystal, the magnitude of b is $a/\sqrt{2}$ for $< 110 >$ Miller index and a for $< 200 >$ where a is the lattice parameter. For CoCrFeMnNi HEA:

$$a = 3.589\,\text{Å} \tag{B.3}$$

The calculation of ρ then follows from a Lorentz fit of the peak $< 200 >$ using Origin. For indexing calculations: Click here

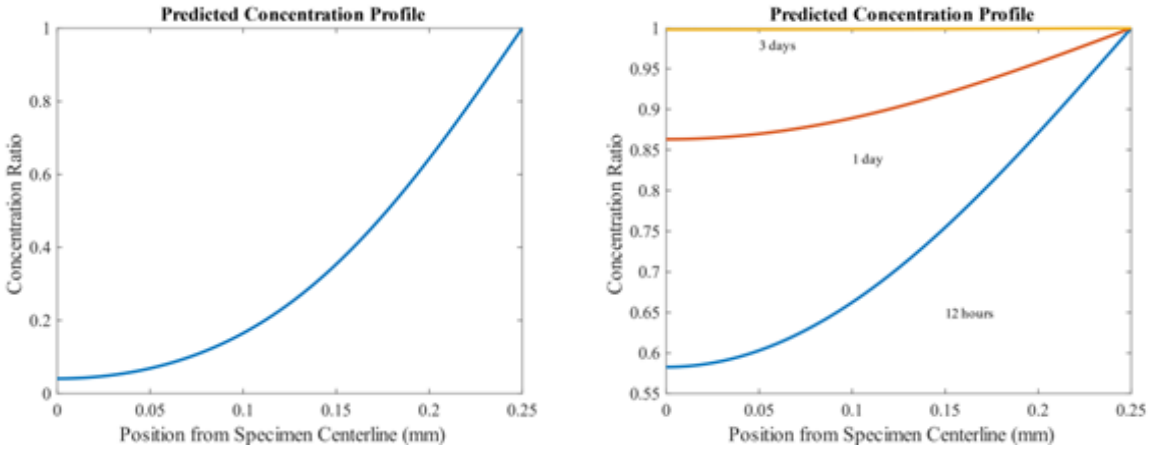
Appendix C

Initial TDS experimental run

Refer to Table 5.1 for the charging conditions used in this initial study.

It can be seen from Figure C.1 that there will be a non-homogeneous H-concentration after charging for 7 days due to the steep concentration gradient from the surface to the center. Since the calculations were based on a fully dense alloy, it is worth taking into consideration that the real concentration profile would show higher hydrogen concentration because AM alloys contain more defects in the form of porosity, voids, vacancies, etc. Preliminary desorption tests from the LPBF-AP specimens revealed a calculated H-diffusivity of $6.54 \times 10^{-13}\ m^2 s^{-1}$ which is two orders of magnitude higher than the one used for prediction calculations. This supports the idea that the defects in AM alloys encourage faster H diffusion. Most importantly, one can see from the real concentration profile that the samples seem to be completely saturated after charging for 3 days or longer.

Figure C.2 shows the stress-strain curves of 0.5 mm thick flat dogbone shaped tensile samples. The tests were done thrice for both uncharged and hydrogen pre-charged specimens. The most striking observation is the complete loss of ductility for the pre-charged samples, which indicate severe embrittlement. Another guiding observation is the variability in the elongation of the three ucnharged replicates. This can be attributed to the presence of stochastic defects in the AM samples which have more proounced effects on the mechanical properties when the thickness is small. Increasing the thickness in the subsequent mechanical testing has significantly reduced the variability in the elongation. Moreover, annealing at 900°C has decreased the yield strength and increased the elongation of the samples as expected.

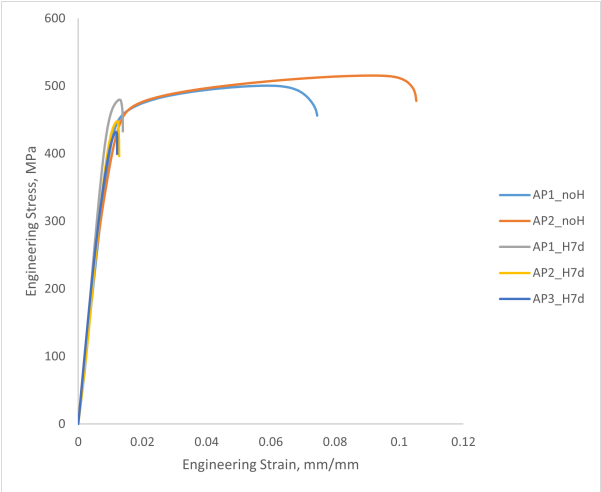


(a) (b)

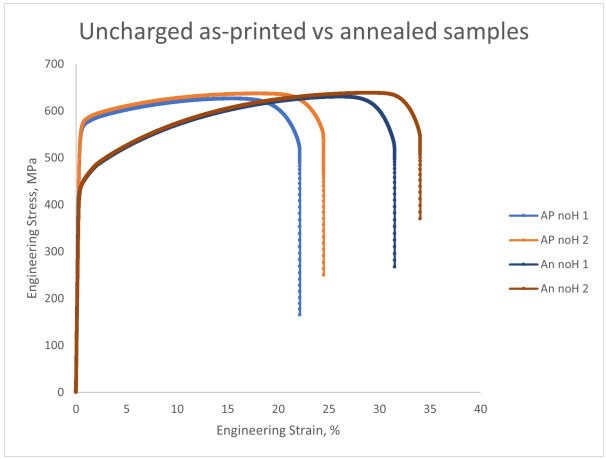
Figure C.1: (a) Predicted concentration profile for $D_H = 9.6 \times 10^{-15}\ m^2/s$ for 7 days vs (b) predicted concentration profiles for $D_H = 6.54 \times 10^{-13} m^2/s$ for different charging times.

Examination of the fracture surface of hydrogen pre-charged 0.5 mm thick samples reveal a brittle fracture throughout the thickness of the sample as shown in Figure C.3 and C.4. The hydrogen desorption curve and the total hydrogen content for these 0.5 mm-thick samples are shown in Figure and Table respectively. The TDS test was done at a heating rate of 22°C /min. One of the samples was subjected to an isothermal TDS test at 80°C and then to a desorption (post-isothermal) test up to 1000°C immediately after. This allows for the calculation of the diffusible C_{diff} and trapped $C_{trapped}$ H concentration.

The hydrogen desorption curves and the total hydrogen content for these 0.5 mm-thick samples are shown in Figure C.5 and Table C.1, respectively. The TDS test was done at 25°C/min. One of the samples was subjected to an isothermal TDS test at 80°C and then to a desorption test up to 1000°C immediately after. This allows for the calculation of the diffusible (C_{diff}) and trapped hydrogen ($C_{trapped}$).

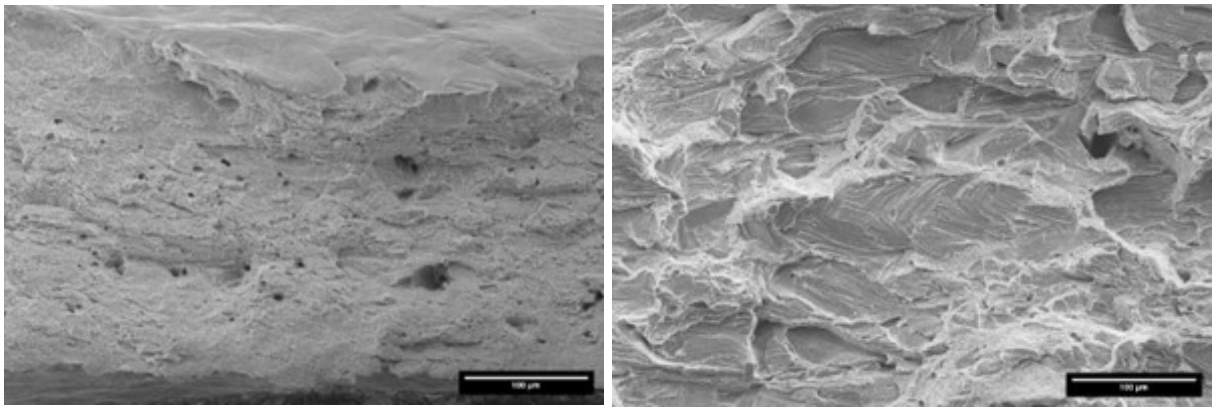


(a)



(b)

Figure C.2: (a) Engineering stress-strain curves for uncharged and pre-charged 0.5 mm thick samples (b) tensile curves for uncharged LPBF-AP and LPBF-Ann with thickness of 1 mm.



(a) (b)

Figure C.3: Fracture surface of (a) uncharged, (b) hydrogen pre-charged tensile samples.

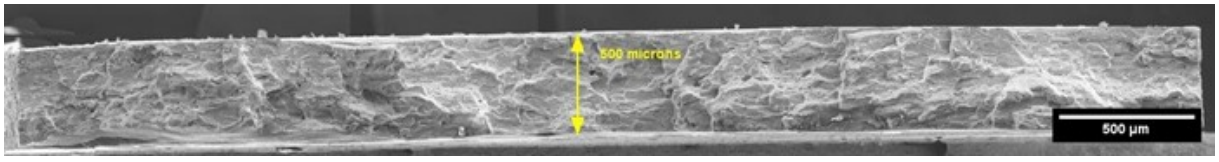


Figure C.4: The entire length and width of the gauge area showing brittle fracture.

Table C.1: Desorbed hydrogen concentration from TDS experiments.

Sample: LPBF-AP			
	C_{diff} (wppm)	$C_{trapped}$ (wppm)	C_{total} (wpmm)
HEA-1	61.9	41.4	103.18
HEA-2			72.59
HEA-3			83.06
Average			86.27 ± 15.55

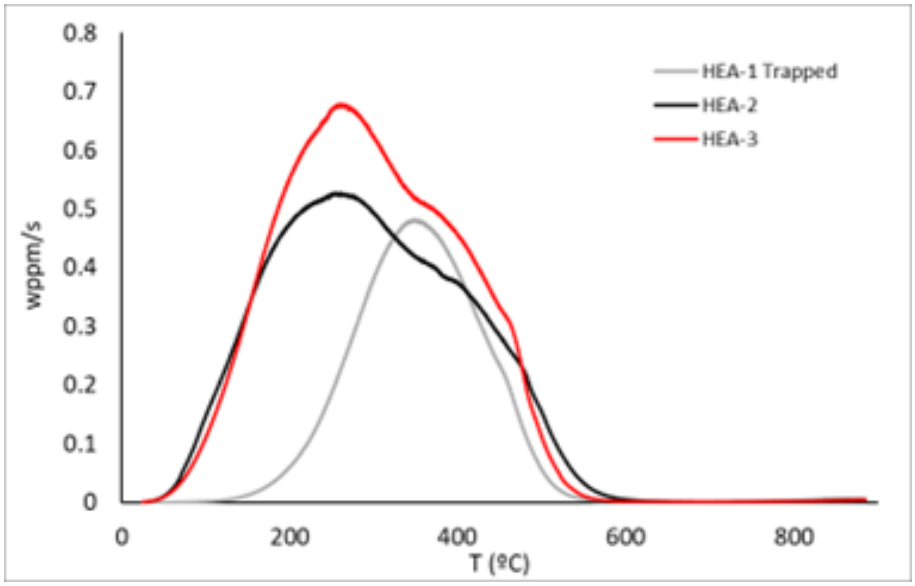


Figure C.5: TDS desorption spectra of the three 0.5 mm thick LPBF-AP HEA samples.

Appendix D

ITDS Fitting

For the determination of the hydrogen diffusivity coefficient for the three microstructural conditions namely LPBF-AP, LPBF-Ann and HEA-W, a total of 11 samples were hydrogen charged and tested, one for every isothermal temperature 22°C, 100°C, 200°C and 300°C at every condition, except 100°C for LPBF-Ann. This exclusion was not deliberate but is justified by the values of the diffusivity at other temperatures for LPBF-Ann which were found to be consistent as exemplified by the strong linear trend of the other three tested temperatures.

The procedure for isothermal TDS fitting involves:

- Data Filtering. The SmoothData and experimental data Matlab® codes using the raw data were used. An example using LPBF-AP specimen isothermal TDS data at 22°C i shown in Figure D.1.
- Subtract the background from the filtered raw hydrogen counts and proceed to calculate the hydrogen concentration in wppm/s using the *TDSisothermal* program. Real time is calculated by adding the rest time to the elapsed time. The hydrogen concentration is converted to $mol\ H/m^3s$ by multiplying by the density of 8.05 g/cm^3 and dividing by 1.01.
- Proceed to fitting using COMSOL®.

The fitted curves obtained from the above representative procedure were re-plotted in Origin®. Results for 22°C and 200°C were shown as examples in Figure D.4 in Chapter 5 and the following figures in Figure D.2 are for 100°C and 300°C. The goodness-of-fit as measured by the coefficient of determination, R^2 is given in Table D.1 which also includes the values for the

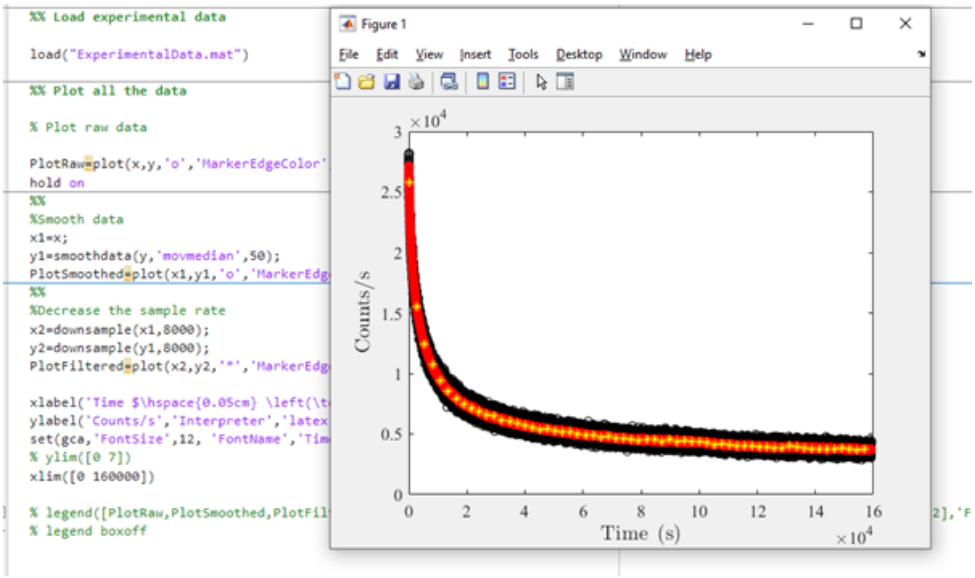


Figure D.1: Filtered Data in Matlab®

Temperature (°C)	AP	Ann	W
22	0.99412	0.99102	0.98808
100	0.972	not tested	0.99136
200	0.98783	0.98487	0.97725
300	0.97635	0.98283	0.51048

Table D.1: The R^2 values for all the diffusivity fittings.

graphs found in the main text. Notice that most values suggest a relatively good fit except for the wrought sample at 300°C. In reality, fittings at very high temperatures tend to be more erratic as the sample is exposed to a massive temperature difference when introduced into the heating chamber.

```
clear all
close all
clc
%%
format long g %more decimal values

load('expValues','tEXP','yEXP');
%%
scFac = 1; % scaling factor for yEXP - change manually in function
time = tEXP';
yEXP = scFac*yEXP;
%Define initial D values for iterating
D0 = 5; %*e-16 [m^2/s]

Du0 = D0;

%Define lower and upper bounds as iteration limits for D
lb = 0.01;
ub = 100;

% Fitting algorithm
options = optimoptions('lsqcurvefit','Algorithm','levenberg-marquardt'...
,'FunctionTolerance',1e-15,'Display','iter-detailed','OptimalityTolerance',1e-15...
,'StepTolerance', 1e-20,'FiniteDifferenceType','central','FiniteDifferenceStepSize',1e-1);

[Du,resnorm2,residual2,exitflag2,output2] = lsqcurvefit(@funCOMSOL,Du0,time,yEXP,lb,ub,options);
%%
% Plot experimental and fitted curve
tPlot = 0:100:200000;
yPlot=funCOMSOL(Du,tPlot);
yfit = funCOMSOL(Du,tEXP);
figure
plot(tEXP,yEXP,'b*')
hold on
plot(tPlot,yPlot,'r','linewidth',2)
xlim([0 140000])
ylim([0 0.05])
grid on

%% R2 of the fit

meanyEXP = sum(yEXP,'all')/size(yEXP,1); % mean of experimental data
SSres = sum((yEXP - yfit).^2); % the sum of squares of residuals
SStot = sum((yEXP - meanyEXP).^2); % the total sum of squares

Rsquared = 1 - SSres/SStot; % R^2
```

(a)

```
          252.344131792527
    11          54                                          5.83534e-19

Optimization stopped because the relative norm of the current step, 2.312455e-21,
is less than options.StepTolerance = 1.000000e-20.

ans =
          252.344131792527
ans =
          252.344131792527
R2 =
                   0.99412
>>
```

(b)

Figure D.2: Matlab® interface showing the (a) main code and (b) output of the COMSOL® fitting.

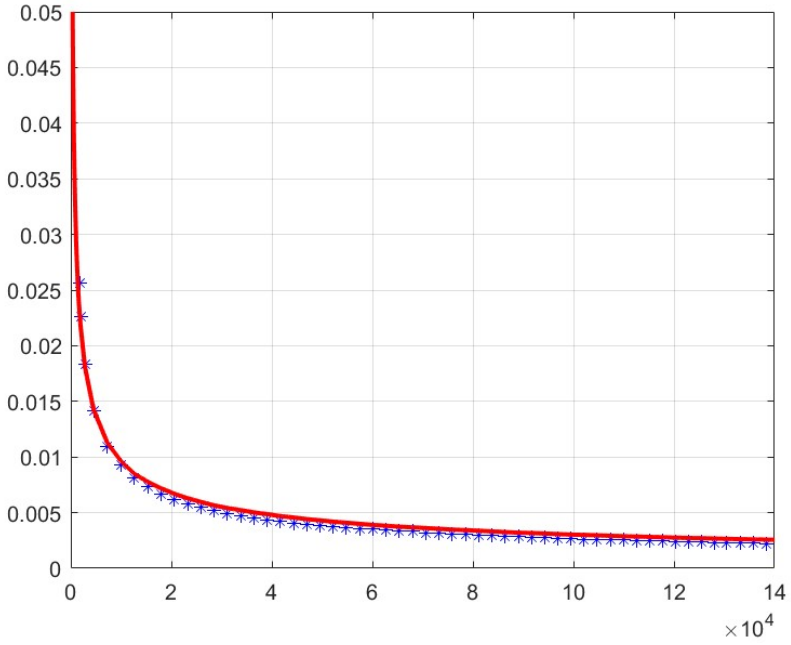
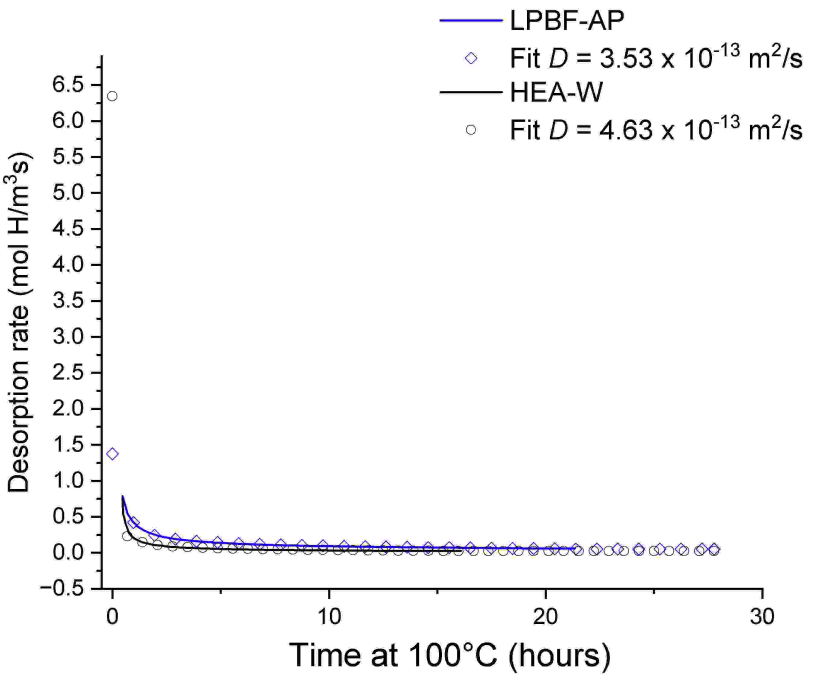
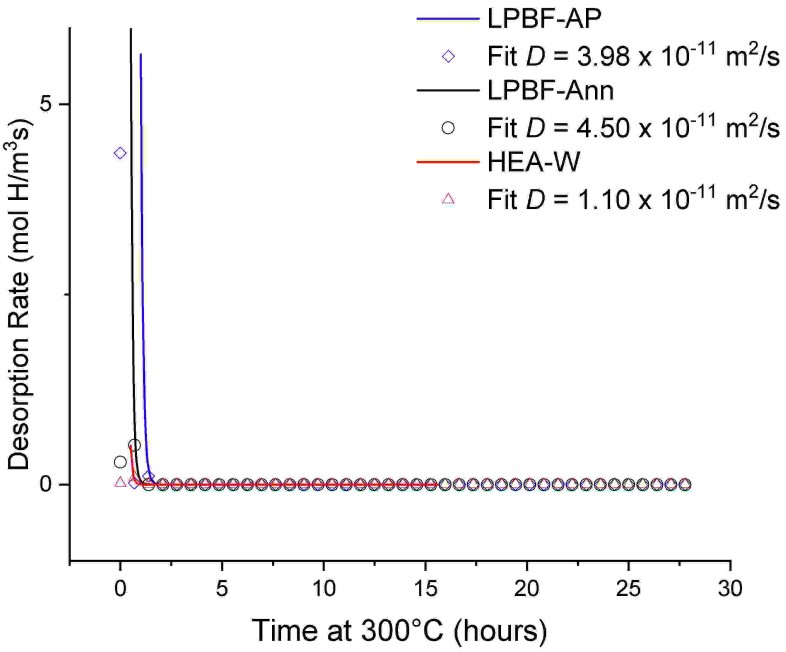


Figure D.3: Output graph of the fitting for LPBF-AP at 22°C



(a)



(b)

Figure D.4: Isothermal TDS and numerical fitting for diffusivity calculations. Isothermal TDS (ITDS) experiments performed at (a) 100°C and (b) 300°C and the best fit to 1-D hydrogen transport FE simulations.

Appendix E

TDS Simulator

The *TDS Simulator* is a Matlab® software tool aimed at modeling thermal desorption spectroscopy (TDS) experiments. It is capable of simulating TDS curves for arbitrary choices of material parameters and hydrogen trap characteristics, using the primary hydrogen diffusion and trapping model (Oriani, McNabb-Foster). Moreover, it is capable of loading experimental TDS data and conducting the inverse calibration of a selected transport model, providing automatic estimates of the density and binding energy of each hydrogen trap type in the material[162]. This second functionality is the one that is relevant in this work.

The major advantage of using the *TDS Simulator* is that it allows determination of trapping parameters with only experimental TDS data from one sample, eliminating the need for multiple TDS tests which are costly and time-consuming. Hence in this work, three samples of less than 0.5 mm thickness were tested, one for each microstructural condition (LPBF-AP, LPBF-Ann and HEA-W) to fully exploit this functionality.

The following figures represent the output from the *TDS Simulator* for LPBF-AP samples:

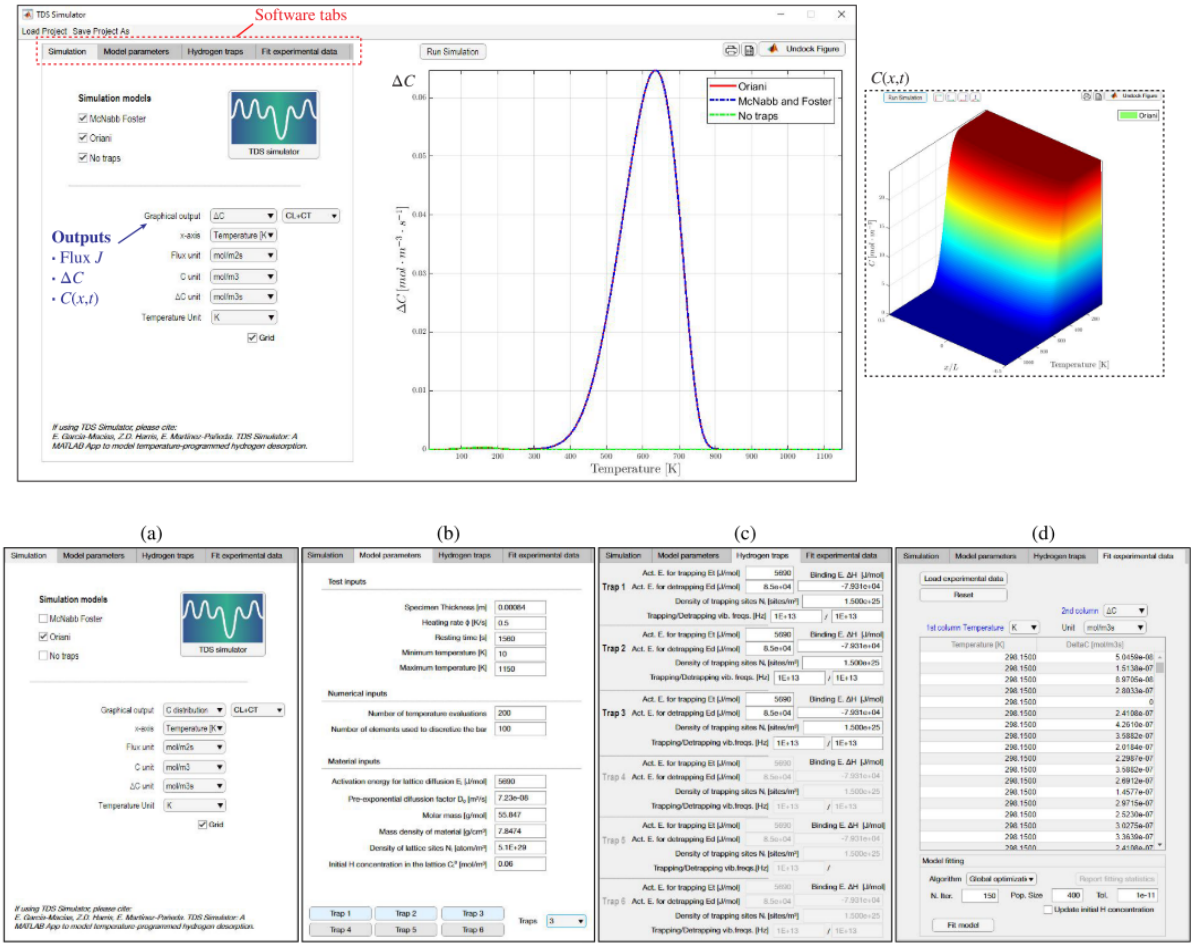


Figure E.1: Main graphical user interface (GUI) of the *TDS Simulator* in Matlab® and the four main tabs: a), model parameters tab (b), hydrogen traps tab (c), fit experimental data tab (d).

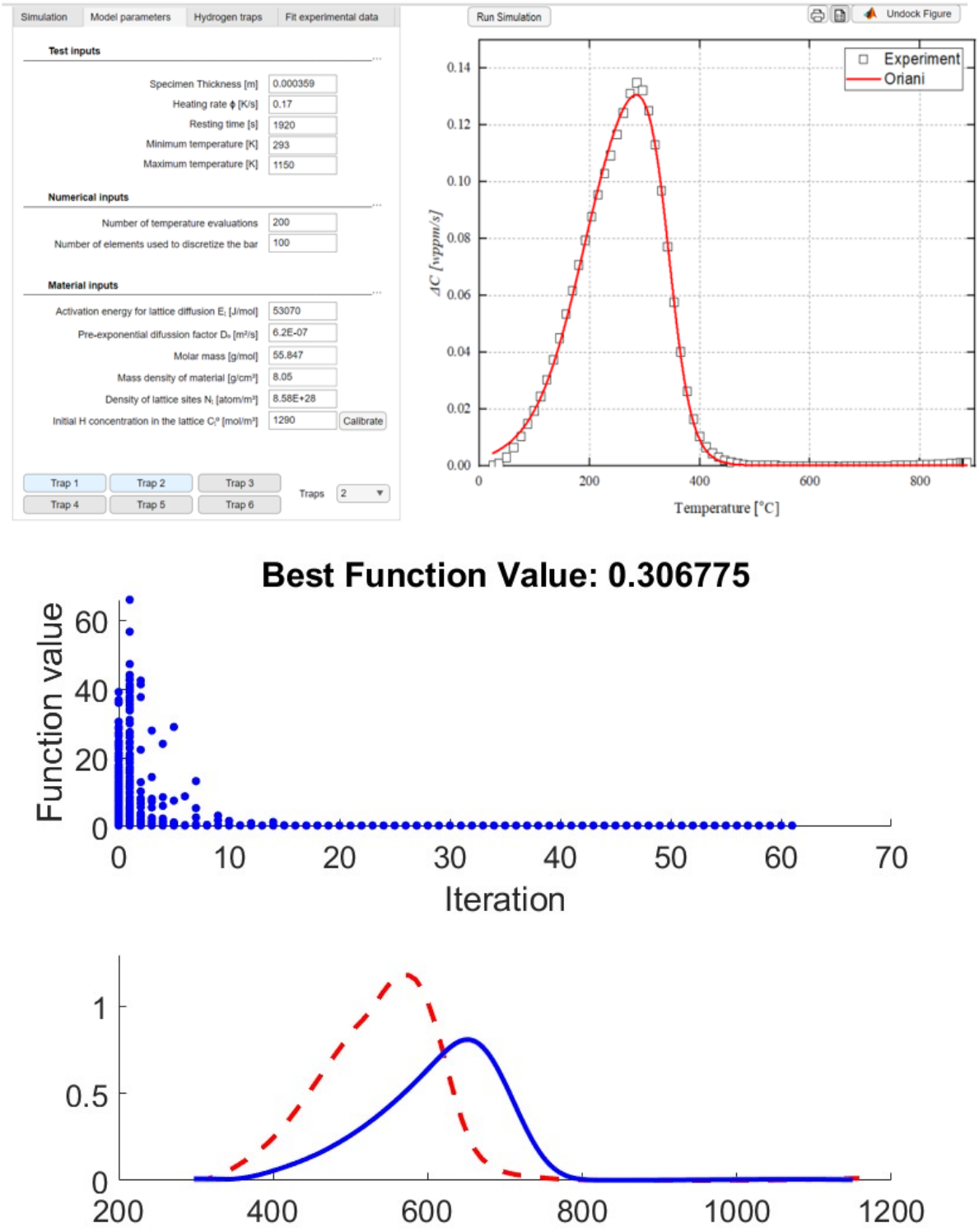


Figure E.2: *TDS Simulator* raw output for LPBF-AP sample showing fit to the experimental data and the iterative process (bottom figure).

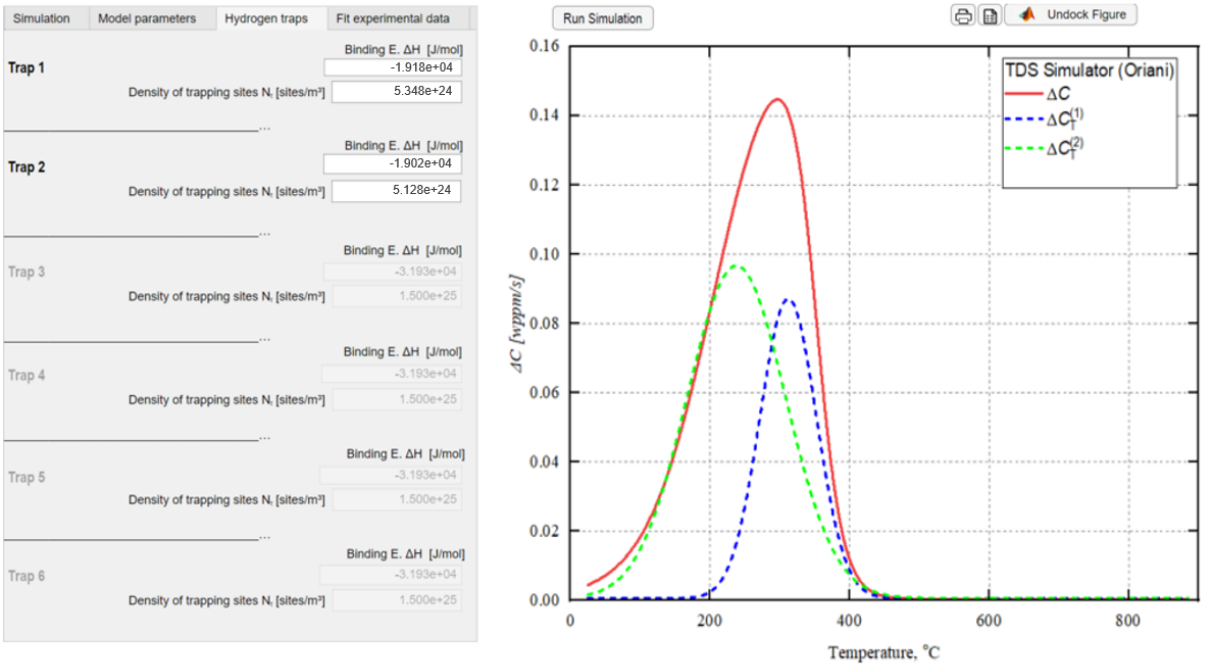
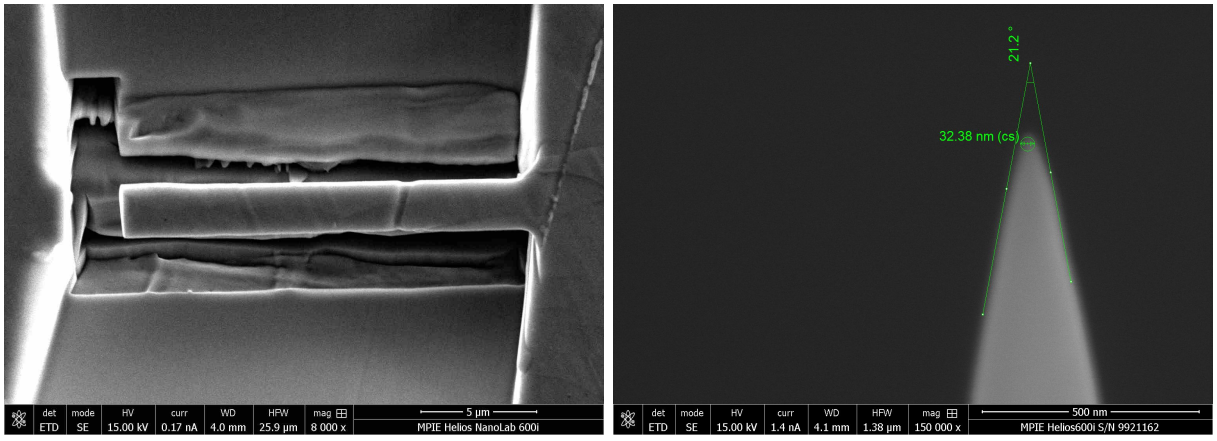


Figure E.3: *TDS Simulator* raw output for LPBF-AP showing the trap densities and binding energies related to the fitting of experimental data.

Appendix F

Sample preparation for atom probe tomography



(a) (b)

Figure F.1: (a) Lamella lift-out showing grain boundary, (b) sharpened tip of annealed specimen